

UNIVERSITY OF OKLAHOMA

GRADUATE COLLEGE

FLOW STRUCTURE OF LOW-DENSITY GAS JETS AND
GAS JET DIFFUSION FLAMES

A DISSERTATION

SUBMITTED TO THE GRADUATE FACULTY

in partial fulfillment of the requirements for the

degree of

Doctor of Philosophy

By

RAJANI P. SATTI
Norman, Oklahoma
2006

UMI Number: 3237836



UMI Microform 3237836

Copyright 2007 by ProQuest Information and Learning Company.
All rights reserved. This microform edition is protected against
unauthorized copying under Title 17, United States Code.

ProQuest Information and Learning Company
300 North Zeeb Road
P.O. Box 1346
Ann Arbor, MI 48106-1346

FLOW STRUCTURE OF LOW-DENSITY GAS JETS AND
GAS JET DIFFUSION FLAMES

A DISSERTATION APPROVED FOR THE
SCHOOL OF AEROSPACE AND MECHANICAL ENGINEERING

BY

Dr. Ajay K. Agrawal, Co-Chair

Dr. M. Cengiz Altan, Co-Chair

Dr. Ramkumar Parthasarathy

Dr. Feng-Chyuan Lai

Dr. Dimitrios V. Papavassiliou

ACKNOWLEDGEMENTS

My dissertation work has been challenging and extensive, but in the first place exciting and enlightening. Without help, support, and encouragement from several persons, I would never have been able to finish this work.

I am deeply indebted to my advisor Dr. Ajay Agrawal for his continuous support and guidance during my doctoral study. In spite of his busy schedule, he relentlessly worked with me to complete my dissertation write up on time. He was accessible at all times to discuss my work and to help with the problems encountered. His mentorship, patience and his belief in me made this work possible. It was under his direction and guidance that I developed a focus and became interested in both the numerical and experimental aspects of fluid dynamics. His understanding, expertise, commitment and sincerity have added significantly to my graduate experience.

My special thanks to my co-advisor, Dr. Cengiz Altan for his support and guidance throughout my graduate study. I would like to thank the members of my committee Dr. Ramkumar Parthasarathy, Dr. Feng-Chyuan Lai and Dr. Dimitrios Papavassiliou for taking time to review my work.

My gratitude also extends to my roommates, Vijaykant and Pankaj for all their help and support during the documentation of my dissertation. Many thanks are extended to all my friends and colleagues including Nandakishore Vedantam,

Kasyap Pasumarthi, Chendhil Periasamy, Sudhakar Peravalli, Vijay Chary, Kiran Kumar, Kalyan Srinivasan and Sumanth Peravalli.

Most importantly, I would like to thank my parents, Gopala Reddy and Anuradha and my sister, Rajitha for their love and encouragement in every stage of my career. I would like to especially thank my father, my best friend Chandu and my wife Jyotshna for encouraging me to pursue doctoral studies. I am deeply grateful for the love, encouragement and understanding of my beloved wife, Jyotshna who shared all my good and bad times during my graduate study. Without her, this work would not be possible.

My gratitude also extends to the staff of the AME department at OU and NASA's Office of Biological and Physical Research for funding my research.

This dissertation is dedicated to my family and my best friend Chandu.

TABLE OF CONTENTS

1. BACKGROUND.....	1
1.1 Low-Density Gas Jets	4
1.2 Crossbeam Rainbow Schlieren Deflectometry	6
1.3 Miniature Rainbow Schlieren Deflectometry	8
2. OBJECTIVES	10
3. CFD ANALYSIS OF THE FLOW STRUCTURE OF LOW-DENSITY GAS JETS	14
3.1 Overview of the Chapter	14
3.2 Literature Review	14
3.3 Model Description	18
3.3.1 Model Assumptions	18
3.3.2 Governing Equations	19
3.3.3 Boundary and Initial Conditions	20
3.3.4 Computational Details	21
3.3.5 Grid Convergence and Model Validation	21
3.4 Results and Discussion	23
3.4.1 Global Flow Characteristics.....	25
3.4.2 Steady Jet	27
3.4.2.1 Re=40	27
3.4.2.2 Re=70	28
3.4.3 Oscillating Jet	29
3.4.3.1 Simultaneous Visualization of Velocity and Concentration Fields	29
3.4.3.2 Vorticity Dynamics	32
3.4.3.3 Instantaneous Flow Structure	33
3.4.3.4 Mean and RMS Flow Structure	35
3.4.4 Instability Mechanism	37
3.5 Conclusions	38
4. BUOYANCY EFFECTS IN LOW-DENSITY GAS JETS	64
4.1 Overview of the Chapter	64
4.2 Literature Review	64
4.3 Model Description	68
4.4 Results and Discussion	69
4.4.1 Buoyant Jet	70
4.4.1.1 Flow and Concentration Fields in Earth Gravity.....	70
4.4.1.2 Flow and Concentration Fields during the Change	

From Earth Gravity to Microgravity	71
4.4.1.3 Temporal Evolution of Axial Velocity and Concentration Fields	73
4.4.1.4 Flow Structure: Dependence on Gravitational Forcing	74
4.4.2 Inertial Jet	75
4.4.2.1 Flow and Concentration Fields in Earth Gravity.....	75
4.4.2.2 Flow and Concentration Fields during the Change From Earth Gravity to Microgravity	76
4.4.2.3 Temporal Evolution of Axial Velocity and Concentration Fields	77
4.4.3 Comparison of Flow Behavior in Buoyant and Inertial Jets.....	78
4.4.3.1 Vortex Convection Velocity	78
4.4.3.2 Axial Velocity Profiles	78
4.4.3.3 Mean and RMS Flow Structure	80
4.4.3.4 Jet Half Radius	82
4.4.3.5 Flow Behavior in Microgravity.....	83
4.5 Conclusions	84
 5. CROSSBEAM CORRELATION TECHNIQUE FOR SCALAR TURBULENCE MEASUREMENTS IN GAS JETS/FLAMES	
5.1 Overview of the Chapter	109
5.2 Literature Review	109
5.3 Experimental System	113
5.3.1 Quantitative Rainbow Schlieren Deflectometry	113
5.3.2 Experimental Details	114
5.3.3 Optical Considerations	115
5.4 Experimental Observations	119
5.4.1 Turbulent Helium-Air Jet.	119
5.4.2 Turbulent Hydrogen Jet Diffusion Flame	121
5.5 Analysis Procedures	122
5.5.1 Introduction	122
5.5.2 Covariance and Variance Derivations	124
5.5.3 Crossbeam Correlation Analysis	129
5.6 Algorithm Validation: Laminar Case	135
5.6.1 Synthetic Data Generation	136
5.6.2 Results and Discussion	137
5.6.2.1 Case-1 (Near-Field)	137
5.6.2.2 Case-2 (Far-Field)	139
5.6.3 Limitations	141
5.7 Algorithm Validation: Turbulent Flow	142

5.7.1 Data Generation-RFG Code	142
5.7.2 Results and Discussion	145
5.7.2.1 Nature of Data	145
5.7.2.2 Angular Deflections	147
5.7.2.3 Mixing Function	147
5.7.2.4 Crossed Beam Covariance	148
5.8 Conclusions	149
6. MINIATURE RAINBOW SCHLIEREN DEFLECTOMETRY SYSTEM	208
6.1 Overview of the Chapter	208
6.2 Literature Review	208
6.3 Experimental Details	212
6.3.1 Experimental System	212
6.3.2 Optical Hardware	213
6.3.2.1 Light Source, Fiber Optic Cable and Source Aperture	213
6.3.2.2 Collimating and Decollimating Lenses	214
6.3.2.3 Rainbow Filter	216
6.3.2.4 Camera System	217
6.3.3 Test Media	217
6.3.4 Analysis Procedure	218
6.4 Results and Discussion	219
6.4.1 Helium Jet	220
6.4.2 Hydrogen Jet Diffusion Flame	221
6.4.3 Under-expanded Nitrogen Jet	222
6.4.4 Unsteady Flows	223
6.5 Conclusions	223
7. CONCLUSIONS	245
8. RECOMMENDATIONS	247
BIBLIOGRAPHY	249
APPENDIX A: NOMENCLATURE	256
APPENDIX B: DETAILS OF THE CFD MODEL	257
APPENDIX C: ABEL INVERSION	259
APPENDIX D: TRAPEZOIDAL RULE OF INTEGRATION	261

LIST OF TABLES

Table		Page
3.1	Summary of Test Conditions	24
4.1	Summary of Test Conditions	69

LIST OF FIGURES

FIGURE		PAGE
3.1	Schematic diagram of the computational domain	41
3.2	Temporal evolution of helium mole percentage for various grid sizes	42
3.3	Experimental-numerical comparison of helium mole percentage profiles in a steady helium jet, $Re=150$, $Ri=0.07$, $d=7.2\text{mm}$. (a) $z/d=1.0$ (b) $z/d=3.4$.	43
3.4	Comparison between computed and measured Strouhal number versus jet Richardson number.	44
3.5	Experimental (top) and computational (bottom) helium mole percentage contours during an oscillation cycle for $Re = 150$, $Ri = 6.4$ and $d = 31.8\text{ mm}$ at Earth gravity.	45
3.6	Variation of oscillation frequency with jet Reynolds number for $d=31.8\text{mm}$.	46
3.7	Velocity vectors for $d=31.8\text{mm}$. (a) $Re=40$, $Ri=85$ (steady) (b) $Re=70$, $Ri=30$ (steady) (c) $Re=90$, $Ri=17$ (Oscillating) (d) $Re=150$, $Ri=6.4$ (Oscillating).	47
3.8	Jet half radius in the flow direction based on helium concentration.	48
3.9	Jet half radius in the flow direction based on axial velocity profiles.	49
3.10	Profiles (inside the tube) of (a) axial velocity and (b) helium mole percentage, $Re=40$, $Ri=85$, $d=31.8\text{mm}$.	50
3.11	Profiles (outside the tube) of (a) axial velocity and (b) helium mole percentage, $Re=40$, $Ri=85$, $d=31.8\text{mm}$.	51
3.12	Profiles (inside the tube) of (a) axial velocity and (b) helium mole percentage, $Re=70$, $Ri=30$, $d=31.8\text{mm}$.	52

3.13	Profiles (outside the tube) of (a) axial velocity and (b) helium mole percentage, $Re=70$, $Ri=30$, $d=31.8\text{mm}$.	53
3.14	Contours of helium mole percentage overlapped by velocity vectors in an oscillation cycle for $Re = 150$, $Ri = 6.4$ and $d = 31.8 \text{ mm}$. (a) $t=0.0 \text{ ms}$; (b) $t=16.03 \text{ ms}$ (c) $t=32.06 \text{ ms}$; (d) $t=48.09 \text{ ms}$; (e) $t=64.12 \text{ ms}$; (f) $t=80.16 \text{ ms}$.	54
3.15	Normalized vortex convection velocity, $Re = 150$, $Ri = 6.4$ and $d = 31.8 \text{ mm}$.	55
3.16	Normalized axial velocity along the jet centerline in an oscillation cycle, $Re = 150$, $Ri = 6.4$ and $d = 31.8 \text{ mm}$.	56
3.17	Contours of vorticity magnitude overlapped by helium mole percentage in an oscillation cycle for $Re = 150$, $Ri = 6.4$ and $d = 31.8 \text{ mm}$. (a) $t=0.0 \text{ ms}$; (b) $t=16.03 \text{ ms}$ (c) $t=32.06 \text{ ms}$; (d) $t=48.09 \text{ ms}$; (e) $t=64.12 \text{ ms}$; (f) $t=80.16 \text{ ms}$.	57
3.18	Time trace plots of axial velocity and helium mole percentage at different radial locations for $Re = 150$, $Ri = 6.4$, $d = 31.8 \text{ mm}$. (1) $z/d=0.05$ (2) $z/d=0.6$ (3) $z/d=1.5$ (4) $z/d=2.5$.	58
3.19	Profiles of mean and RMS axial velocity, $Re = 90$, $Ri = 17$, $d = 31.8 \text{ mm}$.	59
3.20	Profiles of mean and RMS helium mole percentage, $Re = 90$, $Ri = 17$, $d = 31.8 \text{ mm}$.	60
3.21	Profiles of mean and RMS axial velocity, $Re = 150$, $Ri = 6.4$, $d = 31.8 \text{ mm}$.	61
3.22	Profiles of mean and RMS helium mole percentage, $Re = 150$, $Ri = 6.4$, $d = 31.8 \text{ mm}$.	62
3.23	Radial profiles of density gradient in radial direction at $z/d=0.3$.	63

4.1	Velocity vectors superimposed by contours of helium mole percentage during an oscillation cycle in Earth gravity for the buoyant jet, $Ri=1.52$, $Re=300$, $d=31.8\text{mm}$ (Case 1).	86
4.2	Measured (1) and computed (2) helium mole fraction contours during the change from Earth gravity to microgravity for the buoyant jet, $Ri=1.52$, $Re=300$, $d=31.8\text{mm}$ (Case 1).	87
4.3	Velocity vectors superimposed by contours of helium mole percentage during the change from Earth gravity to microgravity for the buoyant jet, $Ri=1.52$, $Re=300$, $d=31.8\text{mm}$ (Case 1).	88
4.4	Measured (a) and computed (b) time traces of helium mole fraction during the change from Earth gravity to microgravity for the buoyant jet, $Ri=1.52$, $Re=300$, $d=31.8\text{mm}$ (Case 1) at $z/d=1.0$.	89
4.5	Time traces of 1) helium mole percentage and 2) axial velocity during the change from Earth gravity to microgravity for the buoyant jet, $Ri=1.52$, $Re=300$, $d=31.8\text{mm}$ (Case 1) at (a) $z/d=0.15$ (b) $z/d=2.0$.	90
4.6	Vortex convection velocity at various gravitational levels.	91
4.7	Oscillation frequency Vs normalized gravitational acceleration.	92
4.8	Velocity vectors superimposed by contours of helium mole percentage during an oscillation cycle in Earth gravity for the inertial jet, $Ri=0.018$, $Re=800$, $d=14.5\text{mm}$ (Case 2).	93
4.9	Velocity vectors superimposed by contours of helium mole percentage during the change from Earth gravity to microgravity for the inertial jet, $Ri=0.018$, $Re=800$, $d=14.5\text{mm}$ (Case 2).	94
4.10	Figure 4.10. Time traces of 1) helium mole percentage and 2) axial velocity during the change from Earth gravity to microgravity for the inertial jet, $Ri=0.018$, $Re=800$,	

	d=14.5mm (Case 2) at (a) $z/d=0.5$ (b) $z/d=2.0$.	95
4.11	Vortex convection velocity normalized by the average jet exit velocity (U_v/U_j).	96
4.12	Axial velocity normalized by the jet exit velocity at the same radial location ($U/U_e(r)$) for Buoyant jet, $Ri=1.52$, $Re=300$, $d=31.8\text{mm}$ (Case 1).	97
4.13	Axial velocity normalized by the jet exit velocity at the same radial location ($U/U_e(r)$) for Inertial jet, $Ri=0.018$, $Re=800$, $d=14.5\text{mm}$ (Case 2).	98
4.14	Profiles of mean and RMS helium mole percentage for Buoyant jet, $Ri=1.52$, $Re=300$, $d=31.8\text{mm}$ (Case 1).	99
4.15	Profiles of mean and RMS axial velocity for Buoyant jet, $Ri=1.52$, $Re=300$, $d=31.8\text{mm}$ (Case 1).	100
4.16	Profiles of mean and RMS helium mole percentage for Inertial jet, $Ri=0.018$, $Re=800$, $d=14.5\text{mm}$ (Case 2).	101
4.17	Profiles of mean and RMS axial velocity for Inertial jet, $Ri=0.018$, $Re=800$, $d=14.5\text{mm}$ (Case 2).	102
4.18	Jet half radius determined from helium concentration.	103
4.19	Jet half radius determined from axial velocity.	104
4.20	Profiles of helium mole percentage in microgravity for the Buoyant jet, $Ri=1.52$, $Re=300$, $d=31.8\text{mm}$ (Case 1).	105
4.21	Profiles of axial velocity in microgravity for Buoyant jet, $Ri=1.52$, $Re=300$, $d=31.8\text{mm}$ (Case 1).	106
4.22	Profiles of helium mole percentage in microgravity for Inertial jet, $Ri=0.018$, $Re=800$, $d=14.5\text{mm}$ (Case 2).	107
4.23	Profiles of axial velocity in microgravity for Inertial jet, $Ri=0.018$, $Re=800$, $d=14.5\text{mm}$ (Case 2).	108

5.1	Schematic of the Crossbeam Schlieren apparatus.	151
5.2	Photograph of the Crossbeam Schlieren apparatus.	152
5.3	Photograph of the light source.	153
5.4	Instantaneous rainbow schlieren images (top) and space-time images (bottom) of a hydrogen jet diffusion flame for different exposure times at $z/d=1.5$.	154
5.5	Schlieren Images of a hydrogen diffusion flame for different filter configurations.	155
5.6	Instantaneous rainbow schlieren images of a turbulent helium-air jet at $Re=4000$, $d=10.0mm$, Crossbeam mode-1.	156
5.7	Instantaneous rainbow schlieren images of a turbulent helium-air jet at $Re=4000$, $d=10.0mm$, Crossbeam mode-2.	157
5.8	Time-space image of the turbulent helium-air jet at $Re=4000$, $d=10.0mm$, (a) Crossbeam mode-1 (b) Crossbeam mode-2.	158
5.9	Mean image of the turbulent helium-air jet at $Re=4000$, $d=10.0mm$, (a) Crossbeam mode-1 (b) Crossbeam mode-2.	159
5.10	RMS image of the turbulent helium-air jet at $Re=4000$, $d=10.0mm$, (a) Crossbeam mode-1 (b) Crossbeam mode-2.	160
5.11	Instantaneous schlieren images of a turbulent hydrogen diffusion flame at $Re=2400$, $d=1.19mm$, Crossbeam mode-1.	161
5.12	Instantaneous schlieren images of a turbulent hydrogen diffusion flame at $Re=2400$, $d=1.19mm$, Crossbeam mode-2.	162
5.13	Time-space image of a turbulent hydrogen diffusion flame at $Re=2400$, $d=1.19mm$, (a) Crossbeam mode-1 (b) Crossbeam mode-2.	163

5.14	Mean images of a turbulent hydrogen diffusion flame at $Re=2400$, $d=1.19mm$, (a) Crossbeam mode-1 (b) Crossbeam mode-2.	164
5.15	RMS image of a turbulent hydrogen diffusion flame at $Re=2400$, $d=1.19mm$, (a) Crossbeam mode-1 (b) Crossbeam mode-2.	165
5.16	Instantaneous schlieren images of a turbulent hydrogen diffusion flame at $Re=4200$, $d=1.19mm$, Crossbeam mode-1.	166
5.17	Instantaneous schlieren images of a turbulent hydrogen diffusion flame at $Re=4200$, $d=1.19mm$, Crossbeam mode-2.	167
5.18	Time-space image of a turbulent hydrogen diffusion flame at $Re=4200$, $d=1.19mm$, (a) Crossbeam mode-1 (b) Crossbeam mode-2.	168
5.19	Mean image of a turbulent hydrogen diffusion flame at $Re=4200$, $d=1.19mm$, (a) Crossbeam mode-1 (b) Crossbeam mode-2.	169
5.20	RMS image of a turbulent hydrogen diffusion flame at $Re=4200$, $d=1.19mm$, (a) Crossbeam mode-1 (b) Crossbeam mode-2.	170
5.21	Schematic illustrating the cross beam correlation technique.	171
5.22	Single beam schlieren system along the z direction	172
5.23	Illustration of the crossbeam technique using rainbow schlieren apparatus.	173
5.24	Profile of the refractive index (top) and contour plot representing the cross sectional plane after sweeping the profile in cartesian coordinates (bottom).	174
5.25	Variance of angular deflection-Case 1.	175

5.26	Exact Vs Inverted mixing function profiles-Case 1.	176
5.27	Contour plot of mixing function -Case 1.	177
5.28	Profiles of deflection angle covariance -Case 1.	178
5.29	Exact Vs CBC based integral length scales-Case 1.	179
5.30	Exact Vs CBC based intensity profiles-Case 1.	180
5.31	Variance of angular deflection-Case 2.	181
5.32	Exact Vs Inverted mixing function profiles-Case 2.	182
5.33	Contour plot of mixing function -Case 2.	183
5.34	Profiles of deflection angle covariance -Case 2.	184
5.35	Exact Vs CBC based integral length scales-Case 2.	185
5.36	Exact Vs CBC based intensity profiles-Case 2.	186
5.37	Flowchart illustrating the execution of the spectral generator (genspec).	187
5.38	Flowchart illustrating the execution of the vector-field generator (genvec).	188
5.39	Instantaneous snapshots of turbulent refractive index gradient field generated from RFG code.	189
5.40	(a) Mean and (b) Variance of the turbulent refractive index gradient field generated from RFG code (sample size=100000 time steps).	190
5.41	Instantaneous snapshots of two-point auto correlation coefficients.	191
5.42	Contour plot of integral length scale (l_z).	192
5.43	Contour plot of integral length scale (l_y).	193

5.44	Instantaneous deflection angle profiles of the turbulent refractive index field computed along the z direction.	194
5.45	Instantaneous deflection angle profiles of the turbulent refractive index field computed along the y direction.	195
5.46	Mean deflection angle profiles in y and z directions.	196
5.47	Profile of deflection angle variance along the z direction.	197
5.48	Contour plot of z-direction mixing function (f_z) given in eq. 5.16.	198
5.49	Exact Vs CBC based z-direction mixing function (f_z) profiles.	199
5.50	Profile of deflection angle variance along the y direction.	200
5.51	Contour plot of y-direction mixing function (f_y) given in eq. 5.17.	201
5.52	Exact Vs CBC based mixing function (f_y) profiles.	202
5.53	Contour plot of crossed beam covariance of deflection angles	203
5.54	Profile of the crossed beam covariance of deflection angles.	204
5.55	Refractive index gradient intensity calculated using eqs. 5.27 & 5.28.	205
5.56	Refractive index gradient intensity calculated using eqs. 5.29 & 5.30.	206
5.57	Refractive index gradient intensity calculated using eqs. 5.31, 5.32 & 5.33.	207
6.1	A photograph of the rainbow schlieren apparatus.	225

6.2	A photograph of the light source and the camera control unit.	226
6.3	Optical layout of the miniature schlieren apparatus.	227
6.4	Rainbow filter.	228
6.5	Filter calibration curves.	229
6.6	Schematic showing the working of the camera unit with (bottom) and without (top) the extension tube.	230
6.7	Optical components and injectors used for experiments.	231
6.8	Rainbow schlieren image for the helium jet, $d = 650 \mu\text{m}$, $\text{Re} = 375$.	232
6.9	Hue contours for the helium jet, $d = 650 \mu\text{m}$, $\text{Re} = 375$.	233
6.10	Radial profiles of helium mole percentage, $d = 650 \mu\text{m}$, $\text{Re} = 375$.	234
6.11	Contours of helium mole percentage, $d = 650 \mu\text{m}$, $\text{Re} = 375$.	235
6.12	Rainbow schlieren image for the hydrogen diffusion flame, $d = 50 \mu\text{m}$, $\text{Re} = 410$.	236
6.13	Hue contours for the hydrogen diffusion flame, $d = 50 \mu\text{m}$, $\text{Re} = 410$.	237
6.14	Radial profiles of temperature distribution, $d = 50 \mu\text{m}$, $\text{Re} = 410$.	238
6.15	Radial profiles of oxygen mole percentage, $d = 50 \mu\text{m}$, $\text{Re} = 410$.	239
6.16	Contours of temperature distribution, $d = 50 \mu\text{m}$, $\text{Re} = 410$.	240
6.17	Contours of oxygen mole percentage, $d = 50 \mu\text{m}$, $\text{Re} = 410$.	241

6.18	Schlieren images showing the formation of shock diamonds, $d = 650\text{ }\mu\text{m}$ at 60psi.	242
6.19	Schlieren images showing the effect of supply pressure on shock cell structure, a) $d = 650\text{ }\mu\text{m}$, b) $d = 300\text{ }\mu\text{m}$.	243
6.20	Schlieren images of a hydrogen diffusion flame, $d = 50\text{ }\mu\text{m}$.	244

ABSTRACT

Buoyant jets and flames have been a subject of significant research in fluid dynamics. Such flows are influenced by near field instabilities, turbulence, buoyancy, chemistry, heat release, etc. The present research deals with computational and experimental studies to improve understanding of laminar-turbulent jets and flames.

As a first step, computational analysis of the near-field flow structure in an isothermal helium jet injected into quiescent ambient air environment was conducted. Laminar, axisymmetric, unsteady flow conditions were considered for the analysis. The transport equations of helium mass fraction coupled with the conservation equations of mixture mass and momentum were solved using a staggered grid finite-volume method. The jet Reynolds number, Re was varied from 40 to 150 to encompass steady and oscillating jet flow regimes. Comparison with experimental data revealed excellent agreement, proving reliability of the model in predicting global flow characteristics. At low jet Reynolds numbers, the flow was steady and the concentration shear layer at the tube exit was stratified by mixing between jet and ambient fluids inside the tube. At higher jet Reynolds numbers ($Re = 90$ and 150), buoyancy induced acceleration contracted the jet core to form a toroidal vortex by entrainment of the ambient fluid. The mechanism of instability in low-density gas jets was also explored.

Next, the effects of buoyancy on buoyant and inertial low-density gas jets were studied by initiating computations in Earth gravity and subsequently, reducing the gravity to simulate microgravity conditions in the 2.2 s drop tower. Computed results again concurred with experimental observations, i.e., a self-excited buoyant jet with periodic flow oscillations in Earth gravity becomes steady in microgravity. In an inertial jet, the flow oscillations occur at the same frequency regardless of the buoyancy, although the oscillation amplitude decreases in microgravity.

From an experimental perspective, past applications of rainbow schlieren deflectometry, an optical diagnostic technique to measure scalar properties across the whole field were limited to measuring only laminar jets/flames. In order to facilitate turbulence measurements, a crossbeam rainbow schlieren deflectometry system was developed and demonstrated by presenting schlieren visualizations of turbulent jets and flames. The schlieren images captured the instantaneous scalar structure of turbulent jets and flames. Statistical analysis of schlieren data demonstrated the well known axisymmetry assumption of turbulence in round jets and flames. Subsequently, the theoretical framework of the crossbeam correlation technique requiring assumptions of homogeneous and isotropic turbulence was presented. The validity of the technique was also verified using laminar and turbulent data generated synthetically. The limitations of the technique were also discussed.

As a successive step towards development of advanced optical diagnostic systems for measuring fluid flow phenomena in small scale turbulent structures, a miniature rainbow schlieren deflectometry system to non-intrusively measure species concentration and temperature data across the whole field was developed. The optical layout of the miniature schlieren system was similar to that of a macro-scale system, although the field of view was smaller by an order of magnitude. Employing achromatic lenses of 10 mm diameter, and a CCD sensor with camera sensor and extension tubes, the system achieved spatial resolution down to 4 μm per pixel. Quantitative measurements required a careful evaluation of the optical hardware. The capability of the system configured using off-the-shelf optical components was demonstrated by obtaining concentration measurements in a helium micro-jet (diameter, $d = 650 \mu\text{m}$) and temperature and concentration measurements in a hydrogen jet diffusion flame from a micro-injector ($d = 50 \mu\text{m}$). Finally, the flow field of under-expanded nitrogen jets was visualized to reveal details of the shock structures existing downstream of the jet exit.

CHAPTER 1. BACKGROUND

Over the past 50 years, turbulent jets and flames have received extensive research attention that has resulted in various experimental, theoretical and numerical studies. Turbulent jets and flames are of significant interest in many engineering applications and in natural phenomena involving environmental and geophysical science. Important examples linked to residential or industrial activity are smoke plumes from chimneys or oil fires, engine exhaust, fuel leaks, effluent from submerged pollution outlets, jet propulsion, or even the extreme case of a nuclear accident, while naturally occurring flows include activity of seafloor hydrothermal vents, convection in clouds and, most energetic of all, stratospheric plumes caused by explosive volcanic eruptions.

The structure of the above mentioned flows is predominantly influenced by turbulence, buoyancy, chemical kinetics, heat release, mass diffusion, etc. The complex interaction of these physical processes makes it difficult to develop a fundamental understanding of turbulent jets and flames. In particular, the effect of buoyancy on the global flow structure of jets/flames can be significant. The study of the effect of buoyancy is however complicated by the difficulty of isolating buoyancy from competing effects in the system. One particularly useful method for studying this effect is to compare flows in earth gravity to those in a microgravity environment, produced for example in a drop-tower. The drop tower

studies are however difficult to perform when unsteady reacting flows with species transport and complex chemistry are involved. In order to simplify the above issues, one could consider the case of a non-reacting jet flow which does not have the added flow complexities of chemical reactions. In particular, many key features of turbulent flames can be represented in a turbulent low-density jet. Hence, a comprehensive understanding of buoyant non-reacting jets is an important step towards the study of reacting jets.

Based on the foregoing discussion, the present research is first focused on the analysis of a non-reacting low-density gas jet using numerical and experimental methods. From a numerical perspective, it is well known that the laminar and turbulent regions of low-density gas jets exhibit time-dependent behavior and are susceptible to a variety of instabilities. In the laminar near field region, the unsteadiness is characterized by the periodic shedding of coherent vortical structures (often termed as self-excited oscillations) at a well defined frequency. On the contrary, random and irregular vortical structures define the unsteadiness in the turbulent regime. This complex unstable behavior (laminar or turbulent) exhibited by low-density gas jets has highlighted the need for detailed numerical studies. However, before developing turbulence models for a complete simulation of turbulent gas jets, it is imperative to first gain insight into the unsteady features (self-excited oscillations) of laminar gas jets. Besides, the study

of laminar jet instabilities is important in its own right because of its direct influence on the turbulent mixing and entrainment processes in the far-field.

The numerical simulation of laminar near field jets followed by a complete laminar-turbulent simulation of low-density gas jets would provide an in-depth understanding of turbulent jets. However, turbulence models can only be used with confidence if they have been tested using experimental data. Moreover, theoretical or numerical predictions involve modeling assumptions, so there is a need for experimental testing and measurements of turbulent jets/flames to validate such assumptions. As scalar turbulence is an influential factor in the fluid mechanics of combusting jets, the fluctuations of scalar variables, such as density and temperature gain importance. The need for accurate scalar measurements without disturbing the flow along with high spatio-temporal resolution precludes the use of traditional probe techniques. Therefore, in recent years, much of the effort has been expended in developing non-intrusive optical diagnostics for the measurements of fluid flows associated with combustion processes.

With the rapid development of modern optical diagnostics and image processing techniques, whole field optical diagnostics are assuming ever expanding roles in the diagnostic probing of fluid mechanics and combustion. Of particular importance to the present study is the development of a crossbeam rainbow schlieren deflectometry apparatus capable of providing whole field turbulent scalar measurements in gas jets and flames. It is also important to

validate the algorithms and analysis procedures used to process the experimental data.

Further, the need for high spatial and temporal resolutions for resolving the fine scales of turbulent jets/flames has also prompted the miniaturization of the schlieren apparatus. Hence, the last part of the present study deals with the development and demonstration of a first generation miniature rainbow schlieren deflectometry apparatus capable of providing scalar measurements at spatial resolution of few microns. The remaining section of this chapter provides brief background on the three main topics covered in this research: (1) Low-density gas jets (2) Crossbeam rainbow schlieren deflectometry (3) Miniature rainbow schlieren deflectometry.

1.1 Low-Density Gas Jets

A low-density gas jet is characterized by the injection of a low-density fluid into a high-density ambient surrounding. The flow structure of a low-density gas jet can be divided into three regions: laminar (near field), transition and turbulent (far-field) regimes. Past studies (So et al., 1990; Papanicolaou and List, 1988; Richards and Pitts, 1993; Panchapakesan and Lumley, 1993) have pointed out that the near field self-excited oscillations affect the far-field turbulent entrainment and mixing characteristics. This oscillating instability has been identified as being similar to the flicker behavior seen in the near field of pool fires and buoyant jet diffusion flames.

The important parameters for analysing the low-density gas jets are the Reynolds number, Richardson number, Strouhal number and the jet density ratio. Based on these non-dimensional numbers, low-density gas jets can be classified as buoyancy-dominated or momentum-dominated and steady or unsteady. Under certain conditions, low-density gas jets exhibit self-excited oscillations in the near-field which makes the time-dependent behaviour coupled with buoyancy effects more important. Several experimental studies involving oscillating laminar low-density gas jets with respect to both velocity and scalar fields have been performed. The experimental works of Subbarao and Cantwell (1992) and Cetegen and co-workers (1996, 1997a, b) provide detailed flow measurements in low-density gas jets. Agrawal and co-workers (2003) have successfully applied quantitative Rainbow Schlieren Deflectometry (RSD) to measure the concentration and/or temperature in the near-field of steady and unsteady gas jets and diffusion flames.

In spite of the recent advances in flow diagnostic instruments, researchers still face difficulties in delineating the global flow structure and buoyancy effects in low-density gas jets. Though drop tower experiments have been used to isolate buoyancy effects in jets and flames, issues relating to test apparatus size, power and weight constraints, equipment survivability, short run times etc are yet to be resolved.

Recent advances in computational techniques have seen the advent of Computational Fluid Dynamics (CFD) to gain insight into the detailed flow structure of jets and flames. The CFD analysis has been used for basic studies of fluid dynamics, for engineering design of complex flow configurations, and for predicting the interactions of chemistry with fluid flow for combustion and propulsion applications. The CFD analysis can also assist in the interpretation of experimental data and to probe regimes that are inaccessible or too costly to study experimentally.

1.2 Crossbeam Rainbow Schlieren Deflectometry

Most of the combustion processes in industry (e.g., furnaces and engines) and nature (e.g., forest fires) are turbulent. Understanding the fundamental processes involved in turbulent combustion can lead to improved predictive capability and practical combustor system designs with high efficiency and low pollutant emissions. It can also lead to improved fire safety and fire protection practices. Hence, detailed measurements of velocity and scalar fields are required to gain insight into the physics of turbulent combustion, as discussed previously. Such measurements are difficult to obtain in the presence of turbulent fluctuations. Many of the past studies have utilized intrusive probes, which are known to perturb the flow and thereby, affect the measurements. Thus, non-intrusive measurements at high spatial and temporal resolutions are necessary to obtain quantitative details of turbulent jets and flames.

In recent years, rainbow schlieren deflectometry or RSD, a path integrated technique, has been employed for measurements in non-reacting and reacting flows by Agrawal and co-workers (1998, 1999, 2003, 2006). In particular, the RSD technique allows measurements across the whole field without relying upon seeding, soot or specific fuel species to mark the flow structure. Past applications of the RSD technique are limited only to steady or unsteady laminar flows. This limitation was imposed because of the tomographic inversion required to deconvolute local properties from the path-integrated deflection angle data measured at one view angle by the schlieren technique. Random fluctuations in turbulent flows require path integrated data at multiple view angles, which complicates the optical configuration and the tomographic inversion procedure.

Studies by Fisher and Krause (1967), Wilson and Damkevala (1969), Davis and co-workers (1970, 1971, 1975) introduced the concept of crossbeam correlation technique to obtain scalar turbulence information from the line-of-sight measurements. The crossbeam correlation technique is an optical technique which is based on the detection of deflections by light beams transmitted through a turbulent flow field. The measured signal represents an integral along the beam path, although Fisher and Krause (1967) have shown that it is possible to extract localized information by statistically cross correlating such fluctuating signals from two mutually perpendicular light beams which intersect inside the flow. Since the crossbeam correlation technique can provide local turbulence

measurements without flow seeding, its use in conjunction with the rainbow schlieren apparatus can be extremely useful. However, the algorithms used to deconvolute local properties from crossbeam measurements must be validated before the technique can be used with confidence for scalar turbulence measurements.

1.3 Miniature Rainbow Schlieren Deflectometry

It is well known that the flow physics of turbulent jets/flames is affected by the jet Reynolds number. In high Reynolds number turbulent flows, the size of the turbulent structures varies from the largest (macro) to the smallest (micro) scales. In such cases, the large spectrum of flow scales requires the instantaneous measurements of the flow field quantities over regions including the larger flow scales, and with sufficiently high spatial resolution to detect the smaller flow scales. The resolution of these fine scales of turbulence requires miniaturization of the present day flow diagnostic systems, which can provide high spatio-temporal resolution without disturbing the flow.

In the past few years, the development of micro-Particle Image Velocimetry (Santiago et al., 1998; Meinhart and Zhang, 2000) and laser Doppler velocimetry technique (Onofri (2006)) has led to velocity measurements at high spatial resolution. Though several techniques are available to measure the velocity field, the diagnostics of scalar fields (e.g., temperature and species concentration) using non-intrusive techniques as such has received little attention. Hence, a

miniature rainbow schlieren deflectometry system capable of providing scalar measurements at high spatial resolution is required to probe micro-scale fluid flows and also aid in resolving the finest scales of turbulence in jets/flames.

The above background study on laminar-turbulent jets and flames thus emphasizes the need for the following studies:

- Numerical simulations of unsteady, laminar, buoyant low-density gas jets
- Development of experimental procedures and validation of analysis techniques to facilitate non-intrusive scalar turbulence measurements in jets/flames
- Development of a miniature experimental system capable of probing fluid flow phenomena at high spatial resolution.

CHAPTER 2. OBJECTIVES

The present research deals with numerical and experimental studies to improve understanding of laminar-turbulent jets/flames. As a first step, unsteady laminar flow analysis of buoyant and inertial low-density gas jets was performed using CFD. Next, a crossbeam rainbow schlieren deflectometry system was proposed to facilitate scalar turbulence measurements in jets and flames. Subsequently, theoretical and mathematical modeling procedures for the application of crossbeam correlation technique with rainbow schlieren apparatus were developed and validated. As an extension to the experimental capabilities, a miniature schlieren system to probe micro-scale fluid flow phenomena was developed and demonstrated by taking scalar measurements in micro jets and flames. The specific tasks are divided into four steps and are outlined below.

Step 1: CFD Analysis of the Flow Structure of Low-Density Gas Jets (Chapter 3)

- Model the laminar axisymmetric helium jet injected into quiescent air environment.
- Achieve qualitative and quantitative comparisons of computational model by comparing with experimental data of stable/unstable modes in low-density gas jets.

- Present simultaneous visualizations of concentration and velocity/vorticity fields to gain insight into the near field flow dynamics of the helium-air jet.
- Explore the mechanism of jet instability in low-density gas jets.

Step 2: Buoyancy Effects in Low-Density Gas Jets (Chapter 4)

- Quantify the effects of buoyancy on the oscillating flow-structure of low-density gas jets.
- Explore the physical implications of the self-excited instability in low-density gas jets in the buoyant and inertial flow regimes.

Step 3: Crossbeam Correlation Technique for Scalar Turbulence Measurements in Gas Jets/Flames (Chapter 5)

- Design and develop the crossbeam rainbow schlieren deflectometry system to obtain scalar turbulence measurements.
- Present the theoretical framework of the crossbeam correlation technique.
- Analyze and validate the crossbeam correlation technique for scalar measurements using synthetic laminar/turbulent scalar data.

Step 4: Miniature Rainbow Schlieren Deflectometry System (Chapter 6)

- Develop a miniature RSD apparatus using off-the-shelf optical hardware.
- Obtain reliable and accurate scalar measurements in micro-jets and flames at high spatial resolution.

2.1 Organization of the Thesis

The contents of the thesis are organized in the following way. Chapter 3 first reviews the experimental and numerical studies relating to self-excited oscillations in laminar low-density gas jets. The review emphasizes the need for detailed numerical simulations to examine the flow structure of steady/unsteady buoyant low-density gas jets. The governing equations, initial and boundary conditions and solution procedures are subsequently presented. The computed results are validated by comparing with existing experimental data. In the results section, the structural features of steady/unsteady jets are presented. Besides providing details of the flow structure, the mechanism of instability in low-density gas jets is also explored.

The effects of buoyancy on the stable/unstable modes of low density gas jets are presented in Chapter 4. Both buoyant and inertial jets are considered in Earth gravity and microgravity by analyzing instantaneous and time averaged velocity and helium concentration fields. The CFD analysis is used to

concurrently visualize velocity and concentration fields, a difficult experimental task, especially in the constrained environment of the microgravity facilities.

In chapter 5, a literature review of the applications of crossbeam correlation technique for scalar turbulence measurements in jets/flames is presented first. Next, the crossbeam experimental set up and the associated optical hardware are discussed. Rainbow schlieren images of turbulent jets/flames are presented at orthogonal view angles. Finally, the theoretical framework of the crossbeam correlation technique is discussed and then validated using synthetic data of unsteady laminar and turbulent flows.

Chapter 6 deals with the development and demonstration of a miniature rainbow schlieren system for probing micro-scale fluid flow phenomena. The capability of the system is demonstrated by obtaining scalar measurements in micro-jets and flames with spatial resolution down to 4 μm .

In chapter 7, the main conclusions of the present study are presented. Obtained results are discussed and the recommendations for future are presented in Chapter 8.

CHAPTER 3. CFD ANALYSIS OF THE FLOW STRUCTURE OF LOW-DENSITY GAS JETS

3.1 Overview of the Chapter

A comprehensive study of non-reacting jets forms the basis for eventually understanding the fluid mechanics of reacting jets. In this chapter, the steady and oscillating flow structure of laminar low-density gas jets was investigated using computational fluid dynamics. First, a review of the existing experimental and numerical studies on low-density gas jets is presented to provide the justification for a detailed numerical simulation of low-density gas jets. Next, the analysis procedure based on unsteady, laminar, axisymmetric, isothermal flow in a binary flow system is explained. In the results section, computations are first compared with experimental data to verify the analysis procedures. Subsequently, the global flow features of steady and oscillating low-density gas jets are presented. Structural details of the flow field are discussed using instantaneous, mean and RMS profiles of helium concentration and axial velocity. The mechanism of instability in low-density gas jets is also explored.

3.2 Literature Review

Turbulent plumes and jets have been a subject of research in various applications. The dynamics of these flows has attracted several theoretical, numerical and experimental studies since the 1950s. Of particular interest is a low-density gas jet injected into high density ambient with relevance to fuel leaks,

engine exhaust, diffusion flames, materials processing, and natural phenomena such as fires and volcanic eruptions. Early experimental work by Corrsin (1943), Corrsin & Uberoi (1950, 1951) and Wygnanski & Fiedler (1969) used hot wire measurements to measure temperature fluctuations in turbulent jets. Wygnanski & Fiedler (1969) performed hot-wire measurements to study turbulence intermittency, skewness, correlations and mean velocity.

Recent experiments on round jets that provide data on mean velocities, turbulent intensities, turbulent stresses, and scalar statistics include Panchapakesan & Lumley (1993), Hussein et al (1994) and Dowling & Dimotakis (1990). The flow structure in the far-field turbulent regime is however influenced by the near-field processes such as diffusion, buoyancy, entrainment, jet instability, and transition from laminar to turbulent flow. In particular, it is important to study the near-field laminar flow structure in such jets, whereby the effects of buoyancy are significant.

Pera and Gebhart (1963), Tenner and Gebhart (1971), Gebhart (1973) and Mollendorf and Gebhart (1973) studied flow instabilities and transition to turbulence in buoyant plumes and jets. They found that a laminar, buoyant water jet injected from a circular tube into a quiescent medium induced a toroidal vortex. Hamins et al. (1992) identified self-excited periodic oscillations in helium jets injected into air, and reported that a minimum jet exit velocity was required to initiate oscillations. A comprehensive insight into the flow behavior of low-

density gas jets was provided by Subbarao and Cantwell (1992) using helium injected from a tube into a co-flow of air. Experiments revealed highly periodic oscillations in the near field for a range of jet Reynolds numbers, $Re = 300$ to 1500 and jet Richardson numbers, $Ri = 0.5$ to 6.0 . They speculated that the perturbations in the air stream, for example, on the surface boundary layer outside the jet tube, dominated the instability and transition from laminar to turbulent flow.

Cetegen and co-workers (1993, 1996, 1997a, b) performed detailed experiments involving planar and axisymmetric plumes of helium or helium-air mixtures for a range of injector diameters, jet fluid densities, and jet exit velocities. They found that the flow oscillation frequency represented by the Strouhal number (St) correlated with Ri , suggesting that the oscillations were buoyancy induced. Velocity measurements revealed buoyant acceleration of the low-density fluid causing the jet core to contract, and thus, entrain the ambient fluid. Entrainment resulted in the formation of a toroidal vortex that interacted with the jet core while convecting downstream. Pasumarthi and Agrawal (2003) obtained instantaneous concentration measurements across the whole field using quantitative rainbow schlieren deflectometry to characterize the toroidal vortex and its interactions with the jet core. Yep et al. (2003) conducted experiments in drop tower to show that the flow oscillations occurring in Earth gravity

disappeared in microgravity. These experiments provided direct evidence that the self-excited periodic oscillations in low-density gas jets are buoyancy induced.

The experimental observations have also been supported by numerical simulations of Mell et al. (1996), who achieved good agreement between computed and measured flow oscillation frequencies. The computational study by Soteriou et al. (2002) provided flow structure details of planar low-density gas jets. The nature of the instability and relative roles of buoyancy and diffusion in triggering/sustaining the instability were also explored. Using intuitive arguments, they proposed that diffusion was important in initiating the flow instability. Diffusion however assumed a secondary role after the instability was manifested.

In spite of the vast literature on jet flows, the detailed flow structure in the near-field of low-density buoyant jets has not been documented in past studies. Experimental studies have described the flow using either velocity or concentration measurements, which are inadequate to elucidate the strong coupling between velocity and concentration fields in low-density gas jets. In this regard, the analysis based on computational fluid dynamics (CFD) is useful because it provides flow structure details including simultaneous visualization of vector-scalar fields throughout the region of interest. However, past computational studies have considered either the global features of the oscillating jet (Mell et al., 1996) or the planar jets (Soteriou et al. 2002). Detailed CFD analysis is therefore needed to not only characterize the flow structure of steady

and oscillating jets, but also to explain the mechanism of instability in circular jets.

The objective of the present computational study is to examine the flow structure of low-density buoyant gas jets issued from a circular tube into quiescent ambient, which is among the most practical jet configurations. Numerical simulations were performed to identify and explain interactions among velocity and concentration fields over a range of jet Reynolds numbers. Computations were done using an unsteady model and no external perturbations were introduced to ensure that the flow oscillations, if present, were self-excited. The jet flow is characterized by velocity vectors, and profiles of jet half radius, axial velocity and helium concentration, etc. Both instantaneous and mean structure is presented in case of the oscillating flow. Results are presented to highlight unique features of steady and oscillating low-density gas jets. Besides providing details of the flow structure, the mechanism of instability is explored.

3.3 Model Description

3.3.1 Model Assumptions

Experiments have shown that a round helium jet injected into air remains symmetric in the near-field region (Pasumarthi and Agrawal, 2003; Yep et al., 2003). Moreover, the flow symmetry is preserved even in the presence of unsteady effects such as the periodic oscillations. The following approximations were made to simplify the analysis: (i) the flow is incompressible and

axisymmetric, (ii) temperature and pressure variations are negligible and (iii) the flow is a binary fluid system with air treated as a single species. The justification for these simplifications is discussed in detail by Kyle (1991).

3.3.2 Governing Equations

The conservation equations are expressed as follows:

$$\frac{\partial \rho}{\partial t} + \frac{\partial}{\partial z}(\rho v_z) + \frac{\partial}{\partial r}(\rho v_r) + \frac{\rho v_r}{r} = 0 \quad (3.1)$$

$$\begin{aligned} \frac{\partial}{\partial t}(\rho v_z) + \frac{1}{r} \frac{\partial}{\partial z}(r \rho v_z v_z) + \frac{1}{r} \frac{\partial}{\partial r}(r \rho v_r v_z) = & -\frac{\partial p}{\partial z} + \frac{1}{r} \frac{\partial}{\partial z} \left[r \mu \left(2 \frac{\partial v_z}{\partial z} - \frac{2}{3} (\nabla \cdot \vec{v}) \right) \right] \\ & + \frac{1}{r} \frac{\partial}{\partial r} \left[r \mu \left(\frac{\partial v_z}{\partial r} + \frac{\partial v_r}{\partial z} \right) \right] + (\rho - \rho_\infty) g \end{aligned} \quad (3.2)$$

$$\text{where } (\nabla \cdot \vec{v}) = \frac{\partial v_z}{\partial z} + \frac{\partial v_r}{\partial r} + \frac{v_r}{r}$$

$$\begin{aligned} \frac{\partial}{\partial t}(\rho v_r) + \frac{1}{r} \frac{\partial}{\partial z}(r \rho v_z v_r) + \frac{1}{r} \frac{\partial}{\partial r}(r \rho v_r v_r) = & -\frac{\partial p}{\partial r} + \frac{1}{r} \frac{\partial}{\partial z} \left[r \mu \left(\frac{\partial v_r}{\partial z} + \frac{\partial v_z}{\partial r} \right) \right] \\ & + \frac{1}{r} \frac{\partial}{\partial r} \left[r \mu \left(2 \frac{\partial v_r}{\partial r} - \frac{2}{3} (\nabla \cdot \vec{v}) \right) \right] - 2 \mu \frac{v_r}{r^2} + \frac{2}{3} \frac{\mu}{r} (\nabla \cdot \vec{v}) \end{aligned} \quad (3.3)$$

$$\frac{\partial}{\partial t}(\rho Y) + \frac{\partial}{\partial z}(v_z \rho Y) + \frac{\partial}{\partial r}(v_r \rho Y) = \frac{\partial}{\partial z} \left(\rho D_b \frac{\partial Y}{\partial z} \right) + \frac{1}{r} \frac{\partial}{\partial r} \left(r \rho D_b \frac{\partial Y}{\partial r} \right) \quad (3.4)$$

Equation (3.1) is the continuity equation and Equations (3.2) and (3.3) are, respectively, the axial and radial momentum conservation equations. Equation (3.4) is the species mass conservation equation. The density was computed from

the ideal gas law using local pressure and mixture composition (or molecular weight). The dynamic viscosity was computed using Wilke's mixture average formula (Bird et al., 1960) to account for local variations in the mixture composition (see Appendix A). The mass diffusivity of helium into air (or air into helium) was taken as a constant value of $7.44\text{e-}05 \text{ m}^2/\text{s}$ (Geankoplis, 1972).

3.3.3 Boundary and Initial Conditions

Figure 3.1 shows the computational domain whereby the left-side boundary represents the axis of symmetry. The size of the domain was selected in such a way that the near-field results were unaffected by the boundary conditions. For this purpose, domain sizes ranging from $10d \times 3d$ (in axial and radial directions) to $50d \times 10d$ were considered initially. The changes in helium mole percentage and axial velocity at several axial ($z/d=0.0$ to 4.0) and radial stations ($r/d=0.0$ to 1) were monitored for different domain sizes. It was found that the near-field results were not affected by the domain size extending above $13d$ axially and $5d$ radially. Based on this evaluation, the domain size of $15d \times 6d$ was chosen for further analysis. The inlet boundary was placed at a distance of $1d$ upstream from the jet exit plane. This was necessary to capture diffusion upstream of the jet exit observed in experimental studies and back flow of air into the tube reported by Cetegen (1996, 1997a). At the tube inlet, the axial velocity profile was laminar and fully developed and the helium mole fraction was unity. No slip conditions were imposed on the inner and outer walls of the tube. The remaining

boundaries were specified as open boundaries, whereby the normal flow gradients were zero. The initial conditions were zero axial and radial velocities and helium concentration throughout the domain.

3.3.4 Computational Details

An orthogonal grid was generated by splitting the computational domain into five sub regions. The grid points in the radial direction were concentrated to resolve steep gradients in the flow oscillation region (see Fig. 3.1). The grid spacing was gradually increased in the axial direction. A single grid of one radian was used in the circumferential because of the axisymmetric nature of the problem. The governing equations were discretized using the finite volume approach (Fluent, 2005). The convective terms were discretized using the QUICK scheme and the pressure–velocity coupling was implemented using the SIMPLEC algorithm (see Appendix A). The governing equations were solved in a segregated manner using an implicit, second-order time-dependent formulation. Sufficient time was allowed for the flow to achieve either periodic oscillations or steady conditions to ensure that the solution was independent of numerical disturbances and initial conditions.

3.3.5 Grid Convergence and Model Validation

Computations with different grid sizes were performed to obtain grid independent solution for $d=31.8\text{mm}$ and $Re=150$. Based on these trials (see Fig.3.2) the grid with 270 axial and 110 radial nodes (270 x 110) and time step of

1.6ms was chosen for further analysis. The computational model was validated for steady flow using concentration measurements of Shenoy et al. (1998). Figure 3.3 shows an excellent agreement between computed and measured radial profiles of helium concentration at $z/d=1.0$ and 3.4. The discrepancy in the center region is attributed to experimental errors introduced by the line of sight measurement technique used by Shenoy et al. (1998). Results in Fig. 3.3 prove that the model correctly simulated the flow structure of steady, low density gas jets. The next step pertains to the verification of the model to predict flow oscillations in helium jets injected into air. Figure 3.4 compares the computed and measured Strouhal numbers for a range of jet Richardson numbers. The measurements refer to the power law correlation of Hamins et al. (1992) and data taken from Cetegen and Kasper (1996). Again, an excellent agreement between computed and measured oscillation frequencies is reached, proving reliability of the model in predicting the global features of the oscillating flow.

Further, simulations were qualitatively compared with experimental data for an oscillating helium jet in air. Figure 3.5 shows a sequence of computed and experimental contour plots of helium mole percentage to depict an oscillation cycle. Note that the location of $z/d=0.0$ corresponds to the jet exit plane in our discussion. It should be made clear that the plots presented in Fig. 3.5 are presented for qualitative comparison rather than quantitative matching owing to the following reasons: a. Experimental uncertainties related to the flow rate

measurements; b. Quiescent air conditions; c. Flow dependence on external perturbations and/or flow history; d. Effect of tube surface roughness and flow development on exit velocity profile. Hence, one would not expect to obtain one-to-one instantaneous comparisons between experiments and computations over the whole field of view.

Results show that the jet contracts near the exit at $t=0.0$ s. Subsequently, the jet contraction (or concave indentation) continues downstream, as shown by both experimental and computed results. The axial displacement of the indentation in Fig. 3.5 signifies the convective motion of the vortex as explained later. The inward shift of the indentation with the flow direction indicates greater penetration of the vortex into the jet core. Note that the computed concentration contours show features similar to those obtained experimentally. The computed oscillation frequency of 13 Hz matched well with the experimental value of 16 Hz. Based on these observations, it was inferred that the computations replicated the experiment proving the reliability of the model in predicting the complex features of the oscillating flow.

3.4 Results and Discussion

As observed by Hamins et al. (1992), a minimum jet exit velocity is required to initiate periodic flow oscillations. Previous studies have attributed unsteady flow oscillations to relative roles of diffusion and buoyant convection. Motivated by these ideas, computations were performed at several jet exit

velocities (or jet Reynolds numbers) to demarcate the steady and unsteady flow regimes. As explained previously, no external perturbations were introduced and computations were performed for sufficiently long time such that the flow reached either steady conditions or periodic oscillations with no change between consecutive cycles. Figure 3.6 plots the flow oscillation frequency versus jet Reynolds number. The flow was steady for $Re < 70$, and the change from steady to oscillatory state occurred approximately at $Re = 90$ or $U_j = 0.33$ m/s. The computed velocity required to initiate oscillations matches well with the measured velocity of approximately 0.3 m/s reported by Hamins et al. (1992) for $d = 25.0$ mm. Such agreement is fortuitous and further substantiates the effectiveness of the present model. The oscillation frequency increased gradually from 11 Hz for $Re = 90$ to 14.5 Hz for $Re = 300$. Next, the detailed flow structure is examined for four test cases: two cases pertaining to the steady flow and two cases to represent the oscillating flow. The operating conditions for these test cases are summarized in Table 3.1.

Table 3.1: Summary of Test Conditions

Case	d (mm)	U_j (m/s)	Re	Ri	f (Hz)
1	31.8	0.15	40	85	Steady
2	31.8	0.27	70	30	Steady
3	31.8	0.34	90	17	11
4	31.8	0.56	150	6.4	13

3.4.1 Global Flow Characteristics

The flow structure of the low-density gas jet is influenced by the jet Reynolds number. Figure 3.7 shows velocity vectors in the near field ($z/d = -1.0$ to 2.0 , where $z/d = 0.0$ represents the tube exit plane) for different jet Reynolds numbers. The vectors are drawn at selected grid locations to prevent overcrowding. For $Re = 40$, the velocity vectors in Fig. 3.7(a) show strong curvature inside the jet tube. Evidently, the jet core accelerates by buoyant convection of helium. Concurrently, the ambient fluid settles inside the tube in a region adjacent to the wall, because the momentum of the light weight helium is insufficient to displace the heavier ambient fluid. This phenomenon of back flow of air upstream of the jet exit was reported by Cetegen and Kasper (1996), who utilized a flat stainless steel screen at the tube exit to enforce flow uniformity. For $Re = 70$, the back flow of the ambient fluid inside the jet tube is insignificant because of the higher momentum of the jet (see Fig. 3.7b).

For $Re = 90$, the velocity vectors in Fig. 3.7c show a recirculation region at $z/d = 0.3$, indicating that the critical velocity to initiate flow oscillations has surpassed. Fig. 3.7c pertains to the cyclic phase at the onset of the instability characterized by entrainment of ambient fluid into the jet core. Similar features of the vortex are also observed in Fig. 3.7d for $Re = 150$. However, the vortex core is located closer to the jet axis at the lower jet Reynolds number, i.e., $r/d = 0.44$ for

$Re = 90$ compared to $r/d = 0.56$ for $Re = 150$. Moreover, the width of the vortex is greater for $Re = 150$ compared to $Re = 90$.

The jet half width (or radius) is an important parameter to quantify radial growth of the jet in the streamwise direction. Figures 3.8 and 3.9 plot the normalized jet half radius ($r_{1/2}/d$) at several axial locations, computed using helium concentration and axial velocity profiles. The jet half radius ($r_{1/2}$) is defined as the radial location where the axial velocity or helium concentration is half of that at the jet center ($r/d = 0.0$). In case of the oscillating flow, the time-averaged profiles were used to determine the jet half radius. Figures 3.8 & 3.9 reveal several unique features of low-density gas jets. First, the jet half radius is the highest near the tube exit and it decreases in the flow direction for all cases. This trend signifying contraction of the jet in the flow direction is opposite to the radial growth observed in constant density jets. The contraction of the jet is attributed to buoyant acceleration of the low-density jet fluid, which promotes scalar mixing by entraining ambient fluid into the jet core. For all cases, the jet half radius based on axial velocity profiles (Fig. 3.9) is smaller than the scalar jet half radius (Fig. 3.8). Figures 3.8 & 3.9 display another unique feature of low-density gas jets; the jet half radius increases with increasing jet Reynolds number, a trend opposite of constant density gas jets. The jet is wider at higher jet Reynolds numbers because the contraction of the jet by buoyant acceleration of low-density jet fluid is less prominent. Overall, results show significant

differences in the flow structure of low-density jets compared to constant density jets. Next, detailed flow characteristics of steady and oscillating jets are examined in the following sections.

3.4.2 Steady Jet

In this section, structural details of the steady flow are discussed using radial profiles of axial velocity and helium concentration. These profiles are presented at several axial locations inside the tube and near the jet exit to highlight interactions between velocity and concentration fields.

3.4.2.1 $Re = 40$

Figures 3.10 & 3.11 reveal major changes in profiles inside and downstream of the tube for $Re = 40$. For example, the axial velocity at the jet center ($r/d = 0.0$) increased by nearly a factor of four (see fig. 3.10a) within the jet tube; from 0.3 m/s at the injection plane ($z/d = -1.0$) to approximately 1.2 m/s near the tube exit plane ($z/d = -0.25$). Acceleration in the jet core region ($r/d < 0.25$) is accompanied with deceleration in the wall region ($r/d > 0.25$). Moreover, the axial velocity profiles depict flow reversal between $r/d = 0.32$ and tube wall for $z/d > -0.50$ (see fig. 3.10a). This unusual behavior is attributed to the sinking of the heavier ambient fluid (by gravity) above the lighter jet fluid in the low-momentum region adjacent to the wall. In contrast, buoyancy accelerates the jet core region with sufficient momentum to displace the ambient fluid above it. Helium concentration profiles in Fig. 3.10 (b) show vigorous mixing of jet and

ambient fluids inside the tube. For example, air has reached up to $r/d = 0.25$ at $z/d = -0.75$ and almost to the jet center ($r/d = 0.0$) at $z/d = -0.25$. The mixing of the jet and ambient fluids by buoyant convection and molecular diffusion produces a stratified density shear layer at the tube exit. Essentially, such stratification would hinder entrainment of the ambient fluid into the jet core region to prevent the formation of the toroidal vortex downstream of the tube exit.

The development of axial velocity and helium concentration profiles downstream of the tube exit is depicted in Fig. 3.11 (a)-(b) for $Re = 40$. Results show that the flow at all radial locations accelerates in the streamwise direction and positive axial velocity is reached at $z/d = 0.6$. The axial velocity at the center point increases from 1.50 m/s at $z/d = 0.0$ to 2.2 m/s at $z/d = 1.5$, representing only moderate flow acceleration compared to that inside the tube (Fig. 3.11 (a)). The helium concentration profiles in Fig. 3.11 (b) show presence of air in much of the jet core region at the tube exit. Helium concentration at the center point reduces to 98% at $z/d = 0.6$ and to 92% at $z/d = 1.5$, indicating gradual mixing of fluids downstream of the tube exit.

3.4.2.2 $Re = 70$

Figures 3.12 (inside the tube) & 3.13 (outside the tube) show axial velocity and helium concentration profiles for $Re = 70$. The profiles at $z/d = -0.25$ are nearly identical to those at the injection plane $z/d = -1.0$ (see fig.3.12 (a)). At the jet center, the axial velocity increases from 0.54 m/s at the injection plane to

0.68 m/s near the tube exit ($z/d = -0.05$), with much of the change occurring after $z/d = -0.25$. The reverse flow inside the tube is confined to a narrow region, $r/d = 0.45$ to 0.50 , near the tube exit or $z/d = -0.05$. Pure helium is present up to $r/d = 0.33$ at $z/d = -0.10$ and up to $r/d = 0.30$ at $z/d = -0.05$ (see fig.3.12 (b)). Again, mixing inside the tube produces a stratified density shear layer at the tube exit. Figure 3.13 (a) shows significant acceleration of the jet core region downstream of the tube exit. For example, the axial velocity at the center point increases from 0.72 m/s at the tube exit ($z/d = 0.0$) to 2.35 m/s at $z/d = 1.5$, indicating a more than three fold increase. Helium concentration profiles in Fig. 3.13 (b) show vigorous mixing by entrainment/diffusion of ambient fluid into the jet core region. Results show similarities in the flow structure for the two test cases, although mixing and buoyant acceleration are prominent inside the tube for $Re = 40$ and downstream of the tube exit for $Re = 70$.

3.4.3 Oscillating Jet

In this section, the dynamics of the oscillating jet including interactions between velocity and concentration fields, and instantaneous and time-averaged flow structure are presented.

3.4.3.1 Simultaneous Visualization of Velocity and Concentration Fields

Figure 3.14 shows velocity vectors superimposed with contours of helium mole percentage during an oscillation cycle for $Re = 150$. The first plot for $t = 0.0$ ms reveals a small flow recirculation region (vortical motion) described by the

clockwise velocity vectors near $r/d = 0.5$ (the vortex core is indicated by a black dot in the figure). This phase marks the initiation of the instability leading to a larger recirculation zone at $t = 16.03$ ms, where the vortex core is located at $z/d = 0.40$. The vortex formation is associated with buoyant acceleration of the jet fluid causing the jet core to contract, as indicated by the strong concave curvature of the concentration contours between $z/d=0.0$ and 0.30 . Buoyant acceleration entrains the ambient fluid into the jet core, as indicated by radially oriented velocity vectors upstream of the vortex core. At $t = 32.06$ ms and 48.09 ms, we observe the vortex region growing in size and intensity. Figure 3.14 shows that the vortex gains momentum by interacting with the jet core, whereby velocity vectors downstream of the vortex core have higher magnitudes than those upstream. At $t = 64.12$ ms, the vortex convects downstream and it has contaminated much of the jet core region. As the straining effect of the vortex diminishes, the jet expands near the tube exit to initiate another vortex at $t = 80.16$ ms to repeat the oscillation cycle. Similar unsteady features characterized by formation and propagation of vortical structures were observed for $Re = 90$, although those results are not presented here for brevity.

Figure 3.15 shows the vortex convection velocity (normalized by the average jet exit velocity) calculated from vortex core position at various times. The vortex convection velocity was computed from vortex core positions at different times. This was tracked manually and hence there was some noise. A 3rd

order polynomial curve fit was used to show the trend of the vortex convection velocity. Results show that the vortex convection velocity increases and approaches a constant value at a downstream location, which coincided with the results from Pasumarthi and Agrawal (2003).

Buoyant acceleration at the jet center is illustrated by Fig. 3.16 showing normalized centerline axial velocity at different phases during an oscillation cycle. Note that each of these phases corresponds to the plots presented in Fig. 2.14 from $t=0.0\text{ms}$ to $t=64.12\text{ms}$ and the normalization of velocity is based on Cetegen and Kasper (1996). At $t=0.0\text{ms}$, the axial velocity increases slightly between $z/d=0.0$ and 1.0 but rapidly thereafter. In the next phase at $t=16.03\text{ms}$, significant buoyant acceleration is evident between $z/d=0.0$ and 0.3 . However, rapid buoyant acceleration near the jet exit occurs at $t=32.06\text{ms}$, with axial velocity reaching a peak value at $z/d=0.6$. Buoyant acceleration entrains the surrounding fluid to form the vortex as explained previously. The axial velocity decreases after $z/d=0.6$, signifying transfer of the jet momentum to the vortex. At later stages ($t=48.09\text{ms}$ and 64.12ms), the axial velocity decreases near the jet exit because of the diminishing effect of the vortex. However, buoyant acceleration increases towards the downstream, in a region adjacent to the vortex, as indicated by the peaks at different phases of the cycle. These observations are consistent with the velocity measurements of Cetegen [1997b] in a buoyant helium plume.

These observations of the flow structure are summarized as follows: As the helium exits the tube, the jet core accelerates by buoyancy and contracts to conserve the mass. The contraction of the jet results in entrainment of the ambient fluid to form a toroidal vortex which grows in size, accelerates, and convects downstream. As the vortex convects downstream, it penetrates closer to the centerline to contaminate the jet core. In the immediate downstream region of the vortex, the jet core decelerates owing to the transfer of the momentum to the vortex. With the vortex moving away from the tube, the jet expands again near the tube exit. Subsequently, buoyancy manifests to accelerate the jet core to form a toroidal vortex to repeat the oscillation cycle. These observations are consistent with velocity measurements of Cetegen (1997b) and concentration measurements of Pasumarthi and Agrawal (2003) for helium jets in air.

3.4.3.2 Vorticity Dynamics

Figure 3.17 shows contours of vorticity component (on the r-z plane) overlapped with helium mole percentage to depict the flow rotational characteristics of the mixing process during an oscillation cycle. The negative vorticity is confined mainly to a narrow region adjacent to the tube wall. Several regions of high positive vorticity are visible during the oscillation cycle in Fig. 3.17. At $t=0.0\text{ms}$ and 16.03ms , the vorticity for $z/d=0.0$ to 1.0 ranges between $100/\text{sec}$ and $200/\text{sec}$ indicating relatively small rotation of the fluid particles across the mixing layer with helium concentration ranging between 40 to 90

percent. At $t=32.06\text{ms}$, the maximum vorticity of $300/\text{sec}$ is observed between $z/d=0.2$ to 0.6 within a thin mixing layer with helium concentration of 80 to 90 percent. The increase in vorticity is attributed to the buoyancy-induced acceleration of the jet core resulting in an increase of entrainment velocities (radial inflow of air) to establish density and velocity gradients in the so-called vorticity layer. Subsequently, at $t=48.09\text{ms}$, the peak vorticity of $400/\text{sec}$ is observed in the vorticity layer representing the growth and propagation of the vortex. The extent of the vorticity layer has increased to the range between $z/d=0.5$ and 1.2 . This trend continues at $t=60.12\text{ms}$ where the vorticity layer extends from $z/d=1.1$ to 2.3 with peak vorticity of $500/\text{sec}$. These results show that the vorticity is generated by the interaction of the accelerating jet fluid with the vortex convecting downstream.

3.4.3.3 Instantaneous Flow Structure

Instantaneous profiles of axial velocity and helium concentration were obtained to depict the periodicity and stream wise development of the flow structure. Figure 3.18 shows these plots at selected axial and radial locations for a brief period for $Re = 150$. Results show highly periodic oscillations throughout the flow field. Based on the time lag between two consecutive crests/troughs, oscillation frequency of 13 Hz was obtained at all locations, which agrees with experiments showing self-excited global oscillations in the flow field.

Figure 3.18 shows that near the jet exit at $z/d = 0.05$, pure helium is present in the core region ($r/d = 0.0$ and 0.3) at all times. However, large concentration fluctuations are observed in the shear layer region ($r/d = 0.5$) with helium mole percentage ranging from 16 to 70%. The concentration profile at $r/d = 0.6$ indicates that the helium has diffused beyond the tube wall. The axial velocity profiles at $z/d = 0.05$ show periodic oscillations at all radial locations, with the amplitude of oscillations decreasing in the radial direction. Further downstream at $z/d = 0.6$, the jet core at $r/d = 0.3$ has been contaminated by air with helium concentration varying between 35 and 100%. A somewhat flattened peak in the concentration profile indicates that pure helium is present only for a brief interval during the oscillation cycle. At $r/d = 0.5$, the helium concentration has decreased to between 10 and 25% indicating increased penetration of air into the jet core at downstream locations. The helium concentration at $r/d = 0.6$ has also reduced to between 2 and 6% because the jet core is contracting instead of growing outwards. The axial velocity profiles show an increase of velocity in the jet core ($r/d = 0.0$ and 0.3) attributed to buoyant acceleration. The peak values at the jet center are 1.4 m/s and 2.6 m/s, respectively, at $z/d = 0.05$ and 0.60 . The axial velocity fluctuations are highest at the centerline, where the axial velocity is also the highest. The axial velocity and its oscillation amplitude are small at $r/d = 0.5$ and 0.6 , a region coinciding with the vortex core.

At $z/d = 1.5$, pure helium is present at the jet center for all times. However, helium concentration has reduced to between 28 and 96% at $r/d=0.3$ and 8 and 16% at $r/d = 0.5$, by entrainment of air into the jet core. Axial velocity profiles show buoyant acceleration of the jet core with peak axial velocity rising to 4.0 m/s at the centerline. The slope of the axial velocity profile at $r/d = 0.0$ shows a period of slow acceleration followed by rapid acceleration and deceleration phases. Note that the jet flow accelerates by buoyancy and decelerates by momentum transfer to the surrounding vortex. Finally, at $z/d = 2.4$, the ambient fluid has reached the jet centerline where the helium concentration varies between 94 and 100%. A flattened peak at $r/d = 0.0$ indicates that pure helium is present during about half of the oscillation cycle. The concentration levels at $r/d = 0.3$ and 0.5 have decreased because of the mixing of the helium with air. Note that the entrainment of the ambient fluid has prevented the helium to diffuse radially outwards, except near the tube exit. The axial velocity profiles at the jet centerline ($r/d = 0.0$) agree qualitatively with those obtained experimentally by Subbarao and Cantwell (1992) in buoyant helium jets with co-flow of air.

3.4.3.4 Mean and RMS Flow Structure

Figures 3.19-22 show radial profiles of mean and root-mean-square (RMS) axial velocity and helium concentration at various axial planes for $Re=90$ and 150. The mean axial velocity profile at $z/d = 0.05$ is parabolic, representing

fully-developed laminar flow at the tube exit. For both cases, the mean axial velocity increases between $r/d = 0.0$ and 0.28 in the flow direction, signifying buoyant acceleration of the jet core. The increase is the highest at the jet center where the mean axial velocity is also the highest. The RMS axial velocity fluctuations are highest at the jet centerline owing to periodic acceleration of the jet core by buoyancy and deceleration by the passage of the vortex. For $Re = 90$ (see fig.3.19), the peak RMS axial velocity of 0.05 m/sec at $z/d = 0.05$ increases to 0.28 m/sec at $z/d = 0.6$ and to 0.4 m/sec at $z/d = 1.5$. For $Re = 150$ (see fig. 3.21), the peak RMS axial velocity of 0.05 m/sec at $z/d = 0.05$ increases to 0.45 m/sec at $z/d = 0.6$ and to 0.7 m/sec at $z/d = 1.5$. These observations of mean and RMS axial velocity profiles are consistent with velocity measurements of Subbarao and Cantwell (1992).

The concentration profiles near the tube exit ($z/d = 0.05$) show that the helium has reached beyond $r/d = 0.65$ and pure helium is present only up to $r/d = 0.3$ for $Re = 90$ (fig. 3.20) and to $r/d = 0.38$ for $Re = 150$ (fig. 3.22). At $z/d = 0.6$, mixing has caused mean helium concentration at $r/d = 0.5$ to decrease to 5% for $Re = 90$ (fig. 3.20) and to 15% for $Re = 150$ (fig. 3.22). The concentration profile for $Re = 150$ (fig. 3.22) shows an inflection point at $z/d = 1.5$ because of the vortex interacting with the jet core. Note that entrainment by the vortex has restricted the jet from spreading outwards. Overall, the mean flow structure

depicts greater contamination of the jet core for $Re = 90$ compared to $Re = 150$ because of the inward movement of the vortex for the latter.

The RMS concentration profiles reveal larger fluctuations at higher jet Reynolds number. For $Re = 90$ (fig. 3.20), the peak RMS concentration is between 15 and 20% at all axial locations. For $Re = 150$ (fig. 3.22), the peak RMS concentration increases from 20% at $z/d = 0.05$ to approximately 25% at $z/d = 0.6$ and 1.5. The location of the peak concentration shifts inwards in the flow direction. Concentration fluctuations confined to the wake region ($0.4 < r/d < 0.6$) near the jet exit broaden in the axial direction and contaminate most of the flow at $z/d = 1.5$. These observations agree qualitatively with experimental results presented by Pasumarthi and Agrawal (2003).

3.4.4 Instability Mechanism

The above results highlighted interesting features of low-density gas jets in both steady and oscillating flow regimes. In particular, it was shown that a minimum jet exit velocity is required to initiate flow oscillations, a phenomenon reported experimentally by Hamins et al (1992). In our discussion, we alluded that a minimum jet exit velocity was needed to prevent stratification of the concentration shear layer. The adjacent fluid elements in a stratified shear layer will accelerate gradually with respect to each other because buoyancy is proportional to density. However, a sharp interface in the concentration shear layer would cause the low density fluid to accelerate rapidly to entrain the high-

density fluid. The rates of acceleration and entrainment will determine the formation of the toroidal vortex. In this study, the concentration shear layer was stratified by ambient fluid settling inside the tube at low Re .

Thus, the entrainment caused by the accelerating jet core was not sufficient to form a vortex downstream of the tube exit. However, the sharp interface at higher Reynolds numbers accentuated entrainment of ambient fluid into the jet core to create a vortex and hence, periodic oscillations in the flow field. This explanation is supported by Fig. 3.23 showing radial profiles of density gradient in the radial direction for all cases at $z/d = 0.3$. Results show that the peak density gradient increased with increasing jet Reynolds number, indicating a shear layer with sharper density interface at higher Re . The location of the peak density gradient shifted towards the tube wall ($r/d = 0.5$) with an increase in the jet Reynolds number.

3.5 Conclusions

Steady and oscillating flow structure of helium jets injected into quiescent air was simulated using computational fluid dynamics. Comparison with experimental data revealed that the computational model was effective in predicting complex structural details including the change from steady to oscillating flow as the jet Reynolds number was increased. Important results of the study are summarized in the following:

- The flow was steady at low jet Reynolds numbers of 40 and 70. The lighter jet fluid in the core region accelerated by buoyancy, while the heavier ambient fluid settled adjacent to the tube wall. The backflow of ambient fluid inside the tube was significant at the lower jet Reynolds number. The mixing of the jet and ambient fluids inside the tube resulted in a stratified shear layer at the tube exit. Downstream of the tube exit, the mixing was dominated by the entrainment of the ambient fluid into the accelerating jet core.
- Self-excited periodic oscillations at a unique frequency were observed throughout the near field at jet Reynolds numbers of 90 and 150. Flow oscillations were caused by buoyant acceleration of the jet core entraining ambient fluid to form a toroidal vortex. The vortex interacted with the jet core, while growing in size, accelerating, and convecting downstream. The vortex path was oriented more towards the jet center at the higher jet Reynolds number.
- The jet half radius decreased in the flow direction for both steady and oscillating flows. This trend indicating contraction of the jet in the flow direction (because of buoyant acceleration) is opposite of constant density gas jets. Furthermore, in contrast to constant density jets, the jet half radius increased with increase in the jet Reynolds number. At low jet Reynolds numbers, the radial expansion of the jet was suppressed by buoyant

acceleration, an effect that became less prominent at higher jet Reynolds numbers.

- The onset of the instability was related to the shape of the concentration (or density) shear layer near the tube exit. The instability was suppressed in a stratified density shear layer. However, flow oscillations occurred if the density shear layer contained a sharp interface.

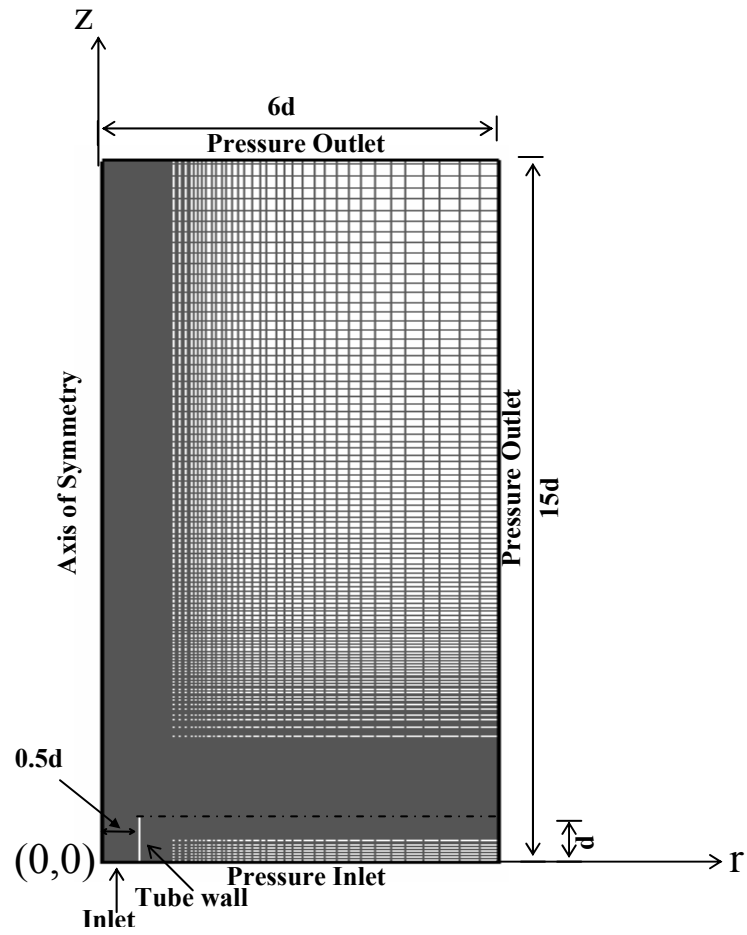


Figure 3.1. Schematic diagram of the computational domain.

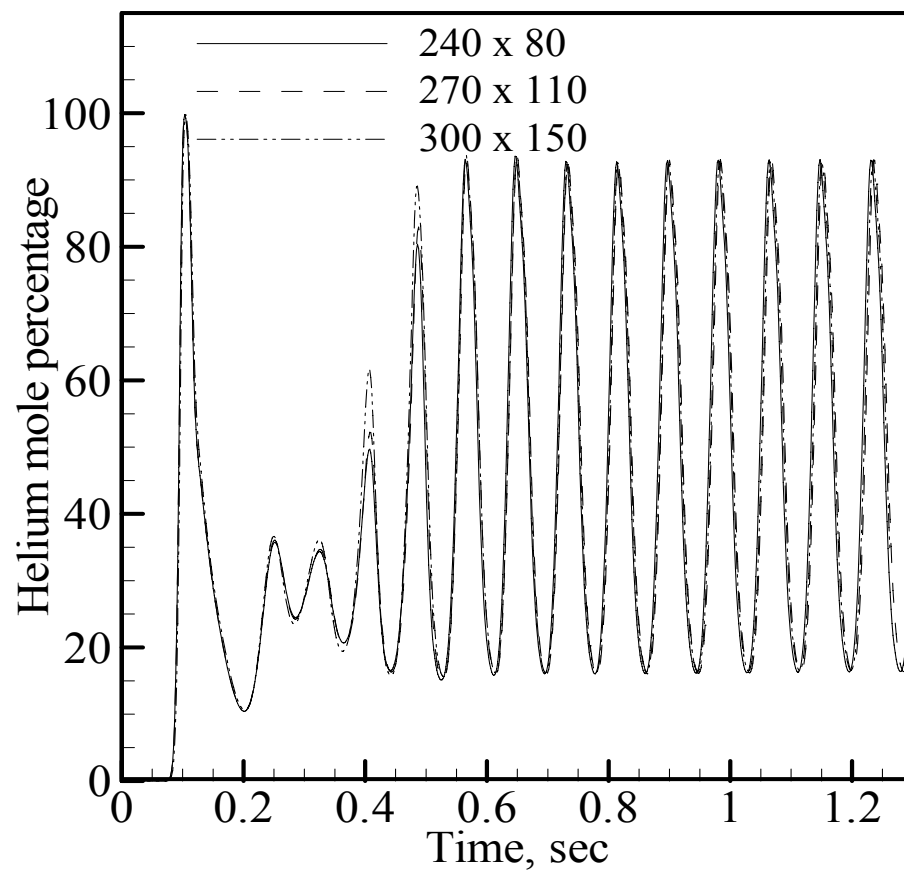


Figure 3.2. Temporal evolution of helium mole percentage for various grid sizes.

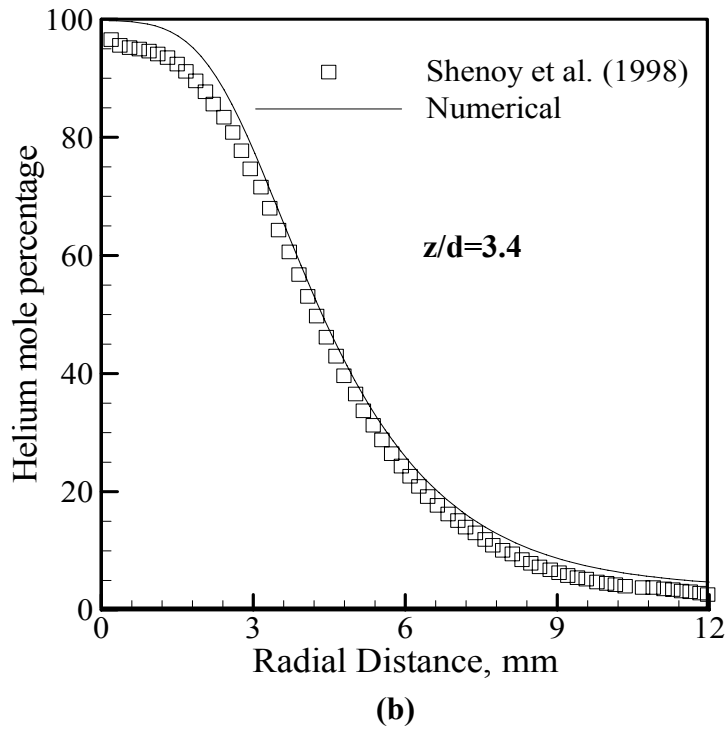
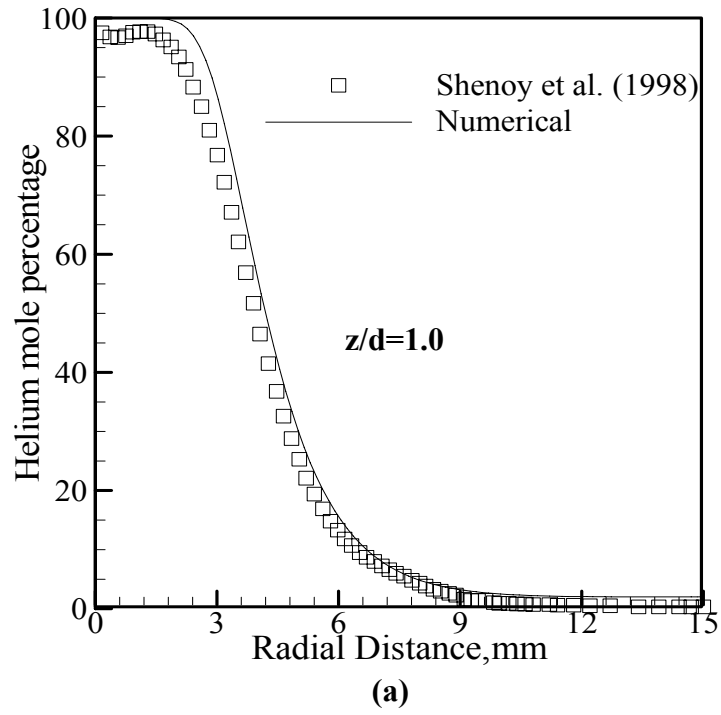


Figure 3.3. Experimental-numerical comparison of helium mole percentage profiles in a steady helium jet, $Re=150$, $Ri=0.07$, $d=7.2$ mm. (a) $z/d=1.0$ (b) $z/d=3.4$.

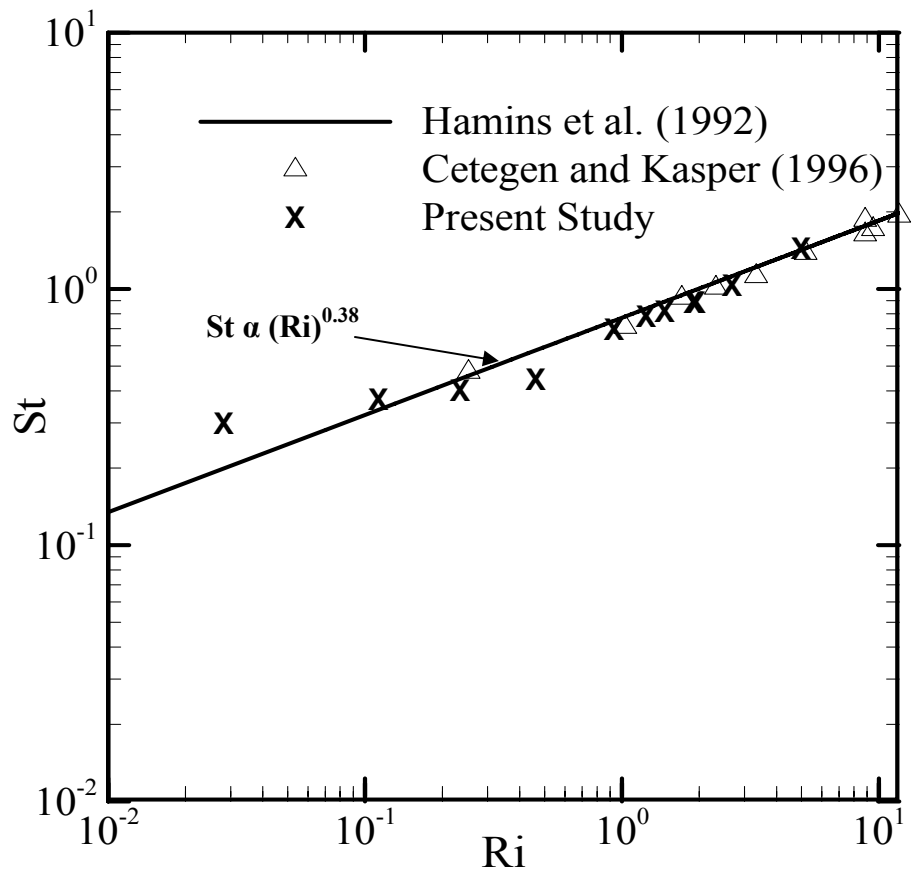


Figure 3.4. Comparison between computed and measured Strouhal number versus jet Richardson number.

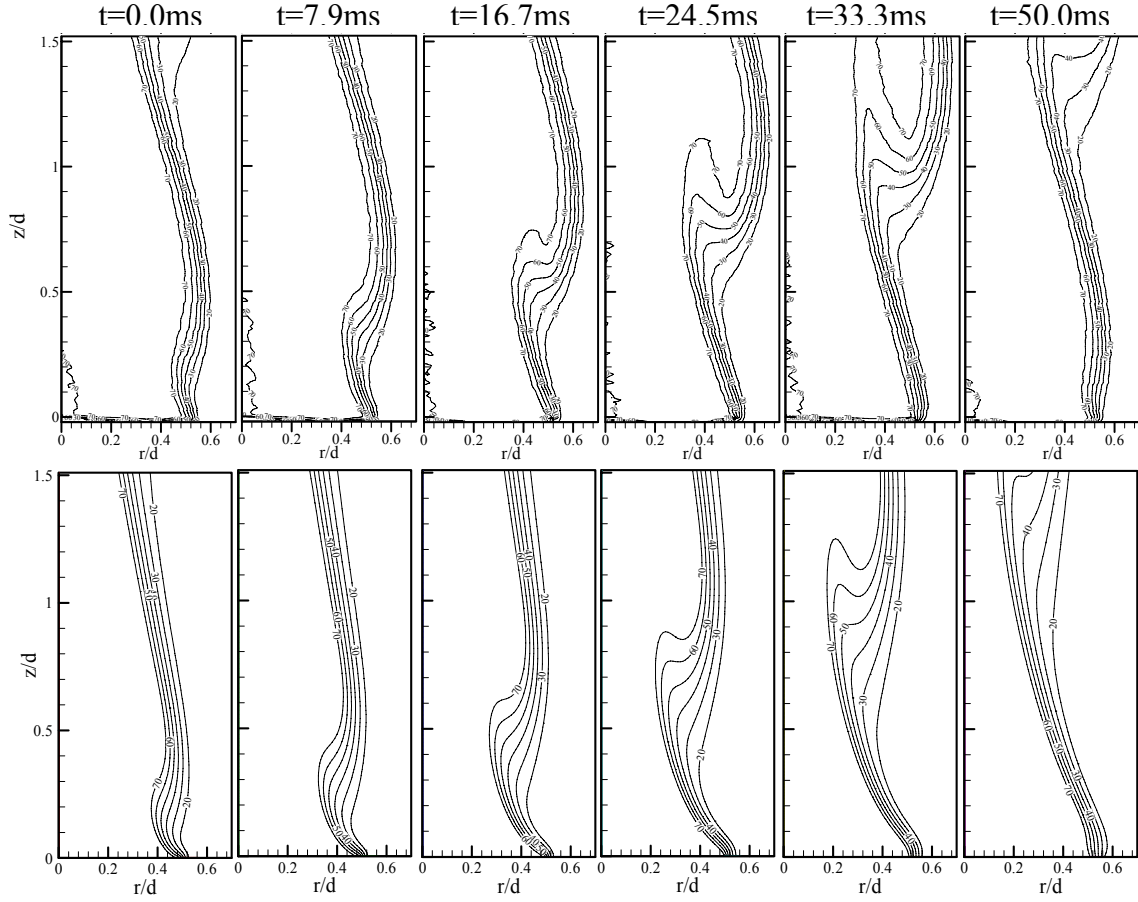


Figure 3.5. Experimental (top) and computational (bottom) helium mole percentage contours during an oscillation cycle for $Re = 150$, $Ri = 6.4$ and $d = 31.8\text{ mm}$ at Earth gravity.

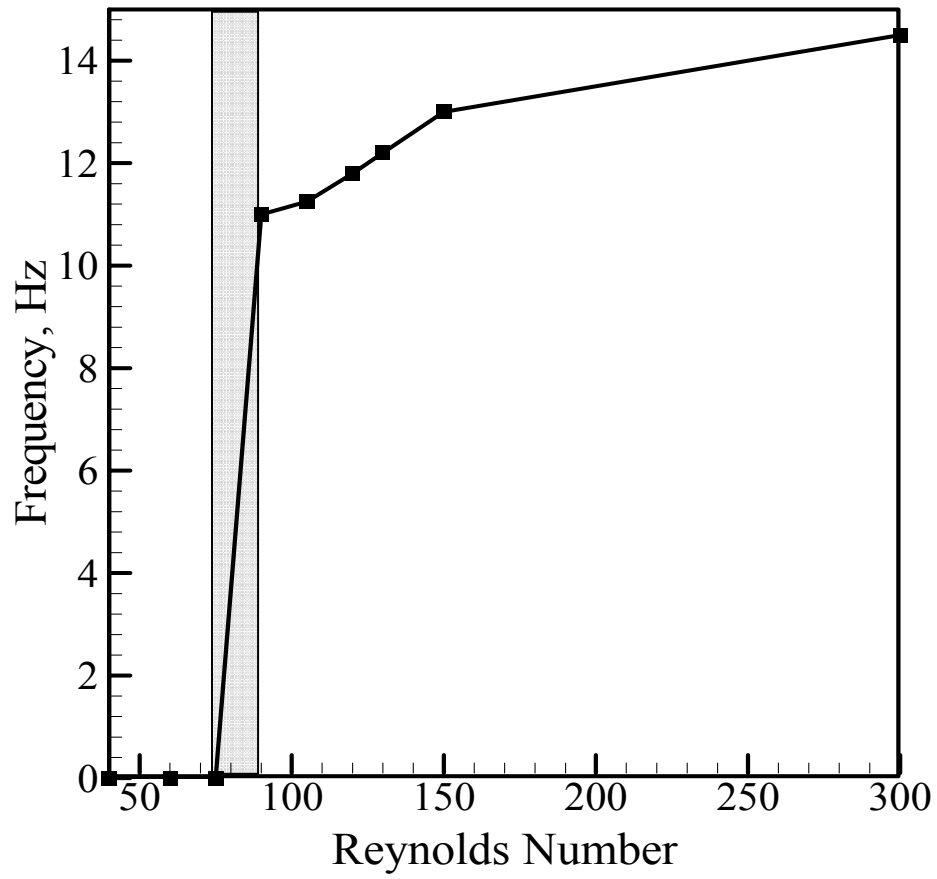


Figure 3.6. Variation of oscillation frequency with jet Reynolds number for $d=31.8\text{mm}$.

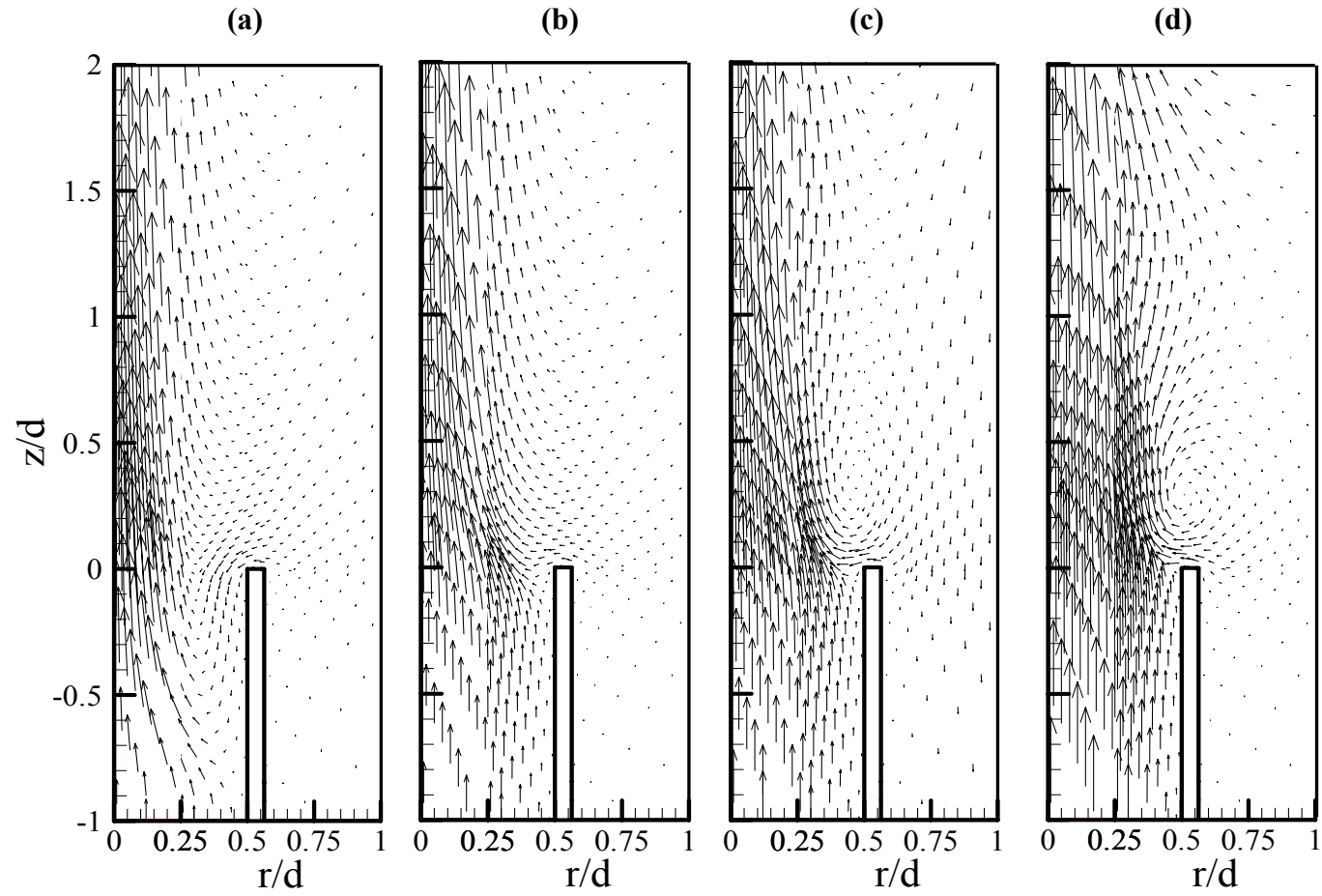


Figure 3.7. Velocity vectors for $d=31.8\text{mm}$. (a) $Re=40$, $Ri=85$ (steady) (b) $Re=70$, $Ri=30$ (steady) (c) $Re=90$, $Ri=17$ (Oscillating) (d) $Re=150$, $Ri=6.4$ (Oscillating).

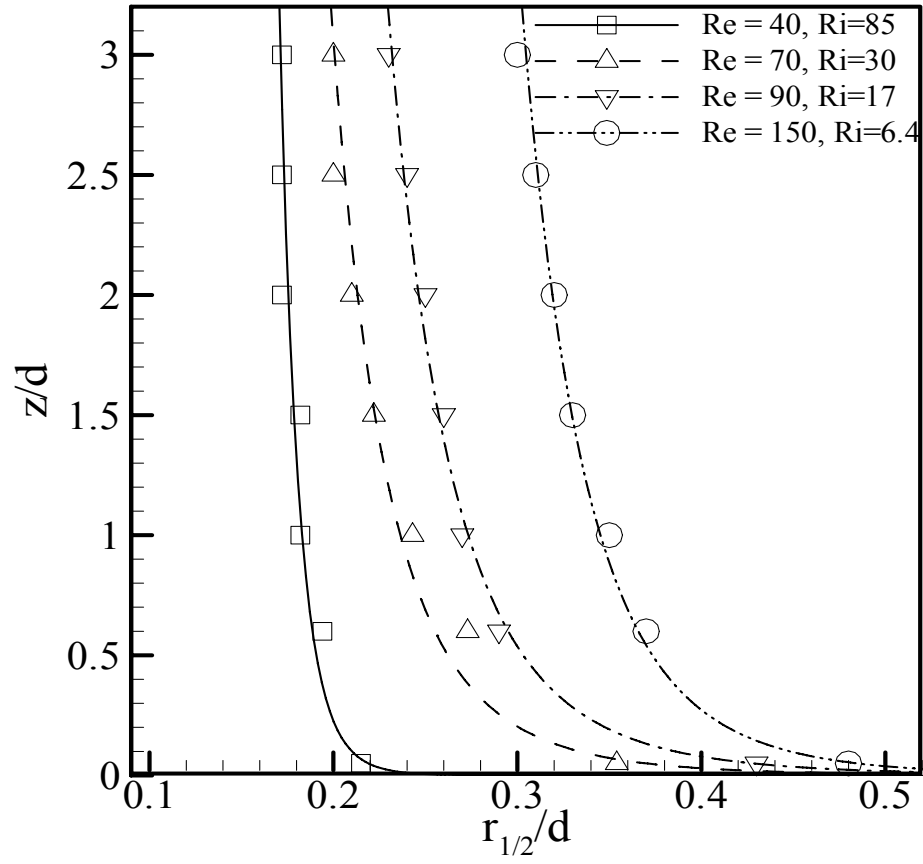


Figure 3.8. Jet half radius in the flow direction based on helium concentration.

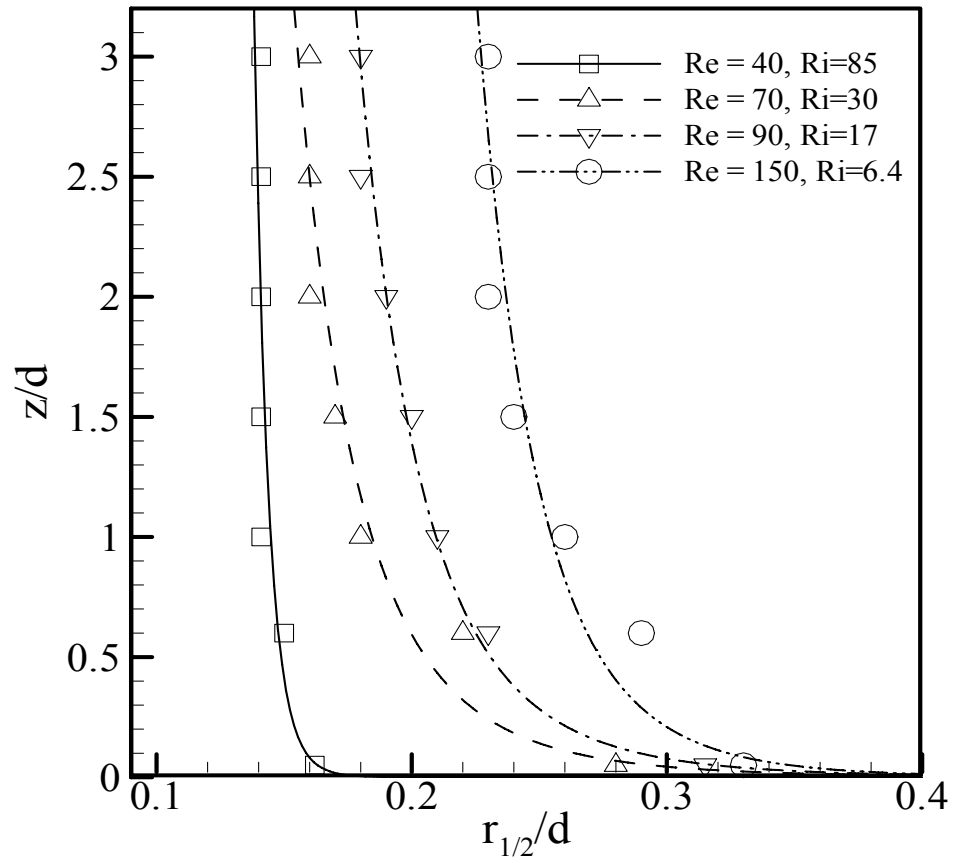


Figure 3.9. Jet half radius in the flow direction based on axial velocity profiles.

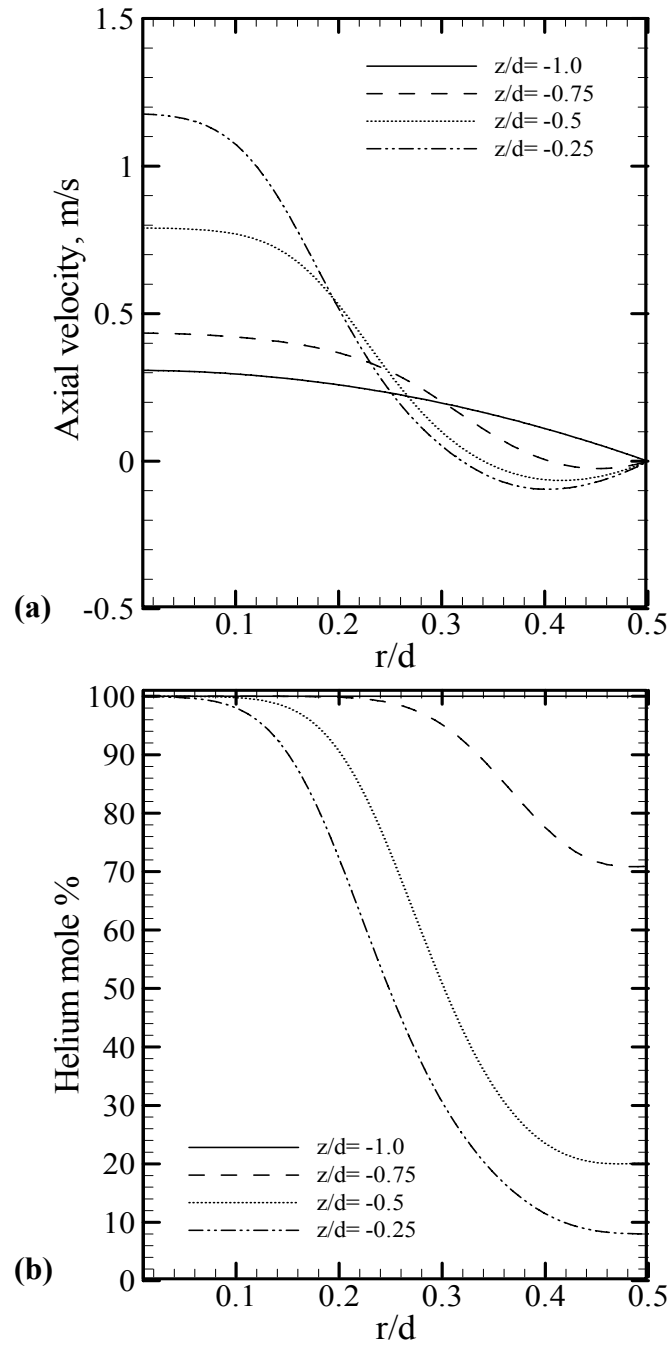


Figure 3.10. Profiles (inside the tube) of (a) axial velocity and (b) helium mole percentage, $Re=40$, $Ri=85$, $d=31.8\text{mm}$.

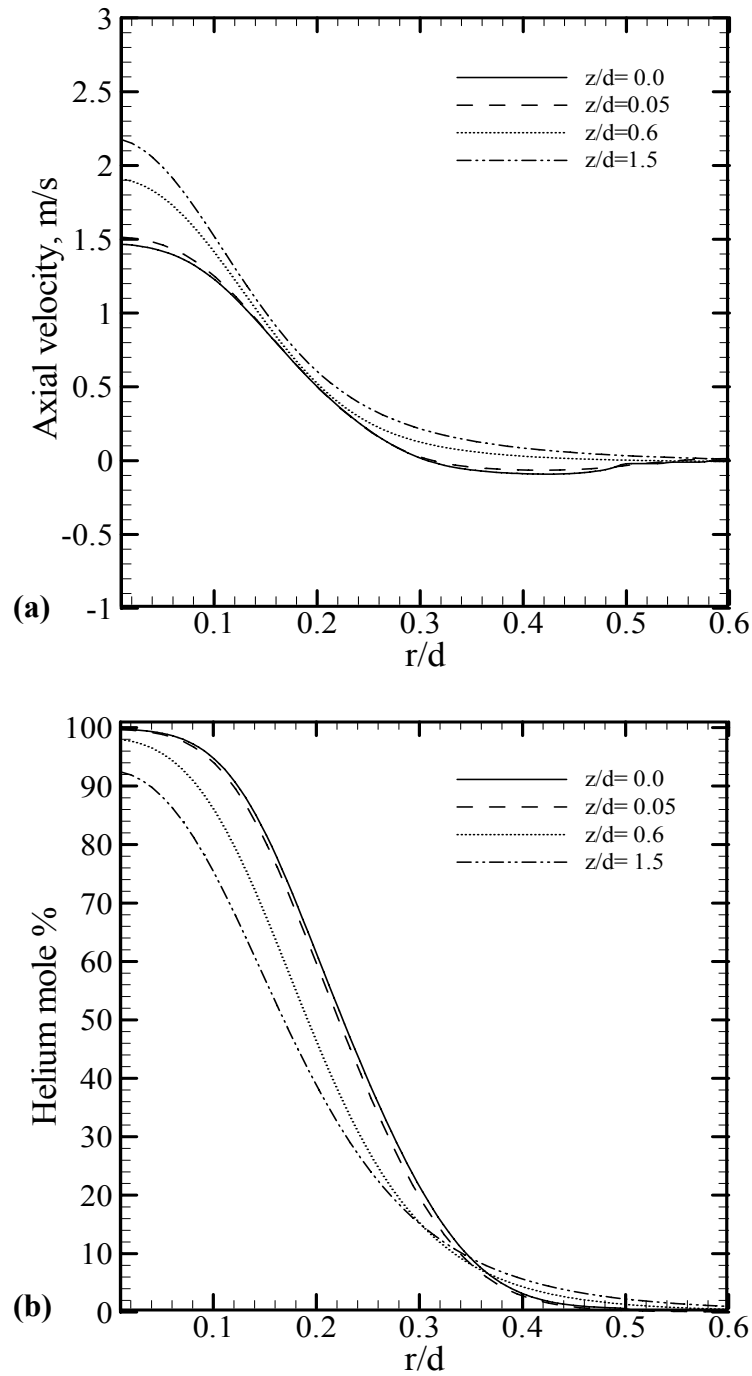


Figure 3.11. Profiles (outside the tube) of (a) axial velocity and (b) helium mole percentage, $Re=40$, $Ri=85$, $d=31.8\text{mm}$.

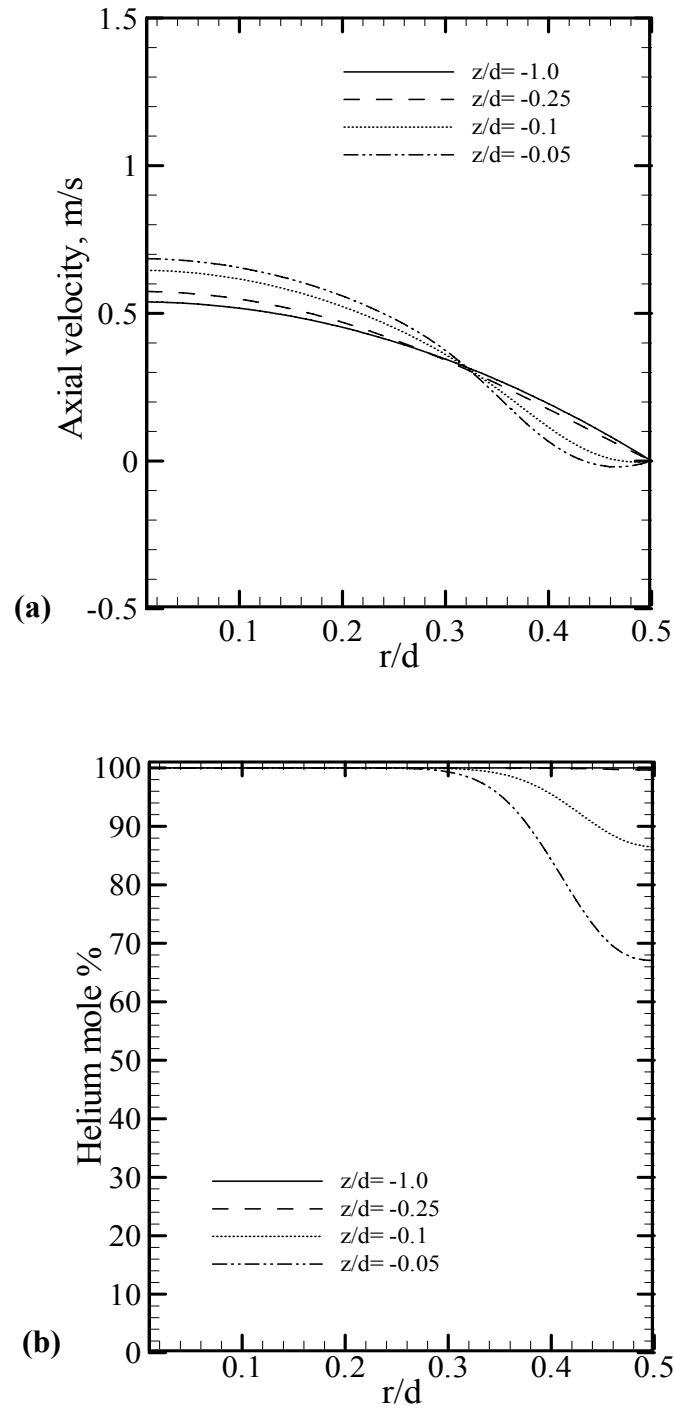


Figure 3.12. Profiles (inside the tube) of (a) axial velocity and (b) helium mole percentage, $Re=70$, $Ri=30$, $d=31.8\text{mm}$.

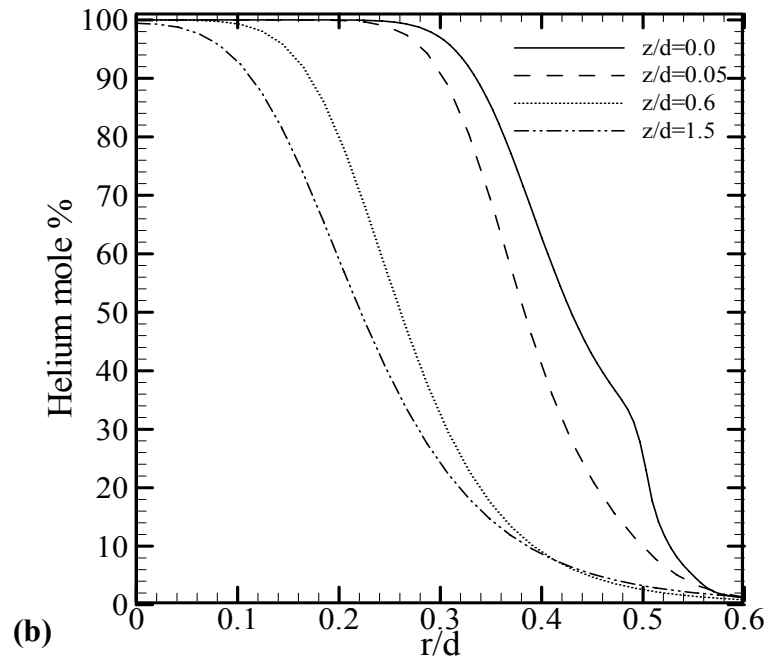
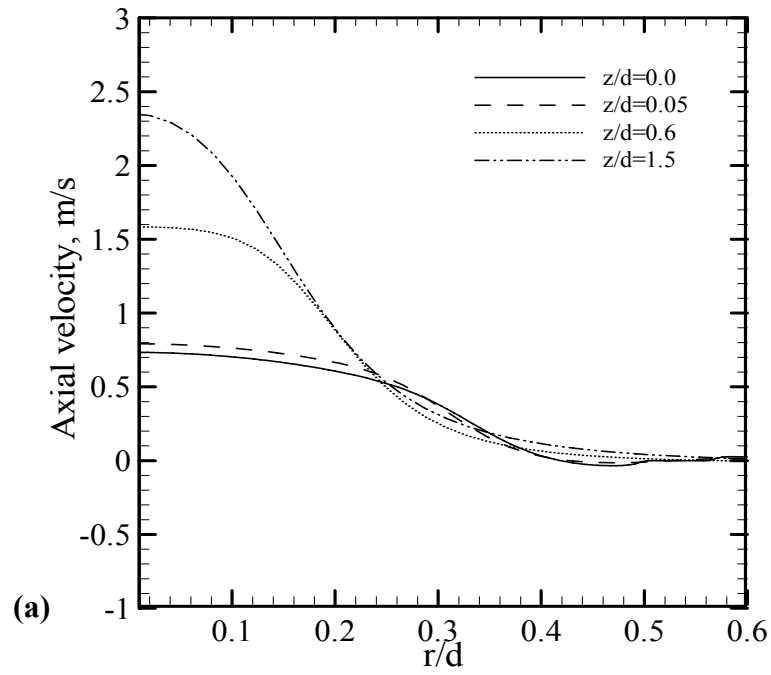


Figure 3.13. Profiles (outside the tube) of (a) axial velocity and (b) helium mole percentage, $Re=70$, $Ri=30$, $d=31.8\text{mm}$.

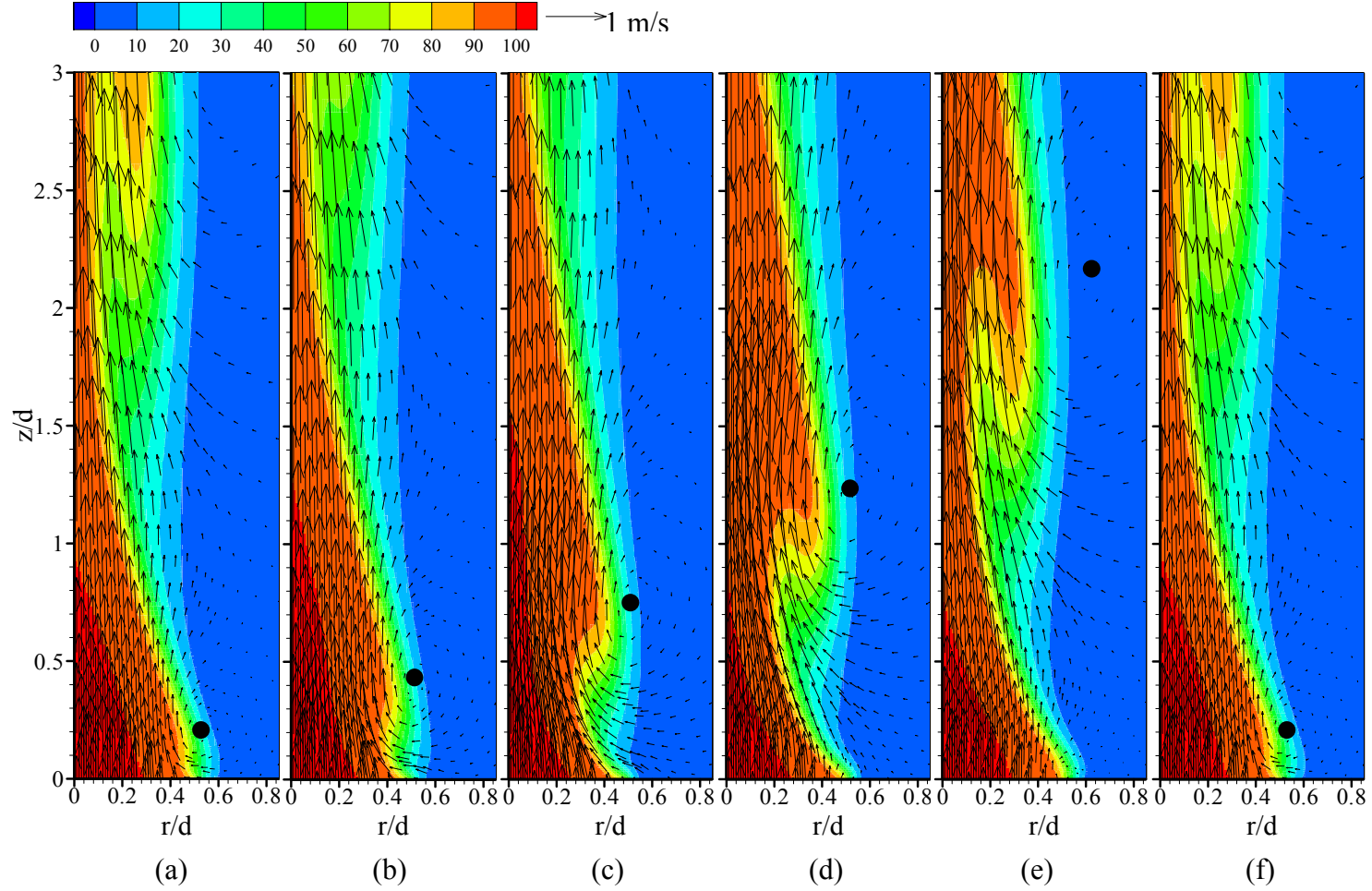


Figure 3.14. Contours of helium mole percentage overlapped by velocity vectors in an oscillation cycle for $Re = 150$, $Ri = 6.4$ and $d = 31.8$ mm. (a) $t=0.0$ ms; (b) $t=16.03$ ms (c) $t=32.06$ ms; (d) $t=48.09$ ms; (e) $t=64.12$ ms; (f) $t=80.16$ ms.

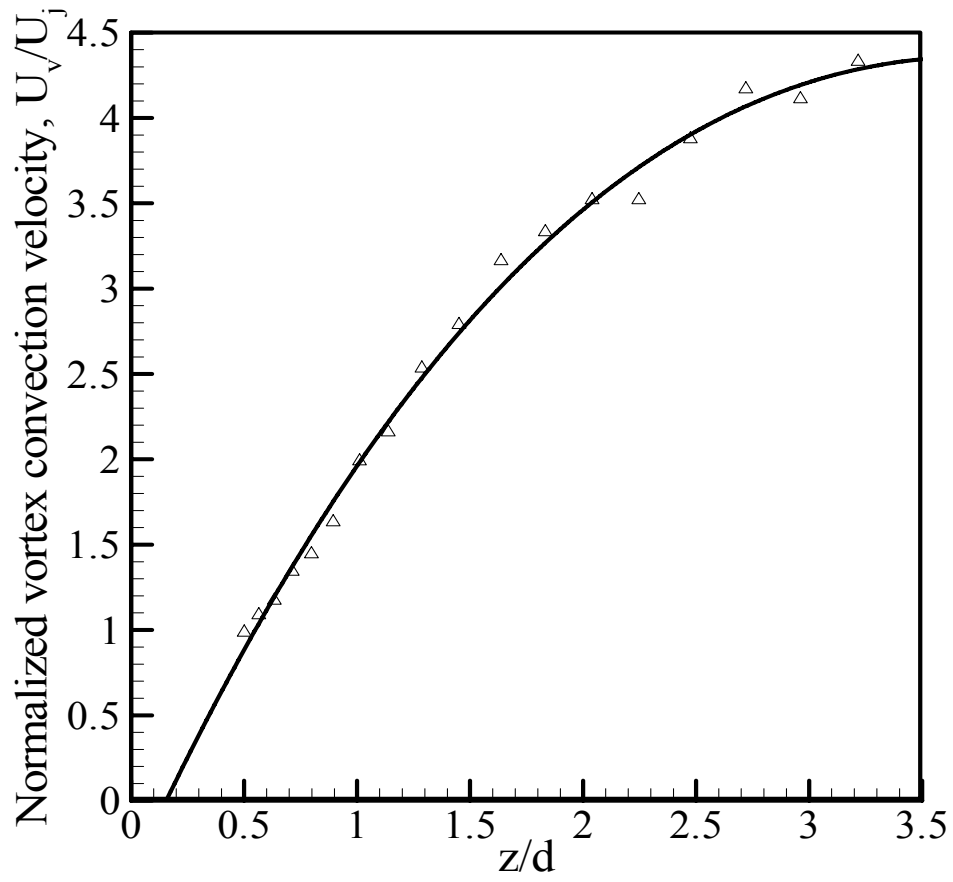


Figure 3.15. Normalized vortex convection velocity, $Re = 150$, $Ri = 6.4$ and $d = 31.8$ mm.

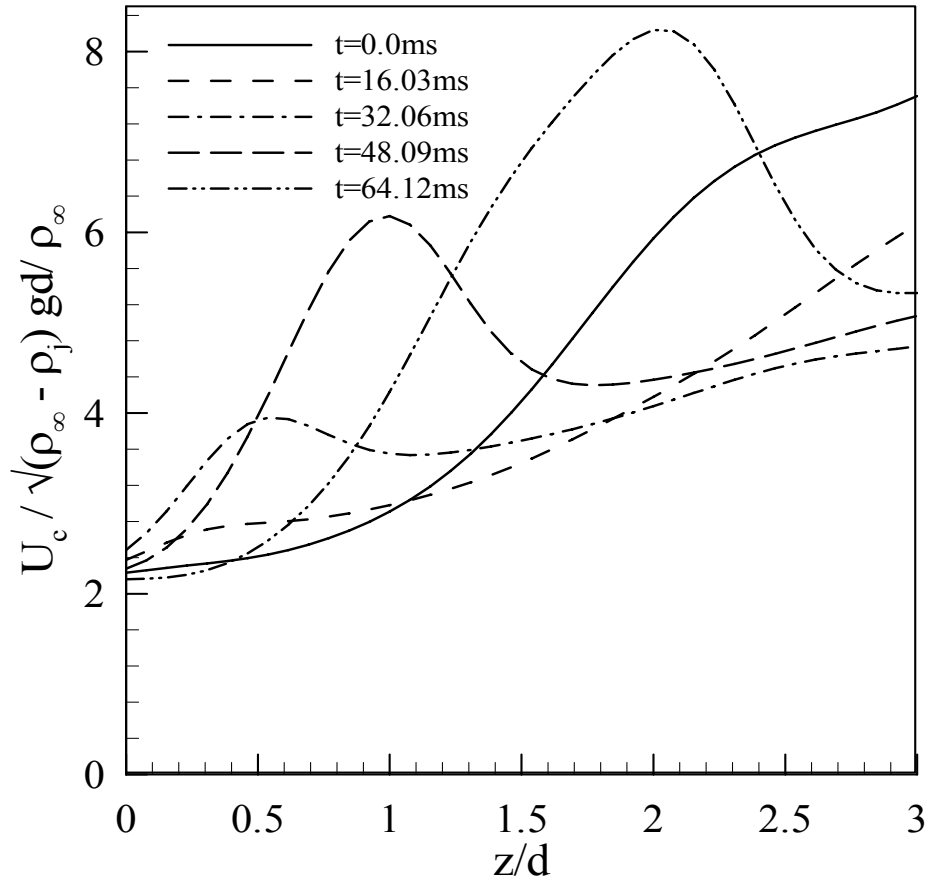


Figure 3.16. Normalized axial velocity along the jet centerline in an oscillation cycle, $Re = 150$, $Ri = 6.4$ and $d = 31.8$ mm.

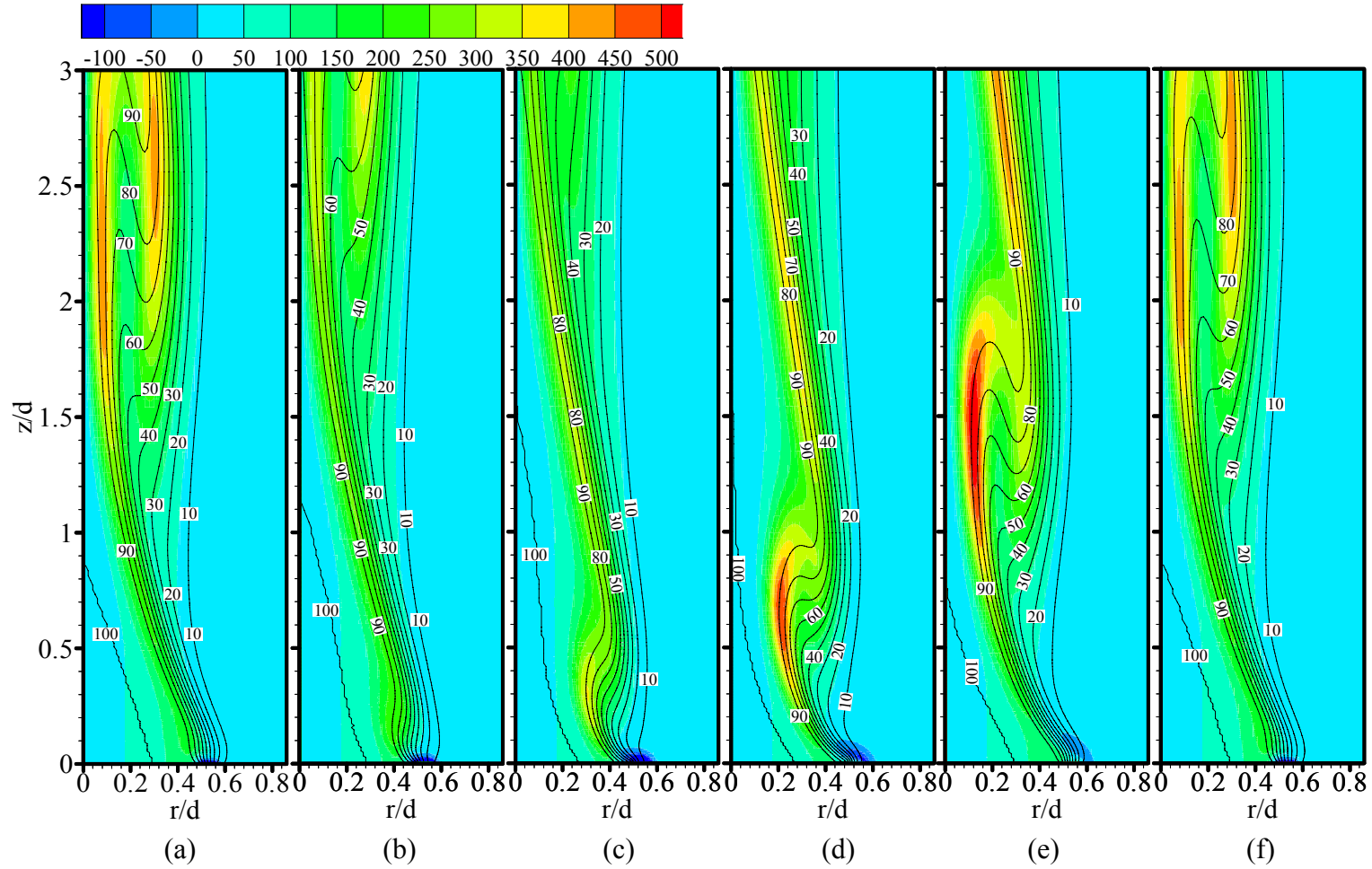


Figure 3.17. Contours of vorticity magnitude overlapped by helium mole percentage in oscillation cycle for $Re = 150$, $Ri = 6.4$ and $d = 31.8$ mm. (a) $t=0.0$ ms (b) $t=16.03$ ms (c) $t=32.06$ ms (d) $t=48.09$ ms (e) $t=64.12$ ms (f) $t=80.16$ ms.

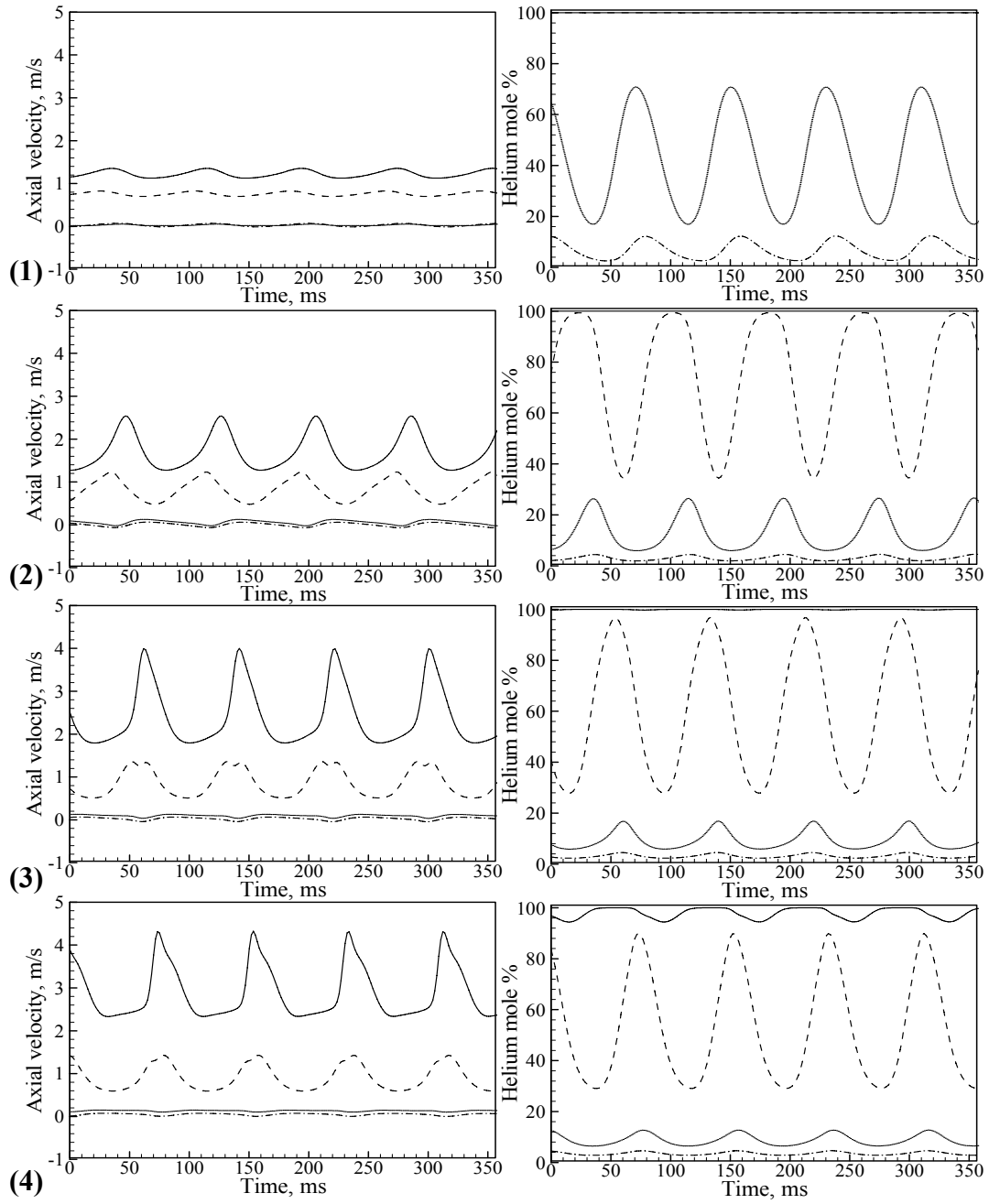


Figure 3.18. Time trace plots of axial velocity and helium mole percentage at different radial locations for $Re = 150$, $Ri = 6.4$, $d = 31.8$ mm. (1) $z/d=0.05$ (2) $z/d=0.6$ (3) $z/d=1.5$ (4) $z/d=2.5$.

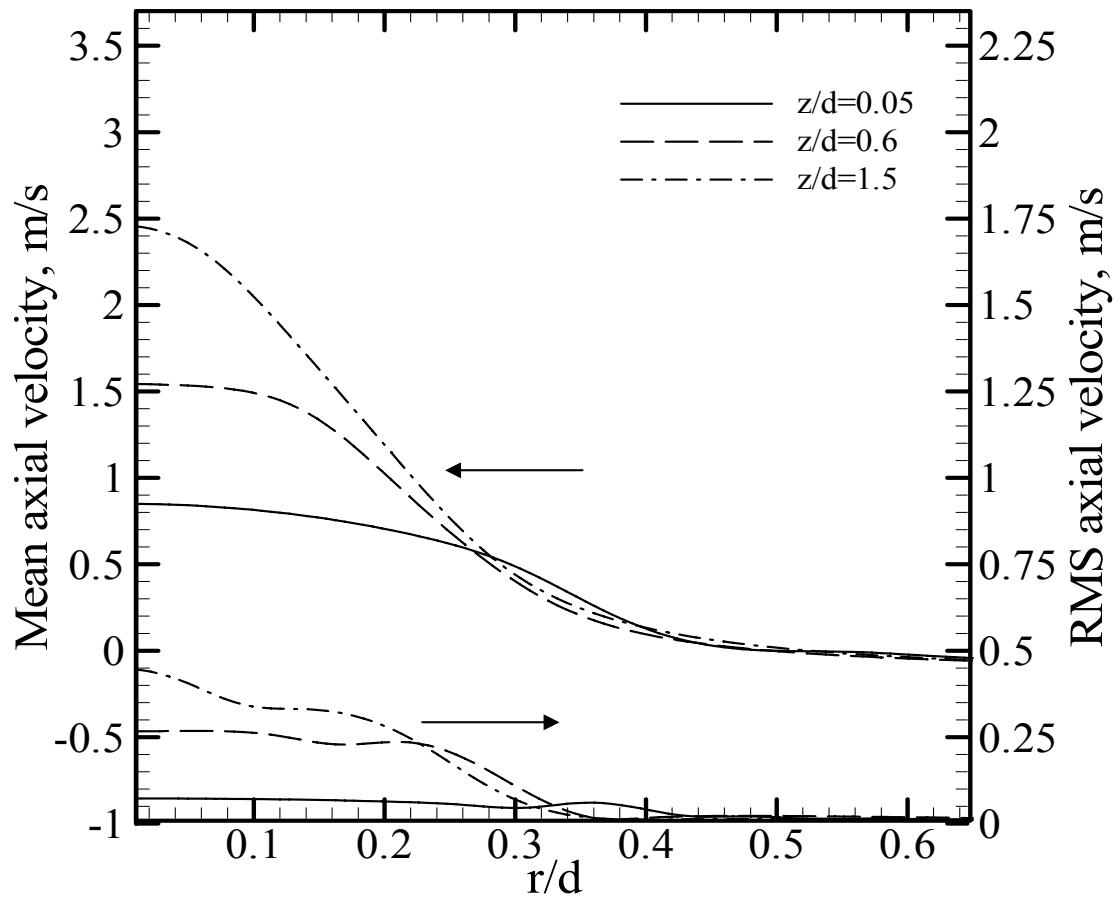


Figure 3.19. Profiles of mean and RMS axial velocity, $Re = 90$, $Ri = 17$, $d = 31.8$ mm.

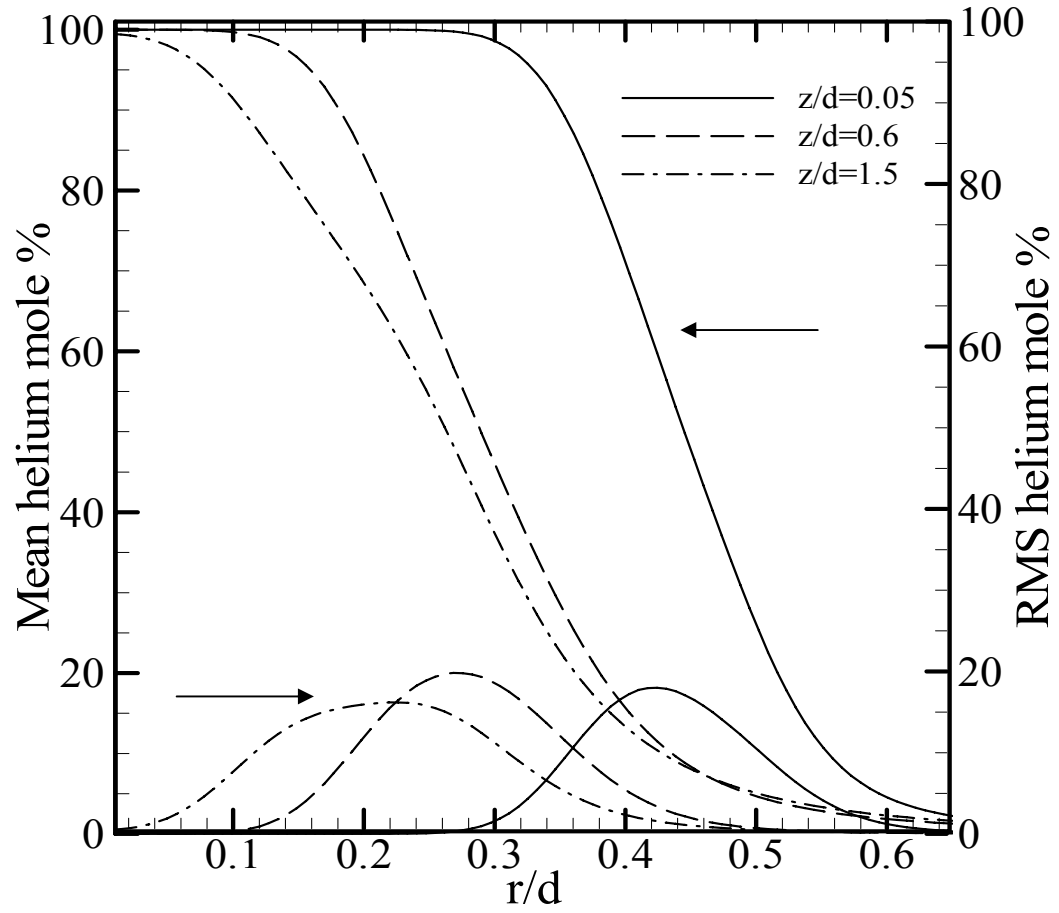


Figure 3.20. Profiles of mean and RMS helium mole percentage, $Re = 90$, $Ri = 17$, $d = 31.8$ mm.

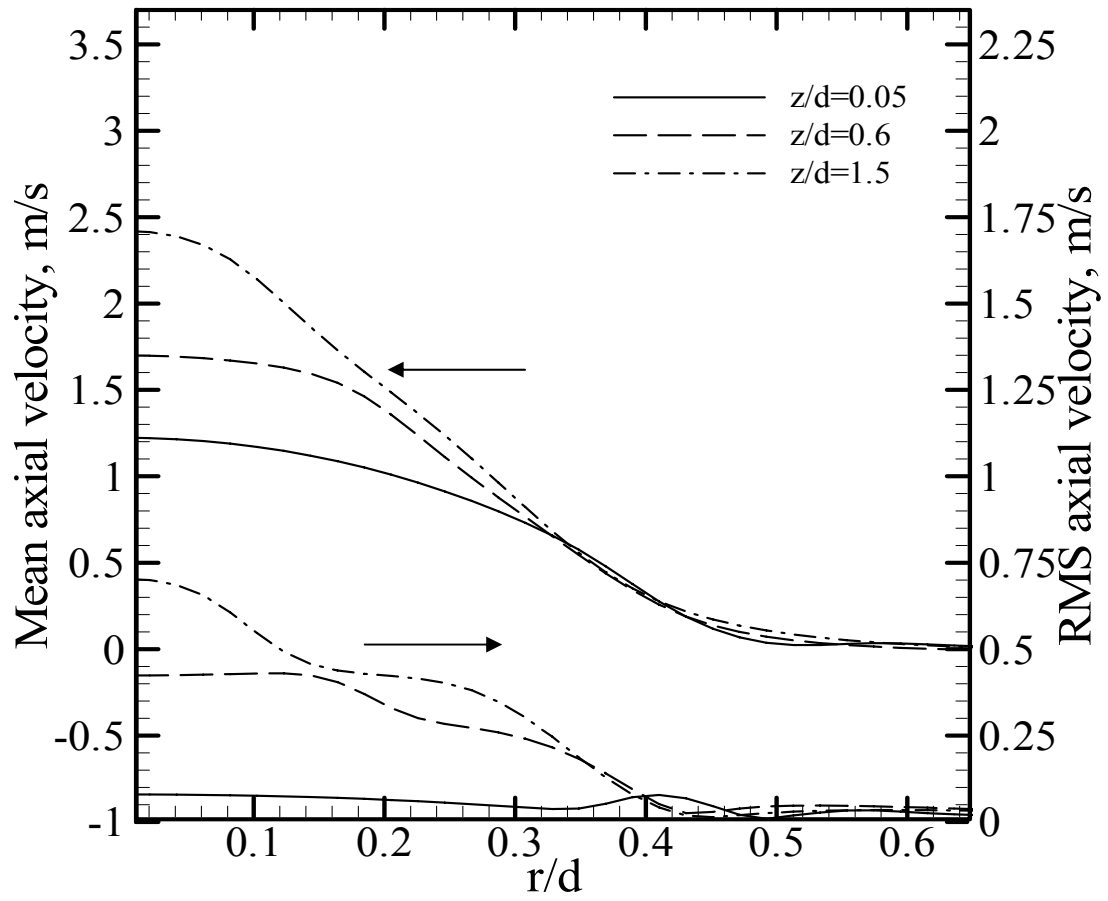


Figure 3.21. Profiles of mean and RMS axial velocity, $Re = 150$, $Ri = 6.4$, $d = 31.8$ mm.

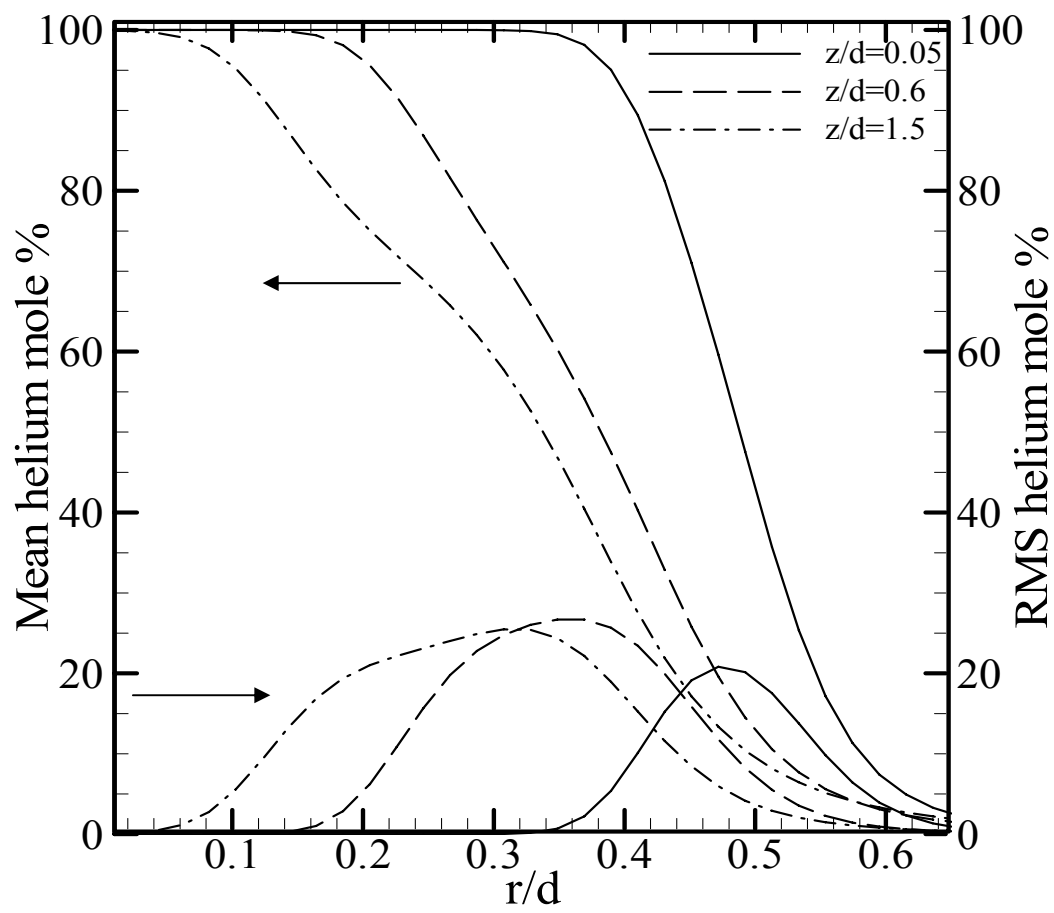


Figure 3.22. Profiles of mean and RMS helium mole percentage, $Re = 150$, $Ri = 6.4$, $d = 31.8$ mm.

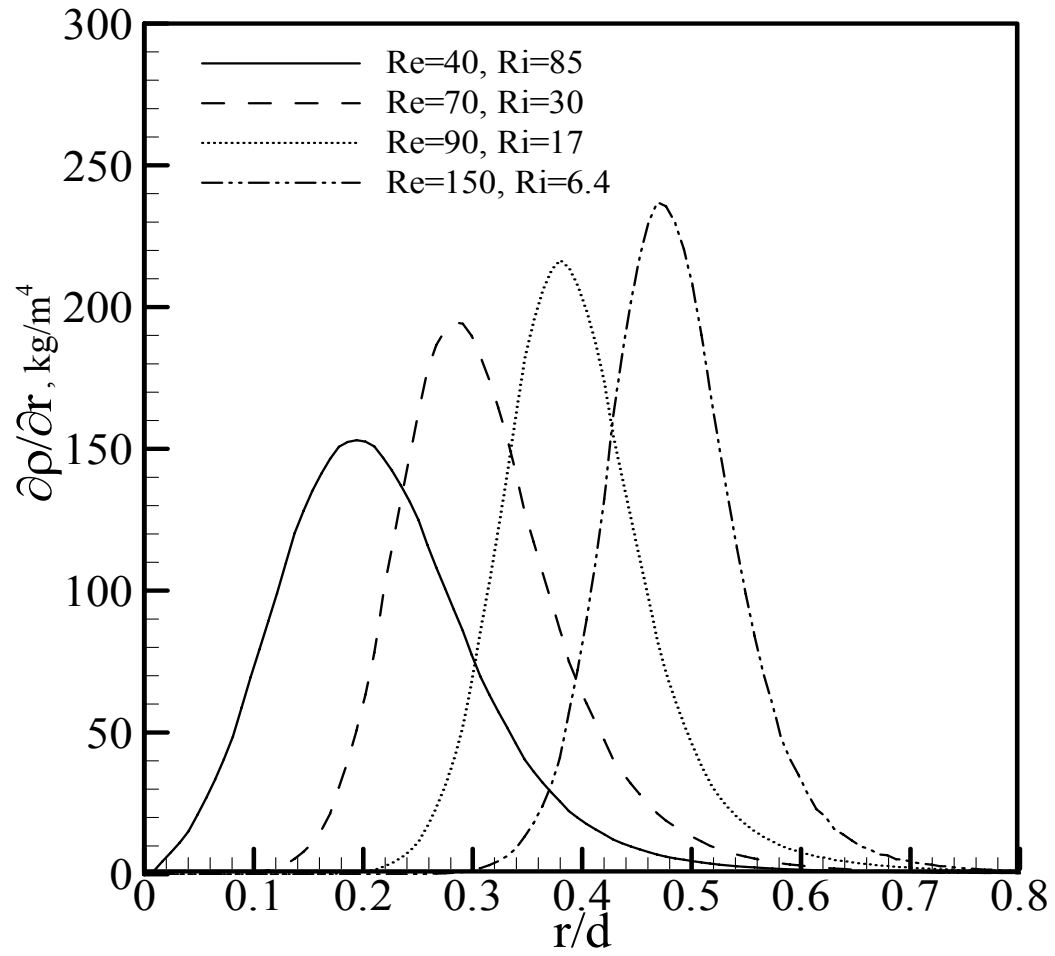


Figure 3.23. Radial profiles of density gradient in radial direction at $z/d=0.3$.

CHAPTER 4. BUOYANCY EFFECTS IN LOW-DENSITY GAS JETS

4.1 Overview of the Chapter

It is well known that buoyancy affects the global flow structure of jets/flames. The study of the effect of buoyancy is experimentally a difficult task, thus prompting the use of computational fluid dynamic analysis. As an extension to Chapter 3, the present chapter deals with CFD analysis to understand the effects of buoyancy on low-density gas jets. Both buoyant and inertial jets are simulated in Earth gravity and subsequently, reducing the gravity to simulate microgravity conditions in the 2.2s drop tower. The CFD analysis is used to concurrently visualize velocity and concentration fields, thereby exploring the physical implications of the self-excited instability in low-density gas jets.

4.2 Literature Review

Buoyant flows play an important role in various technological and environmental issues. For example, dispersal of pollutants, smoke, or volcano exhaust in the atmosphere, vertical motion of air, formation of clouds and other weather systems, and flows in cooling towers and fires are all determined primarily by buoyancy effects. As discussed previously, the near field jet behavior has direct influence on the acoustic noise and flow development in the far field turbulent regime. In particular, if the fluid density is different from that of the ambient, the resulting flow structure is susceptible to buoyancy.

Low-density gas jets are characterized by the injection of a lighter fluid into a dense ambient environment. In general, jets are considered buoyant for jet Richardson number, $Ri = gd(\rho_\infty - \rho_j)/\rho_j U_j^2 > 1.0$ and inertial for $Ri < 1.0$, where g is the gravitational acceleration, d is the injector tube inside diameter, ρ_∞ and ρ_j are, respectively, the ambient and jet fluid densities, and U_j is the average jet exit velocity. The present study examines low-density gas jets in both buoyant and inertial flow regimes, with the goal of delineating gravitational effects on the flow structure in the near-field.

Low-density gas jets are known to exhibit self-excited periodic oscillations in the near-field in both buoyant and inertial flow regimes. In the buoyant flow regime, Subbarao and Cantwell (1992) conducted experiments with helium jets injected into a co-flow of air for Ri varying from 0.5 to 6.0. The frequency (f) of the periodic oscillations expressed by the Strouhal number, $St = fd/U_j$ correlated with the jet Richardson number for $Ri > 1.0$ indicating buoyancy dependent instability. Hamins et al. (1992) observed periodic oscillations in helium jets injected into air, and reported that a minimum jet exit velocity is required to initiate the oscillations. Similar experiments were conducted by Cetegen and co-workers (1996, 1997a-b) in axisymmetric and planar plumes, whereby buoyancy induced toroidal vortical structures contaminating the primary jet flow were observed. Diagnostics involved velocity

measurements using laser Doppler velocimetry and particle image velocimetry. Pasumarthi and Agrawal (2003) conducted experiments to characterize the jet flow by concentration measurements across the whole field of a helium jet injected into quiescent air. Experiments by Yep et al. (2003) demonstrated that the self-excited flow oscillations in Earth gravity were absent in the microgravity environment of the 2.2s drop tower at the NASA Glenn Research Center.

Self-excited oscillations have also been reported in low-density inertial jets for $Ri \ll 1.0$ (Sreenivasan et al. (1989), Monkewitz et al. (1989), Kyle and Sreenivasan (1993), Richards et al (1996)). In these studies, the jet Richardson number was small and hence, buoyancy was considered negligible. Although this assumption is justified within the jet core, buoyancy could be important in the jet shear layer where the density and velocity gradients are large. Experiments by Yildirim and Agrawal (2005) show significant buoyancy effects on flow oscillations and transition to turbulence in high-momentum helium jets. Recently, Pasumarthi (2004) conducted experiments in the 2.2s drop tower using helium jets injected into quiescent air for $Ri < 1.0$. Concentration measurements revealed global self-excited oscillations in the near-field in Earth gravity. In microgravity, the oscillation amplitude decreased for $Ri < 0.01$ and no oscillations were observed for $Ri > 0.1$. These experiments provide direct physical evidence of significant buoyancy effects in low-density gas jets over a range of jet Richardson numbers.

Results by Pasumarthi and Agrawal (2005) show differences in the flow structure and transition behavior with the change of gravity in the drop tower.

Past experiments have characterized buoyancy effects using either concentration or velocity measurements. However, simultaneous visualization of velocity and concentration fields is desired to fully understand the dynamics of the oscillating flow structure. Experimental difficulties in obtaining simultaneous vector-scalar measurements, especially in the low-gravity environment, have prompted studies of gas jets using computational fluid dynamic (CFD) analysis. Mell et al (1996) performed numerical simulations of helium jets injected into air and found that the computed flow oscillation frequency matched with experiments of Hamins et al (1992). Recently, Soteriou et al. (2002) investigated the near-field dynamics of planar buoyant plumes incorporating a Lagrangian transport element method. Computations qualitatively captured the plume instantaneous behavior observed in experiments. The mechanism of vorticity generation and relative roles of buoyancy and viscous forces in explaining the plume instability were discussed. Structural details of the buoyant low-density gas jets were analyzed computationally by Satti and Agrawal (2006). On a related note, several numerical studies have been conducted to understand the dynamics of flickering jet diffusion flames (Katta and Goss 1994, Sato et al. 2002).

The above literature review reveals that the previous computational studies have not delineated the effects of buoyancy in low-density gas jets. In the present study, both buoyant and inertial jets are examined in Earth gravity, microgravity, and during the change from Earth to microgravity. The CFD analysis is utilized to concurrently visualize velocity and concentration fields, a difficult experimental task, especially in the constrained environment of the microgravity facilities. By analyzing instantaneous and time-averaged velocity and helium concentration fields over a range of jet Richardson numbers, this study aims to explore the physical implications of the self-excited instability in low-density gas jets.

4.3 Model Description

The model description for the present study is similar to the assumptions, governing equations, boundary conditions, initial conditions and computational details outlined in Chapter-3. Few additional points to be noted are given below:

- The effects of gravity are simulated as per the conditions of the 2.2 s drop tower. In the 2.2 s drop tower, the gravity changes linearly from Earth gravity to microgravity within 0.1 s after the drop. The gravitational acceleration in microgravity is $100 \mu g$, where g is Earth's gravitational acceleration. The computations replicated these features of the drop tower to simulate the evolving flow structure of the jet during the drop.

- Computations for the inertial jet required a higher number of grid nodes and a smaller time step compared to those for the buoyant jet. The buoyant required a grid size of 30,000 nodes compared to 81,000 nodes for the inertial jet. The time step size was 1.6ms for buoyant jet compared to 0.3ms for the inertial jet.
- No external perturbations were imposed to initiate the flow oscillations.

4.4 Results and Discussion

Time-dependent simulations of the isothermal helium jet injected into ambient air were performed with the objective of quantifying buoyancy effects in the near-field. Although the computations were performed for several cases, detailed results are presented only for one buoyant jet and one inertial jet at test conditions listed in Table 4.1. First, details pertaining to the flow behavior of a buoyant jet in Earth gravity and during the change from Earth gravity to microgravity are presented. Similar information is provided for the inertial jet. Finally, the flow behavior of buoyant and inertial jets is compared in Earth gravity and microgravity.

Table 4.1. Summary of Test Conditions

<i>Case</i>	<i>Re</i>	<i>Ri</i>	<i>d, mm</i>	<i>U_j, m/s</i>	<i>Grid Size</i>	<i>Time Step, ms</i>
Case 1 (Buoyant)	300	1.52	31.8	1.15	31,000	1.67
Case 2 (Inertial)	800	0.018	14.5	6.75	81,000	0.30

4.4.1 Buoyant Jet

4.4.1.1 Flow and Concentration Fields in Earth Gravity

The jet flow evolved gradually from the stationary state and eventually exhibited periodic oscillations in the near-field at a unique frequency. Computations were continued for sufficiently long time such that the effects of initial conditions and numerical disturbances were flushed out. Specifically, the flow periodicity was ascertained by monitoring the flow structure for 50 consecutive cycles indicating no detectable change between cycles. Figure 4.1 shows a sequence of velocity vector plots superimposed with helium mole percentage contours during the oscillation cycle for the buoyant jet (Case 1). At $t=0.0\text{ms}$, buoyancy accelerates the jet core, which contracts to conserve the mass. This results in the entrainment of the ambient fluid to produce a toroidal vortex. Note that the vortex core represented by a dot in Fig. 4.1 is located at $z/d=0.12$ for $t=0.0\text{ms}$.

In the next plot at $t=13.3\text{ms}$, the vortex is characterized by a larger recirculation region accompanied with greater contraction of the jet core, evident from the inward indentations in the concentration field near $z/d=0.2$. Subsequently, between $t=26.7\text{ms}$ and 55.1ms , the vortex grows in size, convects downstream and contaminates a greater portion of the jet core. The vortex gains strength by transfer of the momentum from the jet core. This feature is evident in Fig. 4.1 wherein the velocity vectors downstream of the vortex core are larger

than those upstream before interacting with the jet core. As the vortex propagates downstream, the jet expands near the tube exit to initiate another vortex at $t=68.3\text{ms}$ to repeat the oscillation cycle. These results illustrate self-excited periodicity in the jet at a frequency of 14.6Hz. Yep et al. (2003) measured an oscillation frequency of 12.5Hz at similar test conditions. However, the experiments by Yep et al. (2003) were performed in a drop rig with a short jet tube because of the severe space limitations. Thus, the flow at the jet exit was not fully developed, in contrast to the fully developed flow at the tube inlet specified for the computations. These differences in the inlet flow conditions must be considered when comparing the present results with measurements of Yep et al. (2003).

4.4.1.2 Flow and Concentration Fields during the Change from Earth Gravity to Microgravity

Computations were performed to visualize the jet flow during the change from Earth gravity to microgravity and to depict how the jet flow adjusts itself in microgravity. The simulations were compared with experiments of Yep et al. (2003) to verify the computational model in reduced gravity. Figure 4.2 shows a series of computational-experimental helium mole fraction contour plots during the change from Earth gravity to microgravity (as discussed previously, the gravity varies linearly during the first 100ms). At the onset of the change denoted as $T=0.0\text{s}$, the indentations in the helium concentration level higher than 50%

signify a vortex located at $z/d=0.7$. After 16.7ms, the vortex convects downstream as the jet expands in the near exit region. At $T=50.0\text{ms}$, the jet has expanded at the exit to $r/d= 0.7$. The indentations in the concentration contours have weakened, signifying the diminishing nature of the vortex. Subsequently, the jet widens gradually throughout the near-field as steady conditions are reached in microgravity. The helium mole fraction contours in microgravity are straight lines reminiscent of a non-buoyant jet. The above-mentioned features replicate similar phenomena observed in experiments i.e., the self-excited flow oscillations in Earth gravity subside in microgravity. Results in Fig. 4.2 show that the present model is effective in reproducing experimental features of the jet flow in the 2.2s drop tower, although the radial diffusion was under-predicted.

Figure 4.3 shows velocity vectors superimposed by contours of helium mole percentage during the change from Earth gravity to microgravity to highlight the interaction between velocity and concentration fields. At $T=0.0\text{ms}$, a vortex with its center located at $z/d=1.7$ characterizes the entrainment of ambient fluid into the jet core. Near the jet exit, the helium mole fraction is 10% at $r/d=0.6$. At $T=33.3\text{ms}$, the jet at the exit has expanded to $r/d=0.65$. The vortex has convected downstream with its center located at $z/d=3.2$. At $T=66.6\text{ms}$, the vortex has moved downstream of the field-of-view while another vortex has formed at $z/d=1.2$. In microgravity at $T=133.3\text{ms}$, the flow recirculation decreases and the jet expands to $r/d=0.75$ near the exit. Figs 4.3(b)-(e) show a gradual decrease in

the indentations in the concentration contours as the buoyancy is reduced. Similar features are exhibited at $t=166.6\text{ms}$ as the flow approaches steady state in microgravity. Finally, at $T=2000\text{ms}$ the jet assumes steady columnar shape. Further details of the flow structure during the change from Earth gravity to microgravity are discussed next using the spatio-temporal plots.

4.4.1.3 Temporal Evolution of Axial Velocity and Concentration Fields

Figure 4.4 depicts the temporal evolution of the helium concentration field during the change from Earth gravity to microgravity. Computed and measured (Yep et al. 2003) time traces of helium mole fraction at $z/d=1.0$ illustrate that the oscillating jet flow expands in the radial direction after the change in gravity. Results show that the oscillations sustain during a brief initial period of the change and steady conditions are reached within $T=0.75\text{s}$. Again, the experimental trends are predicted well by the computations. Figure 4.5 shows time trace plots of helium mole percentage and axial velocity at selected locations during the change in gravity. Near the jet exit at $z/d=0.15$, pure helium was present at the jet center ($r/d=0$) for all times. In contrast, the axial velocity at the jet center fluctuates between 2.3m/s and 2.6m/s in Earth gravity. In microgravity, the axial velocity reaches a steady value of 2.2m/s at $T=0.2\text{s}$. The reduction in the axial velocity with the change in gravity is small because the axial plane $z/d=0.15$ is close to the jet exit. In the entrainment region at $r/d=0.45$, the helium mole percentage in Earth gravity varies between 45% and 94%. During the change to

microgravity, the helium concentration peaked almost to 100% within 0.08s. Afterwards, minor variations occurred before a steady value of 95% was reached at $T=0.3s$. The corresponding axial velocity in microgravity is 0.4m/s. Near the jet boundary at $r/d=0.6$, low amplitude oscillations in the concentration field occur in Earth gravity. In microgravity, the helium mole percentage reached a steady value of 50% within $T=0.8s$. In Earth gravity, the axial velocity profile at $r/d=0.6$ shows negative velocities because of the flow recirculation.

At a downstream location, $z/d=2.0$, pure helium is present at the jet center for all times. The axial velocity and its oscillation amplitude have increased at this location, signifying buoyant acceleration in Earth gravity. The flow oscillations diminish within 0.5s of the change in gravity to result in steady axial velocity of 2.1m/s. At $r/d=0.45$, high amplitude concentration oscillations are observed in Earth gravity. At $r/d=0.6$, helium reaches peak concentration level of 64% during the change in gravity and a steady value of 56% is attained at $T=0.6s$. Axial velocity profiles in Fig. 4.5.2(b) depict flow behavior similar to that observed upstream as shown in Fig. 4.5.2(a). These features agree with time traces of the concentration field measured by Yep et al (2003).

4.4.1.4 Flow Structure: Dependence on Gravitational Forcing

In this section, the analysis has been limited only to the vortex movement and the frequency of flow oscillations as functions of the gravitational forcing. Figure 4.6 illustrates the convection velocity of the vortex core at different

gravitational levels. For Martian gravity ($g/g_o=0.37$), we observe that the vortex convected at a uniform acceleration with peak velocity of 0.9 m/s at $z/d=3.0$. Further, in Earth gravity ($g/g_o=1.0$), the vortex convection velocity increased at all the axial stations with a peak velocity of 1.0 m/s. In Jupiter gravity ($g/g_o=2.33$), the vortex convects with higher acceleration throughout the near field as shown by the steep rise of the curve, with peak velocity reaching about 2.0m/s. Notice that with increase in buoyancy, the vortex convection velocity increases throughout the near field. Accordingly, the entrainment rate, which is a function of the vortex convection velocity, would also increase at higher gravitational levels. Higher entrainment rate leads to enhanced mixing and contamination of the jet core in the downstream region.

Figure 4.7 shows the plot explaining the variation of frequency of flow oscillation with the gravitational level. The best fit resulted in the relationship between oscillation frequency and gravitational acceleration as $f = 9.38(g/g_o)^{0.2}$.

4.4.2 Inertial Jet

4.4.2.1 Flow and Concentration Fields in Earth Gravity

Figure 4.8 shows a sequence of velocity vector plots superimposed with helium mole percentage contours to depict an oscillation cycle for the inertial jet. In this case, the computed results are presented between $r/d=0.3$ and 0.65 to visualize the flow oscillation region in greater details. At $t=0.0\text{ms}$, buoyant acceleration contracts the jet core leading to entrainment and formation of the

toroidal vortex. The flow structure including the nature and propagation of the toroidal vortex is similar to that of the buoyant jet in Fig. 4.1. The computed oscillation frequency was 150Hz, compared to a frequency of 120Hz measured in Earth gravity by Pasumarthi (2004) in the drop rig. The deviation between computed and measured frequencies is attributed in part to the differences in the jet inlet conditions as discussed previously.

Although self-excited flow oscillations were observed in both buoyant and inertial jets, some aspects of the flow field are different. First, based on the concentration field, the inertial jet is wider compared to the buoyant jet. The contraction of the jet core and the mixing by entrainment are confined to a narrower region in the inertial jet compared to those in the buoyant jet. The oscillation frequency of the inertial jet is much higher (150Hz) than that for the buoyant jet (14.5Hz). Results illustrate self-excited periodicity in the flow field irrespective of the initial jet momentum, which agrees qualitatively and quantitatively with experiments.

4.4.2.2 Flow and Concentration Fields during the Change from Earth Gravity to Microgravity

Figure 4.9 shows velocity vector plots overlapped with contours of helium mole percentage during the change from Earth gravity to microgravity to highlight the interactions between velocity and concentration fields. At the onset of the change ($T=0.0\text{ms}$), a toroidal vortex is located at $z/d \cong 1.6$. This vortex

convects downstream and a new one is observed at $z/d=1.4$ at $T=24.9\text{ms}$. Subsequently, the jet flow attains a periodic structure in microgravity as depicted in Figs. 4.9(c)-(f). The curvature of the concentration contours is less severe and the vortex is narrower in microgravity. This result is consistent with experiments of Pasumarthi (2004) showing a decrease in the flow oscillation amplitude in microgravity for $Ri < 0.01$. Computations in microgravity were performed for 20 oscillation cycles to ascertain the periodic nature of the flow oscillations. Results confirmed highly-periodic oscillations at the same frequency in both Earth gravity and microgravity. Thus, even though the buoyancy affects the overall flow structure, the self-excited oscillations in the inertial gas jet occurred regardless of the gravity.

4.4.2.3 Temporal Evolution of Axial Velocity and Concentration Fields

Figure 4.10 shows time trace plots of helium mole percentage and axial velocity at selected locations during the change from Earth gravity to microgravity. At $z/d=0.5$, the helium concentration at the jet center remained 100% throughout. Concentration fluctuations for the inertial jet are smaller compared to those for the buoyant jet shown in Fig. 4.5. Axial velocity at the jet center fluctuates between 13 and 14 m/s in Earth gravity and between 12.5 and 13.5 m/s in microgravity. At the downstream location, $z/d=2.0$, the axial velocity fluctuates between 12 and 15 m/s in Earth gravity. These fluctuations are slightly smaller in microgravity. The concentration and velocity fields in Fig. 4.10 reveal

that the flow oscillation amplitude decreases in microgravity, ascertaining the importance of buoyancy in inertial low-density gas jets.

4.4.3 Comparison of Flow Behavior in Buoyant and Inertial Jets

In this section, buoyant and inertial jet flows are compared to identify similarities and differences in the flow behavior.

4.4.3.1 Vortex Convection Velocity

Figure 4.11 shows the vortex convection velocity (U_v) normalized by the average jet exit velocity (U_j) in Earth gravity. The vortex convection velocity was calculated by manually tracking the position of the vortex center at different phases of the oscillation cycle. Results in Figure 4.11 show a gradual increase in the vortex convection velocity in the flow direction. The vortex attains a nearly constant velocity in the downstream region. At $z/d=2.0$, the normalized vortex convection velocity (U_v/U_j) is 1.35, 1.25, and 0.70, respectively, for $Ri=1.52$ (Case 1), $Ri=0.18$, and $Ri=0.018$ (Case 2). At this axial plane, the vortex convection velocity normalized by the buoyant velocity (U_v/U_b) was 2.99, 7.83, 13.84, respectively, for $Ri=1.52$ (Case 1), $Ri=0.18$, and $Ri=0.018$ (Case 2). Here $U_b = \sqrt{gd(\rho_\infty - \rho)/\rho_\infty}$ and $U_j/U_b = 2.22, 6.42, \text{ and } 19.2$, respectively for $Ri=1.52$ (Case 1), $Ri=0.18$, and $Ri=0.018$ (Case 2).

4.4.3.2 Axial Velocity Profiles

As stated previously, buoyancy plays an important role in manifesting the flow instability. Buoyancy is prominent in the jet core for the buoyant jet.

However, in the inertial jet, buoyancy effects are confined to the low-momentum region of the jet shear layer. This phenomenon is illustrated by the profiles of instantaneous axial velocity at various radial locations in Fig.4.12 & 4.13. The axial velocity was normalized by the jet exit velocity ($U_e(r)$) at that particular radial location. The profiles in Fig. 4.12 & 4.13 show the axial velocity in the streamwise direction at different phases of the oscillation cycles depicted in Figs. 4.1 and 4.8.

The normalized axial velocity profiles for the buoyant case (Figs. 4.12a-c) show periods of acceleration and deceleration at any given phase. The phases reveal the periodic flow behavior in the near-field region. Along the jet centerline, at phase A, the flow decelerates slightly up to $z/d=0.8$ and then accelerates rapidly between $z/d=1.0$ and 2.0 . The velocity peaks at $z/d=2.0$, which is upstream of the vortex center at $z/d=2.15$. In Phase B, the flow accelerates near the jet exit, where the vortex is formed. In phase C, rapid flow acceleration is observed near the jet exit, with peak normalized axial velocity of 1.25 at $z/d=0.5$, i.e., upstream of the vortex core at $z/d=0.80$. Subsequently, the flow decelerates because of the momentum exchange between jet core and vortex. Later in phases D and E, the flow decelerates near the exit but accelerates at downstream locations. Note that the normalized peak axial velocity increases to about 1.7 in phase D and to 2.0 in phase E. A common feature is the flow acceleration upstream of the vortex center and deceleration downstream of it. The inertial jet shows a similar behavior.

However, the velocity profiles are elongated implying that the velocity peaks farther downstream. The maximum normalized axial velocity is within 1.1 in all phases (fig. 4.13).

At $r/d=0.3$, both buoyant and inertial jets exhibit flow acceleration and deceleration near the vortex region. The peak normalized axial velocity decreases from 2.0 at $r/d=0.0$ to 1.4 at $r/d=0.3$ for the buoyant jet. However, it increases from 1.1 at $r/d=0.0$ to 1.2 at $r/d=0.3$ in the inertial jet. These results illustrate greater importance of buoyancy in the inertial jet at $r/d=0.3$. At $r/d=0.45$, both buoyant and inertial jets show large increases in the normalized axial velocity because of the smaller initial momentum in the shear layer region near the jet exit. The flow acceleration signified by the peak axial velocity is similar for buoyant and inertial jets at this radial location ($r/d=0.45$).

4.4.3.3 Mean and RMS Flow Structure

The oscillating flow field of buoyant and inertial jets is compared in Fig. 4.14-17 using the mean and RMS profiles of helium mole percentage and axial velocity at several axial locations. Near the jet exit at $z/d=0.05$, the mean concentration shows a top hat profile with finite shear layer thickness. Pure helium is present up to $r/d=0.38$ for the buoyant jet (fig. 4.14) and up to $r/d=0.46$ (fig. 4.16) for the inertial case. A steep reduction in helium concentration occurs thereafter. The jet extends to $r/d \cong 0.8$ for the buoyant case and to $r/d > 0.8$ for the inertial case, indicating greater radial expansion at small Richardson numbers (or

higher Reynolds number). Thus, the radial diffusion of helium in the near-field is inhibited by strong buoyant acceleration in the buoyant jet.

At $z/d=0.5$, the mean helium concentration at $r/d=0.5$ reduces to 50% for the buoyant jet (fig. 4.14) and to 75% for the inertial jet (fig. 4.16), suggesting greater radial mixing for the former case. Farther downstream at $z/d=1.5$, helium concentration profiles show an inflection point associated with the vortex at $r/d=0.29$ for the buoyant jet and at $r/d=0.33$ for the inertial jet. The concentration gradient near the inflection point is higher for the buoyant jet as compared to the inertial jet.

The RMS concentration profiles show large fluctuations near the jet exit for the buoyant jet (fig. 4.14). The peak RMS concentration of 14% at $z/d=0.05$ increases to 25% at $z/d=0.5$ and to 29% at $z/d=1.5$. The location of the peak RMS concentration shifts inwards in the flow direction, which is consistent with the contraction of the jet as the vortex propagates downstream. In agreement with experiments¹², the helium concentration fluctuations confined to a wake region ($0.4 < r/d < 0.6$) near the jet exit broaden in the flow direction and contaminate a greater portion of the flow at $z/d > 1.0$. For the inertial jet (fig. 4.16), the helium concentration fluctuations are negligible at $z/d=0.05$. The peak RMS helium concentration of 10% at $z/d=0.5$ increases to 12% at $z/d=1.5$. Smaller fluctuations signify poor scalar mixing in the inertial jet.

Mean axial velocity at $z/d=0.05$ shows a typical parabolic profile at the tube exit for both buoyant and inertial jets. For the buoyant jet, the axial velocity at the jet centerline increases from 2.4m/s at $z/d=0.05$ to 2.6 m/s at $z/d=0.5$, and to 3.1 m/s at $z/d=1.5$, indicating strong buoyant acceleration. However, the buoyant acceleration is confined mainly to $r/d < 0.3$ (fig. 4.15). In the inertial jet (fig. 4.17), the mean axial velocity is nearly the same at all axial locations. The RMS axial velocity profiles show negligible fluctuations near the jet exit ($z/d=0.05$) for both cases. The peak fluctuations increase in the flow direction. For the buoyant jet, the peak RMS velocity of 0.3m/s at $z/d=0.5$ increases to 0.75m/s at $z/d=1.5$. The corresponding values for the inertial jet are 0.3m/s at $z/d=0.5$ and 1.0 at $z/d=1.5$. Note that the RMS axial velocity decreases from the centerline towards the boundary plane for the buoyant jet. In contrast, the RMS axial velocity is nearly constant up to $r/d \cong 0.4$ for the inertial jet.

4.4.3.4 Jet Half Radius

As discussed above, the jet width increased with increasing initial jet momentum (or the jet Reynolds number). This behavior is quantified by the jet half radius computed at several axial locations; here the jet half radius ($r_{1/2}$) is the radial location where the helium mole fraction or the axial velocity is half of that at the jet center. Figures 4.18-4.19 show the jet half radius normalized by the tube inside diameter, determined from helium concentration and axial velocity profiles. Results in Fig. 4.18 show that the scalar jet half radius (based on helium

concentration profiles) in the axial direction decreases for the buoyant jet, increases for the inertial jet, and remains nearly constant for $Ri=0.18$, $Re=400$, $d=19.05\text{mm}$. The jet half radius determined from axial velocity profiles, shown in Fig. 4.19, also decreases in the axial direction for the buoyant jet, but remains nearly constant for the inertial jet. In a buoyant jet, the ambient fluid is entrained into the jet core because of the rapid acceleration. Consequently, the radial expansion of the jet is constrained and the mixing between jet and ambient fluids is enhanced. In contrast, the high momentum of the inertial jet limits buoyant acceleration and hence, the penetration of the ambient fluid into the jet core. Thus, the jet half radius is greater because the jet core is less contaminated by the ambient fluid.

4.4.3.5 Flow Behavior in Microgravity

Radial profiles of axial velocity and helium concentration in microgravity are presented in Fig. 4.20-4.23 for buoyant and inertial jets. These profiles were obtained after the jet adapted to the change in gravity. In microgravity, the jet assumed steady, non-oscillatory structure for the buoyant case and an oscillatory flow for the inertial jet. For both cases, the jet width increased with reduction in gravity. For the buoyant jet (fig. 4.20), the helium concentration at $r/d=0.7$ is less than 5% in Earth gravity and between 10 and 30% in microgravity. The corresponding values for the inertial jet are between 10 and 20% in Earth gravity and between 20 and 30% in microgravity (fig. 4.22). Figure 4.20-23 shows that

the oscillation amplitude for the inertial jet is smaller in microgravity compared to that in Earth gravity. The increase in the radial extent of the jet in microgravity signifies greater role of molecular diffusion in the absence of buoyancy, a well-known phenomena in flames.

4.5 Conclusions

A laminar, time-dependent, axisymmetric numerical model was developed and validated to predict the flow structure of low-density gas jets. The CFD-based model was used to simulate buoyant and inertial jets in Earth gravity and microgravity. The major conclusions of the study are summarized in the following:

- Both buoyant and inertial jets exhibited self-excited periodic oscillations in Earth gravity. The oscillation frequency was higher, the oscillation amplitude was smaller, and oscillations were confined to a narrower region in the inertial jet as compared to the buoyant jet.
- The buoyant jet depicted flow oscillations for a brief period during the change from Earth gravity to microgravity. The jet eventually attained a steady, columnar structure in microgravity, signifying that the flow oscillations were buoyancy induced.
- The inertial jet exhibited a reduction in the oscillation amplitude during the change from Earth gravity to microgravity. However, the flow oscillated at the same frequency in both Earth gravity and microgravity.

- The jet width in Earth gravity increased with increasing initial jet momentum.
This unusual behavior of low-density gas jets was explained by the buoyant acceleration of the jet core and its interaction with the toroidal vortex.
- The jet width increased with reduction in gravity, signifying a greater role of molecular diffusion in microgravity.

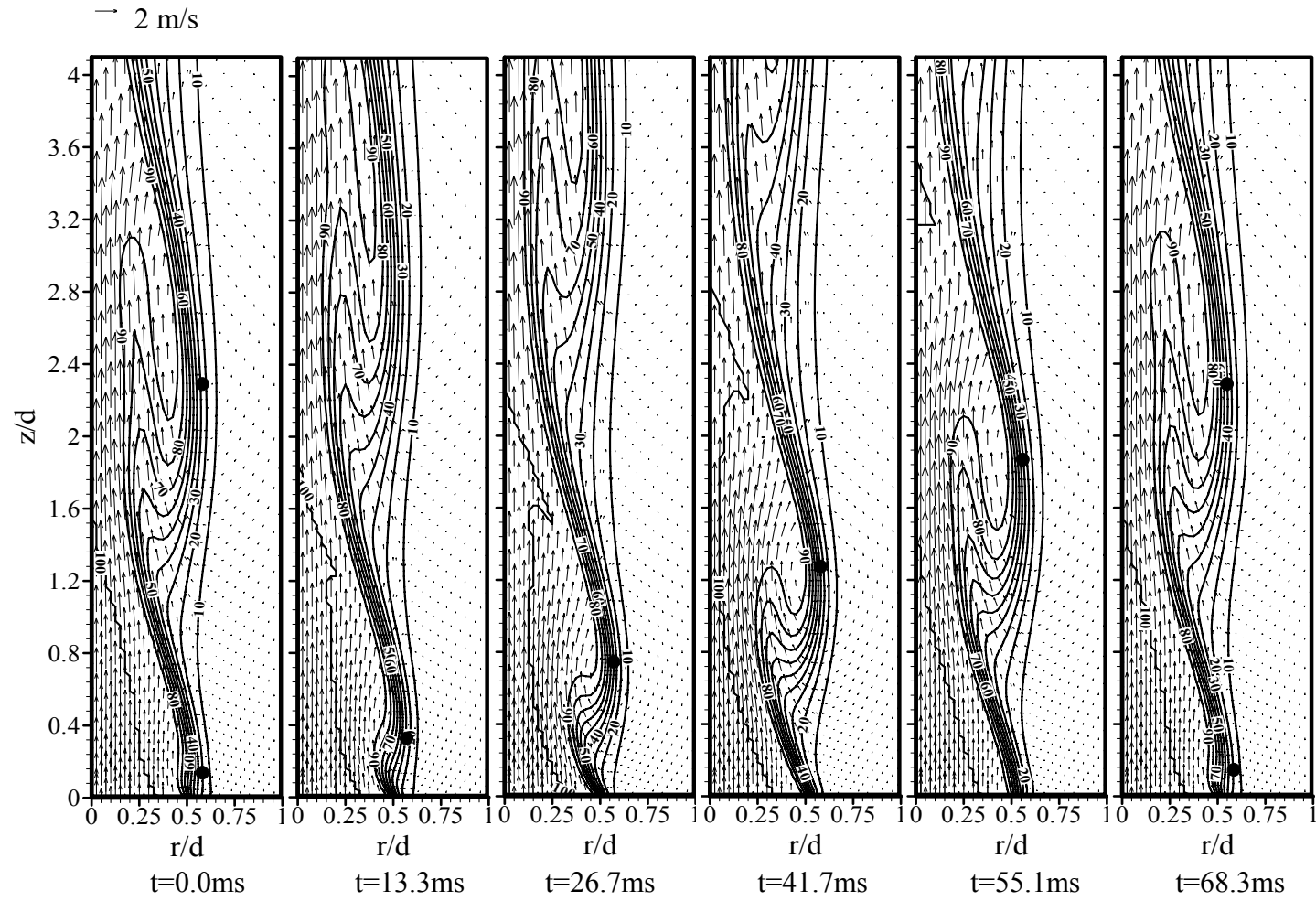


Figure 4.1. Velocity vectors superimposed by contours of helium mole percentage during an oscillation cycle in Earth gravity for the buoyant jet, $Ri=1.52$, $Re=300$, $d=31.8\text{mm}$ (Case 1).

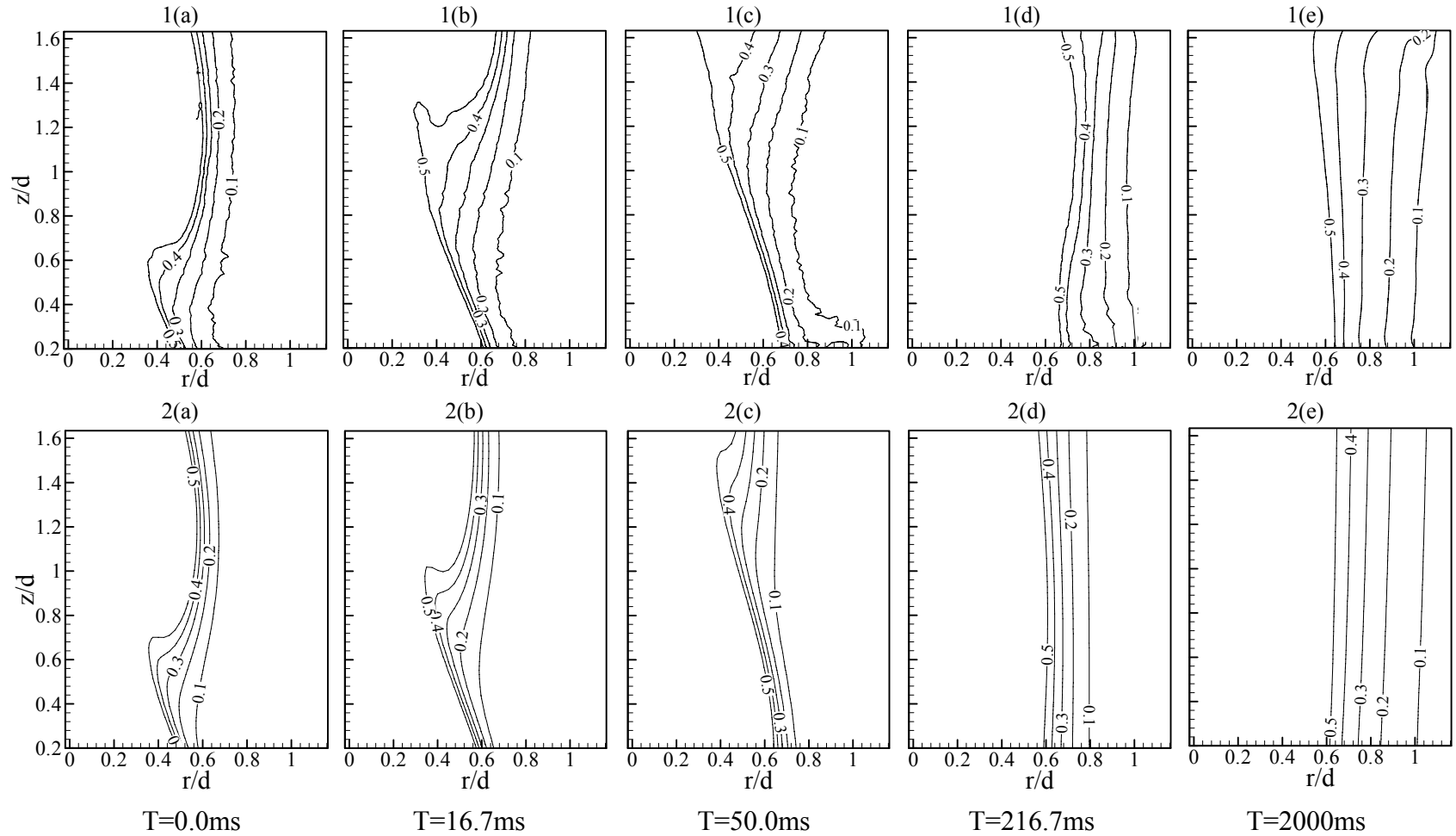


Figure 4.2. Measured (1) and computed (2) helium mole fraction contours during the change from Earth gravity to microgravity for the buoyant jet, $Ri=1.52$, $Re=300$, $d=31.8\text{mm}$ (Case 1).

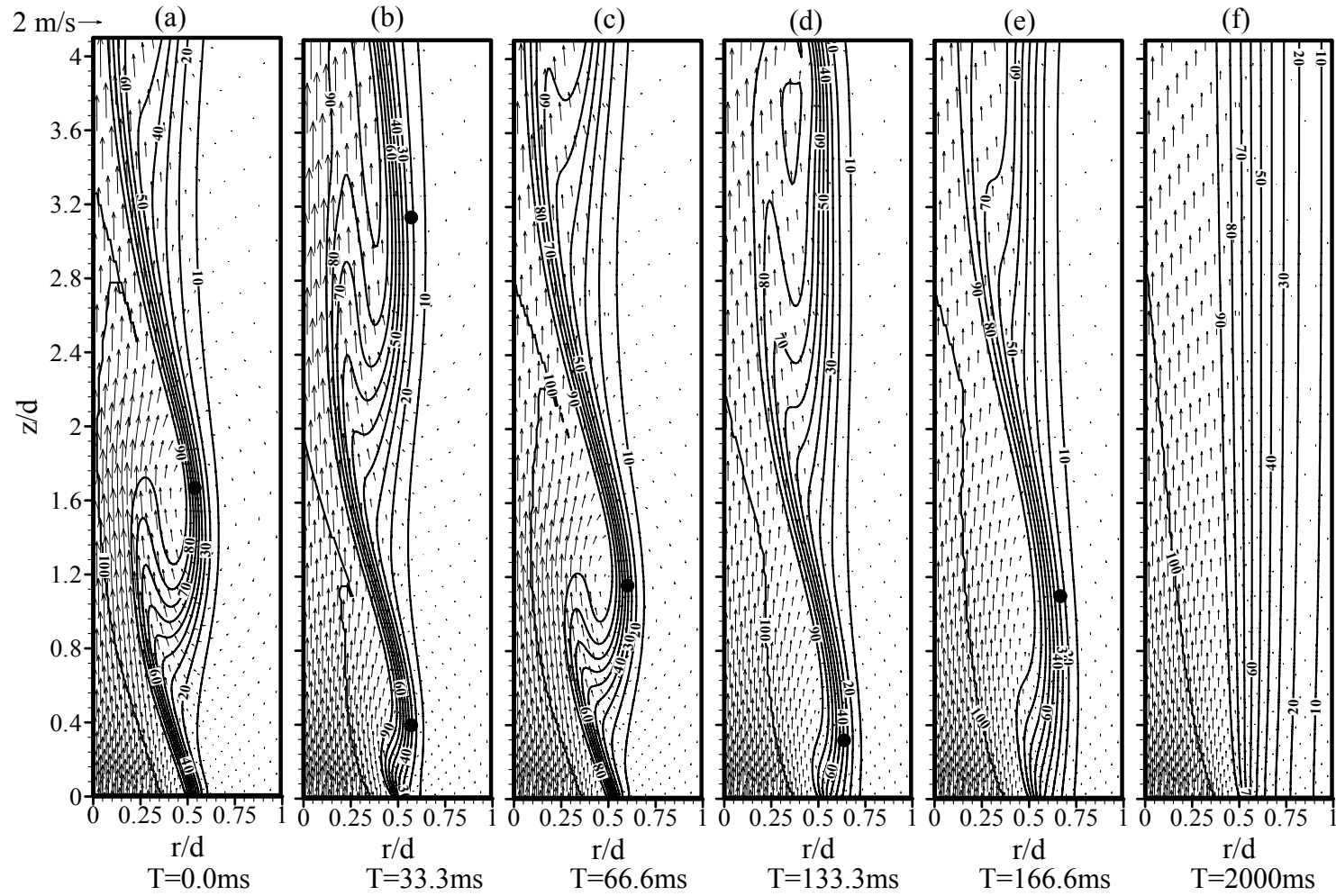


Figure 4.3. Velocity vectors superimposed by contours of helium mole percentage during the change from Earth gravity to microgravity for the buoyant jet, $Ri=1.52$, $Re=300$, $d=31.8\text{mm}$ (Case 1).

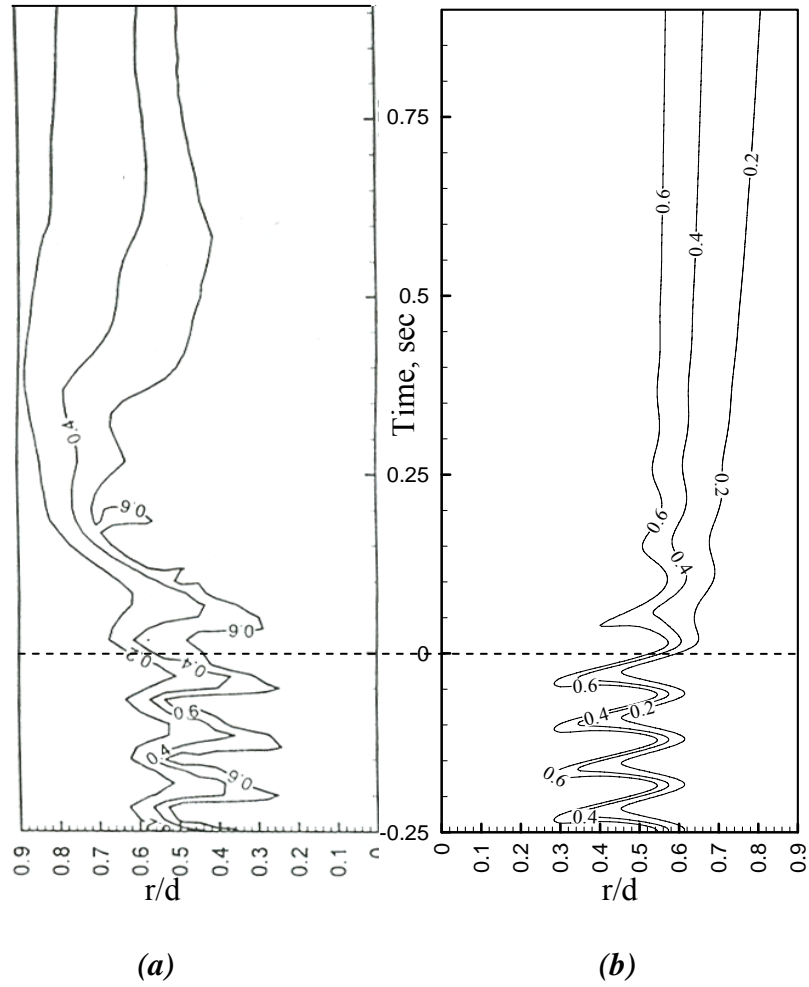


Figure 4.4. Measured (a) and computed (b) time traces of helium mole fraction during the change from Earth gravity to microgravity for the buoyant jet, $Ri=1.52$, $Re=300$, $d=31.8\text{mm}$ (Case 1) at $z/d=1.0$.

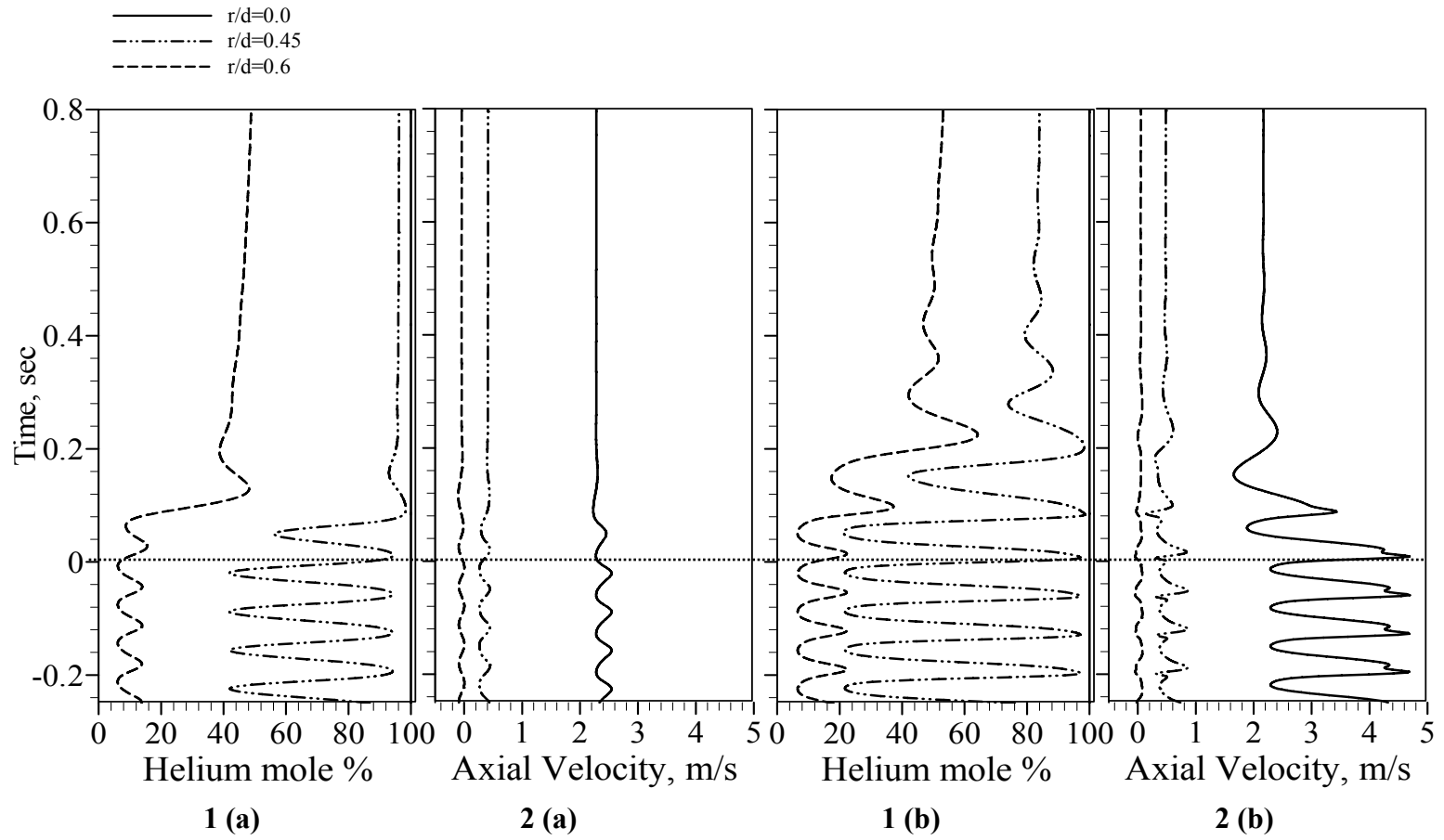


Figure 4.5. Time traces of 1) helium mole percentage and 2) axial velocity during the change from Earth gravity to microgravity for the buoyant jet, $Ri=1.52$, $Re=300$, $d=31.8\text{mm}$ (Case 1) at (a) $z/d=0.15$ (b) $z/d=2.0$.

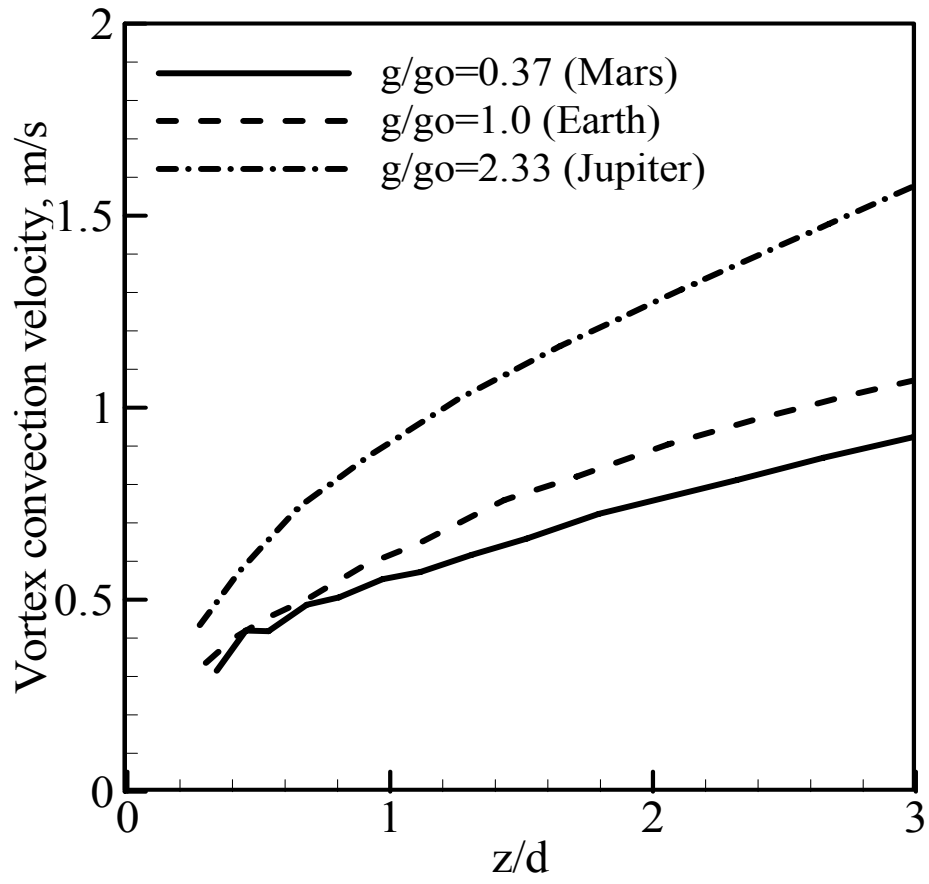


Figure 4.6. Vortex convection velocity at various gravitational levels.

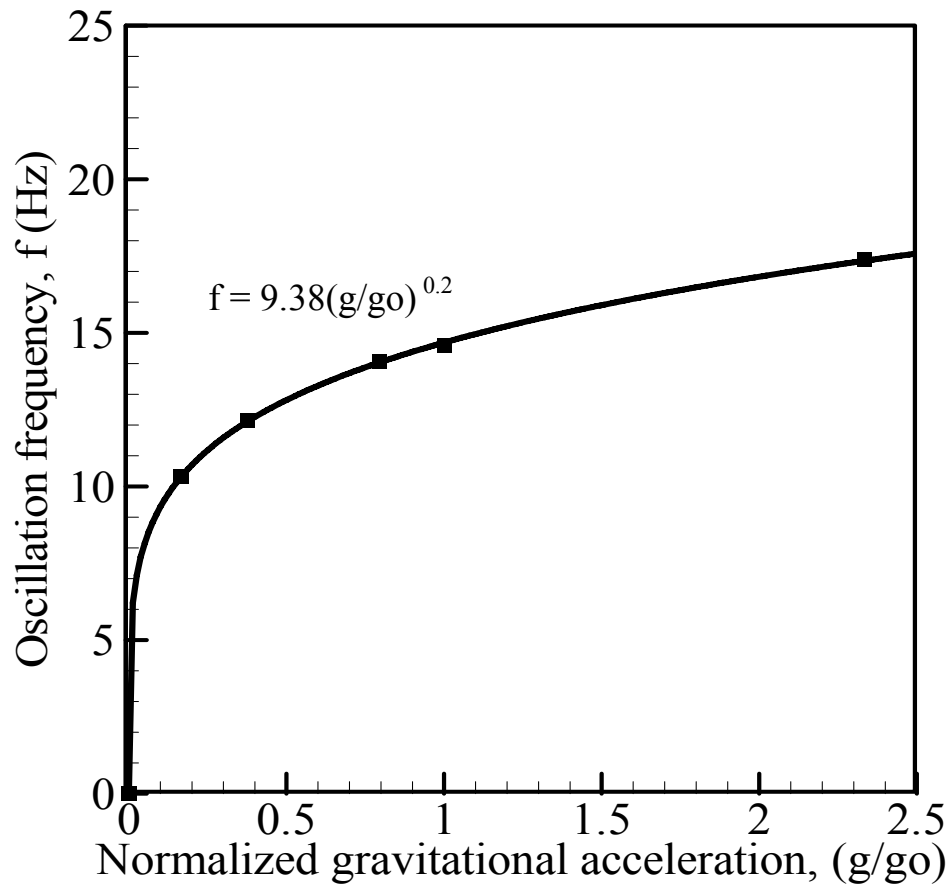


Figure 4.7. Oscillation frequency Vs normalized gravitational acceleration.

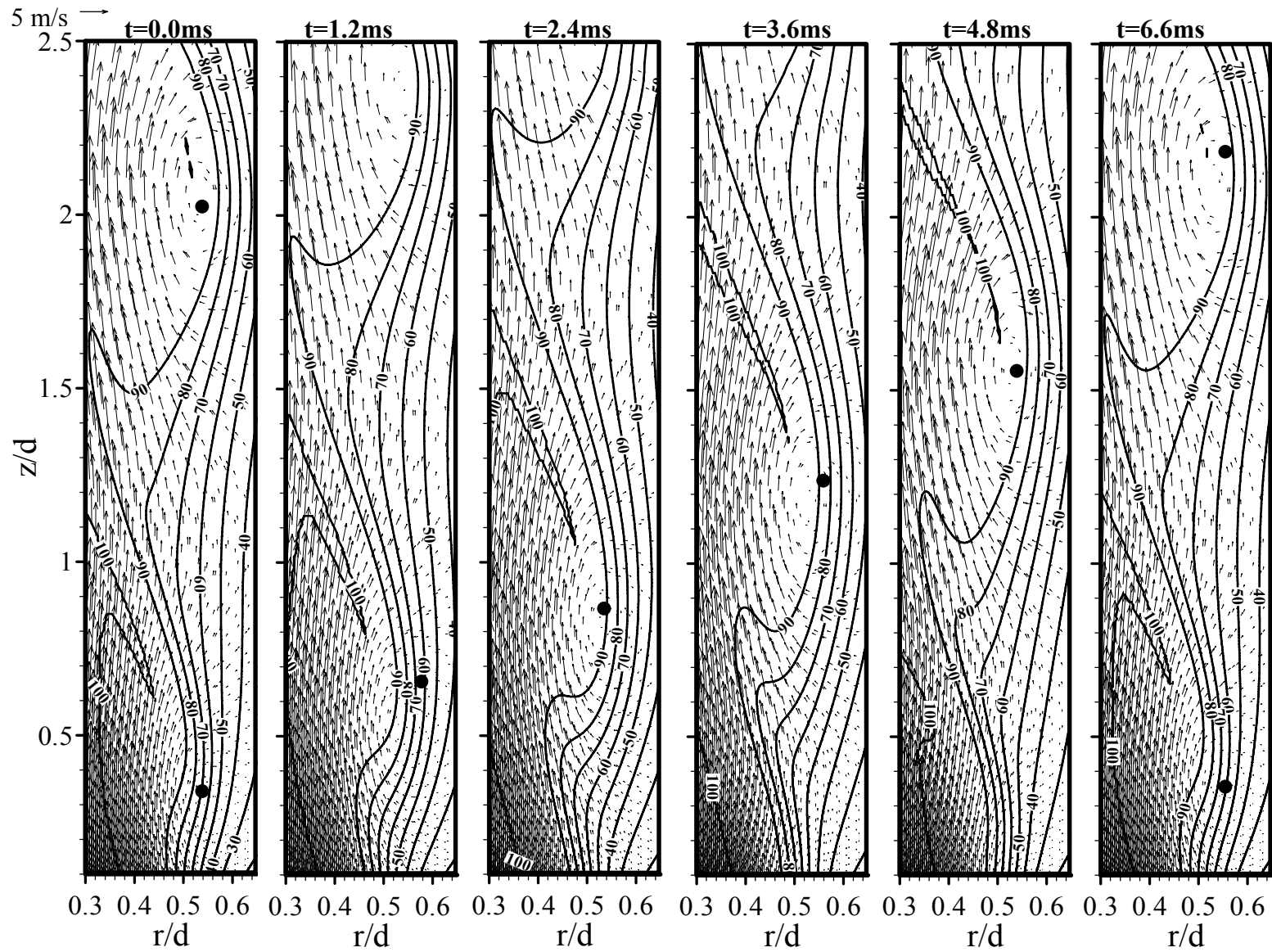


Figure 4.8. Velocity vectors superimposed by contours of helium mole percentage during an oscillation cycle in Earth gravity for the inertial jet, $Ri=0.018$, $Re=800$, $d=14.5\text{mm}$ (Case 2).

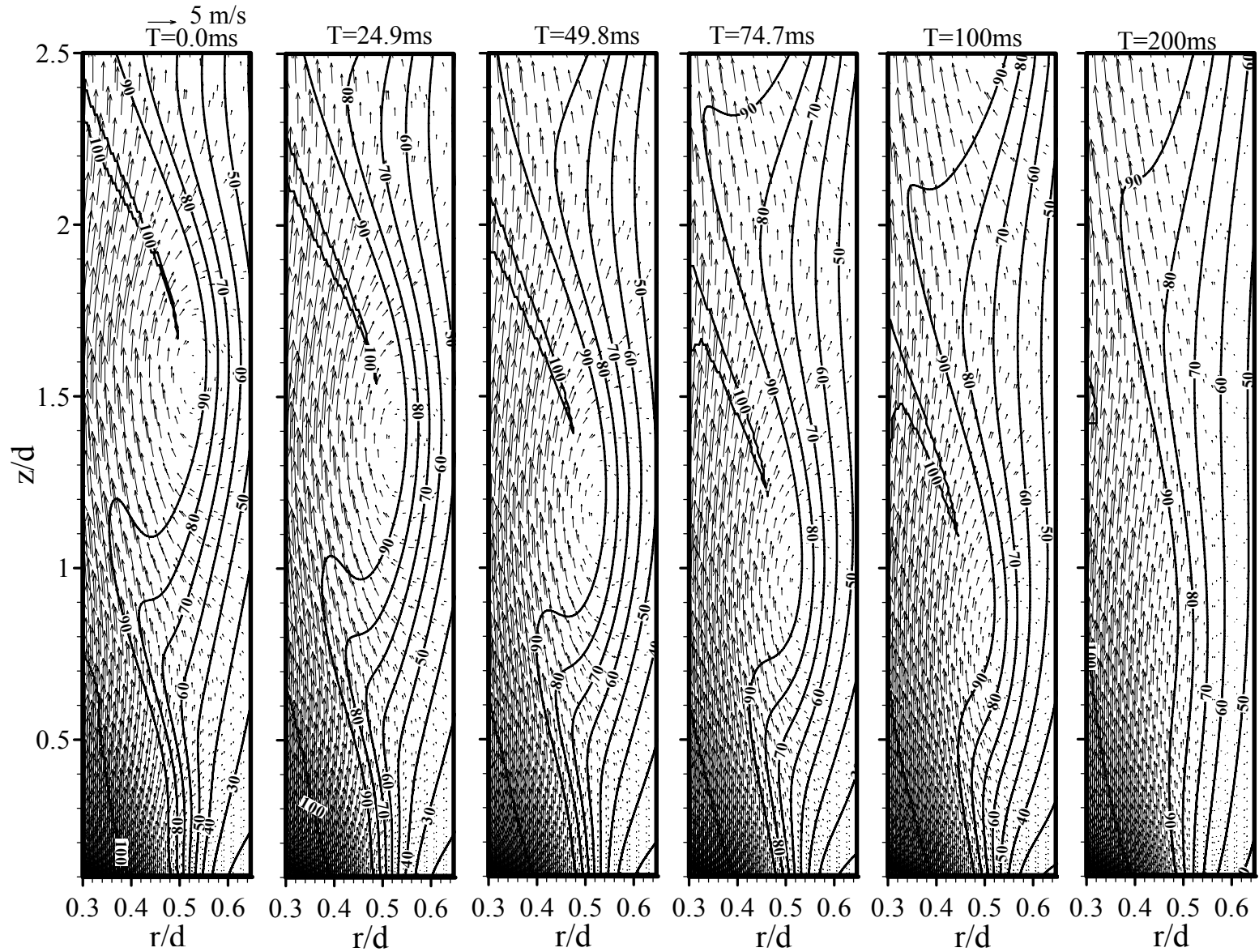


Figure 4.9. Velocity vectors superimposed by contours of helium mole percentage during the change from Earth gravity to microgravity for the inertial jet, $Ri=0.018$, $Re=800$, $d=14.5\text{mm}$ (Case 2).

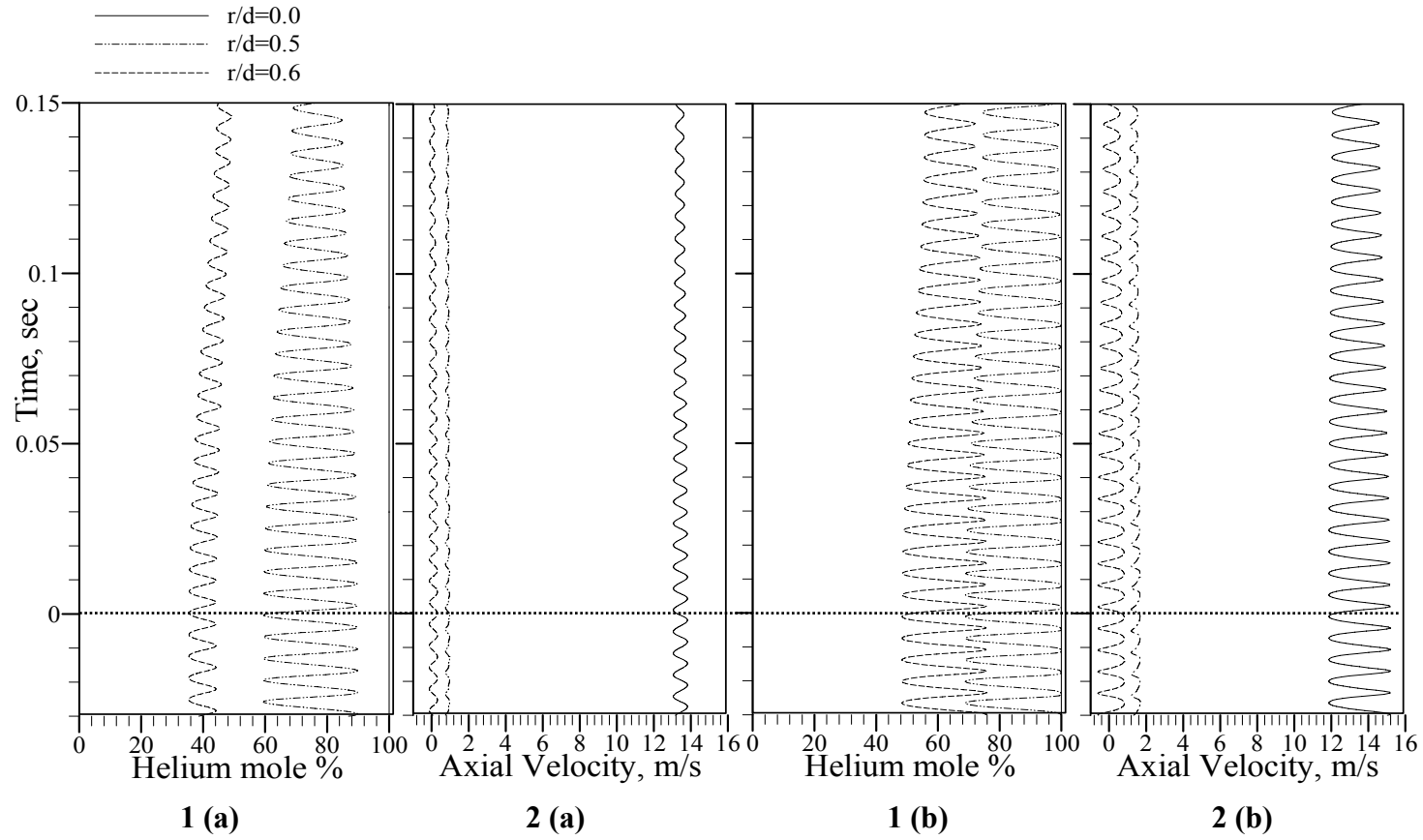


Figure 4.10. Time traces of 1) helium mole percentage and 2) axial velocity during the change from Earth gravity to microgravity for the inertial jet, $Ri=0.018$, $Re=800$, $d=14.5\text{mm}$ (Case 2) at (a) $z/d=0.5$ (b) $z/d=2.0$.

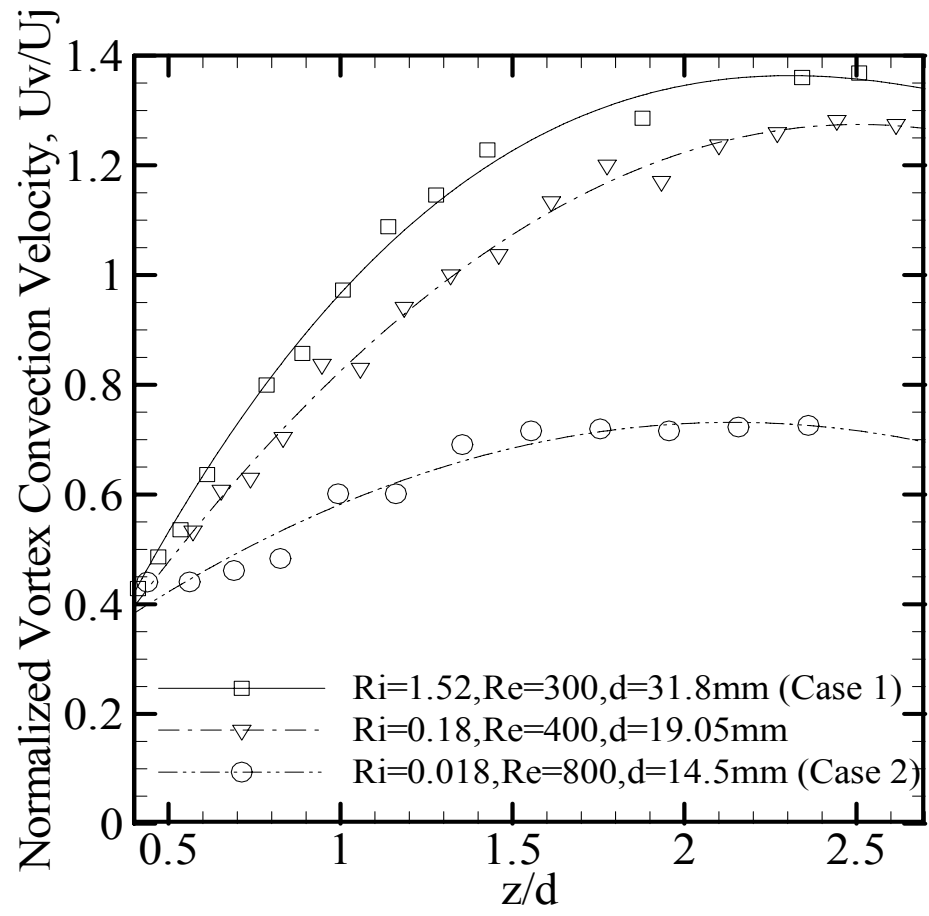


Figure 4.11. Vortex convection velocity normalized by the average jet exit velocity (U_v/U_j).

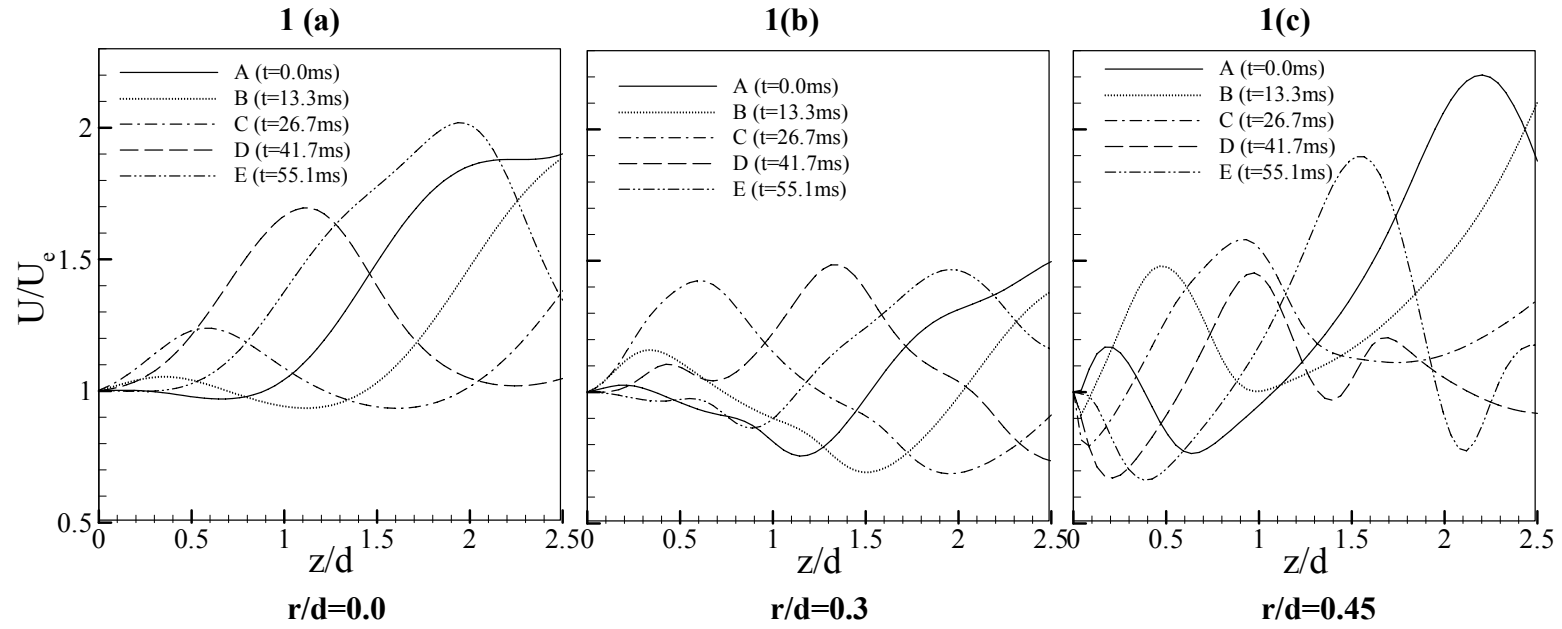


Figure 4.12. Axial velocity normalized by the jet exit velocity at the same radial location ($U/U_e(r)$) for Buoyant jet, $Ri=1.52$, $Re=300$, $d=31.8\text{mm}$ (Case 1).

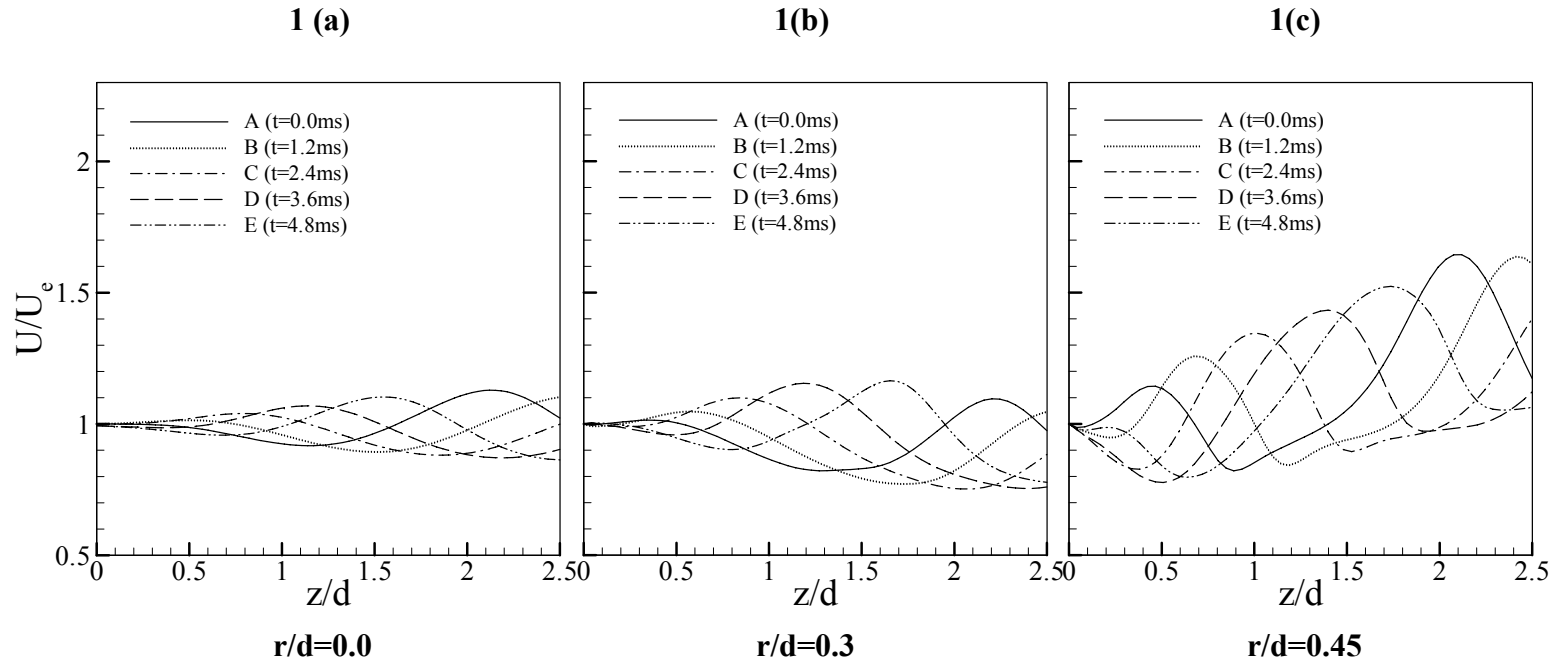


Figure 4.13. Axial velocity normalized by the jet exit velocity at the same radial location ($U/U_e(r)$) for Inertial jet, $Ri=0.018$, $Re=800$, $d=14.5\text{mm}$ (Case 2).

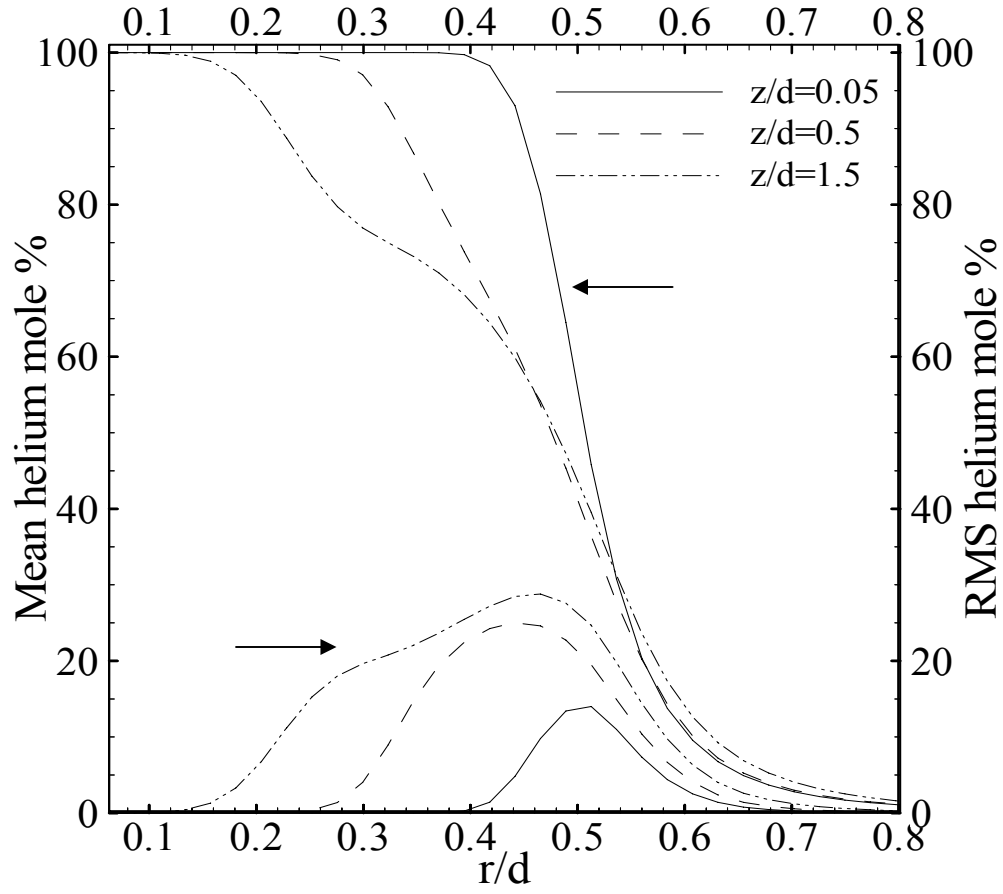


Figure 4.14. Profiles of mean and RMS helium mole percentage for Buoyant jet, $Ri=1.52$, $Re=300$, $d=31.8\text{mm}$ (Case 1).

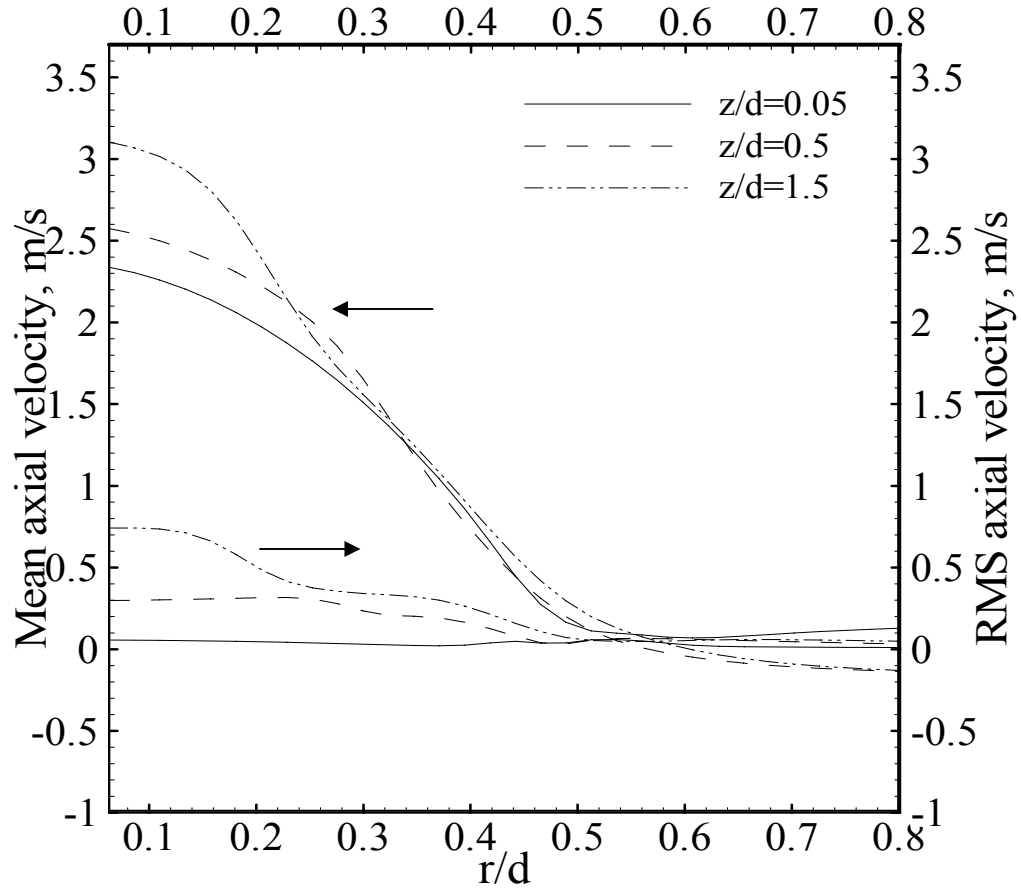


Figure 4.15. Profiles of mean and RMS axial velocity for Buoyant jet, $Ri=1.52$, $Re=300$, $d=31.8\text{mm}$ (Case 1).

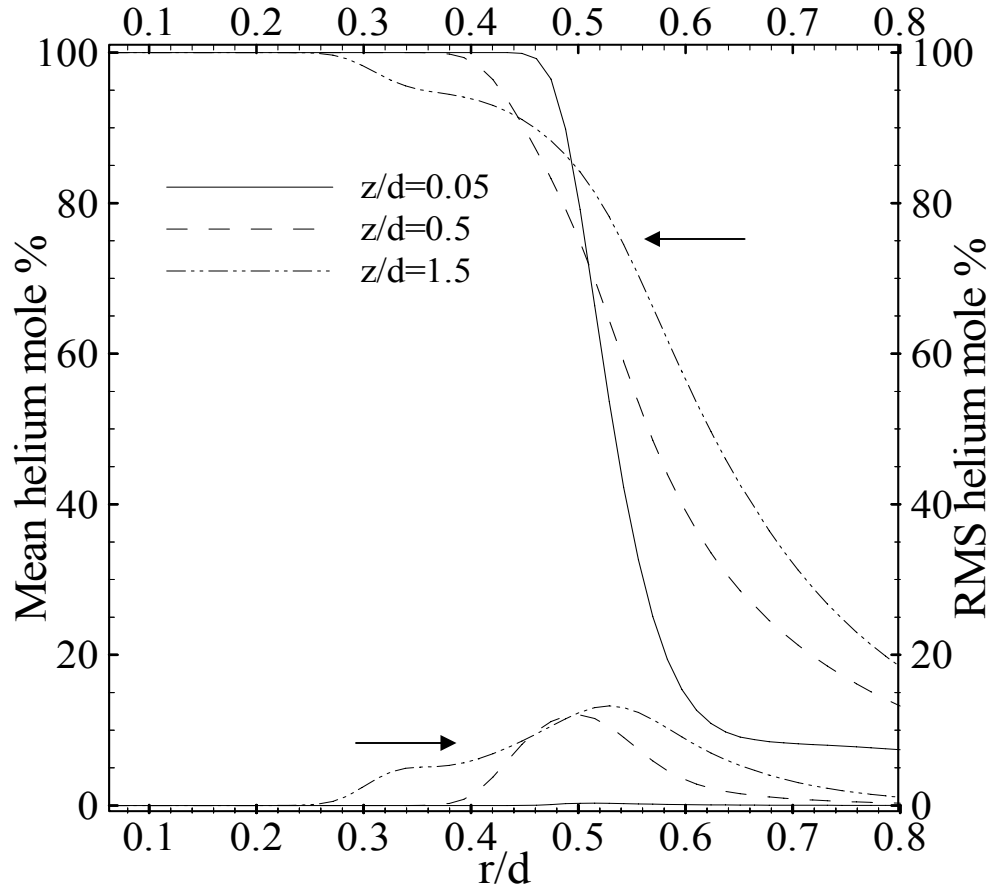


Figure 4.16. Profiles of mean and RMS helium mole percentage for Inertial jet, $Ri=0.018$, $Re=800$, $d=14.5\text{mm}$ (Case 2).

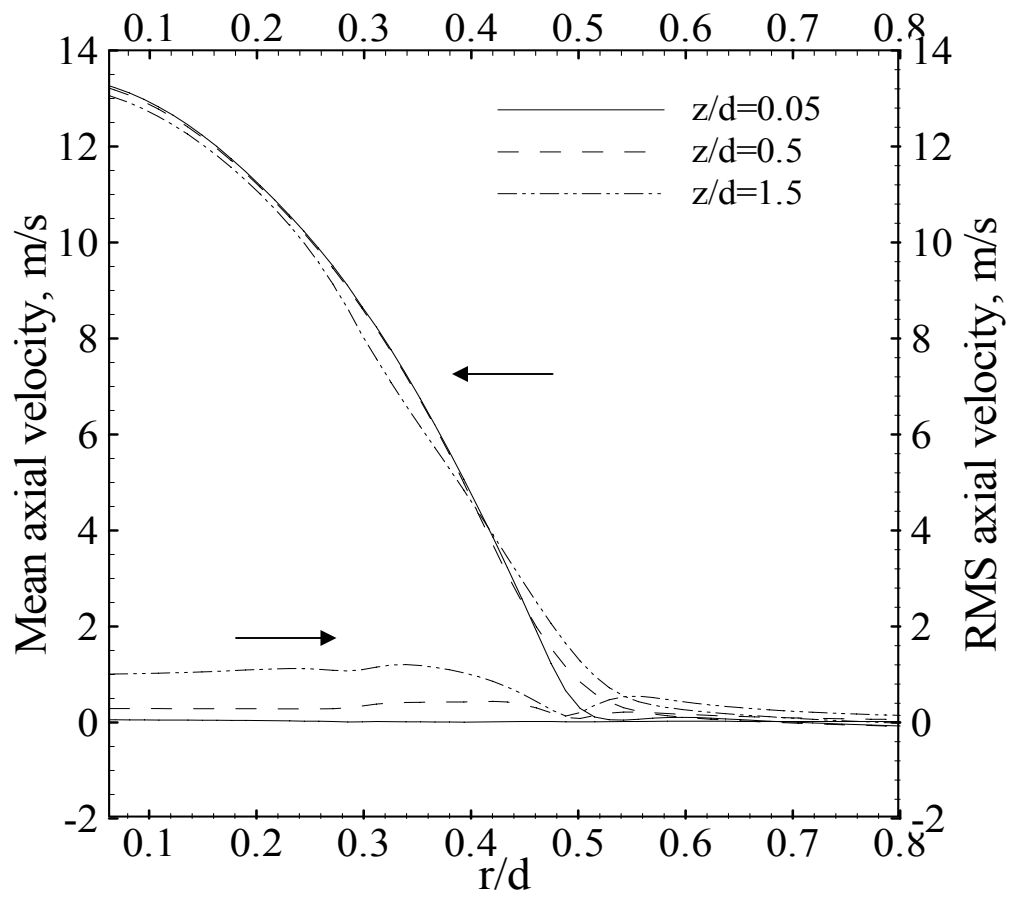


Figure 4.17. Profiles of mean and RMS axial velocity for Inertial jet, $Ri=0.018$, $Re=800$, $d=14.5\text{mm}$ (Case 2).

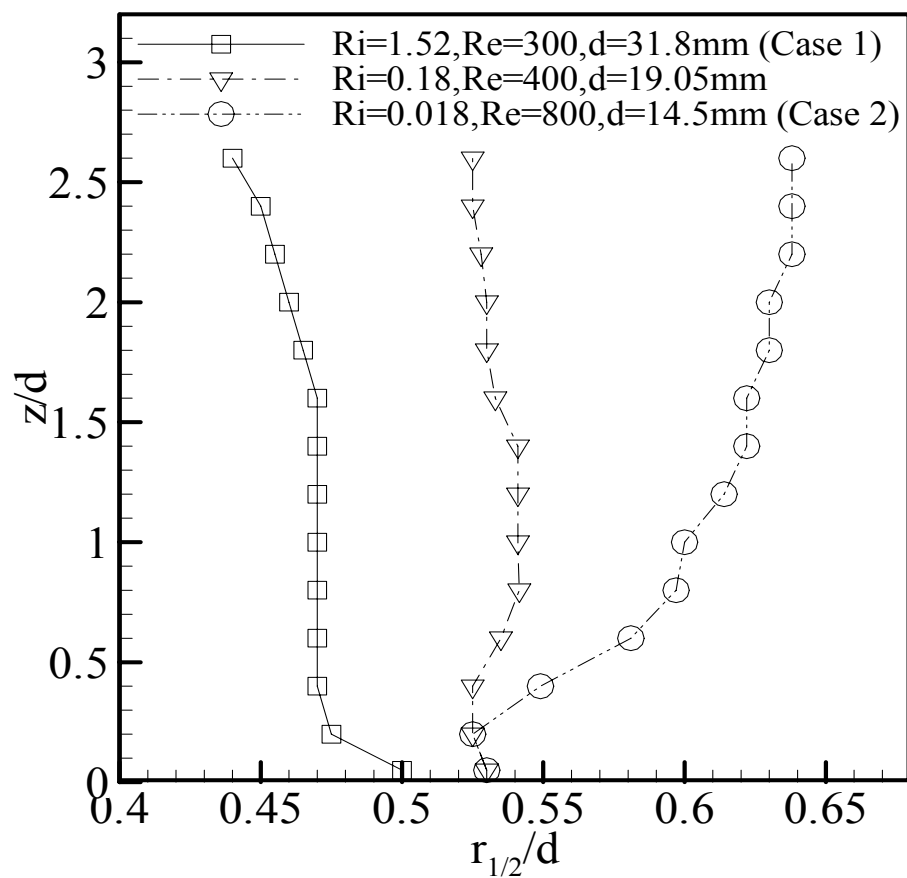


Figure 4.18. Jet half radius determined from helium concentration.

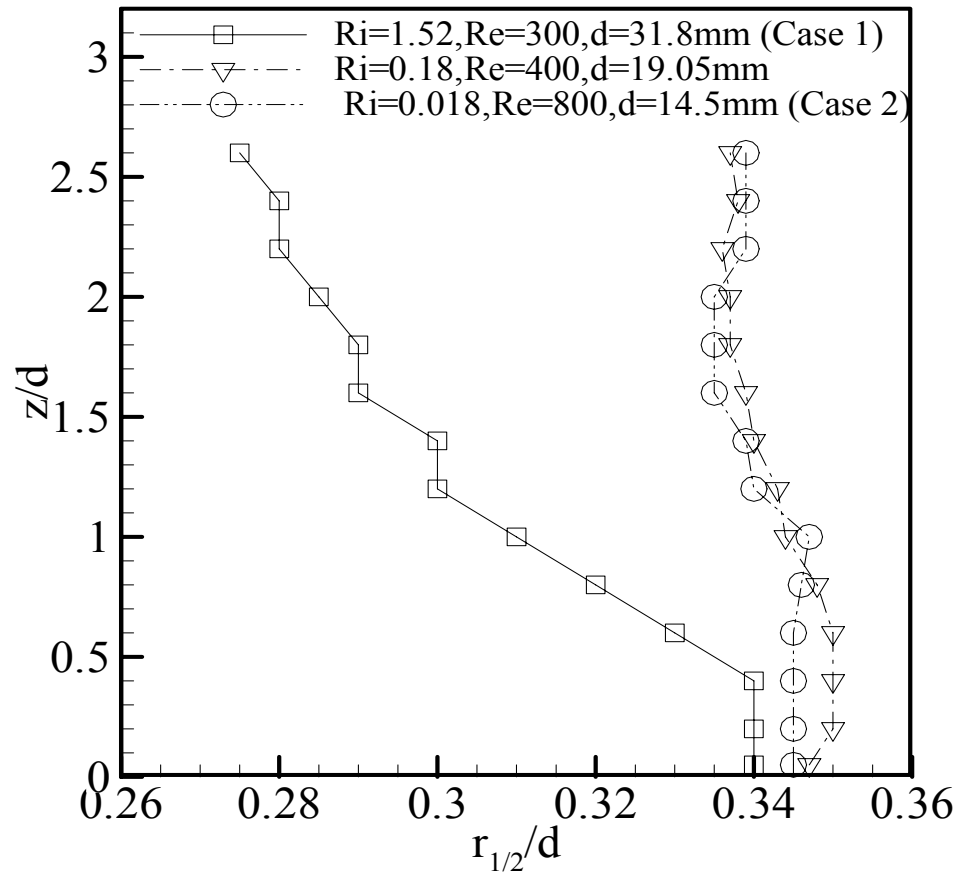


Figure 4.19. Jet half radius determined from axial velocity.

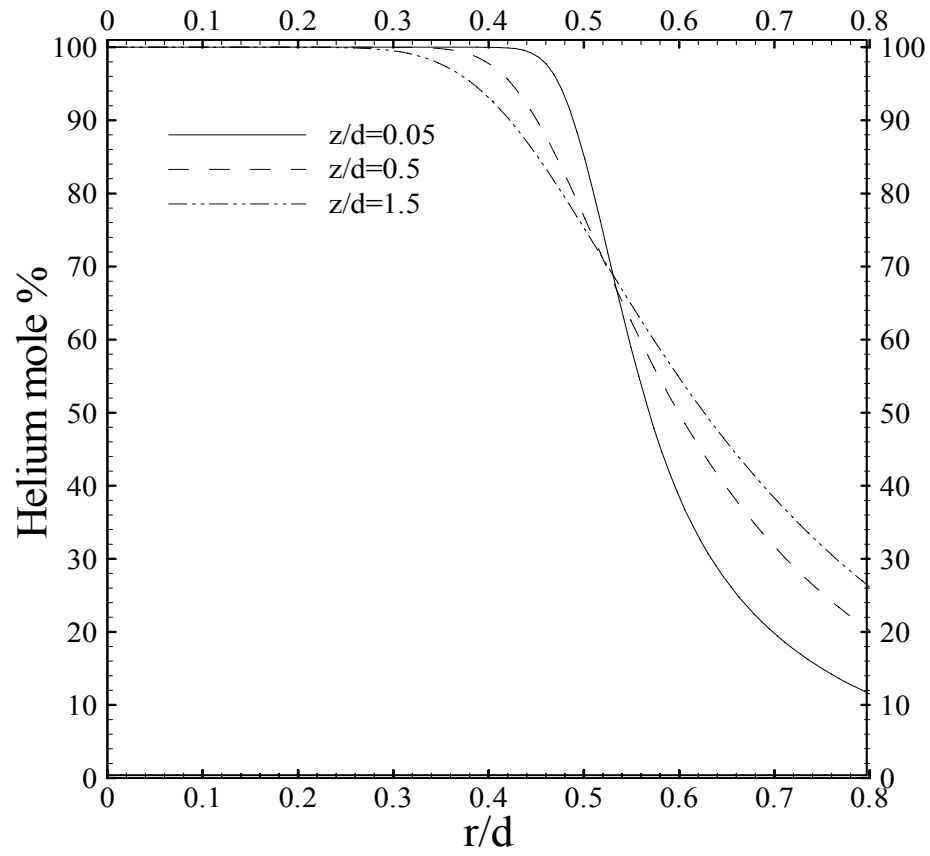


Figure 4.20. Profiles of helium mole percentage in microgravity for the Buoyant jet, $Ri=1.52$, $Re=300$, $d=31.8\text{mm}$ (Case 1).

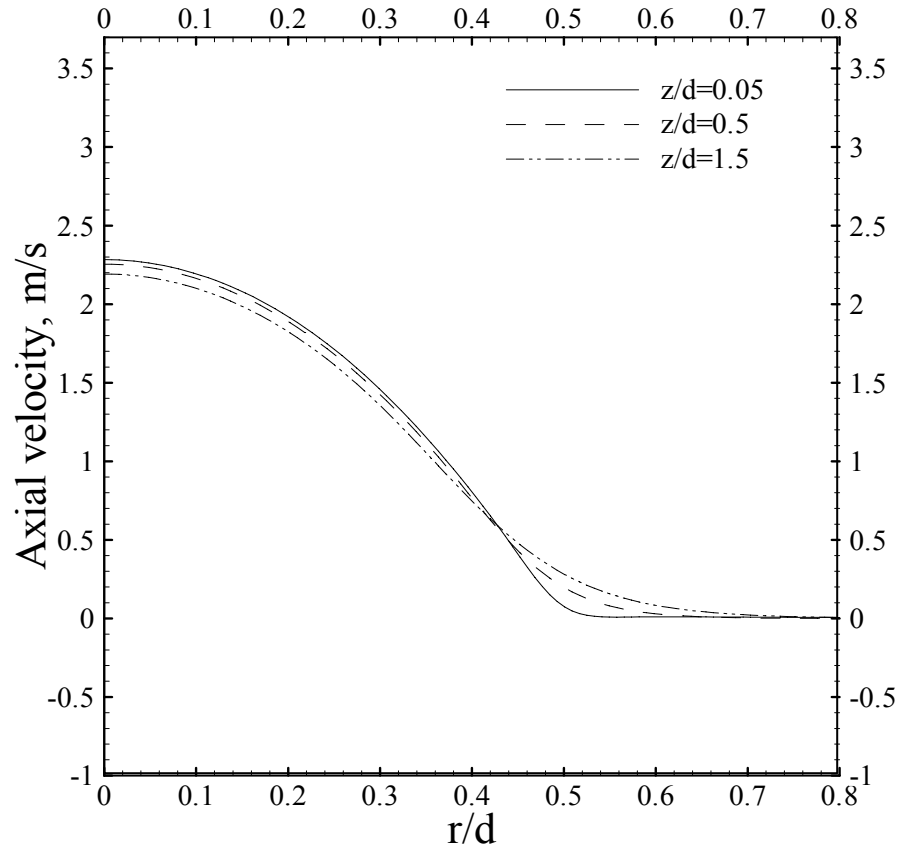


Figure 4.21. Profiles of axial velocity in microgravity for Buoyant jet, $Ri=1.52$, $Re=300$, $d=31.8\text{mm}$ (Case 1).

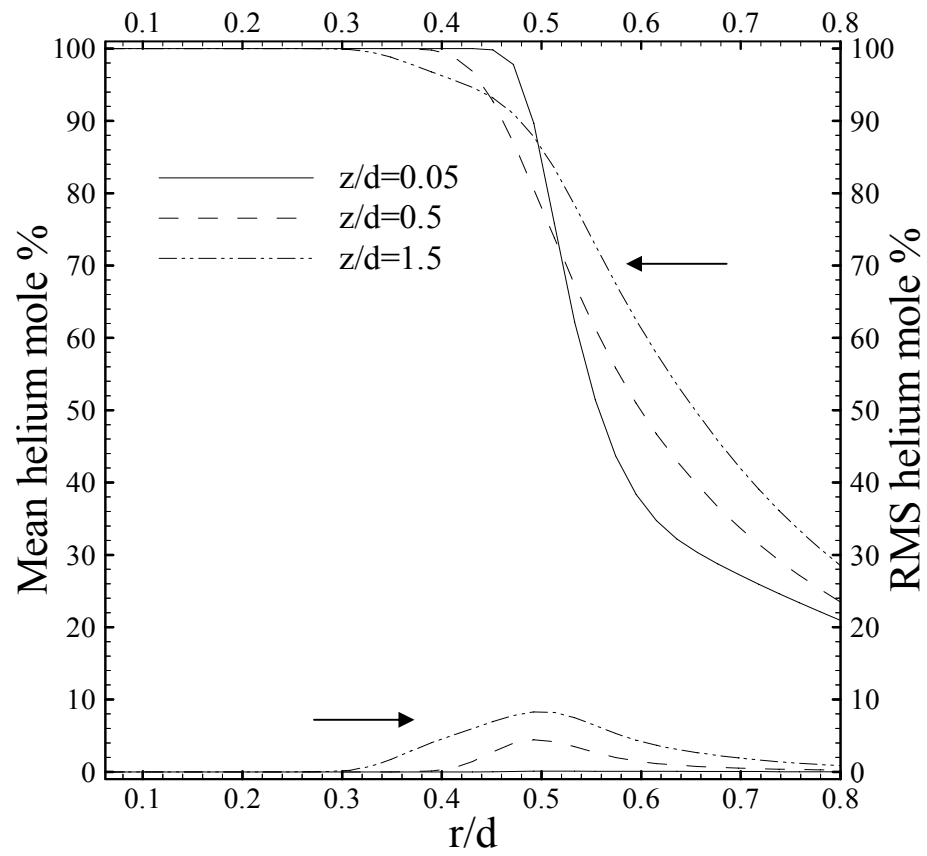


Figure 4.22. Profiles of helium mole percentage in microgravity for Inertial jet, $Ri=0.018$, $Re=800$, $d=14.5\text{mm}$ (Case 2).

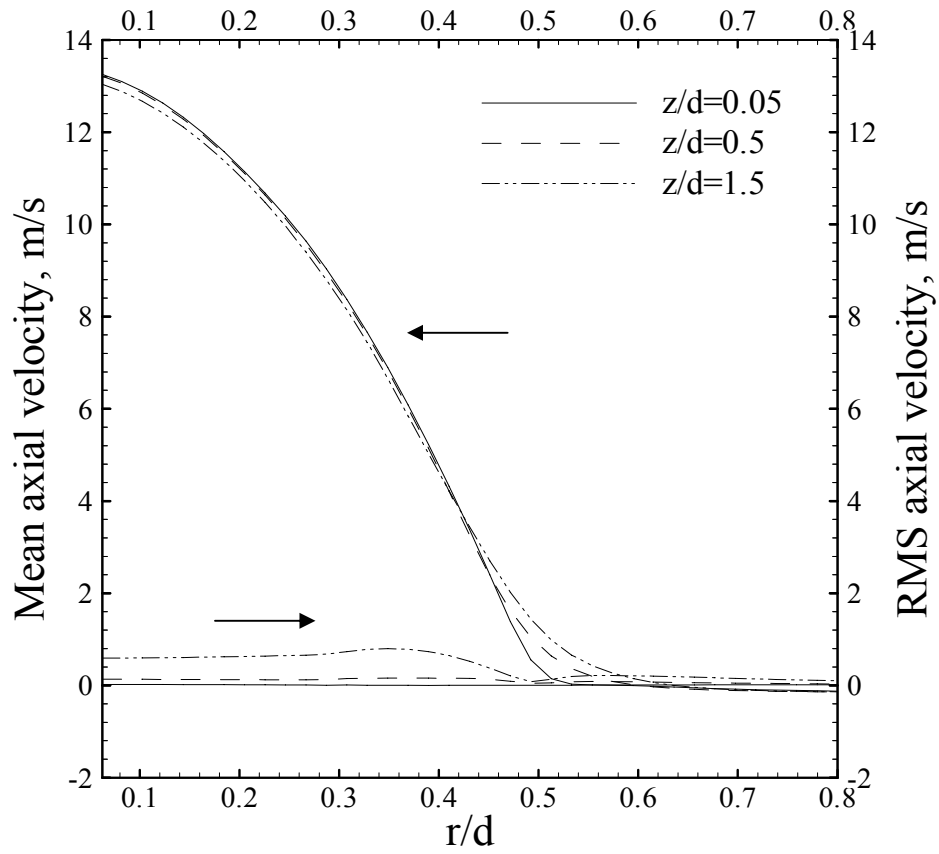


Figure 4.23. Profiles of axial velocity in microgravity for Inertial jet, $Ri=0.018$, $Re=800$, $d=14.5\text{mm}$ (Case 2).

CHAPTER 5. CROSSBEAM CORRELATION TECHNIQUE FOR SCALAR TURBULENCE MEASUREMENTS IN GAS JETS/FLAMES

5.1 Overview of the Chapter

In recent years, rainbow schlieren deflectometry (RSD) has been employed for scalar measurements in various laminar flow configurations. However, the possibility of utilizing the RSD technique to measure scalar turbulence has not been explored. The present chapter reviews literature involving an optical (crossbeam correlation) technique, which can be used in conjunction with RSD apparatus to obtain scalar turbulence measurements. For this purpose, a crossbeam rainbow schlieren deflectometry (CRSD) system was developed and experimental observations of turbulent jets/flames are presented in this chapter. Further, the analytical and validation procedures quantifying the application of crossbeam correlation technique with CRSD apparatus are also presented.

5.2 Literature Review

In the previous chapters, the stability characteristics and the effects of buoyancy on the near-field laminar flow structure of low-density gas jets were presented. It is well known that as a jet or flame convects downstream, the fluid dynamic instabilities and associated combustion processes eventually lead to transition and turbulent mixing. Fundamental understanding of these turbulent mixing processes in jets or flames requires detailed measurements of velocity and scalar fields. Such measurements are complicated in the presence of turbulent

fluctuations, introducing random variations in the flow. In particular, the analysis of fluctuating scalars like temperature, density, or concentration at points within the flow poses complex technical problems. Hence, the present study is focused on the development and validation of a crossbeam rainbow schlieren deflectometry (CRSD) apparatus to obtain statistical scalar turbulent properties in jets and flames.

Experimental measurements of the fluctuating properties of turbulent flows have mainly been obtained using intrusive probes, which are known to perturb the flow and thereby, affect the measurements. The development of an alternative approach is therefore of considerable importance in regard to the study of the turbulent properties of complex flows. Non-intrusive optical techniques are very promising since they do not require the insertion of a physical probe into the flow and are unaffected by the severity of the flow conditions. In addition, optical techniques can provide high spatial and temporal resolutions.

In recent years, rainbow schlieren deflectometry or RSD, a path integrated technique, has been employed for measurements in non-reacting and reacting flows (Pasumarthi and Agrawal, 2003; Albers and Agrawal, 1999). In particular, the RSD technique allows measurements across the whole field without relying upon seeding, soot or specific fuel species to mark the flow structure. Past applications of the RSD technique are limited only to steady or unsteady laminar flows. This limitation is imposed because of the tomographic inversion required

to de-convolute local properties from the path-integrated deflection angle data measured by the schlieren technique. Random fluctuations in turbulent flows require path integrated data at multiple view angles, which complicates the optical configuration and the tomographic inversion procedure.

Fisher and Krause (1967) proposed the crossbeam correlation technique to analyze turbulent properties in the shear layer of turbulent jets using path-integrated data. They showed that it is possible to extract localized information by statistically correlating the fluctuating signals from two mutually perpendicular laser beams which intersect inside the flow. Subsequently, Wilson and Damkevala (1970) and Winarto and Davis (1984) extended the crossbeam correlation technique with laser schlieren to study the density field of a turbulent axisymmetric jet by measuring the angular deflections of two light beams crossing the flow. Wilson and Damkevala (1970) restricted their investigation to measure local mean square density fluctuation in a compressible turbulent flow. Winarto and Davis (1984) used the cross correlation of angular deflections of two perpendicular beams and mean square deflections to obtain the local turbulent intensity and local integral length scale distributions in a supersonic jet. Kalghatgi et al. (1981) used the crossbeam correlation technique to measure the RMS value of the density gradient fluctuation and weighted RMS value of the density fluctuation across an exhaust plume.

Various investigators used similar laser schlieren approach to measure the

covariance of the angular deflection, which was then, related to the flow properties. Davis and co-workers (1975, 1989, 1991, 1993, 1994) extended their previous studies to obtain the convection velocities and power spectra in turbulent diffusion flames and to delineate the influence of turbulent eddies on thermal mixing. All of these studies involved single-point schlieren measurements using laser beams.

In the above studies, the measurements were obtained by using two orthogonal beams, one of which was traversed across the flow cross-section. The present study explores the development and application of crossbeam correlation technique for diagnostics of turbulent flows using the QRSD technique. The major advantage is the capability of the QRSD technique to obtain whole field measurements, thereby, eliminating the need for traversing the equipment or the test section. Potential advantages of the crossbeam correlation technique lie in the fact that it can provide measurements of localized turbulent quantities, and it requires no flow seeding. However, it is important to understand the capability and limitations of the technique before its application to scalar measurements in turbulent flows.

Thus, the objectives of this part of the study are as follows.

1. Configure a rainbow schlieren apparatus in the crossbeam mode and present schlieren observations of turbulent jets and flames.

2. Outline the theoretical framework of the crossbeam correlation technique.
3. Verify the crossbeam correlation technique using laminar data obtained from CFD simulations of near-field flow structure of low-density gas jets.
4. Verify the crossbeam correlation technique using synthetic turbulent data.

5.3 Experimental System

Previous studies of the rainbow schlieren system were limited to laminar flow measurements. Hence, the present system required several changes to make it suitable for measurements in turbulent jets and flames. In this study, an existing experimental system was modified and configured in the crossbeam mode to facilitate scalar turbulence measurements.

5.3.1 Quantitative Rainbow Schlieren Deflectometry

In the present study, the rainbow schlieren technique was used to visualize helium-air jets and hydrogen diffusion flames. The non-intrusive schlieren technique allows visualization of the scalar gradients in a transparent flow field by recording the angular deflection of the collimated light passing through the test media. The quantitative schlieren technique or rainbow schlieren deflectometry, developed by Greenberg et al. (1995), employs a computer generated continuously graded rainbow filter instead of the knife edge in a conventional

schlieren apparatus. The rainbow filter creates a color schlieren image, where each color represents a different angular deflection of the light ray. The color attribute is given by the red, green and blue percentages (RGB). However, the hue, saturation, and intensity (HSI) color model is used in the RSD technique to characterize the color by a single attribute, hue. In contrast, different combinations of red, green, and blue can represent a color in the RGB color model, which complicates the color quantification. Before the image data is quantified using the HSI color model, the rainbow filter must be calibrated to correlate the image hue to the displacement of the light ray at the filter plane in the schlieren image (Pasumarthi and Agrawal, 2003).

5.3.2 Experimental Details

A schematic of the crossbeam rainbow schlieren deflectometry (CRSD) apparatus is shown in Fig. 5.1. It consists of three major components: fuel flow system, rainbow schlieren apparatus (two systems in mutually perpendicular configuration) and image acquisition system. Figure 5.2 shows a photograph of the CRSD system, which is the first of its kind. The jet was visualized from two mutually perpendicular directions (mode-1 & mode-2) using two orthogonal RSD systems mounted on an optical table. The RSD systems consist of identical optical components with the same configurations on either side of the test medium.

The light input was provided by a continuous, 250 W halogen light source

(Fiber Optics Systems, Inc.) connected to two source apertures (10 μm wide, 3 mm high) through a 1000 μm diameter dual head goose neck fiber optic cable (fig. 5.3). For each RSD system, the source aperture is placed at the focal point of an achromatic lens of 82 mm diameter and 300 mm focal length (f_1). The collimated light rays pass through the test medium and the deflected rays are decollimated by a 76.2 mm diameter lens of 750 mm focal length (f_2). The image of the source aperture displaced by the test medium is formed at the focal point of the decollimating lens, wherein a rainbow filter is placed.

The filtered images are acquired by the high-speed CCD camera (Redlake model Motion Xtra HG-TX) at a rate of up to 2000 frames per second (fps) and stored as 24 bit color TIFF files at pixel resolution of 512 \times 384. The image acquisition system includes the high speed camera and a personal computer. Images at specified framing rate are stored in camera memory and subsequently downloaded on the personal computer hard drive through an Ethernet link. The fuel flow system includes compressed hydrogen or helium gas cylinders, a pressure regulator, a calibrated mass flow meter, flexible plastic hoses, a needle valve to control the fuel flow rate and jet tube.

5.3.3 Optical Considerations

The CRSD apparatus was adapted from an existing schlieren system developed by Wong and Agrawal (2006). Wong and Agrawal (2006) developed a single mode schlieren system to study flicker behavior of laminar gas jet diffusion

flames. They used a 150W halogen lamp, 200 μm wide source aperture and acquired images at a framing rate of 1000/sec. The spatial and temporal resolutions of the system ranged from 160 μm to 963 μs .

In the development of the CRSD system, it is very important to improve the spatial and temporal resolution of the system, a prerequisite for turbulence measurements. Note that the measurement resolution and sensitivity of the apparatus depends primarily on the size of the source aperture, the ray displacement at the filter plane, and spatial resolution of color gradients on the filter. Small width source aperture, large ray displacement and finer color gradations on the filter are desired for superior performance. With these objectives in mind, the following optical features were incorporated to modify the RSD apparatus.

1. In the previous RSD system (Wong and Agrawal, 2006), a 150W halogen lamp was used as the light source which limited the minimum exposure time to 963 μs . In this study, a more powerful light source of 250W (Fiber Optics Systems, Inc.) was used to acquire schlieren images at low exposure times. By achieving a balance between the focal length of the camera lens and the available light, exposure times down to 23 μs were achieved. Figure 5.4 shows typical schlieren images of a hydrogen diffusion flame at exposure times of 98 μs and 23 μs . In the schlieren image at an exposure time of 98 μs , one can observe only the buoyancy

driven instability characterized by the periodic oscillations in the flow field. However, as the exposure time is decreased to 23 μ s, the flame visualization interestingly depicts another instability i.e wrinkles on the flame surface along with the buoyancy driven instability. The space-time image shown in fig. 5.4 further quantifies the advantage of going to exposure times as low as 23 μ s. Together, the instability related to the wrinkles is also clearly depicted by the space-time image.

2. A source aperture of smaller width improves color resolution at the filter plane. Previously, RSD apparatus (Wong and Agrawal, 2006) has used slit width of about 200 μ m. However, with increase in the light throughput, slit aperture of 10 μ m was used in this study to improve the accuracy for measuring turbulent flows.
3. A key parameter affecting the measurement accuracy is the transverse ray displacement at the filter plane given as:

$$d(y) = f_2 \varepsilon(t) \quad (5.1)$$

where $\varepsilon(t)$ is the angular ray deflection at the projected location 't' and f_2 is the focal length of the decollimating lens. A large value of f_2 increases the transverse ray displacement and hence, improves the measurement sensitivity. Hence, a decollimating lens with an effective focal length of 750mm was used instead of the 490mm focal length lens used in the previous systems (Wong and Agrawal, 2006).

4. In the QRSD technique, the knife-edge filter in a schlieren system is replaced by a computer generated color filter to relate the angular ray deflection to color (or hue) in the rainbow schlieren image. The rainbow filter is a computer-generated, symmetric filter printed on a 35-mm color slide with a resolution of 115pixels/mm. Depending upon the flow phenomenon to be observed, one could control the filter characteristics by varying the distribution of hue/colors. Figure 5.5 shows examples of different filter configurations together with schlieren images of a hydrogen flame obtained with those filters. Note that in fig. 5.5 (a), one can observe the scalar flow structure of the outer flame surface only. However, with different filter configurations (fig. 5.5b-c), the scalar flow structure of the fuel jet core can also be visualized.
5. Spatial resolution of the schlieren system is a key parameter. A combination of extension tubes and camera lenses were used to improve the spatial resolution. Further details of this procedure are provided in section 6.3.2.4 of Chapter 6.
6. In previous studies (Wong and Agrawal, 2006), the RSD apparatus was used to sense the transverse ray displacements. In contrast, the crossbeam correlation analysis for scalar turbulence measurements is based on axial ray displacements. For this purpose, the slit/aperture and the rainbow filter

were oriented in such a way that the ray deflections measured were indeed the axial deflections.

A crossbeam schlieren system was developed and configured with the above modifications. In the following section, experimental observations of turbulent helium-air jets and hydrogen jet diffusion flames are presented.

5.4 Experimental Observations

The capability of the CRSD system in visualizing and capturing the scalar flow structure is demonstrated by experimental observations of turbulent helium-air jets and hydrogen jet diffusion flames. Subsequently, the schlieren images could be used in combination with relevant analysis procedures to extract information of turbulence quantities. A series of experiments were conducted with helium-air jets (non-reacting) and hydrogen jet diffusion flames (reacting) to visualize the turbulent flow structure across the whole field.

5.4.1 Turbulent Helium-Air Jet

Experiments were first conducted for the non-reacting case of a helium-air jet. Schlieren images were captured in both the modes (see fig. 5.2) of the CRSD system. Figures 5.6 and 5.7 show typical instantaneous schlieren images of the turbulent helium-air jet obtained in the crossbeam modes i.e mode 1 (fig.5.6) and mode-2 (fig 5.7). The operating conditions pertain to $d=10.0$ mm and $Re=4000$. A total of 7200 schlieren images were acquired using a 50mm focal length camera lens at a framing rate of 2000frames/ sec.

The instantaneous images in Figs. 5.6 and 5.7 depict the turbulent region of the jet. Turbulent density fluctuations in the jet lead to color gradations as shown in the images. The images depict the well known characteristics of turbulent jets, i.e. asymmetry, intermittency and randomness in the entire flow field. From the color gradations, one can observe that the turbulent flow structure is characterized by the irregular formation and propagation of turbulent eddies.

Next, a typical space-time image of the turbulent-helium air jet is shown in Fig. 5.8 for both the modes of the schlieren system. This image shows how the schlieren color image changes with time at a given axial plane of 5 diameters from the tube exit. Such space-time images generated at different axial planes can be used to generate the mean and RMS schlieren images, presented subsequently.

The randomness and irregularity of turbulent flows makes it difficult to measure the instantaneous properties. In such cases, the statistical study of turbulence indeed provides valuable information of the turbulent flow structure. Accordingly, the present schlieren data can also be described statistically by the mean and RMS schlieren images. A total of 7200 instantaneous images were used to generate the mean (Fig. 5.9) and RMS (Fig. 5.10) schlieren images of the turbulent helium-air jet. Note that the mean and RMS schlieren images are symmetric in both measuring modes of the crossbeam system. Further, the images in both directions are similar to each other. This indicates that from a statistical point of view, turbulence in the helium-air jet is axisymmetric. This observation

serves as the foundation for developing procedures for measuring the turbulence quantities.

5.4.2 Turbulent Hydrogen Jet Diffusion Flame

Experiments were conducted for a reacting flow i.e a hydrogen jet diffusion flame. Figs. 5.11 and 5.12 show instantaneous schlieren images of a hydrogen diffusion flame in the two modes of the CRSD system. The operating conditions pertain to a Reynolds number of 2400 and $d=1.19\text{mm}$. The instantaneous images in the two modes indicate a laminar region in the near burner region, followed by transition to turbulence. Fig. 5.13 shows a typical space-time image of the turbulent flame. Further, figs. 5.14 and 5.15 show the mean and RMS schlieren images of the hydrogen diffusion flame, which again exhibit excellent symmetry.

Similar experiments were conducted for a fully turbulent hydrogen jet diffusion flame at $Re=4200$. Fig. 5.16 and 5.17 show instantaneous schlieren images in the two modes of the CRSD system. The space-time image of the hydrogen-diffusion flame at $Re=4200$ (Fig. 5.18) depicts large fluctuations (of the color gradations) in comparison with the flame at $Re=2400$ (see fig. 5.13). Nevertheless, the mean and RMS schlieren images of the fully turbulent diffusion flame in Figs. 5.19 and 5.20 indicate excellent symmetry.

In the above experimental observations, it was observed that the schlieren images clearly capture the instantaneous turbulent structure of reacting and non-

reacting jet flows. It was also shown that from a statistical point of view, the schlieren data demonstrated the well known axisymmetry assumption of turbulent round jets. As a next step, analysis procedures were developed to extract the statistics of scalar turbulence observed in jets and flames. In the next section, the basic theory underlying the analysis procedures (crossbeam correlation) along with the necessary assumptions is presented. Subsequently, the validity of these analysis procedures is also determined using synthetic laminar/turbulent data.

5.5 Analysis Procedures

Sections 5.3 & 5.4 of this chapter explained the optical configuration and development of the CRSD apparatus, followed by experimental observations of turbulent jets and flames using color schlieren images. The color schlieren images require digital image processing techniques along with analysis procedures to provide scalar turbulence measurements. For this purpose, it is in the interest of the present study to apply the crossbeam correlation technique with schlieren images (obtained at orthogonal angles) and extract local turbulence information. In the following sections, a detailed explanation of the theory and analysis procedures involved in the application of crossbeam correlation (CBC) technique is presented.

5.5.1 Introduction

Consider the flow field of a turbulent jet or flame as shown in Fig. 5.21 with (x, y, z) representing the Cartesian coordinate system. Let us consider a

cross-sectional plane (y-z plane) of the turbulent region (see fig. 5.21) with the flow being convected in a direction perpendicular to the plane of the diagram (along x direction). Two collimated beams of light, A (parallel to z axis) and B (parallel to y axis) pass through the turbulent flow field respectively. Considering light beam A, from the basics of optics, we know that a light ray passing through a medium of variable refractive index is deflected according to:

$$\Theta_{xz}(y) = \int_{-\infty}^{+\infty} \frac{\partial \delta}{\partial x} dz \quad (5.2)$$

where Θ_{xz} is the instantaneous axial deflection angle of the light beam A. Note

that the first subscript x indicates the flow direction and the second subscript indicates the path of integration i.e. the z direction.

δ is the instantaneous refractive index.

$\frac{\partial \delta}{\partial x}$ represents the instantaneous refractive index gradient in the flow direction.

For a turbulent flow, the instantaneous refractive index (δ) can be expressed as the sum of the mean refractive index ($\bar{\delta}$) and the fluctuating refractive index (δ'). Equation 5.2 can therefore be expressed as:

$$\Theta_{xz}(y) = \int_{-\infty}^{+\infty} \frac{\partial (\bar{\delta} + \delta')}{\partial x} dz$$

$$= \int_{-\infty}^{+\infty} \frac{\partial \bar{\delta}}{\partial x} dz + \int_{-\infty}^{+\infty} \frac{\partial \delta'}{\partial x} dz \quad (5.3)$$

where the first and second terms on the RHS of eq. 5.3 represent the mean and the fluctuating axial deflection angles. In a similar fashion, the instantaneous deflection angle for the light beam B along the y direction (see fig. 5.21) is expressed as:

$$\Theta_{xy}(z) = \int_{-\infty}^{+\infty} \frac{\partial \bar{\delta}}{\partial x} dy + \int_{-\infty}^{+\infty} \frac{\partial \delta'}{\partial x} dy \quad (5.4)$$

5.5.2 Covariance and Variance Derivations

From eqs. (5.3) and (5.4), the expressions for covariance and mean square fluctuating beam deflection angles (variance) can be derived as shown in the following two steps.

Step 1: Covariance

Multiplying Θ_{xz} and Θ_{xy} from eqs. 5.3 & 5.4 and averaging over a long time interval, for statistically stationary turbulence,

$$\begin{aligned} \overline{\Theta_{xz}(y)\Theta_{xy}(z)} &= \overline{\int_{-\infty}^{+\infty} \frac{\partial \bar{\delta}}{\partial x} dz \int_{-\infty}^{+\infty} \frac{\partial \bar{\delta}}{\partial x} dy} + \overline{\int_{-\infty}^{+\infty} \frac{\partial \bar{\delta}}{\partial x} dz \int_{-\infty}^{+\infty} \frac{\partial \delta'}{\partial x} dy} + \overline{\int_{-\infty}^{+\infty} \frac{\partial \delta'}{\partial x} dz \int_{-\infty}^{+\infty} \frac{\partial \bar{\delta}}{\partial x} dy} \\ &\quad + \overline{\int_{-\infty}^{+\infty} \frac{\partial \delta'}{\partial x} dz \int_{-\infty}^{+\infty} \frac{\partial \delta'}{\partial x} dy} \\ &= \overline{\theta_{xz} \theta_{xy}} + \overline{\theta_{xz} \theta'_{xy}} + \overline{\theta'_{xz} \theta_{xy}} + \overline{\theta'_{xz} \theta'_{xy}} \end{aligned} \quad (5.5)$$

$$\text{Now, } \overline{\overline{\theta_{xz}' \theta_{xy}'}} = \overline{\theta_{xz}'} \overline{\theta_{xy}'} \text{ and } \overline{\overline{\theta_{xz}' \theta_{xy}'}} = \overline{\theta_{xy}'} \overline{\theta_{xz}'} \quad (5.6)$$

From the basics of turbulence, we know that the mean of fluctuations is zero.

Therefore $\overline{\theta_{xy}'} = \overline{\theta_{xz}'} = 0$ leads to the cancellation of second and third terms on the

RHS in eq. (5.5). Equation 5.5 thus simplifies to:

$$\overline{\overline{\Theta_{xz} \Theta_{xy}}} = \overline{\overline{\theta_{xz}' \theta_{xy}'}} + \overline{\overline{\theta_{xz}' \theta_{xy}'}} \quad (5.7)$$

where the first term on RHS represents the mean of the product of the mean axial deflection angles computed in y and z directions. The second term on RHS represents the mean of the product of the fluctuating axial deflection angles (covariance). Thus, the covariance between the two angular deflections can be written as:

$$\overline{\theta_{xz}'(y) \theta_{xy}'(z)} = \overline{\int_{-\infty}^{+\infty} \frac{\partial \delta'}{\partial x} dz \int_{-\infty}^{+\infty} \frac{\partial \delta'}{\partial x} dy} \quad (5.8)$$

Let us define a local coordinate system (ξ, ς, η) at the beam intersection point in the x-y-z coordinate system shown in Fig. 5.21. Note that the axial separation between the two beams is zero i.e $\xi=0$ throughout the analysis. Accordingly eq.

(5.8) can also be written as:

$$\begin{aligned} \overline{\theta_{xz}'(y) \theta_{xy}'(z)} &= \overline{\int_{-\infty}^{+\infty} \frac{\partial \delta'(0,0,\eta)}{\partial x} dz \int_{-\infty}^{+\infty} \frac{\partial \delta'(0,\varsigma,0)}{\partial x} dy} \\ &= \overline{\int_{-\infty}^{+\infty} \int_{-\infty}^{+\infty} \frac{\partial \delta'(0,0,\eta)}{\partial x} \frac{\partial \delta'(0,\varsigma,0)}{\partial x} dz dy} \end{aligned} \quad (5.9)$$

$$\begin{aligned}
&= \overline{\int \int_{-\infty-\infty}^{+\infty+\infty} \frac{\partial \delta'(0,0,0)}{\partial x} \frac{\partial \delta'(0,0,\eta)}{\partial x} \frac{\partial \delta'(0,\zeta,0)}{\partial x} dz dy} \\
&= \frac{\partial \delta'(0,0,0)}{\partial x} \int \int_{-\infty-\infty}^{+\infty+\infty} \frac{\partial \delta'(0,0,\eta)}{\partial x} \frac{\partial \delta'(0,\zeta,0)}{\partial x} dz dy \\
&= \frac{\partial \delta'(0,0,0)}{\partial x} \int \int_{-\infty-\infty}^{+\infty+\infty} R dz dy \tag{5.10}
\end{aligned}$$

where $\int \int_{-\infty-\infty}^{+\infty+\infty} R dz dy$ represents the double integral of the two point refractive index

gradient correlation function, R.

Step 2: Mean Square Angular Deflections (Variance)

Consider the conventional single beam measurements in the schlieren system as shown in fig. 5.22. Revisiting equation 5.3,

$$\begin{aligned}
\Theta_{xz}(y) &= \int_{-\infty}^{+\infty} \frac{\partial \bar{\delta}}{\partial x} dz + \int_{-\infty}^{+\infty} \frac{\partial \delta'}{\partial x} dz \\
&= \bar{\theta}_{xz}(y) + \theta'_{xz}(y) \text{ where } \bar{\theta}_{xz} \text{ is the mean axial deflection angle and } \theta'_{xz} \text{ is the}
\end{aligned}$$

fluctuating axial deflection angle. Now an expression for the variance of the axial deflection angle can be derived as follows:

$$\overline{\Theta_{xz}(y)\Theta_{xz}(y)} = (\overline{\bar{\theta}_{xz} + \theta'_{xz}})(\overline{\bar{\theta}_{xz} + \theta'_{xz}}) = \overline{\bar{\theta}_{xz}\bar{\theta}_{xz}} + \overline{\bar{\theta}_{xz}\theta'_{xz}} + \overline{\theta'_{xz}\bar{\theta}_{xz}} + \overline{\theta'_{xz}\theta'_{xz}} \tag{5.11}$$

As already explained above, $\overline{\theta'_{xz}}=0$ leading to the cancellation of the second and third terms on RHS of eq. 5.11. Therefore,

$$\overline{\Theta_{xz}(y)\Theta_{xz}(y)} = \overline{\theta_{xz}\theta_{xz}} + \overline{\theta'_{xz}\theta'_{xz}} \quad (5.12)$$

It can be observed from eq. 5.12 that the second term on RHS represents the variance (mean square fluctuation) of the axial deflection angle of beam A in the z direction. Now if the light beam A is traversed over a section of the flow such that the distance from the beam to the flow axis (Y) varies, then the distribution of the mean square fluctuating deflection angle i.e $\overline{\theta'_{xz}{}^2}(y)$ from eq. 5.12 can be written as:

$$\begin{aligned} \overline{\theta'_{xz}\theta'_{xz}}(y) &= \overline{\theta'_{xz}{}^2}(y) = \overline{\int_{-\infty}^{\infty} \frac{\partial \delta'}{\partial x} dz \int_{-\infty}^{\infty} \frac{\partial \delta'}{\partial x} dz} \\ &= \overline{\int_{-\infty}^{\infty} \int_{-\infty}^{\infty} \frac{\partial \delta'(0,0,0)}{\partial x} \frac{\partial \delta'(0,0,\eta)}{\partial x} dz dz} \\ &= \int_{-\infty}^{+\infty} \int_{-\infty}^{+\infty} \frac{\partial \delta'(0,0,0)}{\partial x} \frac{\overline{\frac{\partial \delta'(0,0,0)}{\partial x} \frac{\partial \delta'(0,0,\eta)}{\partial x}}}{\frac{\overline{\partial \delta'(0,0,0)}^2}{\partial x}} dz dz \\ &= \int_{-\infty}^{+\infty} \frac{\partial \delta'(0,0,0)}{\partial x} \int_{-\infty}^{+\infty} \frac{\overline{\frac{\partial \delta'(0,0,0)}{\partial x} \frac{\partial \delta'(0,0,\eta)}{\partial x}}}{\frac{\overline{\partial \delta'(0,0,0)}^2}{\partial x}} dz dz \end{aligned} \quad (5.13)$$

At this point, we define the integral length scale in the z direction as:

$$l_z = \frac{1}{2} \int_{-\infty}^{+\infty} \frac{\overline{\frac{\partial \delta'(0,0,0)}{\partial x} \frac{\partial \delta'(0,0,\eta)}{\partial x}}}{\overline{\frac{\partial \delta'(0,0,0)}{\partial x}}^2} dz \quad (5.14)$$

Substituting for l_z in eq. (5.13),

$$\overline{\theta'_{xz}}^2(Y) = 2 \int_{-\infty}^{+\infty} \frac{\overline{\frac{\partial \delta'(0,0,0)}{\partial x}}^2}{\overline{\frac{\partial \delta'(0,0,0)}{\partial x}}^2} l_z dz = 4 \int_0^{\infty} \frac{\overline{\frac{\partial \delta'(0,0,0)}{\partial x}}^2}{\overline{\frac{\partial \delta'(0,0,0)}{\partial x}}^2} l_z dz \quad (5.15)$$

$$= 4 \int_0^{\infty} f_z(y) dz \quad \text{where } f_z(y) = \frac{\overline{\frac{\partial \delta'^2}{\partial x}}}{\overline{\frac{\partial \delta'(0,0,0)}{\partial x}}^2} l_z \quad (5.16)$$

Note that $f_z(y)$ is the z-direction mixing function. In a similar way, the mean square angular deflection in the perpendicular direction y is given by:

$$\overline{\theta'_{xy}}^2(z) = 4 \int_0^{\infty} f_y(z) dy \quad \text{where } f_y(z) = \frac{\overline{\frac{\partial \delta'^2}{\partial x}}}{\overline{\frac{\partial \delta'(0,0,0)}{\partial x}}^2} l_y \quad (5.17)$$

$$\text{where } l_y = \frac{1}{2} \int_{-\infty}^{+\infty} \frac{\overline{\frac{\partial \delta'(0,0,0)}{\partial x} \frac{\partial \delta'(0,\zeta,0)}{\partial x}}}{\overline{\frac{\partial \delta'(0,0,0)}{\partial x}}^2} dy \quad (5.18)$$

Note that $f_y(z)$ is the z-direction mixing function. To summarize, the expressions for the variance and covariance relations were derived in this section given by:

$$\overline{\theta'_{xz}(y) \theta'_{xy}(z)} = \frac{\overline{\frac{\partial \delta'(0,0,0)}{\partial x}}^2}{\overline{\frac{\partial \delta'(0,0,0)}{\partial x}}^2} \int_{-\infty}^{+\infty} \int_{-\infty}^{+\infty} R dz dy \quad (5.10)$$

$$\overline{\theta_{xz}'^2}(y) = 4 \int_0^\infty f_z(y) dz \quad \text{where } f_z(y) = \frac{\overline{\partial \delta'^2}}{\partial x} l_z \quad (5.16)$$

$$\overline{\theta_{xy}'^2}(z) = 4 \int_0^\infty f_y(z) dy \quad \text{where } f_y(z) = \frac{\overline{\partial \delta'^2}}{\partial x} l_y \quad (5.17)$$

5.5.3 Crossbeam Correlation Analysis

Before proceeding further to employ the above expressions and compute scalar turbulence quantities, it is essential to make the following assumptions:

- 1) The time-averaged flow is axisymmetric.
- 2) Turbulence is locally isotropic. Hence the integral length scales are independent of direction i.e $l_y = l_z = l_r$. Here subscript 'r' is the radius.
- 3) It is assumed that $\int_{-\infty}^{+\infty} \int_{-\infty}^{+\infty} R dz dy = l_y l_z$ for a locally homogeneous flow.

This assumption has been discussed in detail by Fisher and Krause (1967). In a *locally homogeneous* flow, if the intensity does not vary appreciably over the correlated area (i.e the region for which the correlation coefficient is finite), then the double integral of the two point correlation function is approximately equal to the product of the integral length scales. Hence, to a useful degree of

$$\text{approximation } \int_{-\infty}^{+\infty} \int_{-\infty}^{+\infty} R dz dy = l_y l_z.$$

The results from eq.5.16 & 5.17 show that the measured mean square value of the deflection angle in either direction i.e $\overline{\theta'_{xz}{}^2}(y)$ or $\overline{\theta'_{xy}{}^2}(z)$ takes the form of an integral of the product of local intensity of the refractive index gradient fluctuation and local integral length scale along the beam path (l_y or l_z). In order to proceed further, one can solve for either $f_z(y)$ or $f_y(z)$ from known distributions of $\overline{\theta'_{xz}{}^2}(y)$ and $\overline{\theta'_{xy}{}^2}(z)$ (obtained by measurements). If the time-averaged flow is axisymmetric (assumption-1), $\left(\overline{\frac{\partial \delta'}{\partial x}}\right)^2$ and the integral length scales will also be axisymmetric. Further, under the assumption of local isotropy $l_y = l_z = l_r$ (assumption-2). One can now define a function $f(r)$, which is dependent only on the radial coordinate. Thus, eqs.5.16 & 5.17 can be transformed to radial coordinates and written as:

$$\overline{\theta'_{xz}{}^2}(y) = 4 \int_z^\infty \left(\overline{\frac{\partial \delta'}{\partial x}}\right)^2 l_r \frac{r dr}{\sqrt{r^2 - y^2}} = 4 \int_z^\infty f(r) \frac{r dr}{\sqrt{r^2 - y^2}} \quad (5.19)$$

Similarly,

$$\overline{\theta'_{xy}{}^2}(z) = 4 \int_y^\infty \left(\overline{\frac{\partial \delta'}{\partial x}}\right)^2 l_r \frac{r dr}{\sqrt{r^2 - z^2}} = 4 \int_y^\infty f(r) \frac{r dr}{\sqrt{r^2 - z^2}} \quad (5.20)$$

where $f(r) = \left(\overline{\frac{\partial \delta'}{\partial x}}\right)^2 l_r$ is the axisymmetric mixing function

From known measurements of $\overline{\theta'_{xz}{}^2}(y)$ or $\overline{\theta'_{xy}{}^2}(z)$, the local distribution of the mixing function, $f(r)$ can be computed by using the two point Abel deconvolution formula (see Appendix B). Note that in writing eqs. 5.19 and 5.20, it is assumed that the integral length scale is the same in all directions in the y-z plane. A rather similar equation for the interpretation of integrated measurements taken through axisymmetric flows has been discussed by Gyarmathy (1969).

Next, considering eq. 5.10, the double integral of the two point correlation coefficient $\int_{-\infty}^{+\infty} \int_{-\infty}^{+\infty} R dz dy$ can be expressed in form of integral length scales as

$\int_{-\infty}^{+\infty} \int_{-\infty}^{+\infty} R dz dy = l_y l_z$ (assumption-3). This relation given by Davis (1969) is an

approximation based on local homogeneity and can be expressed as follows:

$$\begin{aligned} \overline{\theta'_{xz}(y)\theta'_{xz}(z)} &= \frac{\overline{\partial \delta'(0,0,0)^2}}{\partial x} \int_{-\infty}^{+\infty} \int_{-\infty}^{+\infty} R dz dy \\ &= \frac{\overline{\partial \delta'(0,0,0)^2}}{\partial x} \int_{-\infty}^{+\infty} \int_{-\infty}^{+\infty} \frac{\overline{\partial \delta'(0,0,\eta) \partial \delta'(0,\zeta,0)}}{\frac{\partial \delta'(0,0,0)^2}{\partial x}} dz dy \end{aligned}$$

Now, we know that

$$l_z = \frac{1}{2} \int_{-\infty}^{+\infty} \frac{\overline{\partial \delta'(0,0,0) \partial \delta'(0,0,\eta)}}{\frac{\partial \delta'(0,0,0)^2}{\partial x}} dz \quad \text{and} \quad l_y = \frac{1}{2} \int_{-\infty}^{+\infty} \frac{\overline{\partial \delta'(0,0,0) \partial \delta'(0,\zeta,0)}}{\frac{\partial \delta'(0,0,0)^2}{\partial x}} dy$$

Assuming $\int_{-\infty}^{+\infty} \int_{-\infty}^{+\infty} R dz dy = l_y l_z$ (for a locally homogeneous flow)

$$\begin{aligned}
\overline{\theta'_{xz}(y)\theta'_{xz}(z)} &= 4 \overline{\frac{\partial \delta'(0,0,0)}{\partial x}}^2 \int_{-\infty}^{+\infty} \int_{-\infty}^{+\infty} \frac{\overline{\frac{\partial \delta'(0,0,\eta)}{\partial x} \frac{\partial \delta'(0,0,0)}{\partial x}}}{\overline{\frac{\partial \delta'(0,0,0)}{\partial x}}^2} \frac{\overline{\frac{\partial \delta'(0,\zeta,o)}{\partial x} \frac{\partial \delta'(0,0,0)}{\partial x}}}{\overline{\frac{\partial \delta'(0,0,0)}{\partial x}}^2} dz dy \\
&= 4 \overline{\frac{\partial \delta'(0,0,0)}{\partial x}}^2 \int_{-\infty}^{+\infty} \frac{\overline{\frac{\partial \delta'(0,0,\eta)}{\partial x} \frac{\partial \delta'(0,0,0)}{\partial x}}}{\overline{\frac{\partial \delta'(0,0,0)}{\partial x}}^2} dz \int_{-\infty}^{+\infty} \frac{\overline{\frac{\partial \delta'(0,\zeta,o)}{\partial x} \frac{\partial \delta'(0,0,0)}{\partial x}}}{\overline{\frac{\partial \delta'(0,0,0)}{\partial x}}^2} dy \\
&= 4 \overline{\frac{\partial \delta'(0,0,0)}{\partial x}}^2 l_z l_y
\end{aligned} \tag{5.21}$$

Under the assumption of local isotropy with respect to integral length

scales, $l_z = l_y = l_r$. Therefore,

$$\overline{\theta'_{xz}(y)\theta'_{xz}(z)} = 4 \overline{\frac{\partial \delta'^2}{\partial x}} l_r^2 \tag{5.22}$$

To summarize,

$$f(r) = \overline{\left(\frac{\partial \delta'}{\partial x} \right)^2} l_r \tag{5.23}$$

$$\overline{\theta'_{xz}(y)\theta'_{xz}(z)} = 4 \overline{\frac{\partial \delta'^2}{\partial x}} l_r^2 \tag{5.24}$$

By solving the above equations, we can calculate the fluctuation intensity and the integral length scales of the turbulent flow field assuming that the intensity and integral length scales are purely functions of radius, r only.

$$l_r = \frac{\overline{\theta'_{xz} \theta'_{xy}}}{4f(r)} \quad (5.25)$$

$$\frac{\overline{\partial \delta'^2}}{\partial x} = \frac{\overline{\theta'_{xz} \theta'_{xy}}}{4l_r^2} \quad (5.26)$$

From the above discussion, it is clear that one can use either $\overline{\theta'^2_{xz}}(y)$ or $\overline{\theta'^2_{xy}}(z)$ to calculate the axisymmetric mixing function and then use the covariance relation to resolve the intensity and integral length scales. Another alternative approach would be to use $\overline{\theta'^2_{xz}}(y)$ and $\overline{\theta'^2_{xy}}(z)$ independently, calculate intensities and compare the results as illustrated by the three methods. Hence, the refractive index gradient fluctuations can be calculated by three different methods as explained next:

Method 1:

$$l_y = \frac{\overline{\theta'_{xz} \theta'_{xy}}}{4f_z} \quad \text{where} \quad f_z(y) = \frac{\overline{\partial \delta'^2}}{\partial x} l_z \quad (5.27)$$

$$\frac{\overline{\partial \delta'^2}}{\partial x} = \frac{\overline{\theta'_{xz} \theta'_{xy}}}{4l_y^2} \quad (5.28)$$

Method 2:

$$l_z = \frac{\overline{\theta'_{xz} \theta'_{xy}}}{4f_y} \quad \text{where} \quad f_y(z) = \frac{\overline{\partial \delta'^2}}{\partial x} l_z \quad (5.29)$$

$$\frac{\overline{\partial \delta'^2}}{\partial x} = \frac{\overline{\theta'_{xz} \theta'_{xy}}}{4l_z^2} \quad (5.30)$$

Method 3:

$$l_y = \frac{\overline{\theta'_{xz} \theta'_{xy}}}{4f_z} \quad \text{where} \quad f_z(y) = \frac{\overline{\partial \delta'^2}}{\partial x} l_z \quad (5.31)$$

$$l_z = \frac{\overline{\theta'_{xz} \theta'_{xy}}}{4f_y} \quad \text{where} \quad f_y(z) = \frac{\overline{\partial \delta'^2}}{\partial x} l_z \quad (5.32)$$

$$\frac{\overline{\partial \delta'^2}}{\partial x} = \frac{\overline{\theta'_{xz} \theta'_{xy}}}{4l_y l_z} \quad (5.33)$$

Although the crossbeam correlation technique discussed above is developed using correlation of two orthogonal beams, the rainbow schlieren deflectometry apparatus facilitates crossing of two orthogonal planes. Thus, large amounts of data are available to simultaneously form cross-correlation points throughout the field of interest as illustrated in Fig. 5.23. However, the present study does not investigate the correlation between the whole field data.

Based on the theoretical framework of the crossbeam correlation technique, it can be inferred that the accuracy/validity of the technique is dependent upon the underlying assumptions of local isotropy, homogeneity and axisymmetry. The technique in its schlieren mode can be applied with confidence only after verifying its applicability. In the following sections, synthetic laminar/turbulent data are utilized to understand the accuracy and limitations of the crossbeam correlation technique with respect to the inherent nature of data.

5.6 Algorithm Validation: Laminar Flow

From the preceding section, it is important to demonstrate the validity of the crossbeam correlation (CBC) technique before applying the technique with CRSD system to measure scalar turbulence quantities. Synthetic laminar and turbulent data are therefore generated and utilized to understand the workability of CBC technique. The concept of the procedure is as follows. Laminar or turbulent data are generated synthetically and the deflection angles in two mutually perpendicular directions are computed using path integration techniques. The deflection angle data are then used to compute the variance and covariance. From the statistical expressions, deconvolution procedures are carried out using the analysis procedures described in section 5.5. Finally, it is expected that the results obtained from the analysis procedures should match with the original synthetic data.

Implementing the above procedure, the CBC technique is first verified using time-dependent data from CFD simulations of a laminar helium-air jet. The data generation process, results and the limitations imposed by the technique because of the inherent nature of the laminar data are presented in the following sections.

5.6.1 Synthetic Data Generation

The unsteady laminar data were extracted from the numerical simulations of an oscillating buoyant helium jet at $Re=300$ (already presented in Chapter 4) and the procedure is given as follows:

1. First, radial profiles of helium mole percentage for one complete oscillation cycle were extracted from the numerical simulations at two consecutive axial planes ($z/d=3.0$ and 3.1 for $Re=300$, $d=31.8\text{mm}$).
2. The helium mole percentage data were used to calculate density and thus the refractive index.
3. Since the data obtained from the numerical simulations are axisymmetric, the radial profiles of the refractive index field were swept in the circumferential direction to represent the instantaneous refractive index field at a given cross sectional plane in the Cartesian coordinate system. Figure 5.24 shows an instantaneous refractive index profile and its respective contour plot in the cartesian coordinates (y - z plane).

4. Finally, the refractive index gradients were computed from the cross-sectional data of each plane at different times (1 oscillation cycle of 65 time steps) using the forward differencing techniques.
5. The refractive index gradient field was then used to calculate the deflection angles in the y and z directions using trapezoidal rule of integration (see Appendix C).

5.6.2 Results and Discussion

A computer code was developed to implement and validate the theoretical framework presented in the previous section. In the following sections, results representing axisymmetric mixing function, integral length scale, refractive index gradient fluctuation intensity are presented and analyzed. The statistical quantities are evaluated for two test cases replicating typical flow features in the near field (case 1) and far field (case 2) of low-density gas jets.

5.6.2.1 Case-1 (Near-field)

As a first step, the instantaneous deflection angles were computed using the refractive index gradient data in both the directions y and z given in eqs.5.3 and 5.4. Figure 5.25 shows the profiles of the variance of angular deflections ($\overline{\theta_{xz}'^2}(y)$) and $\overline{\theta_{xy}'^2}(z)$. Owing to symmetry, only one side of the profiles are presented. The measured mean square value (variance) of deflections is nearly constant close at the center and reaches a peak value at around 0.012m. Since the

data considered are instantaneously axisymmetric, the mean square value ($\overline{\theta'_{xy}{}^2(z)}$) was found to be exactly the same as that of $\overline{\theta'_{xz}{}^2(y)}$.

The radial profile of mean square deflection angle ($\overline{\theta'_{xz}{}^2(y)}$) was then used to compute the laminar mixing function using the Abel inversion process (Appendix B). Figure 5.26 compares the profiles of mixing function obtained from original local data and inverted data using the crossbeam correlation technique (see eq. 5.23). Note that the exact value of the mixing function is expressed as product of the density gradient fluctuation intensity and integral length scale (eq. 5.16). Figure 5.26 shows a good qualitative agreement between exact and inverted mixing function profiles. The peak of the laminar mixing function is observed at $r=0.013\text{m}$ for both the exact and CBC based profiles. However, the CBC based result at $r=0.013\text{m}$ is 20% more than the exact value at that point. The discrepancy in the results is attributed to the nature of the data considered. The actual distributions of $f(r)$ are not axisymmetric, as the integral length scales are not axisymmetric, thus contradicting the application of inversion process used to derive Eq. 5.23.

Figure 5.27 shows contour plot of the mixing function f_z obtained by direct calculations using the definition in Eq. 5.16. The contour plots reveal asymmetry over the region. The discrepancy between exact and inverted profiles is therefore attributed to the asymmetry in f_z . Figure 5.28 shows profile of

computed covariance of angular deflections obtained in y and z directions (eq. 5.8). Again, owing to symmetry, profiles are shown only for one side of the jet. The covariance is nearly constant near the jet center, peaks at around $r=0.01\text{m}$ and then decreases to attain zero value far away from the jet center as expected. By using the mixing function and the covariance relations given in eqs 5.23 and 5.24, the distribution of the integral length scale and the density gradient fluctuations were found from the equations 5.25 & 5.26. Figure 5.29 shows plots of the integral length scale obtained from synthetic data and crossbeam technique. Note that definition of the length scale is given in eq. 5.14. The actual value of the integral length scale is evaluated from the integral of the correlation coefficient and the crossbeam technique employs Eq. (5.25) to calculate the length scale.

It can be observed that the CBC based integral length scale matches very well with the actual length scale. In particular, excellent agreement is reached in regions of peak fluctuations. Figure 5.30 shows plot of refractive index gradient fluctuations (intensity) obtained from actual data and crossbeam technique. Qualitatively, results show a good agreement between actual refractive index gradient fluctuations and those obtained using CBC method. The discrepancy in the results is again attributed to the nature of the integral length scales.

5.6.2.2 Case-2 (Far-field)

Similar to case-1, the instantaneous deflection angles were computed in both y and z directions as explained in eqs.5.3 and 5.4. Figure 5.31 (case-1) shows the

profile of the variance of angular deflections $\overline{\theta'_{xy}{}^2(z)}$ and $\overline{\theta'_{xz}{}^2(y)}$ obtained from the synthetic data. Again, owing to symmetry, only one side of the profiles is presented. Unlike case-1, the measured mean square value of deflections increases steadily from the center to reach a peak value at 0.007m compared to a peak value of 0.012m for case-1.

Figure 5.32 compares the profiles of the laminar mixing function obtained from actual data and inversion process. The peak of the laminar mixing function is observed at the center unlike case-1, where the peak is at $r=0.013$ m. However, the discrepancy in the results is again attributed to the asymmetric nature of the mixing function shown in Fig. 5.33. Next, the two beam covariance profile of angular deflections is shown in Fig. 5.34. The nature of the profile indicates peak cross-correlation at the center compared to $r=0.013$ for case-1. The profile of the covariance changes from a constant value in the center region to zero value radially far way from the jet. The integral length scales and the refractive index gradient intensity were subsequently computed using the covariance and variance information as already discussed for case-1. Again it can be observed from Fig. 5.35 that the CBC based integral length scale matches very well with the actual length scale for both the test cases. Figure 5.36 shows plots of refractive index gradient fluctuations obtained from actual data and crossbeam technique.

Qualitatively, results show a reasonable agreement between actual refractive index gradient fluctuations and crossbeam based fluctuations.

To summarize, the crossbeam correlation technique was applied for data generated from the numerical simulations of a laminar helium-air jet. Results indicate that the CBC technique is a promising approach to obtain statistical properties.

5.6.3 Limitations

In the preceding section, the validity of crossbeam correlation technique was tested using synthetic laminar data. On a qualitative basis, the integral length scale and intensities computed from the crossbeam showed expected trends in comparison with the actual synthetic data. As discussed in section 5.5, crossbeam correlation technique is based on the assumptions that turbulence is axisymmetric, locally isotropic and homogeneous field. Unfortunately, the conditions of local isotropy and homogeneity were irrelevant to an axisymmetric laminar flow field. Moreover, the distribution of the mixing function $f(r)$ should be axisymmetric in order to apply the Abel inversion process.

The contour plots depicted in fig. 5.27 and 5.33 clearly indicate the asymmetry in the mixing function, which violates the application of eq.5.19. It should also be pointed out that the asymmetry in the mixing function points out that the integral length scales are not axisymmetric. Owing to these limitations, the validity of the crossbeam correlation technique cannot be completely

ascertained from laminar data. An accurate validation procedure would require synthetic turbulent data which satisfies the conditions of local isotropy and homogeneity. Moreover, since the present study aims to apply the crossbeam correlation technique for scalar measurements of turbulent jets/flames, it is essential to use synthetic turbulent data for a comprehensive validation process.

5.7 Algorithm Validation: Turbulent Flow

In the previous section, the CBC technique was applied for an axisymmetric laminar flow field. However, the validity of the technique with laminar data could not be ascertained due to the inherent nature of data that violated the assumptions of homogeneity and isotropy. A systematic validation of the technique therefore requires synthetic data generated in turbulent flows with temporally and spatially correlated fluctuations. Hence, a computer code called random flow generation (RFG) developed by Smirnov et al. (2001) was used to generate synthetic turbulent fluctuation data. The details of the synthetic turbulent data generation process are explained, followed by the application of CBC technique to process synthetic data generated using the RFG code.

5.7.1 Data Generation – RFG code

The Random Flow Generation (RFG) procedure provides a random divergence free vector field under the conditions of isotropy and homogeneity. It has been used to generate inflow and initial flow field for large eddy simulations and to serve as a sub grid-turbulence model in applications of particle-laden flows

(see Smirnov et al. 2001). The RFG procedure is developed on the basis of the work of Kraichnan (1970), who suggested a simple method of generating a Gaussian random field which resembles a pseudo-isotropic turbulence. Accordingly, the non-dimensional instantaneous fluctuating velocity is given as:

$$\bar{u}^{I*}(\bar{x}^*, t^*) = \sqrt{\frac{2}{N}} \left\{ \sum_{n=1}^N \bar{u}_1(\bar{k}_n) \cos(\bar{k}_n \bar{x}^* + \omega_n t^*) + \sum_{n=1}^N \bar{u}_2(\bar{k}_n) \sin(\bar{k}_n \bar{x}^* + \omega_n t^*) \right\} \quad (5.34)$$

$$\text{In this equation, } \bar{u}_1(\bar{k}_n) = \bar{\zeta}_n \times \bar{k}_n, \bar{u}_2(\bar{k}_n) = \bar{\xi}_n \times \bar{k}_n \quad (5.35)$$

$$\text{with } \bar{k}_n \bar{u}_1(\bar{k}_n) = \bar{k}_n \bar{u}_2(\bar{k}_n) = 0 \quad (5.36)$$

ensures the compressibility condition. The components of vectors $\bar{\zeta}_n$ and $\bar{\xi}_n$ and the frequencies ω_n are picked from a Gaussian distribution with a standard deviation of unity. Each component of \bar{k}_n is a Gaussian random number with a standard deviation of $1/2$. Here N is the number of terms in the fourier series. In equation 5.34, the dimensionless quantities are defined as

$$x^* = \frac{x}{l_0}, \quad t = \frac{x}{t_0}, \quad u_i^{I*} = \frac{u_i^{I'}}{u_0^*} \quad (5.37)$$

where l_0 , t_0 and u_0^* are the characteristic length, time and velocity scales of turbulence and $u_i^{I'}$ is the fluctuating fluid velocity.

The RFG code consists of two functions: (1) spectral generator (genspec) (2) vector-field generator (genvec). Figure 5.37 shows a flowchart depicting the execution of the spectral generator (genspec). User supplies the input data in the form of a spectral sample size, characteristic length and time scales. As illustrated by fig. 5.37, the spectral generator algorithm consists of four arrays: Ω , u_1, u_2 and k . The first one i.e Ω is an array of scalar values picked from a Gaussian distribution with a standard deviation of unity. The other three are all arrays of 3D vectors picked from a Gaussian distribution with a standard deviation of $1/2$. These four arrays are global variables and computed only once in the spectral generator function, which initializes the spectral data of these four arrays. Once initialized by the spectral generator, they are repeatedly used in the genvec function (Fig. 5.38) to generate the random vector field for different spatial locations and time.

As discussed above, the RFG code generates a random fluctuating velocity field (u_1, u_2, u_3) satisfying the conditions of global homogeneity and isotropy, with a constant fluctuation intensity throughout. The crossbeam correlation technique is based on the assumptions of local homogeneity and isotropy and it deals with a fluctuating scalar like temperature, concentration or density. Therefore, the data generated from the RFG code was appropriately scaled using the following procedure. First, one component of the velocity field, u_3 was scaled to represent the scalar fluctuating field, for example refractive index gradient. Secondly, the

generated data represented a globally homogeneous field. Hence, in order to represent a locally homogeneous field, the scalar fluctuation field was rescaled to represent a specified distribution of fluctuation intensity. The scaling procedure resulted in a smoothly varying scalar field with appropriate space-time correlations, although the isotropy was no longer fully preserved.

5.7.2 Results and Discussion

5.7.2.1 Nature of data

The validation of the crossbeam correlation technique requires processing of instantaneous refractive index gradient to obtain the deflection angle data. As discussed in the previous section, data from one of the fluctuating velocity components, u_3 were taken from the RFG code, scaled and superimposed with a mean profile to obtain a close approximation of a turbulent refractive index gradient field.

Figure 5.39 shows snapshots of synthetically generated instantaneous refractive index gradient field on a cross-sectional plane. Unlike laminar data, it can be seen that the instantaneous refractive index gradients are asymmetric, because of the random turbulent fluctuations. Figure 5.40 shows contour plots of the mean and the variance of the turbulent refractive index field. A total of 100,000 time steps were used to generate these images. As can be observed from the contour plots, the mean and variance are axisymmetric, illustrating that on time average basis, synthetic data are axisymmetric. This property of the

generated random scalar field is important in applying the crossbeam correlation technique as discussed in section 5.5.

Figure 5.41 shows the contour plots of the auto-correlation coefficients calculated as follows:

$$R_{ii}(r) = \frac{\langle G_i(x_i, t) G_i(x_i + r, t) \rangle}{\langle G_i^2 \rangle} \quad (\text{One time, two point correlation})$$

where $G = \frac{\partial \delta}{\partial x}$

and the double-i subscript in $R_{ii}(r, t)$ indicates the autocorrelation function (i.e. the correlation of a scalar component with itself). In a locally isotropic field, one would expect the autocorrelation coefficient to be finite within the correlation region and zero elsewhere. However, the contour plots indicate non-zero values of correlation coefficients outside the local correlation region. This result is attributed to the inherent noise in the RFG code and to errors introduced during the scaling process. From the above discussion, it can be observed that although the randomly generated turbulent scalar field is axisymmetric, the noise introduced in the code generation and scaling leads to anisotropy as seen from the correlation coefficient plots. Contour plots of integral length scales shown in Fig. 5.42 and 5.43 depict this behavior in the flow field. The value of the integral length scale (l_z) varies between 0.0 and 3.5 as seen from fig.5.42. On the other hand, the integral length scale (l_y) varies between 5 and 8. Ideally for a locally isotropic scalar field, one would expect the integral length scales l_y and l_z to be

equal and axisymmetric. However, the noise present outside the correlation region introduces errors into the calculation of integral length scales.

5.7.2.2 Angular Deflections

The refractive index gradient data were used to calculate the deflection angle in both z and y directions. Figures 5.44 and 5.45 show profiles of the instantaneous deflection angles computed using the trapezoidal rule of integration in z and y directions based on equations 5.3 and 5.4 (see Appendix B). Obviously the instantaneous profiles are asymmetric because of the random turbulent fluctuations. However, the mean deflection angle is axisymmetric as shown in the profile in fig. 5.46. Fig. 5.46 shows the mean deflection angle profiles computed along y and z directions, the two profiles are exactly the same, as expected in an axisymmetric turbulent flow. Results show that the sample size (100,000 time steps) is sufficiently large to obtain the statistics of the turbulent flow.

5.7.2.3 Mixing Function

The first step in applying the crossbeam correlation technique involves calculation of the mixing function (f_z). Thus, the variance of the angular deflection along the z direction was computed first (see fig. 5.47). From the profile of the variance of the deflection angle, the turbulent mixing function can be computed using Abel inversion. However, the application of Abel inversion requires the mixing function to be axisymmetric. Hence, before calculating the turbulent mixing function by inversion, the exact value of the mixing function was

calculated from the product of the refractive index gradient intensity (see fig.5.40b) and the integral length scale (l_z) given in eq. 5.16. Figure 5.48 shows the distribution of the exact value of the mixing function, which is approximately axisymmetric; unlike the laminar case (see fig. 5.27 & 5.33). The asymmetry is caused by anisotropy introduced in the scaling procedure.

Figure 5.49 compares the profiles of the z-direction mixing function obtained from actual data and the crossbeam correlation (CBC) process. Results indicate a good agreement between exact and inverted mixing function profiles. The difference is attributed to imperfect axisymmetry in the mixing function. Similar procedure was followed in obtaining the variance profiles in the y direction (Fig. 5.50) and then computing the distribution of the exact value of the y direction mixing function (fig. 5.51). Figure 5.52 shows the comparison of the profiles of CBC based and exact mixing functions in the y direction. Excellent agreement between the computed and exact value of mixing function is obtained as seen from the plots.

5.7.2.4 Crossed Beam Covariance

Figure 5.53 shows the contour plot of the crossed beam covariance of the deflection angle computed in z and y directions. The covariance contours depict reasonable axisymmetry and a profile of the covariance is also presented in Fig. 5.54. From known distributions of the mixing function and the covariance, one can easily calculate the distribution of the refractive index gradient fluctuations

based on equation 5.23 and 5.24. Figures 5.55, 5.56 and 5.57 show the comparison plots of the refractive index fluctuation intensity obtained using the three methods listed in section 5.4.

It can be observed that although the plots depict a good qualitative agreement with the actual values, they exhibit varied degrees of quantitative agreement. The fluctuation intensity computed using integral length scale (l_z) (fig. 5.56) gives the best results when compared to the methods using the product of the length scales ($l_z l_y$) and integral length scale (l_y). Ideally, one would expect to get similar results using the three different methods. However, the anisotropy of the integral length scales causes the difference between the three methods.

5.8 Conclusions

A crossbeam rainbow schlieren deflectometry system was developed and demonstrated to obtain scalar turbulence measurements in jets/flames. The theoretical framework and the validation of the analysis procedures were presented in this study. Important results of the study are summarized as follows:

- The existing rainbow schlieren system was modified to configure the crossbeam rainbow schlieren deflectometry system capable of obtaining scalar turbulence measurements in jets/flames. Experimental observations provided excellent flow visualizations of the scalar flow structure of turbulent jets/flames.

- The crossbeam correlation technique was developed and presented to compute scalar turbulence parameters from schlieren images.
- The validity of the crossbeam correlation technique was verified using synthetic laminar and turbulent data. Results indicated that the crossbeam correlation technique is a promising approach to obtain scalar and statistical properties of turbulent flows.

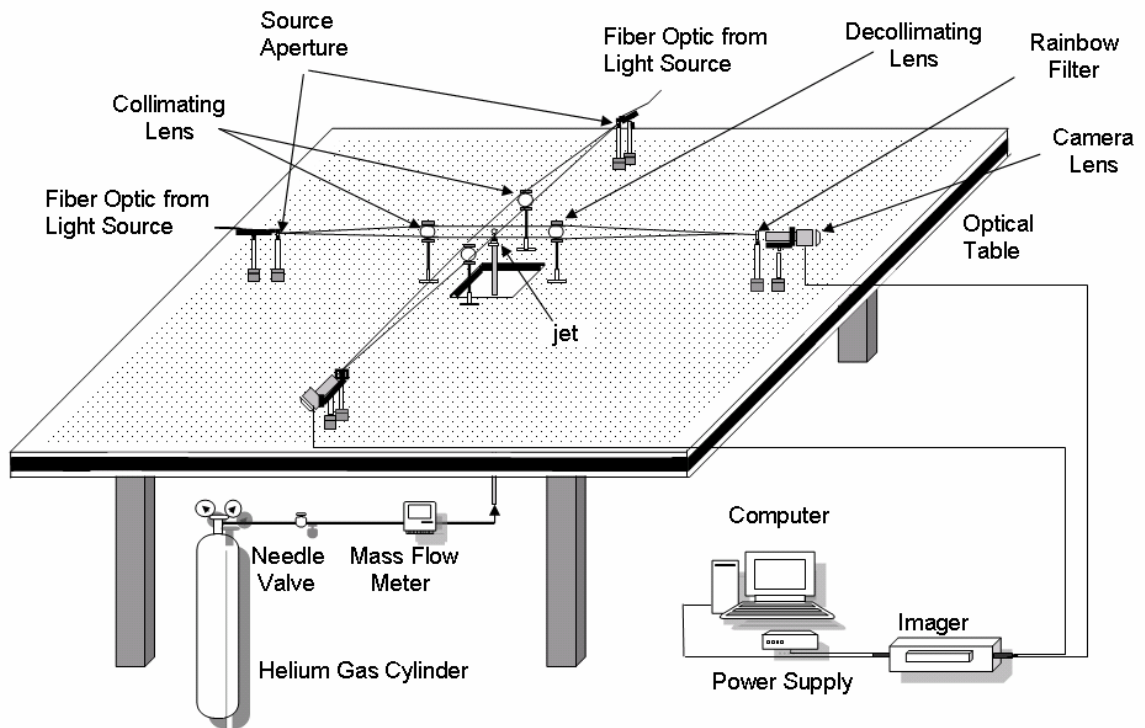
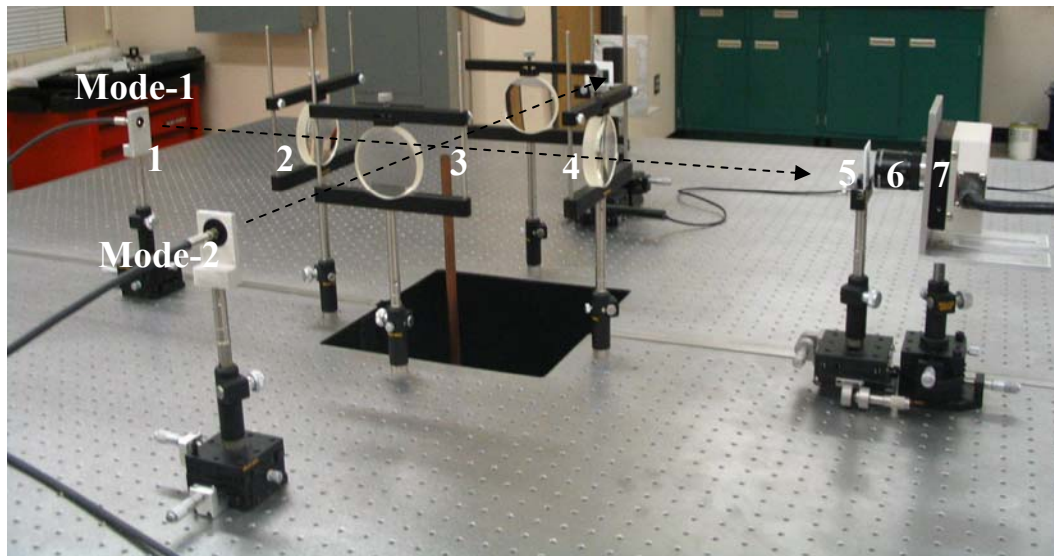


Figure 5.1. Schematic of the Crossbeam Schlieren apparatus.



- | | | |
|-----------------------|---------------------|----------------|
| 1. Slit/Aperture | 2. Collimating lens | 3. Test media |
| 4. Decollimating lens | 5. Rainbow filter | 6. Camera lens |
| 7. Camera sensor | | |

Figure 5.2. Photograph of the Crossbeam Schlieren apparatus.

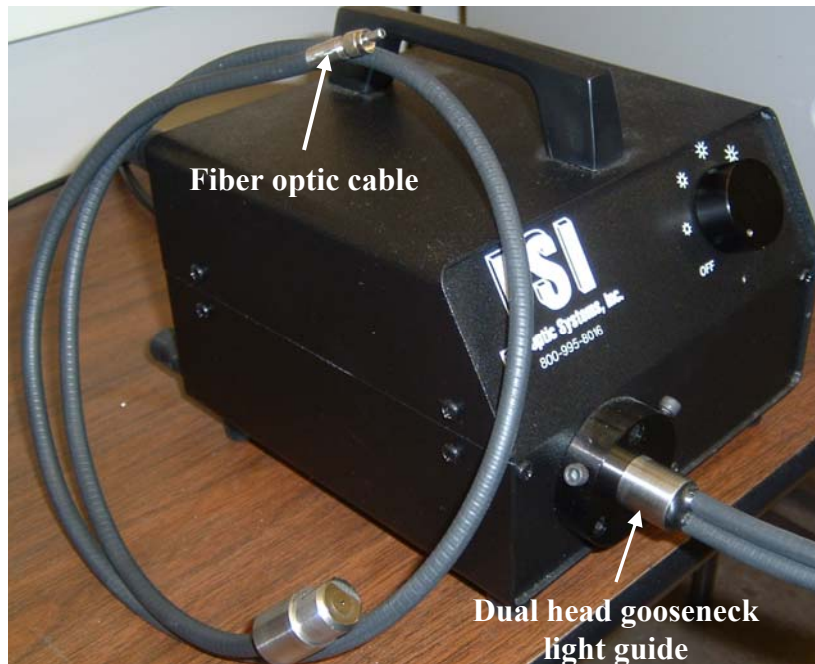


Figure 5.3. Photograph of the light source.

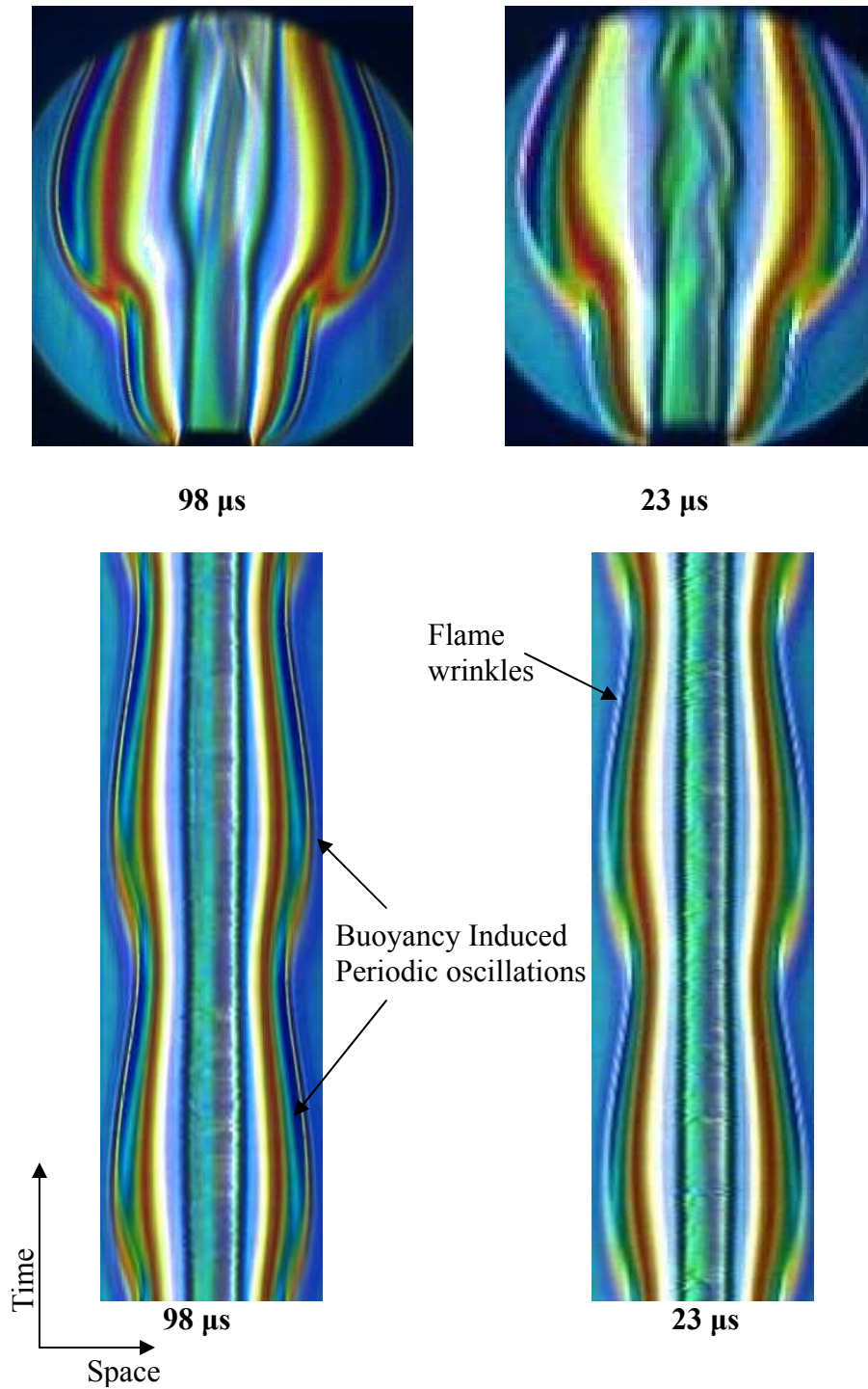


Figure 5.4. Instantaneous rainbow schlieren images (top) and space-time images (bottom) of a hydrogen jet diffusion flame for different exposure times at $z/d=1.5$.

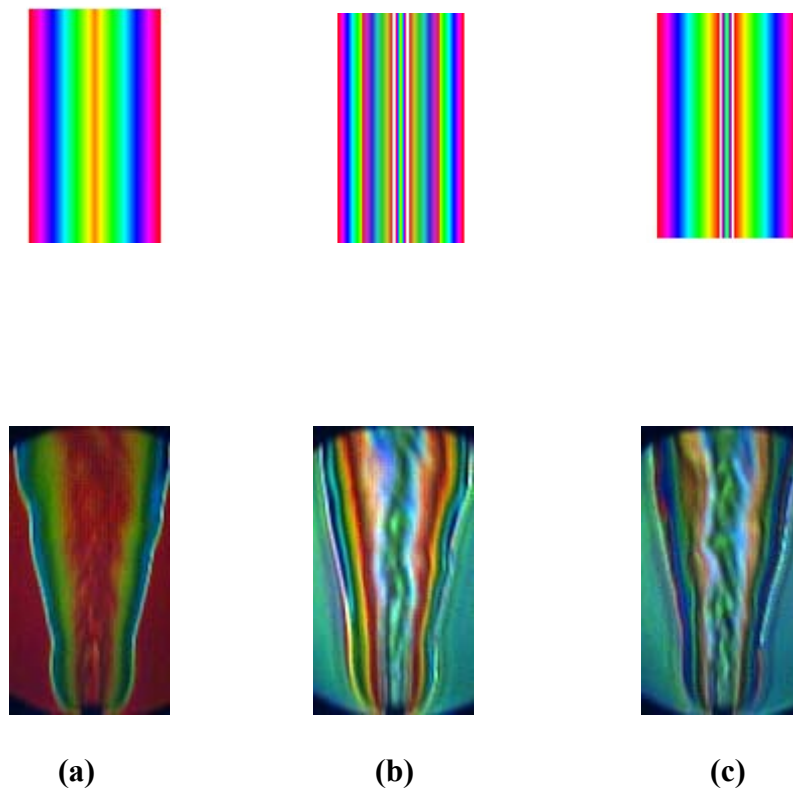


Figure 5.5. Schlieren images of a hydrogen diffusion flame for different filter configurations.

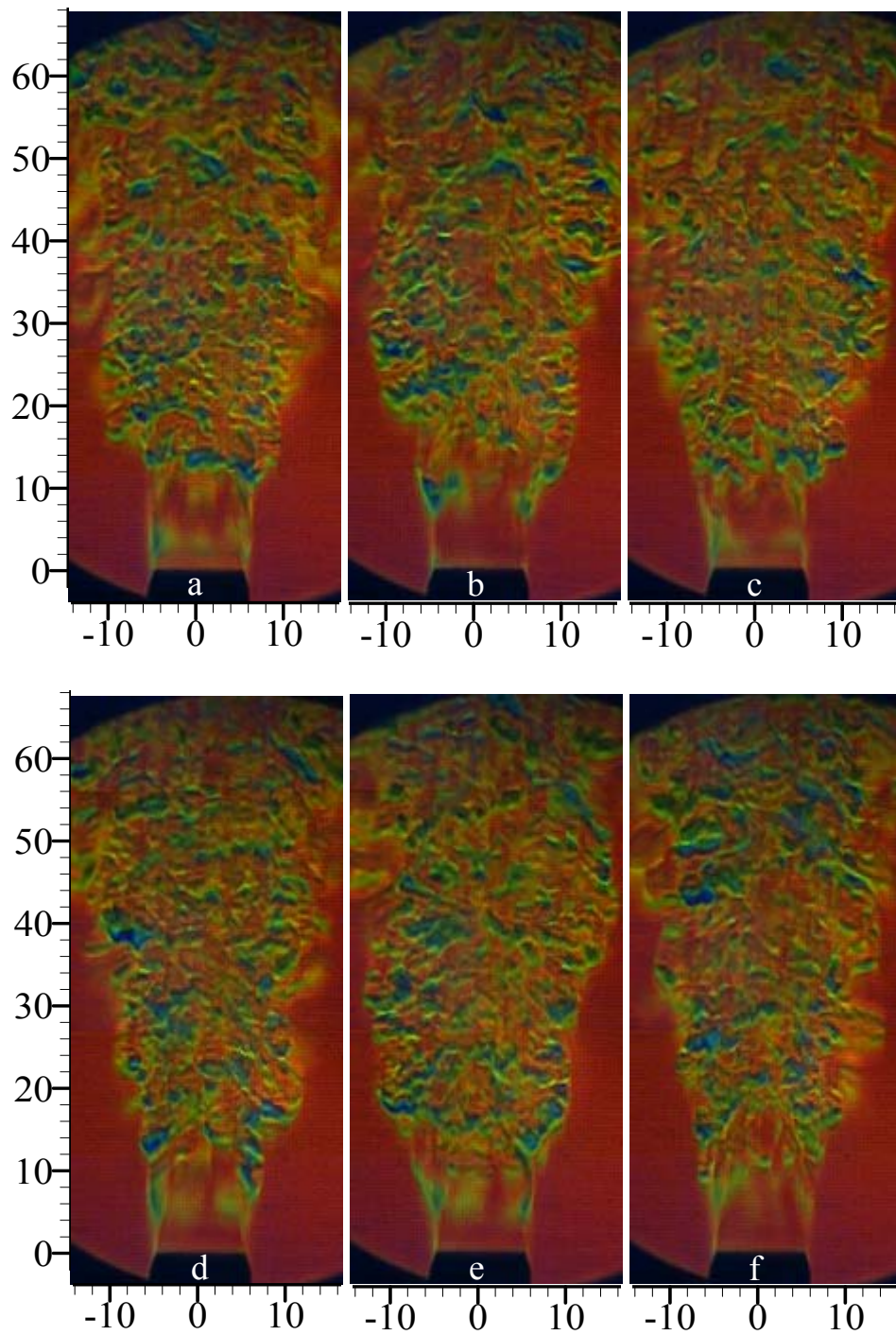


Figure 5.6. Instantaneous rainbow schlieren images of a turbulent helium-air jet at $Re=4000$, $Ri=0.0002$, $d=10.0\text{mm}$, Crossbeam mode-1.

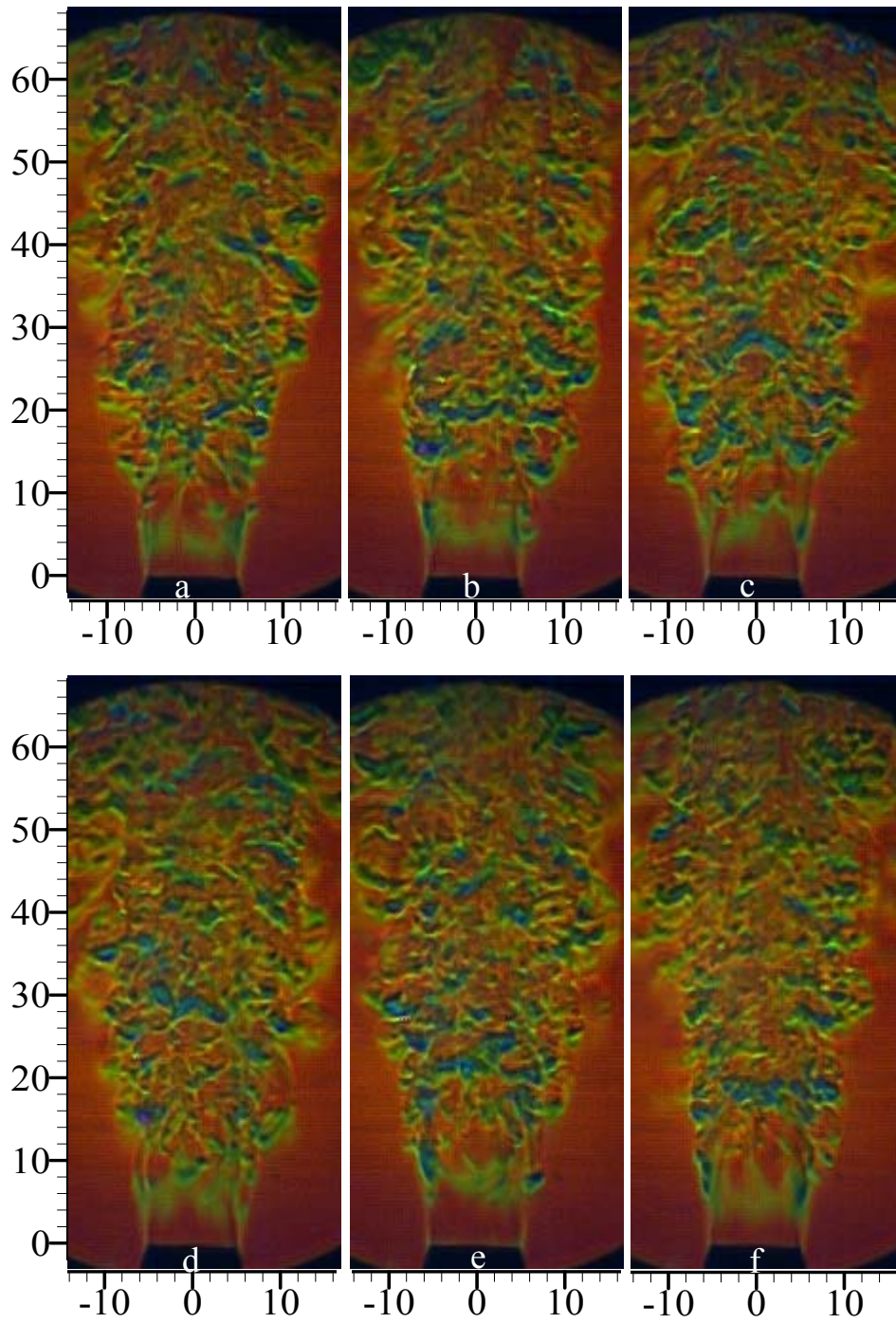


Figure 5.7. Instantaneous rainbow schlieren images of a turbulent helium-air jet at $Re=4000$, $Ri=0.0002$, $d=10.0\text{mm}$, Crossbeam mode-2.

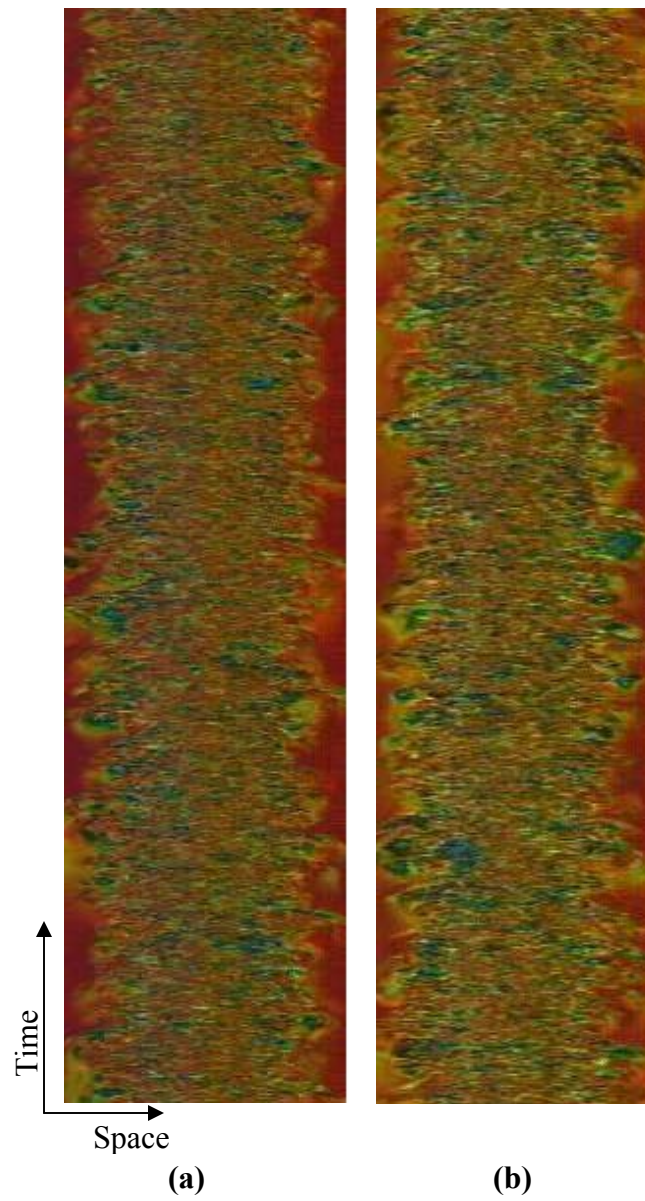


Figure 5.8. Time-space image of the turbulent helium-air jet at $Re=4000$, $Ri=0.0002$, $d=10.0\text{mm}$, (a) Crossbeam mode-1 (b) Crossbeam mode-2.

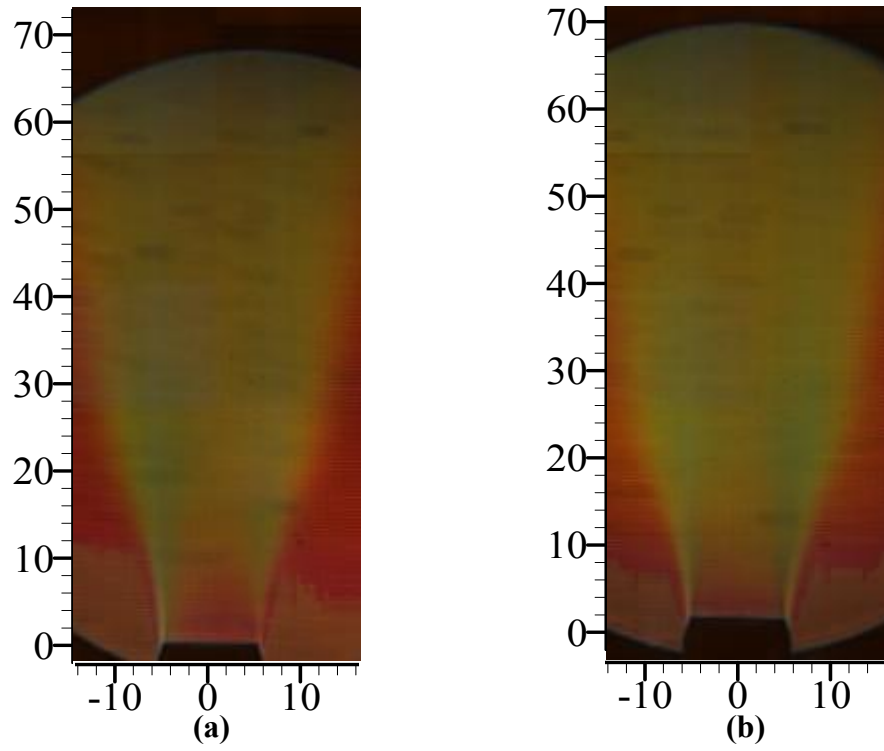


Figure 5.9. Mean image of the turbulent helium-air jet at $Re=4000$, $Ri=0.0002$, $d=10.0\text{mm}$, (a) Crossbeam mode-1 (b) Crossbeam mode-2.

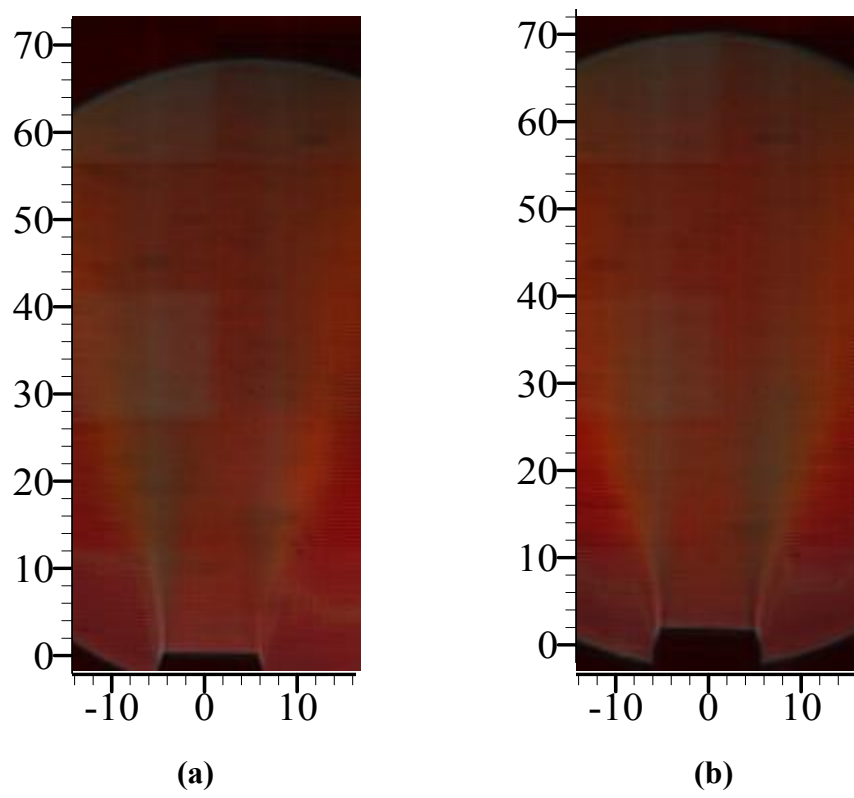


Figure 5.10. RMS image of the turbulent helium-air jet at $Re=4000$, $Ri=0.0002$, $d=10.0\text{mm}$, (a) Crossbeam mode-1 (b) Crossbeam mode-2.

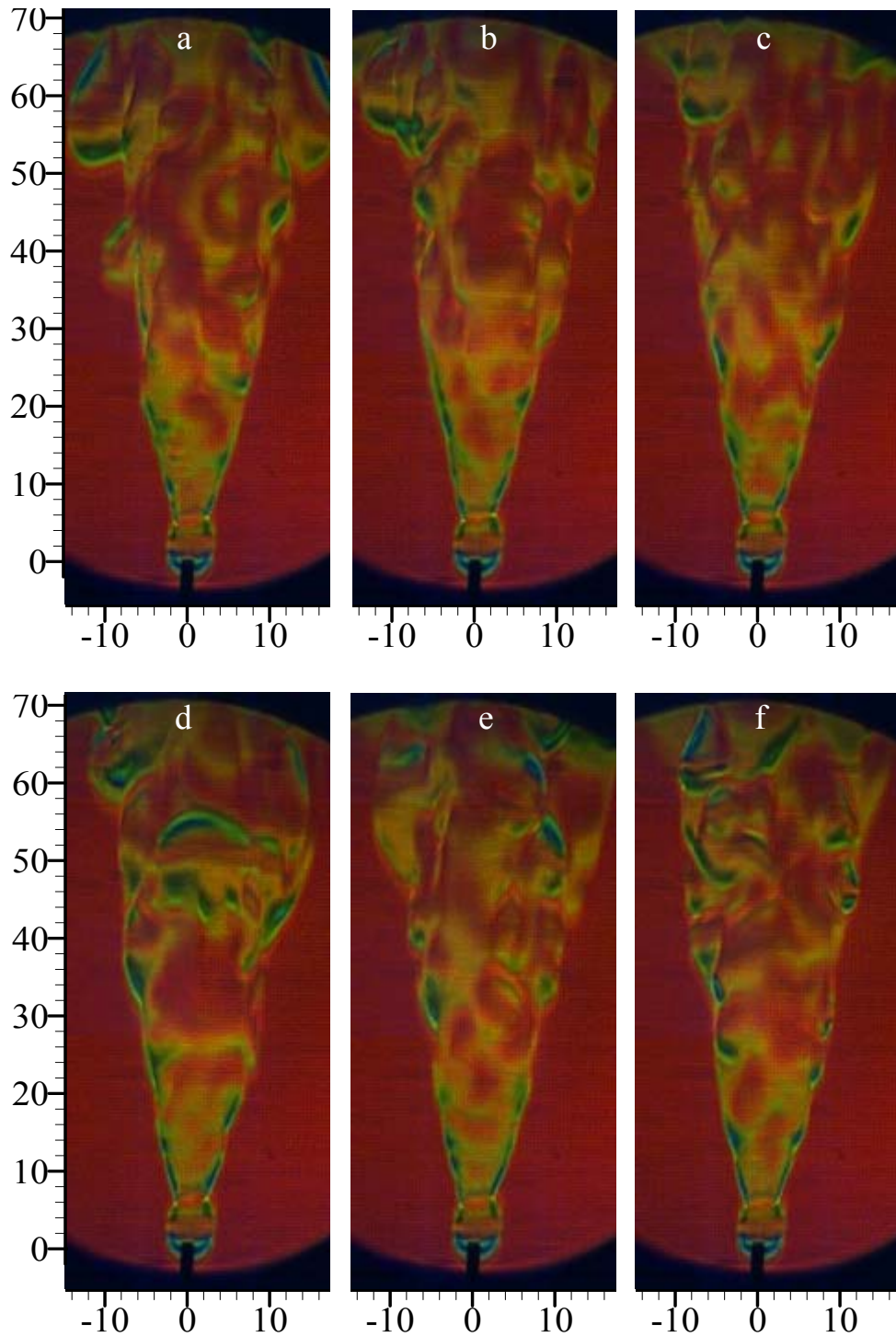


Figure 5.11. Instantaneous schlieren images of a turbulent hydrogen diffusion flame at $Re=2400$, $Ri=3.7e-06$, $d=1.19mm$, Crossbeam mode-1.

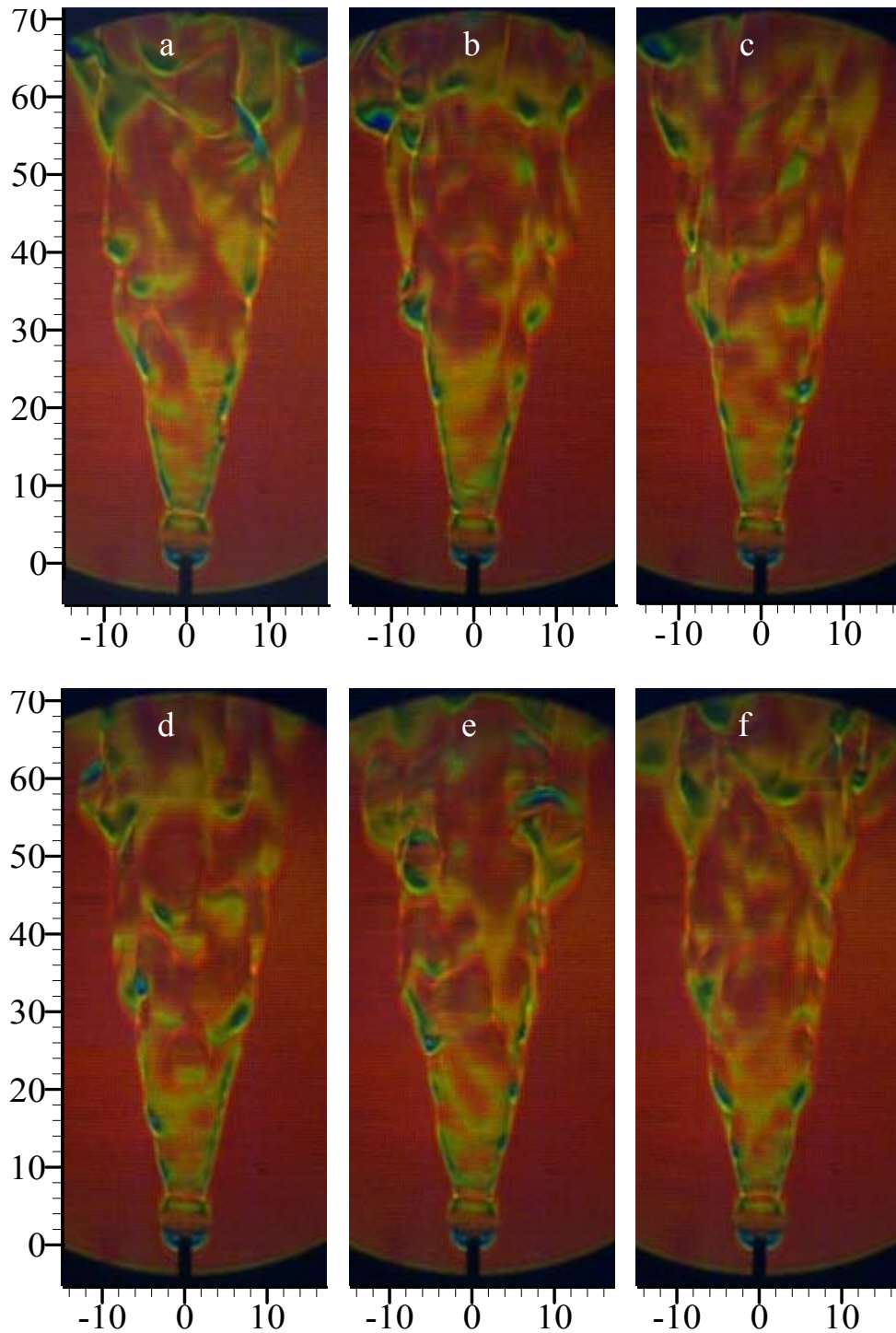


Figure 5.12. Instantaneous schlieren images of a turbulent hydrogen diffusion flame at $Re=2400$, $Ri=3.7e-06$, $d=1.19mm$, Crossbeam mode-2.

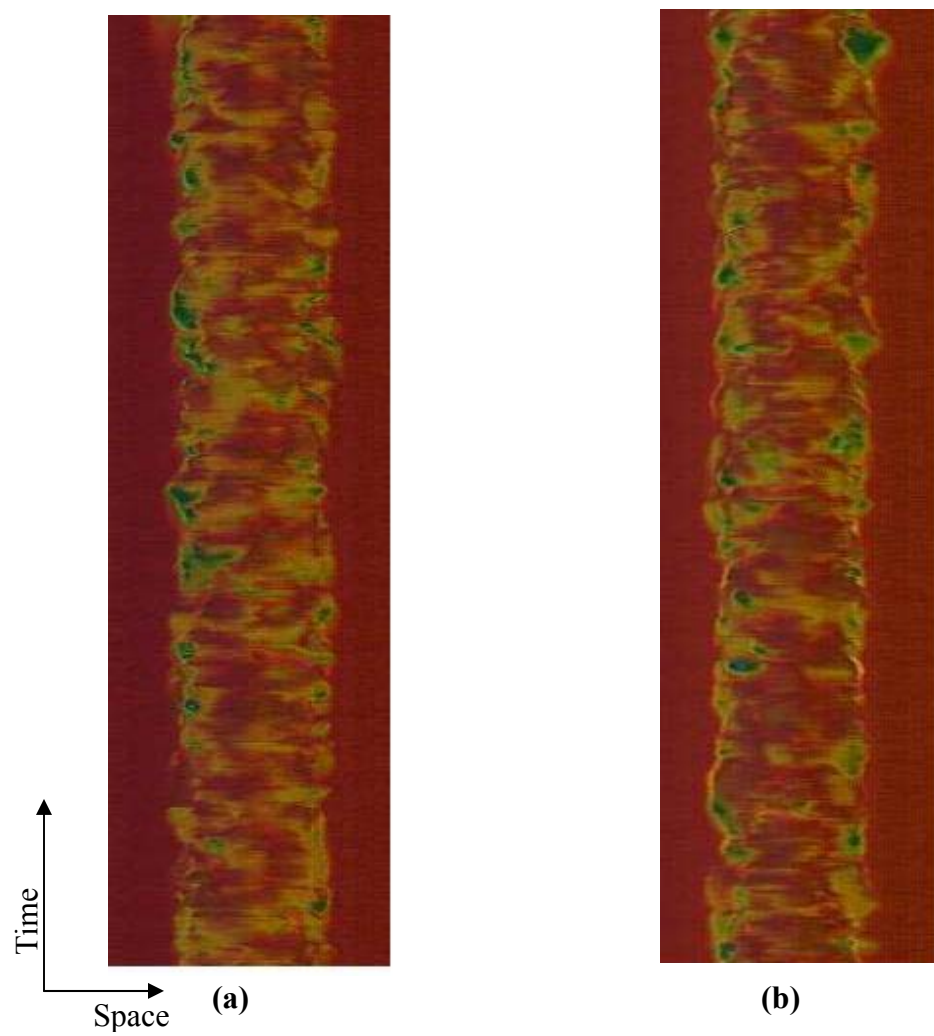


Figure 5.13. Time-space image of a turbulent hydrogen diffusion flame at $Re=2400$, $Ri=3.7e-06$, $d=1.19mm$, (a) Crossbeam mode-1 (b) Crossbeam mode-2.

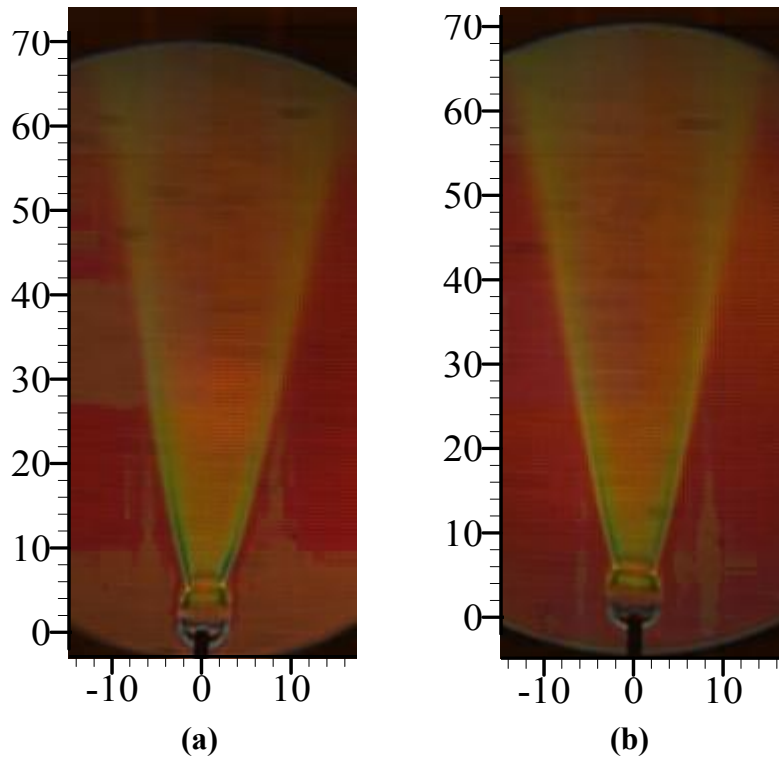


Figure 5.14. Mean image of a turbulent hydrogen diffusion flame at $Re=2400$, $Ri=3.7e-06$, $d=1.19mm$, (a) Crossbeam mode-1 (b) Crossbeam mode-2.

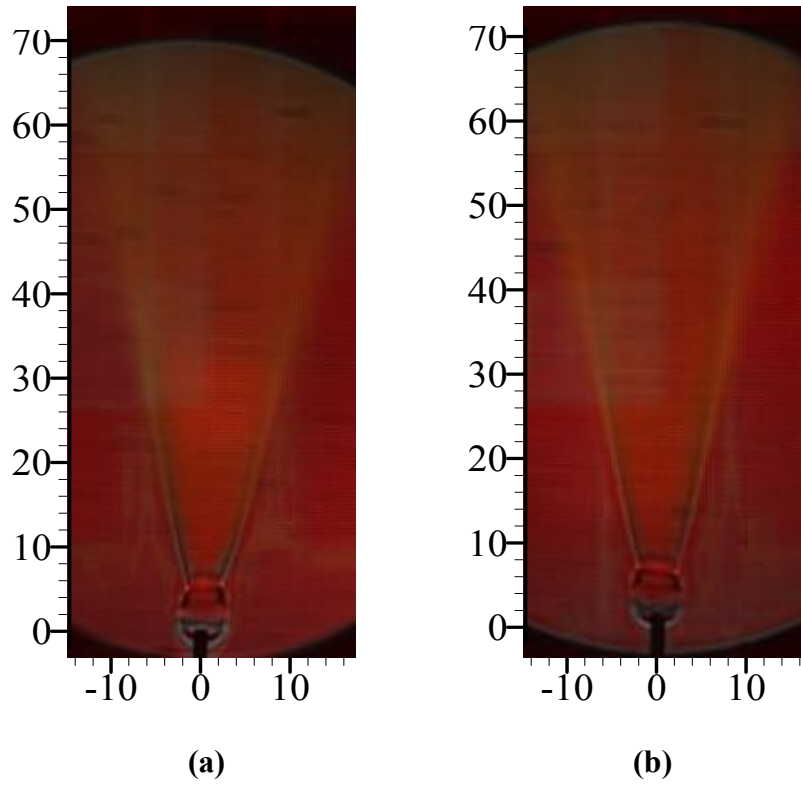


Figure 5.15. RMS image of a turbulent hydrogen diffusion flame at $Re=2400$, $Ri=3.7e-06$, $d=1.19mm$, (a) Crossbeam mode-1 (b) Crossbeam mode-2.

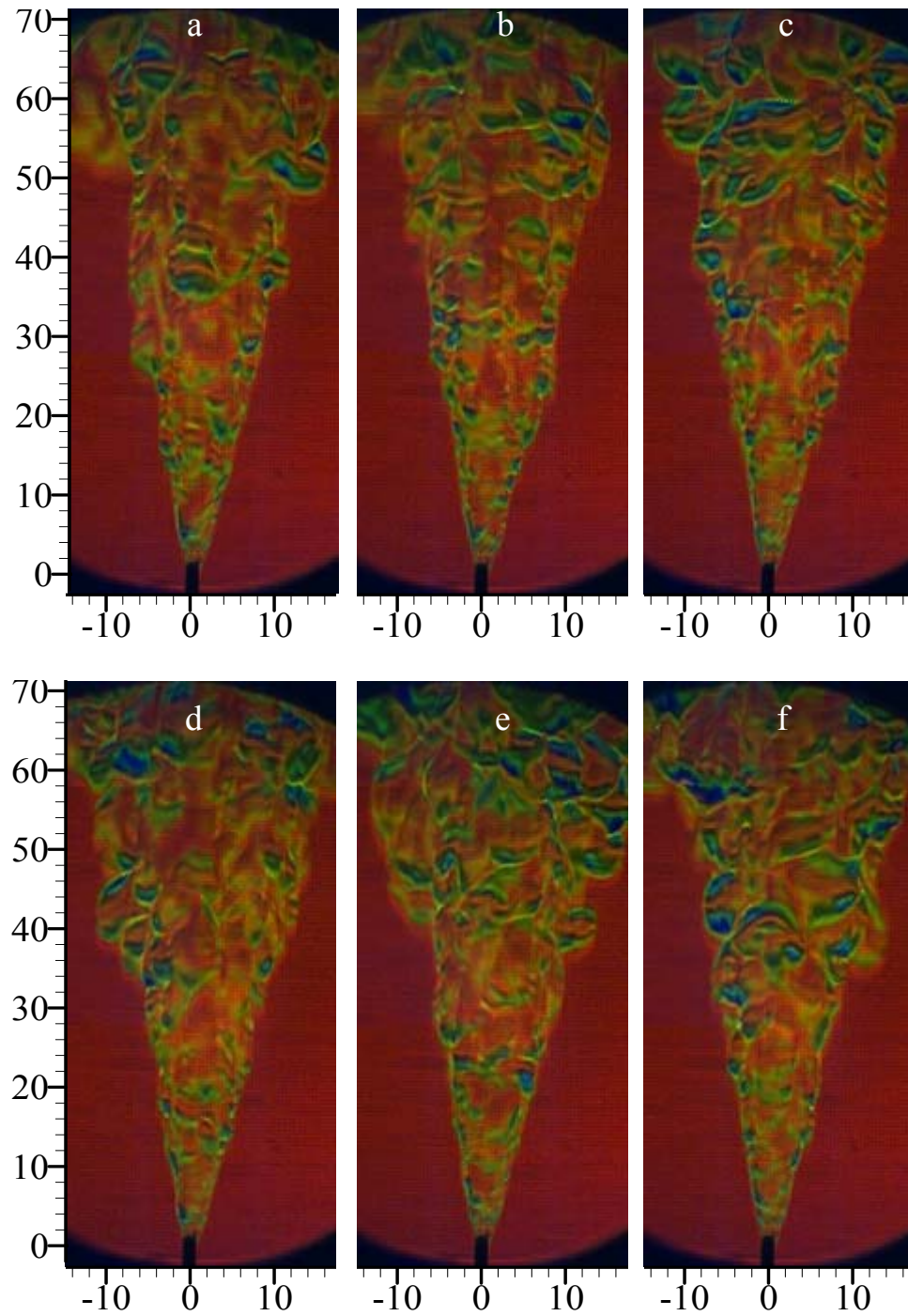


Figure 5.16. Instantaneous schlieren images of a turbulent hydrogen diffusion flame at $Re=4200$, $Ri=1.27e-06$, $d=1.19mm$, Crossbeam mode-1.

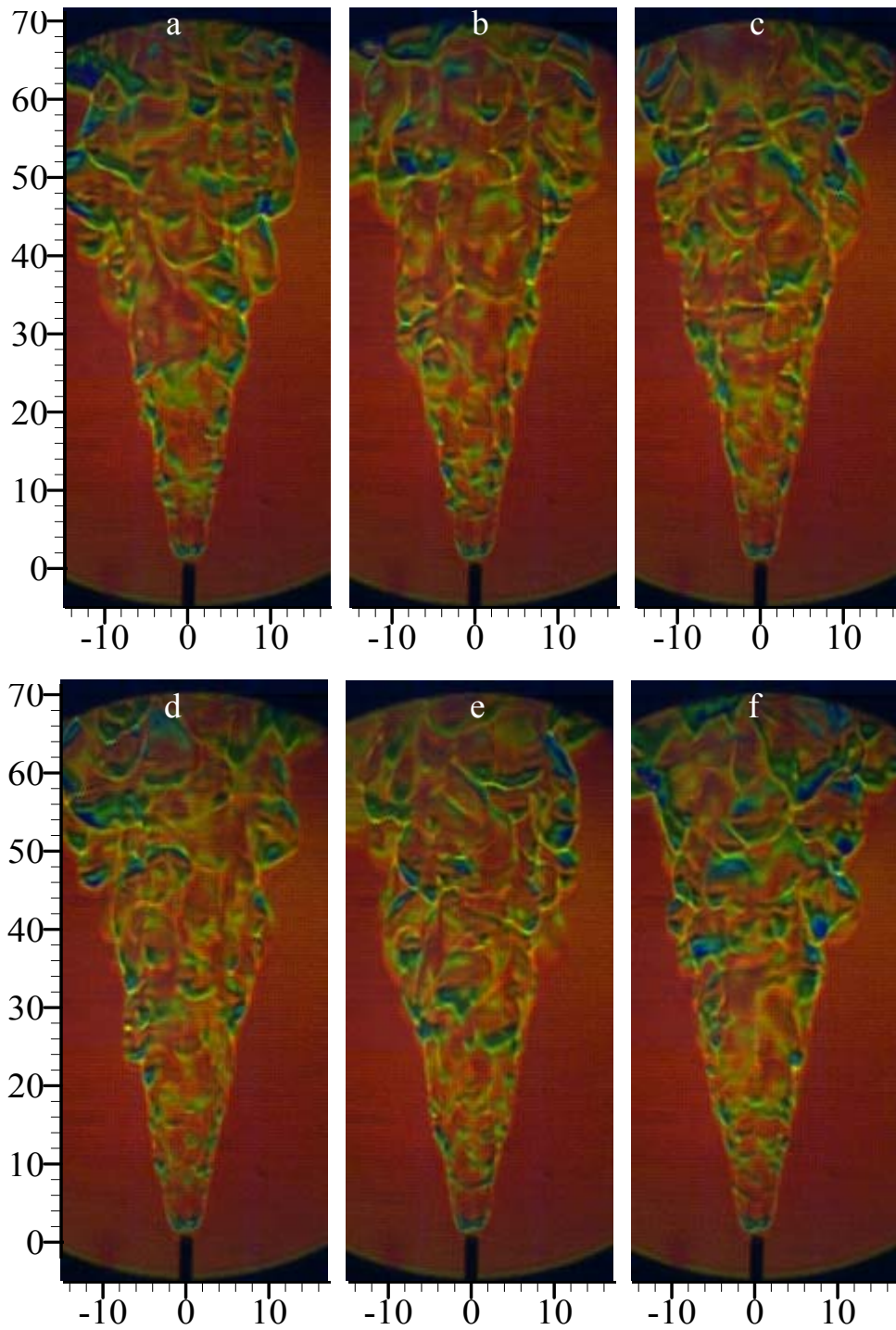


Figure 5.17. Instantaneous schlieren images of a turbulent hydrogen diffusion flame at $Re=4200$, $Ri=1.27e-06$, $d=1.19mm$, Crossbeam mode-2.

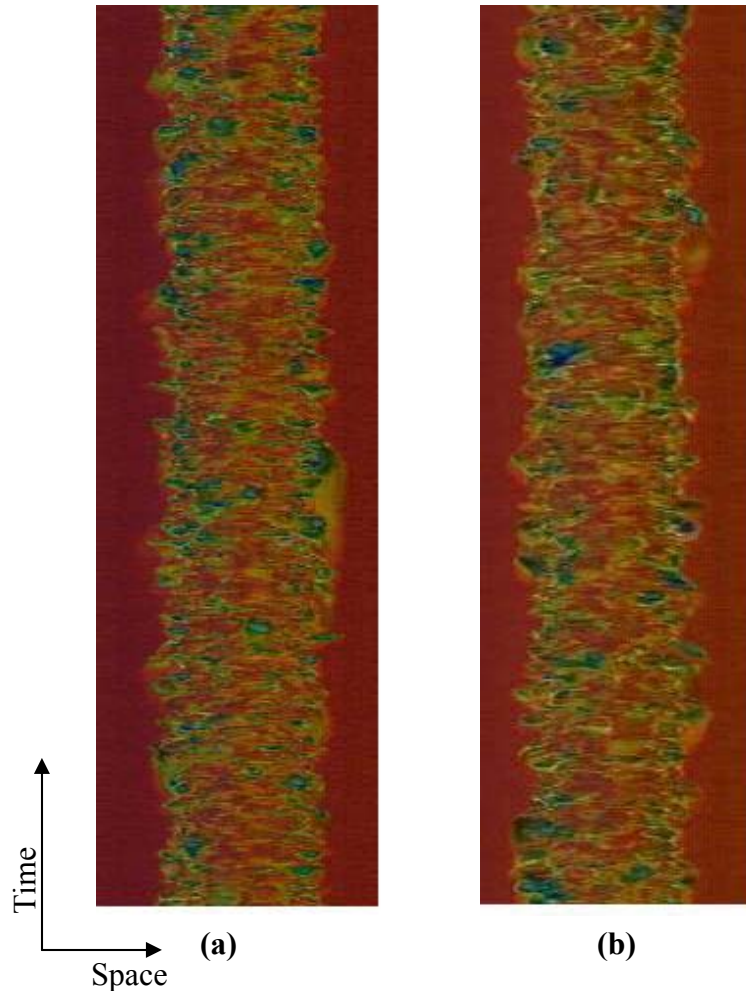


Figure 5.18. Time-space image of a turbulent hydrogen diffusion flame at $Re = 4200$, $Ri = 1.27 \times 10^{-6}$, $d = 1.19 \text{ mm}$, (a) Crossbeam mode-1 (b) Crossbeam mode-2.

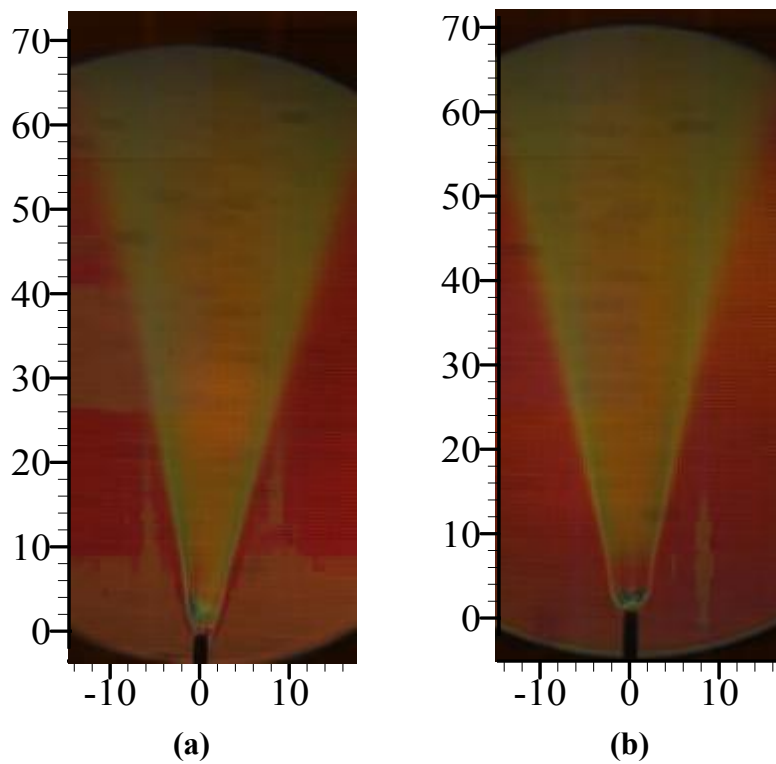


Figure 5.19. Mean image of a turbulent hydrogen diffusion flame at $Re=4200$, $Ri=1.27e-06$, $d=1.19mm$, (a) Crossbeam mode-1 (b) Crossbeam mode-2.

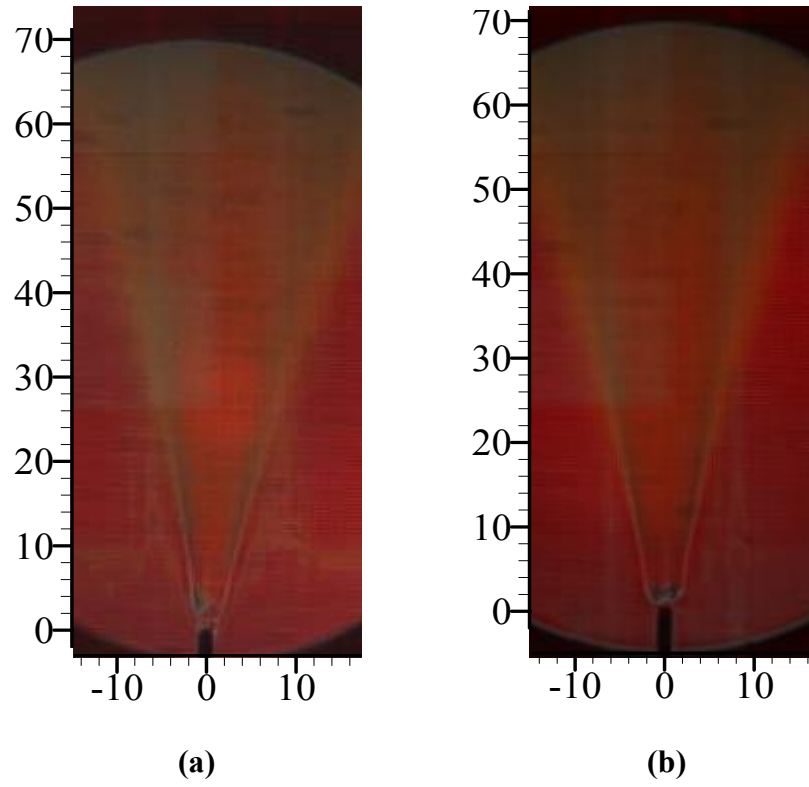


Figure 5.20. RMS image of a turbulent hydrogen diffusion flame at $Re=4200$, $Ri=1.27e-06$, $d=1.19mm$, (a) Crossbeam mode-1 (b) Crossbeam mode-2.

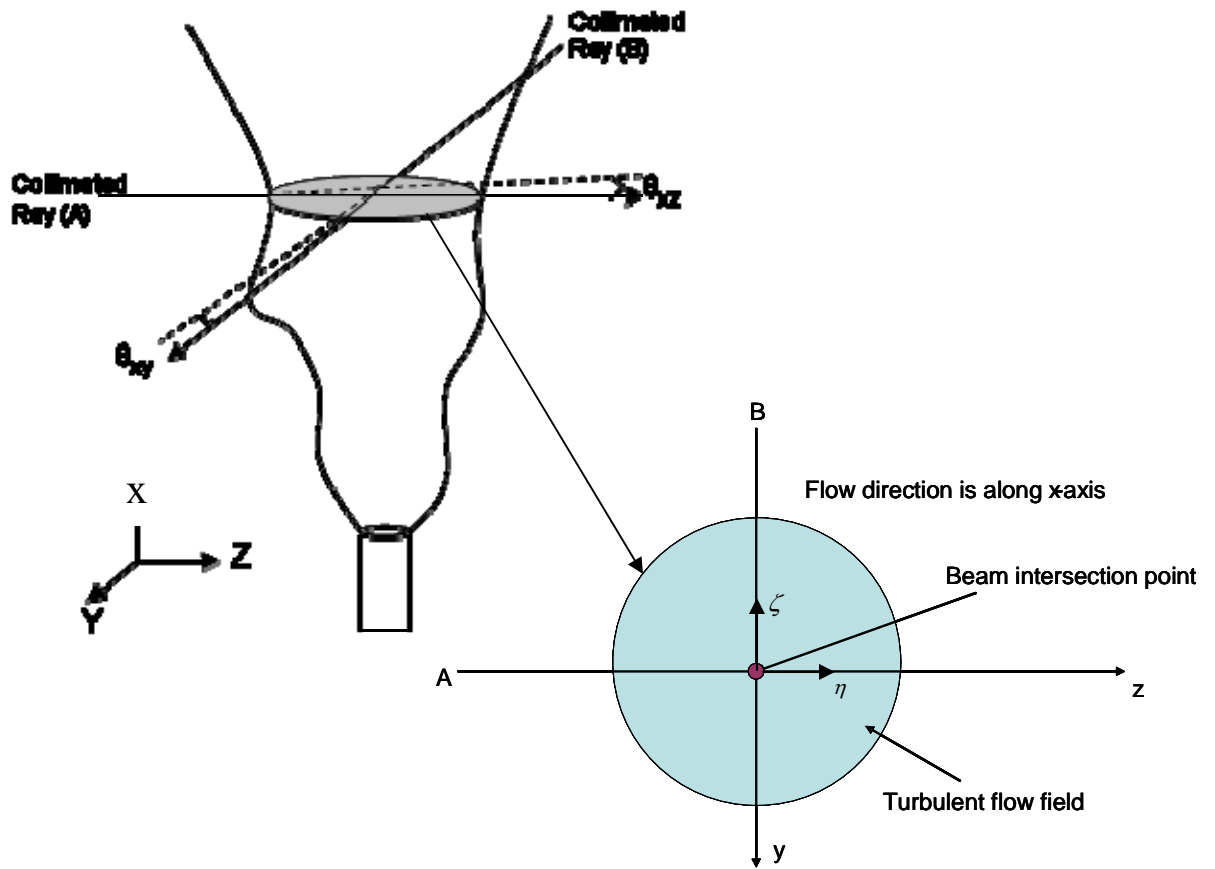


Figure 5.21. Schematic illustrating the cross beam correlation technique

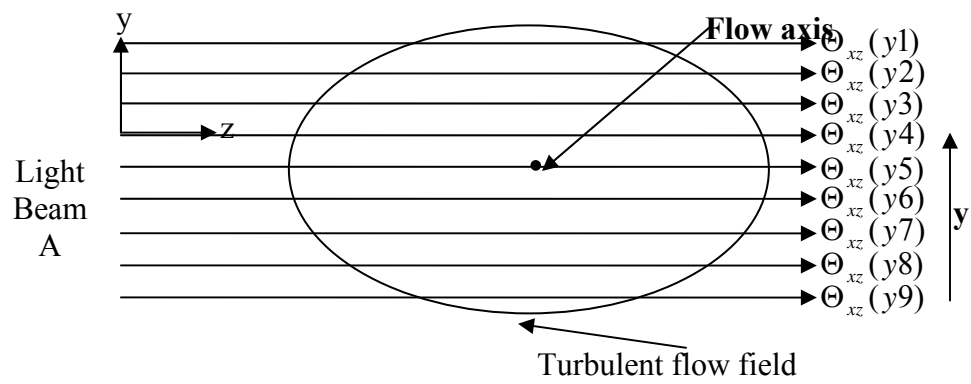


Figure 5.22. Single beam schlieren system along the z direction

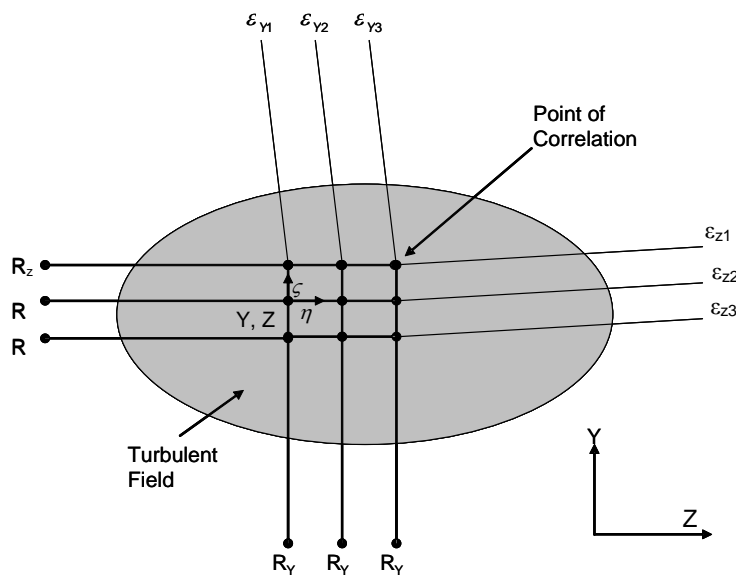


Figure 5.23. Illustration of the crossbeam technique using rainbow schlieren apparatus.

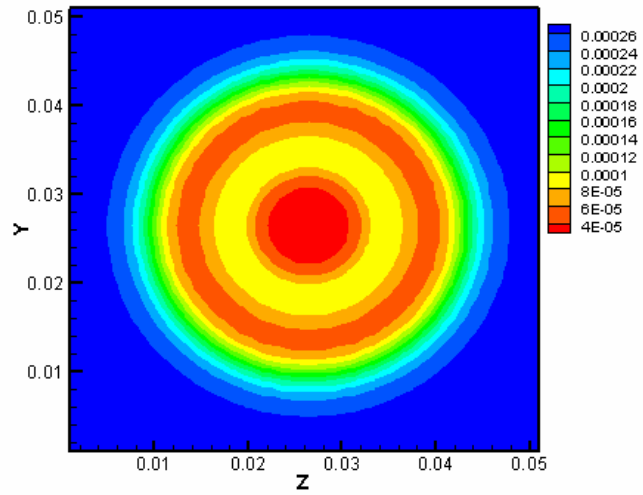
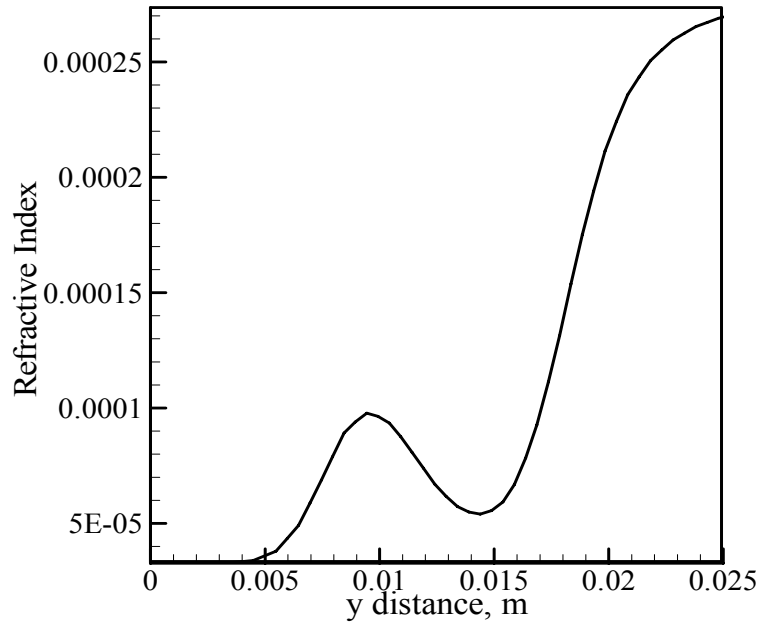


Figure 5.24. Profile of the refractive index (top) and contour plot representing the cross sectional plane after sweeping the profile in cartesian coordinates (bottom).

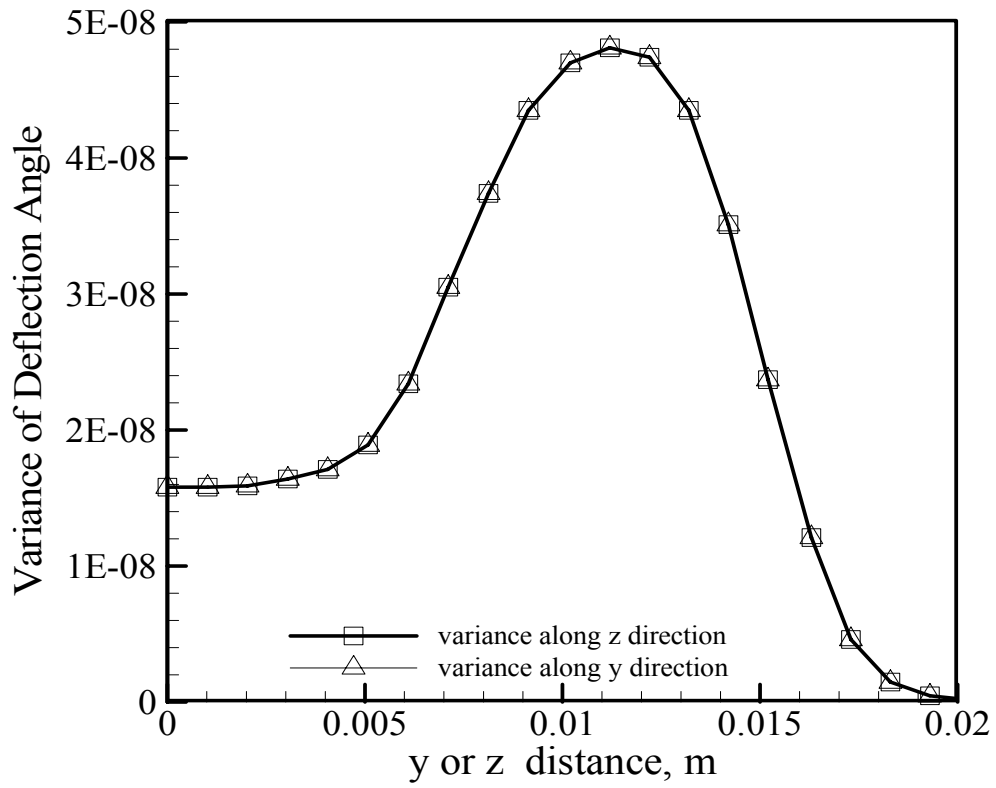


Figure 5.25. Variance of angular deflection-Case 1.

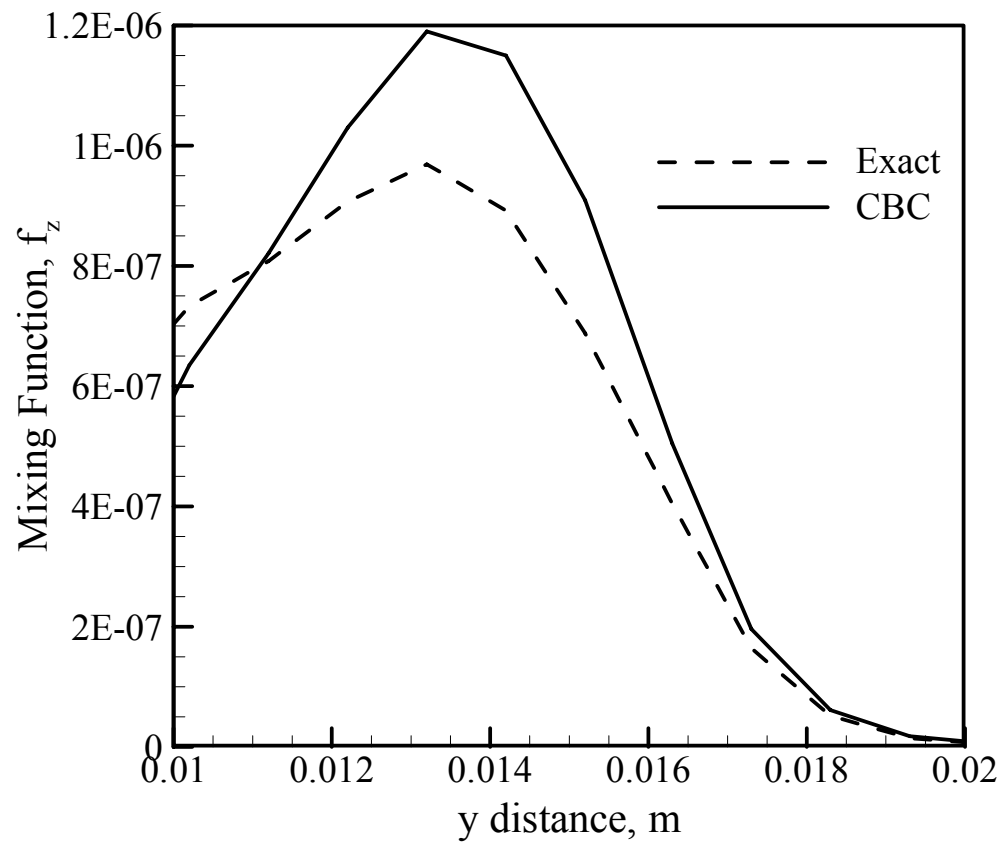


Figure 5.26. Exact Vs Inverted mixing function profiles-Case 1.

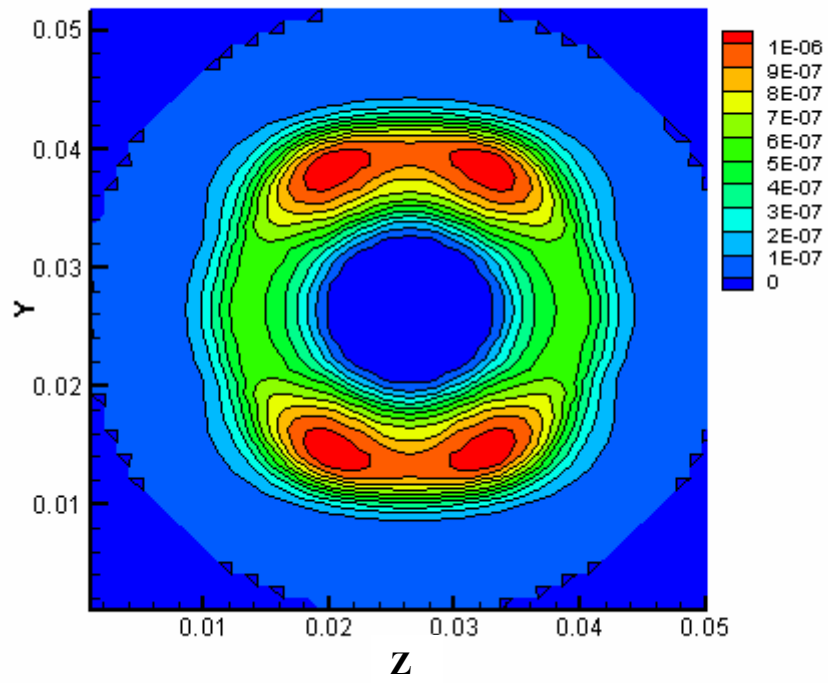


Figure 5.27. Contour plot of mixing function -Case 1.

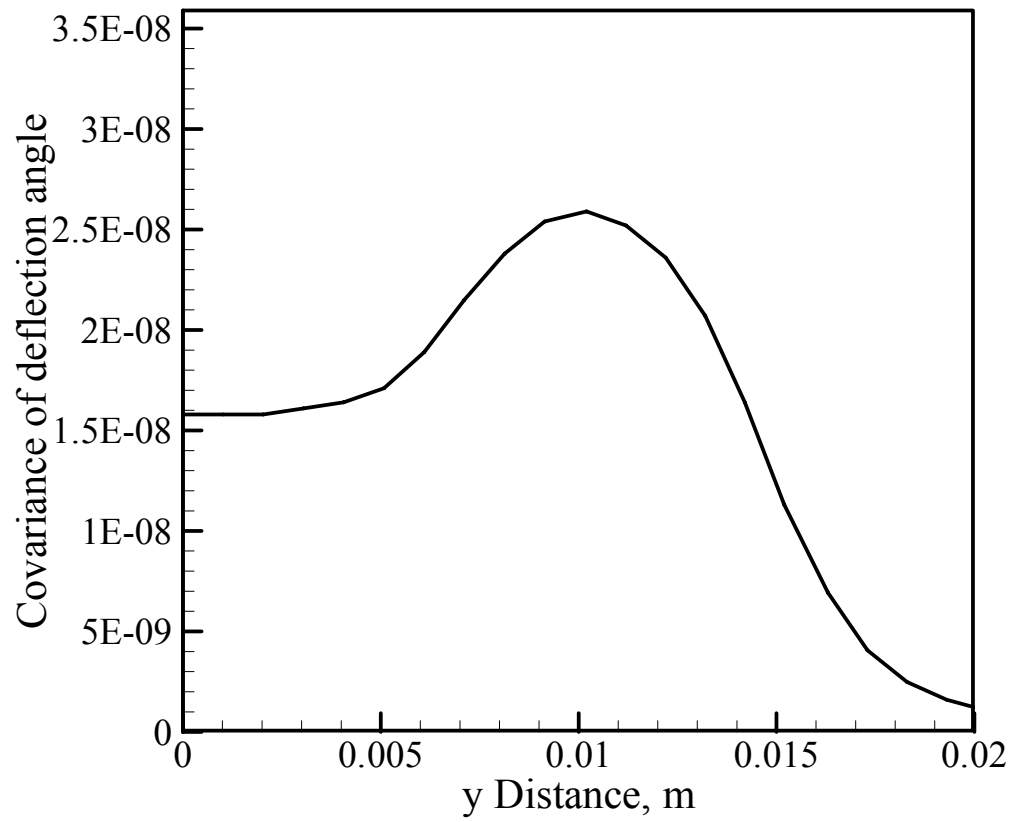


Figure 5.28. Profiles of deflection angle covariance -Case 1.

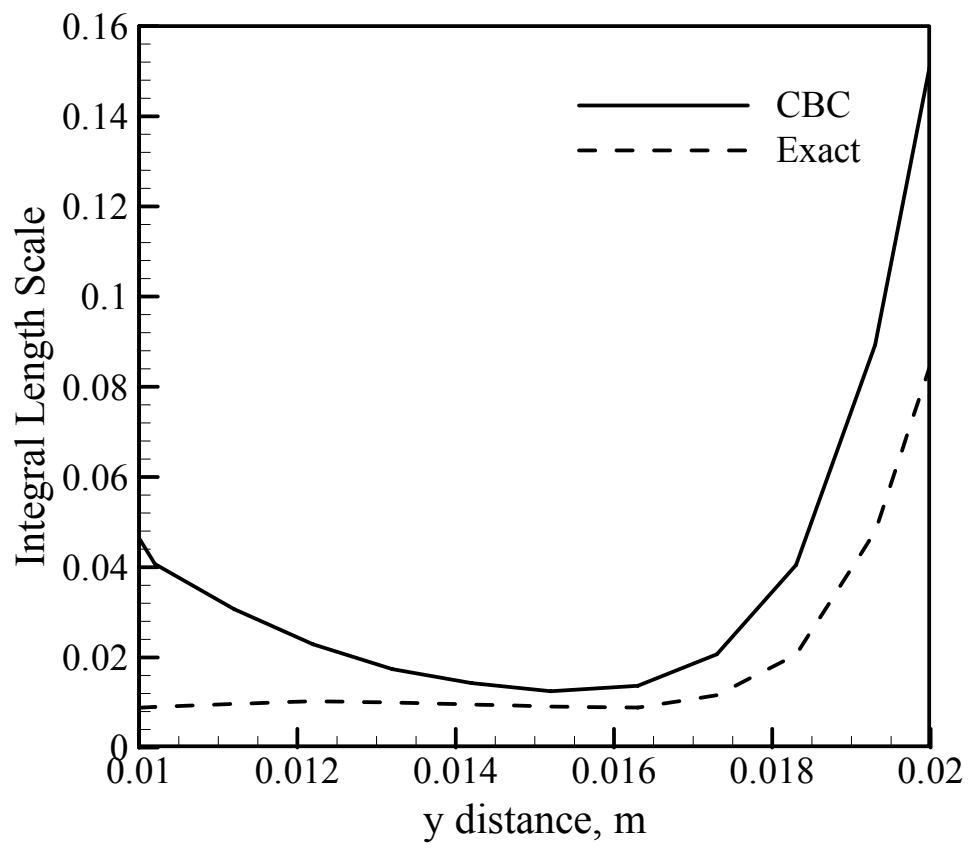


Figure 5.29.Exact Vs CBC based integral length scales-Case 1.

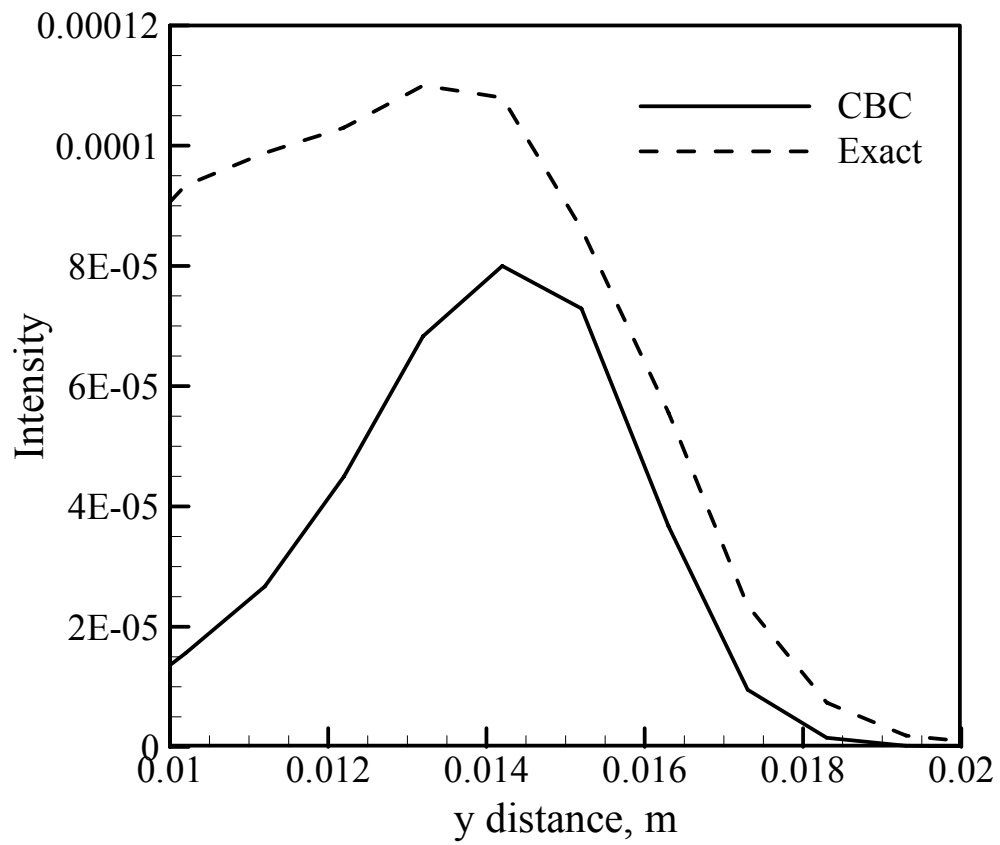


Figure 5.30. Exact Vs CBC based intensity profiles-Case 1.

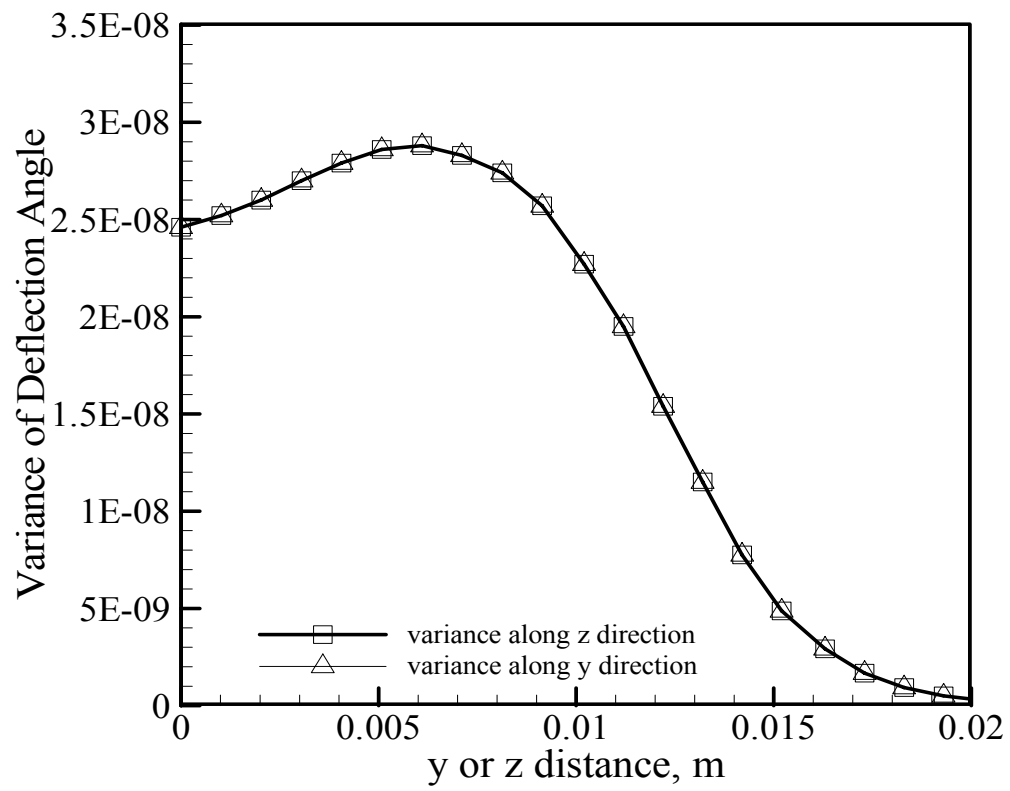


Figure 5.31. Variance of angular deflection-Case 2.

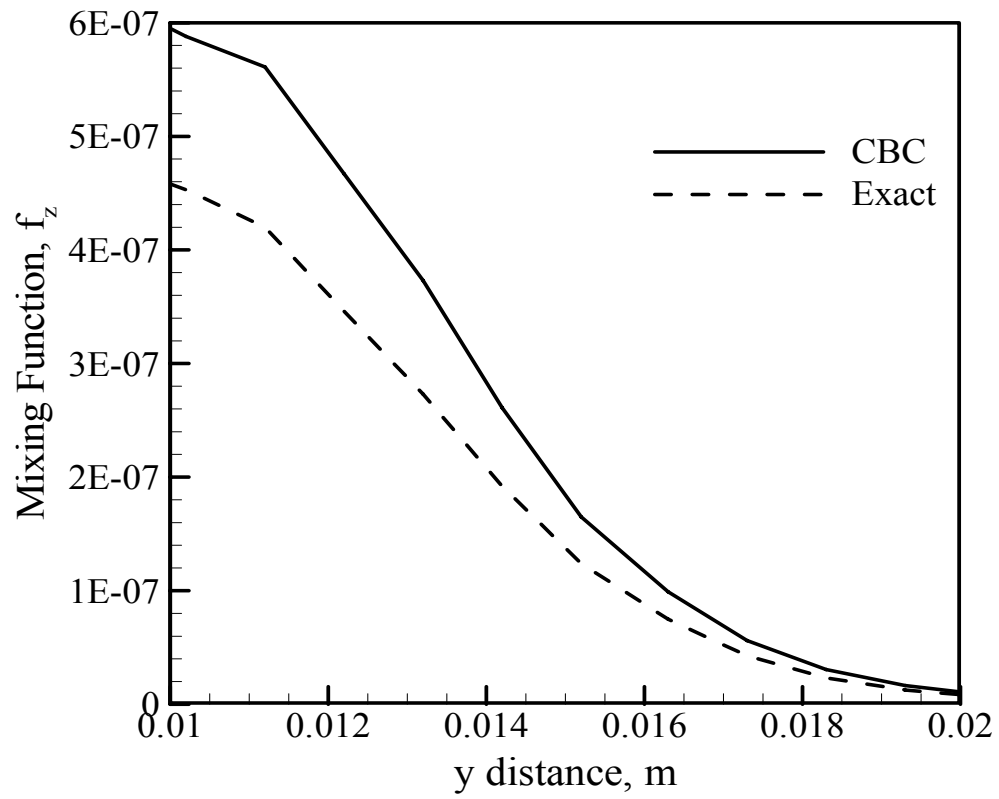


Figure 5.32. Exact Vs Inverted mixing function profiles-Case 2.

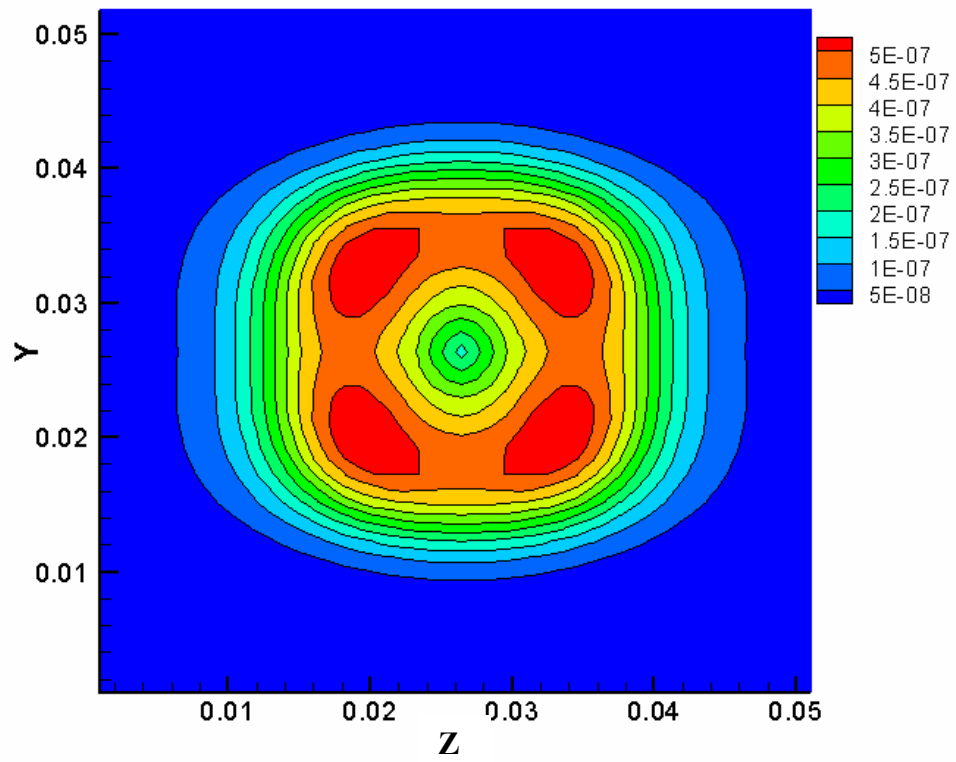


Figure 5.33. Contour plot of mixing function -Case 2.

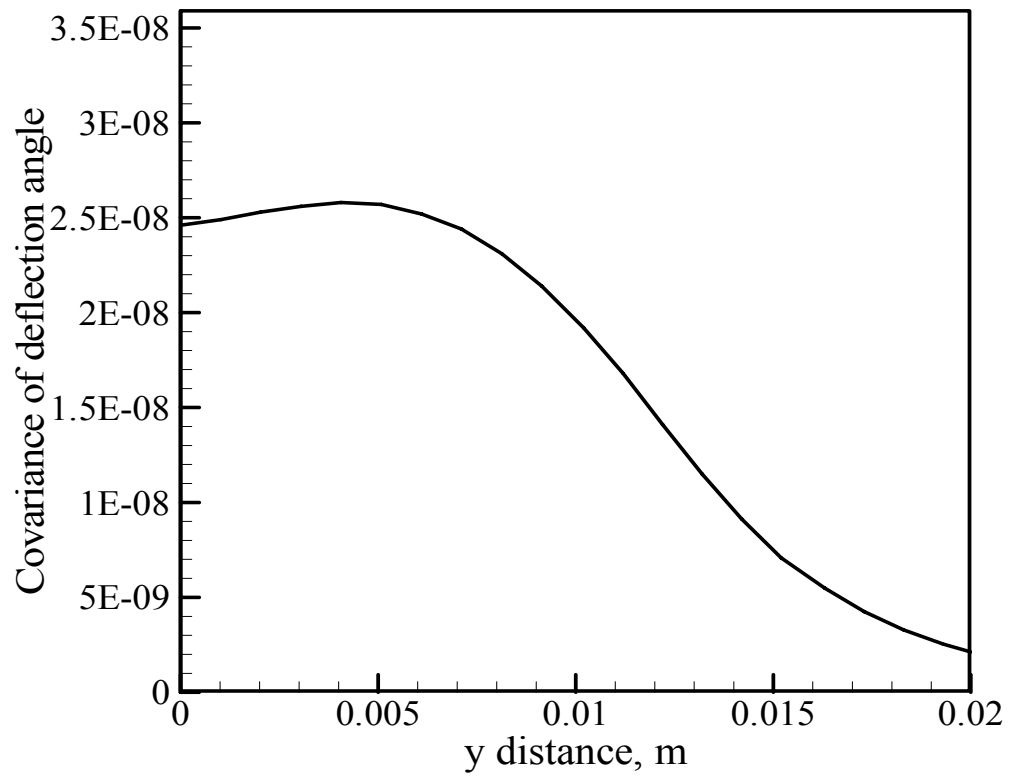


Figure 5.34. Profiles of deflection angle covariance -Case 2.

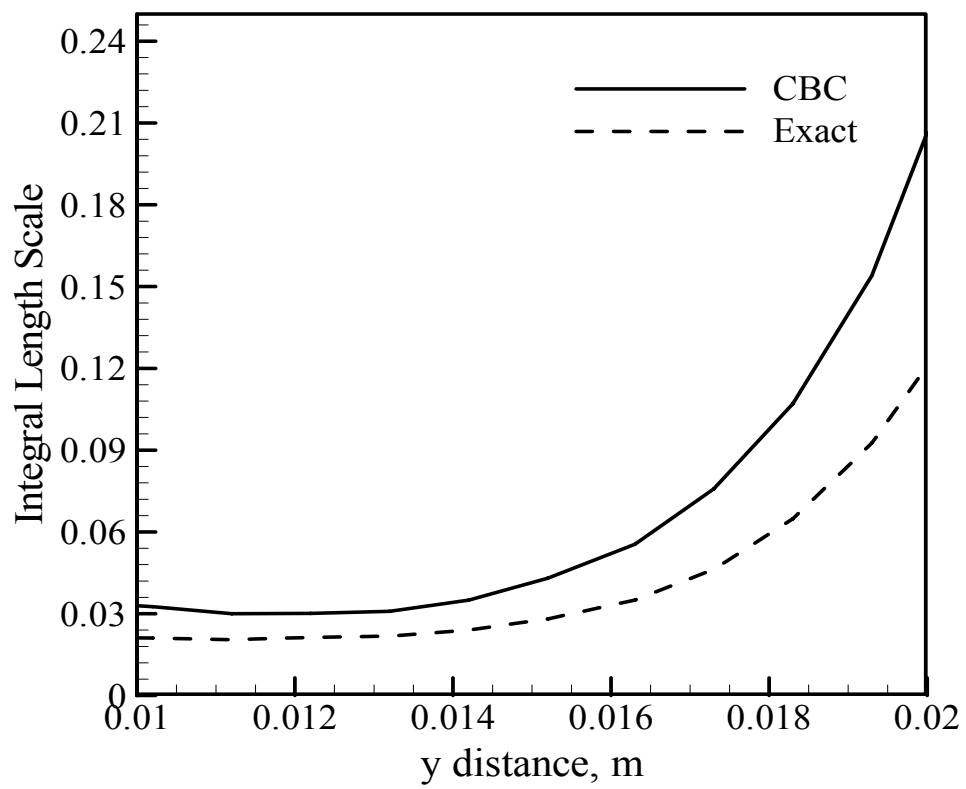


Figure 5.35. Exact Vs CBC based integral length scales-Case 2.

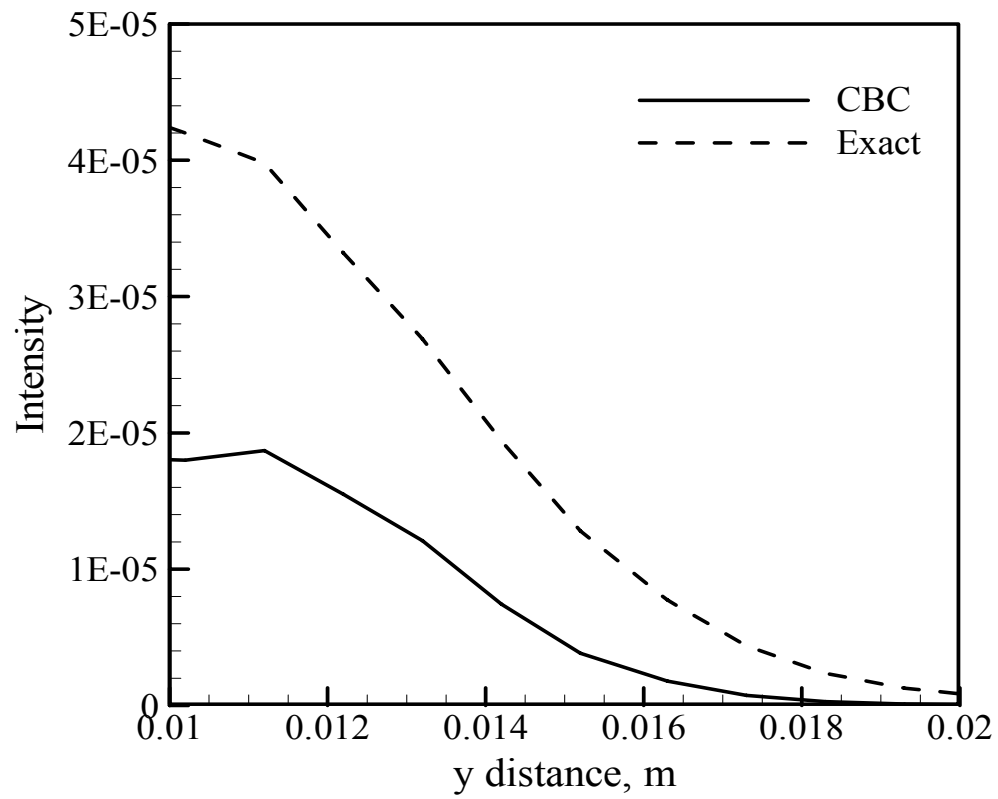


Figure 5.36. Exact Vs CBC based intensity profiles-Case 2.

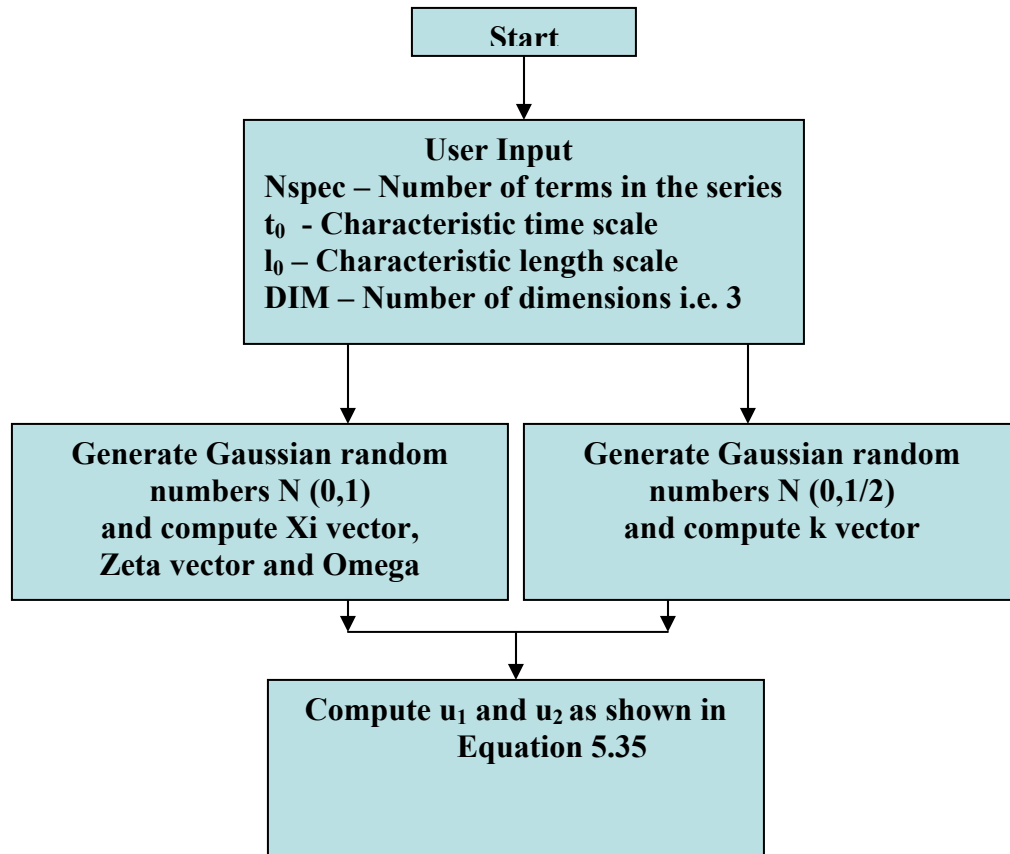


Figure 5.37. Flowchart illustrating the execution of the spectral generator (genspec).

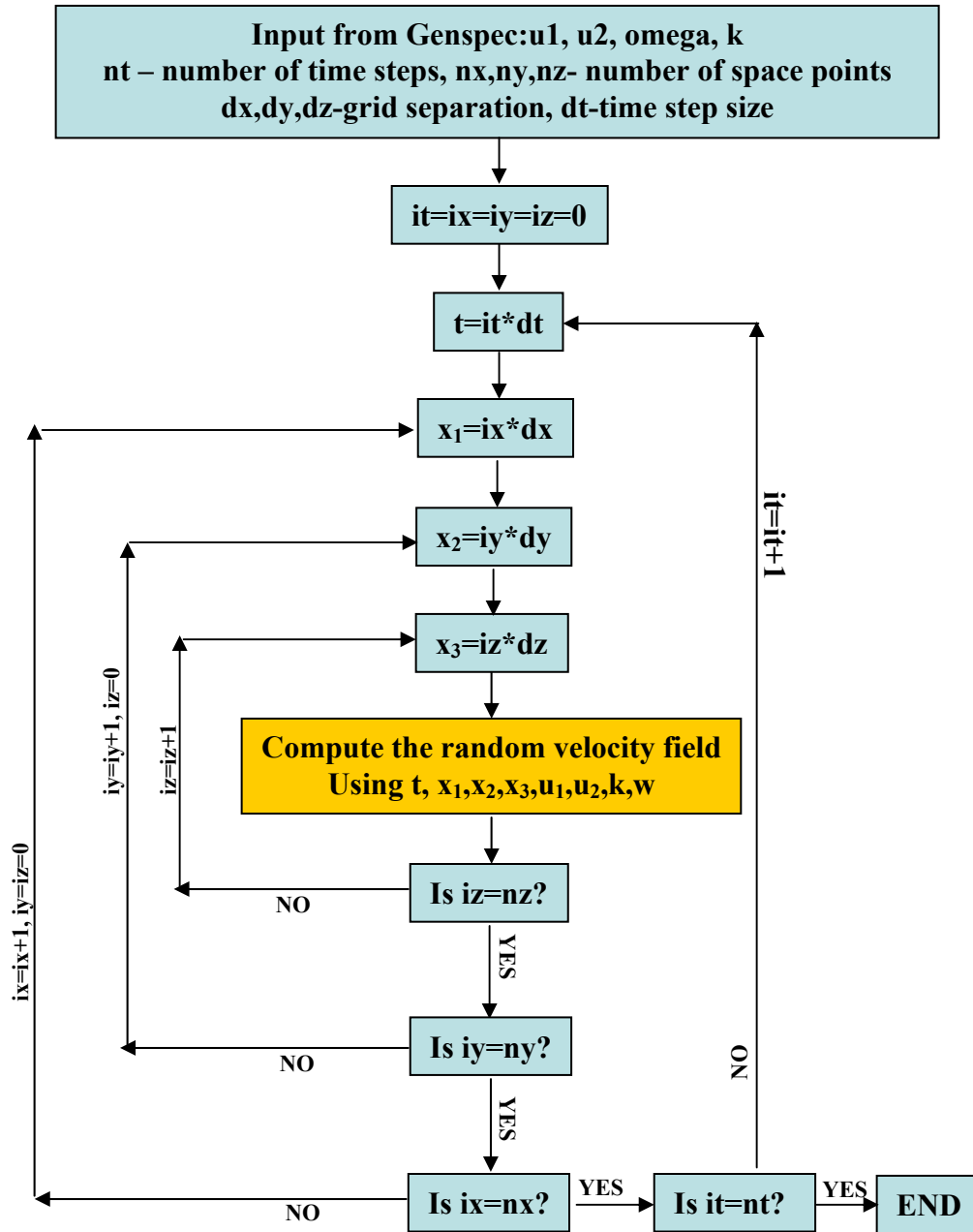


Figure 5.38. Flowchart illustrating the execution of the vector-field generator (genvec).

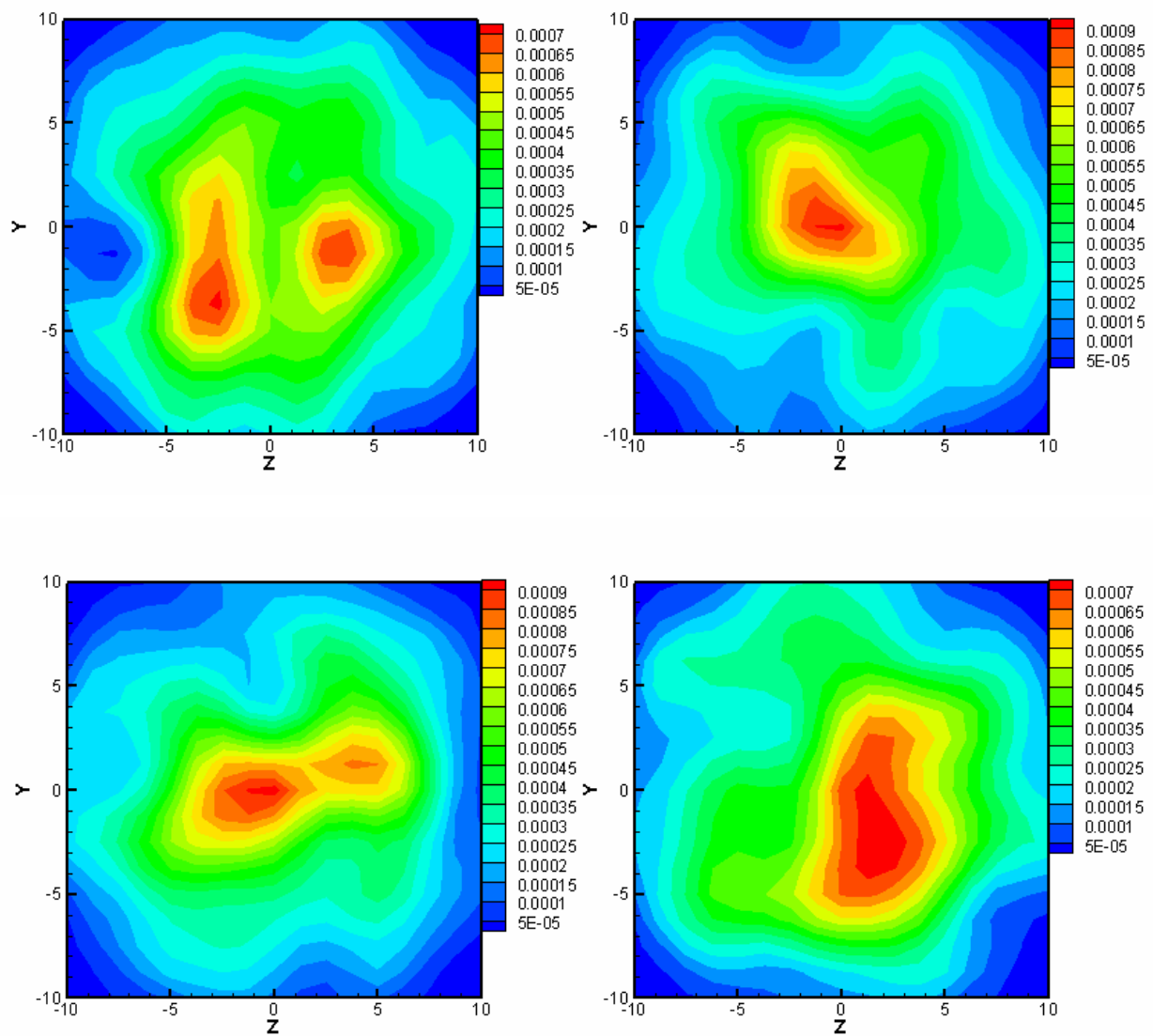
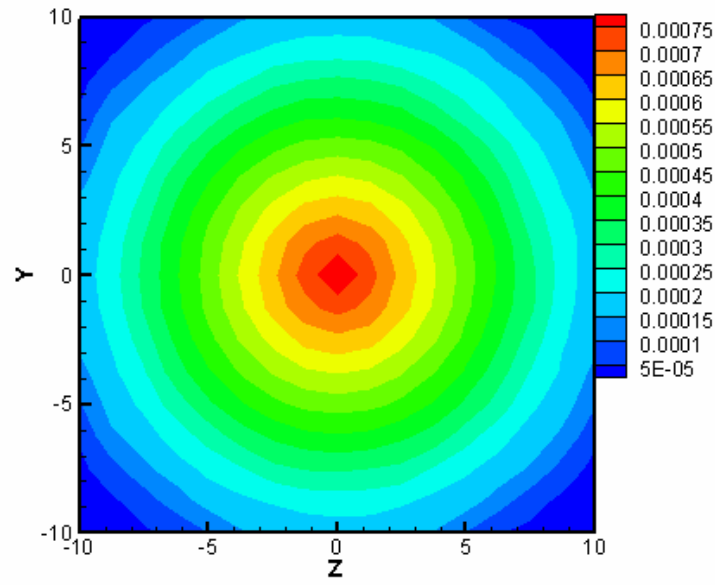
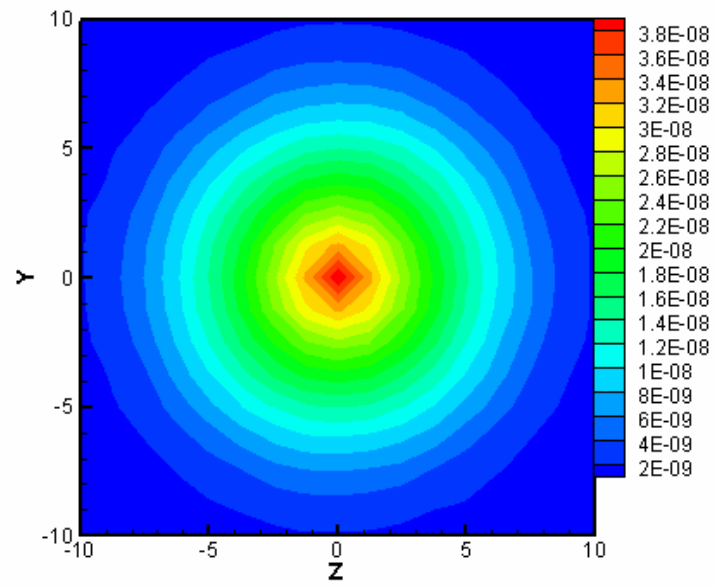


Figure 5.39. Instantaneous snapshots of turbulent refractive index gradient field generated from RFG code.



(a)



(b)

Figure 5.40. (a) Mean and (b) Variance of the turbulent refractive index gradient field generated from RFG code (sample size=100000 time steps).

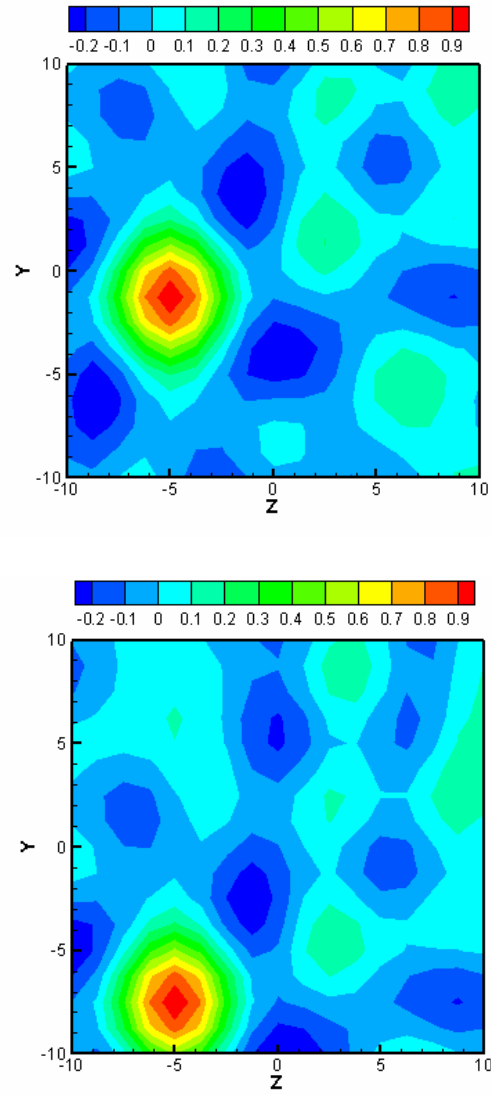


Figure 5.41. Instantaneous snapshots of two-point auto correlation coefficients

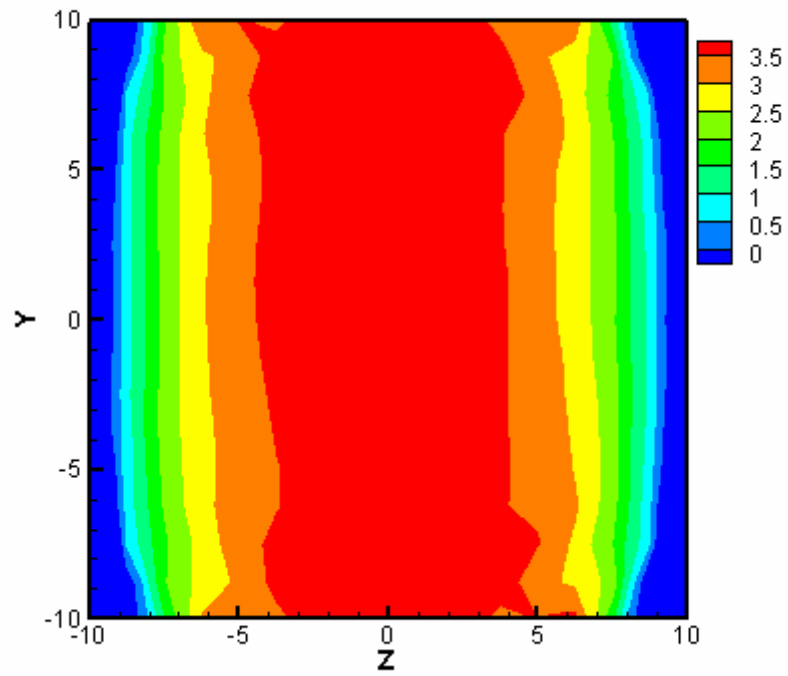


Fig. 5.42. Contour plot of integral length scale (l_z).

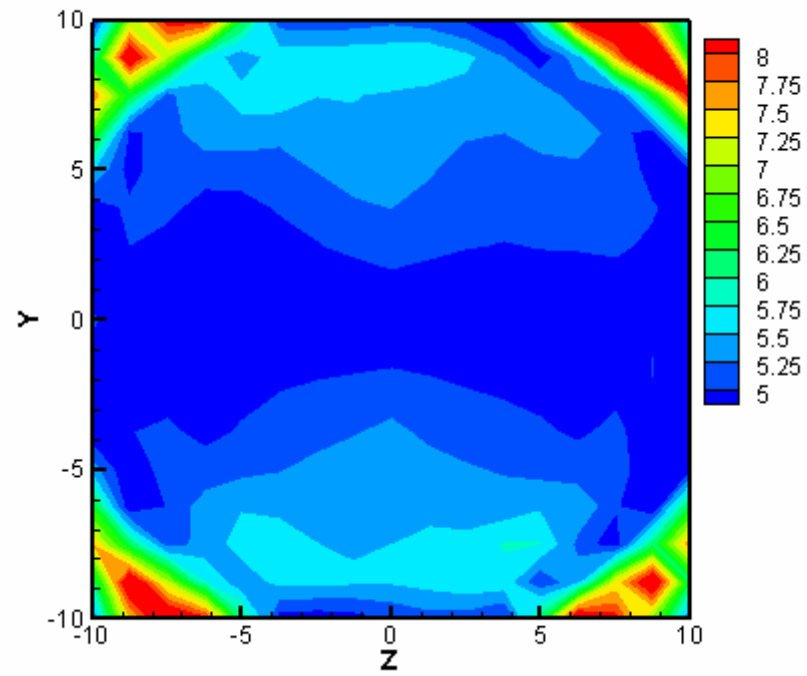


Fig. 5.43. Contour plot of integral length scale (l_y).

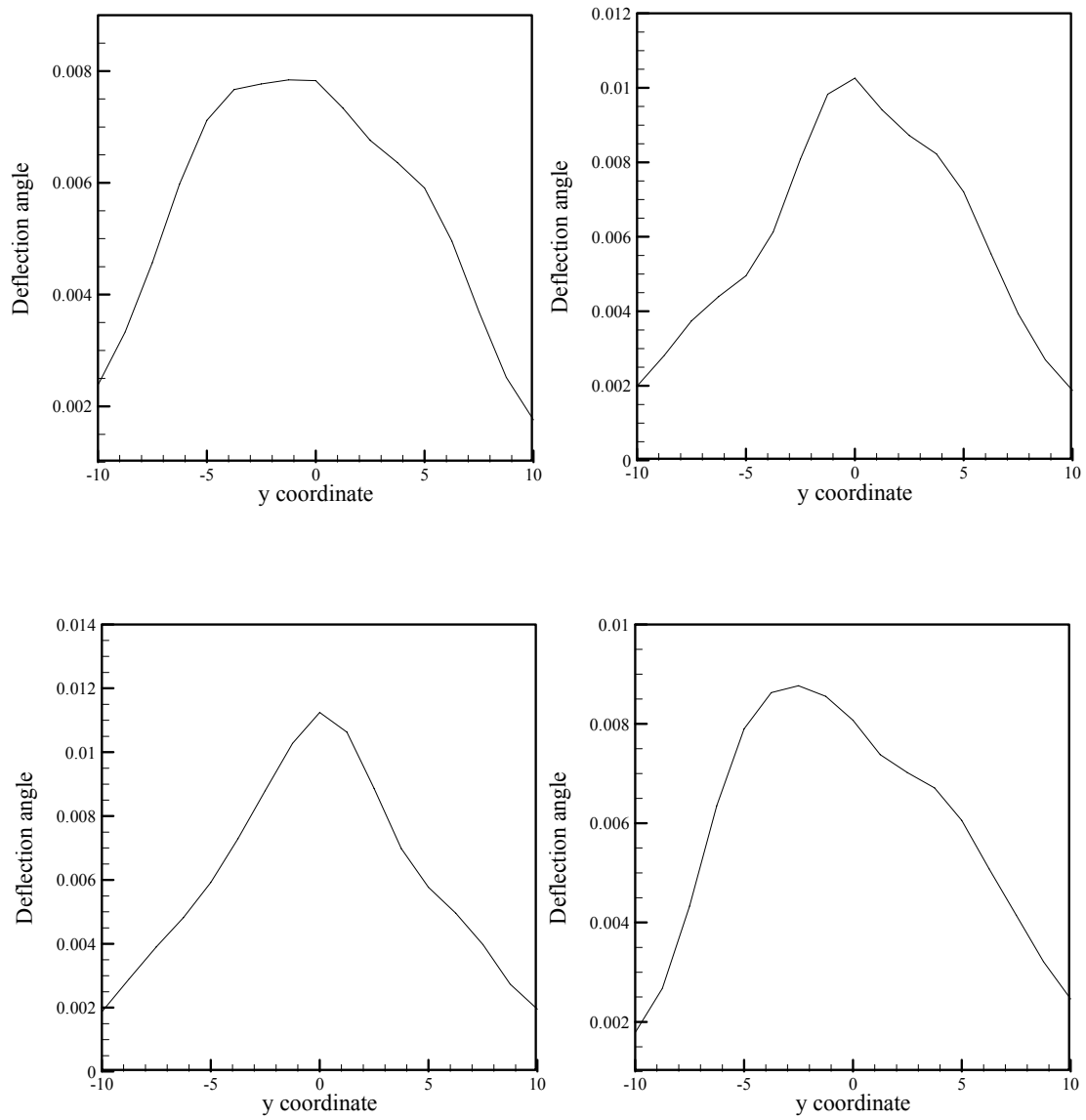


Figure 5.44. Instantaneous deflection angle profiles of the turbulent refractive index field computed along the z direction.

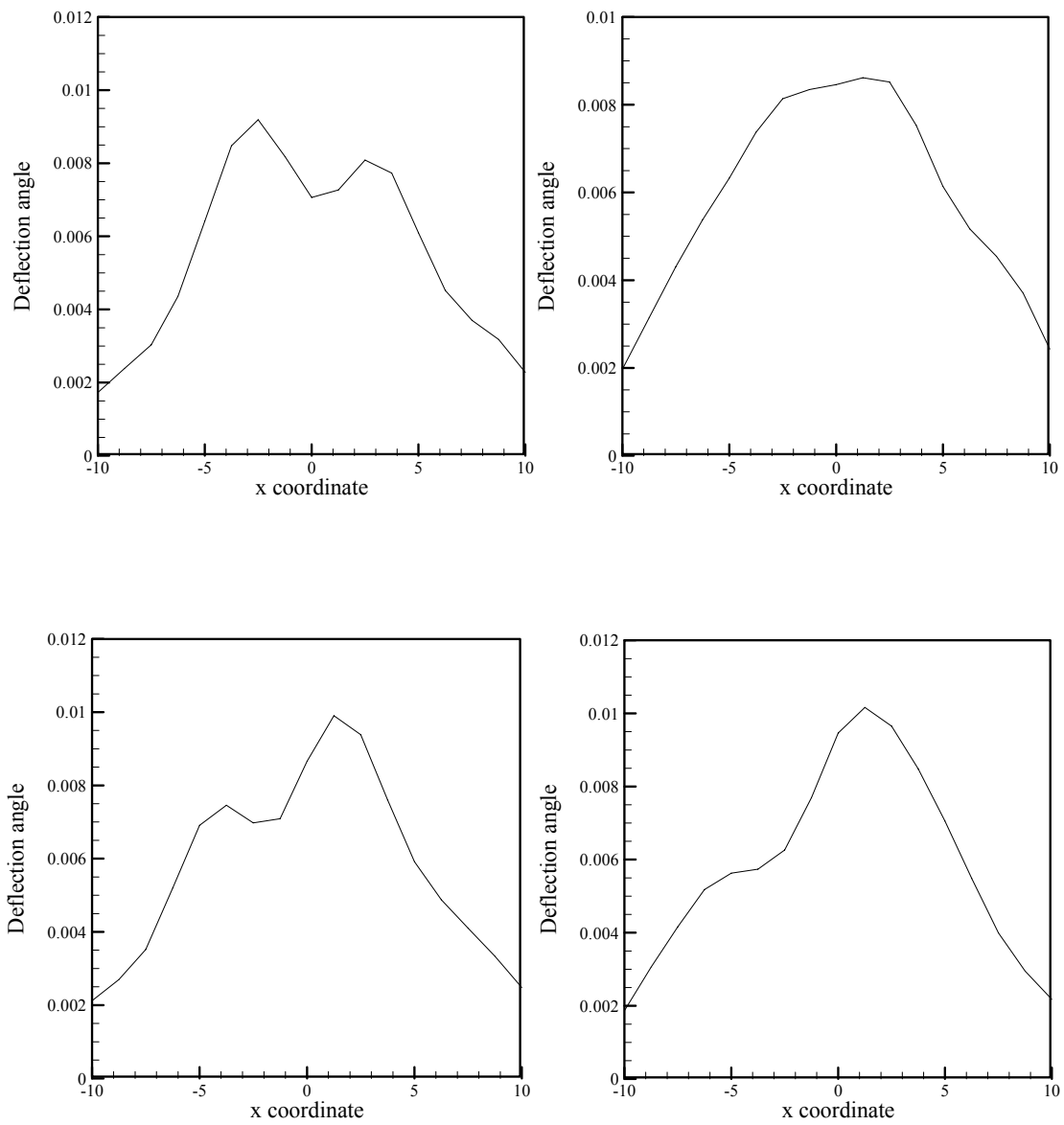


Figure 5.45. Instantaneous deflection angle profiles of the turbulent refractive index field computed along the y direction.

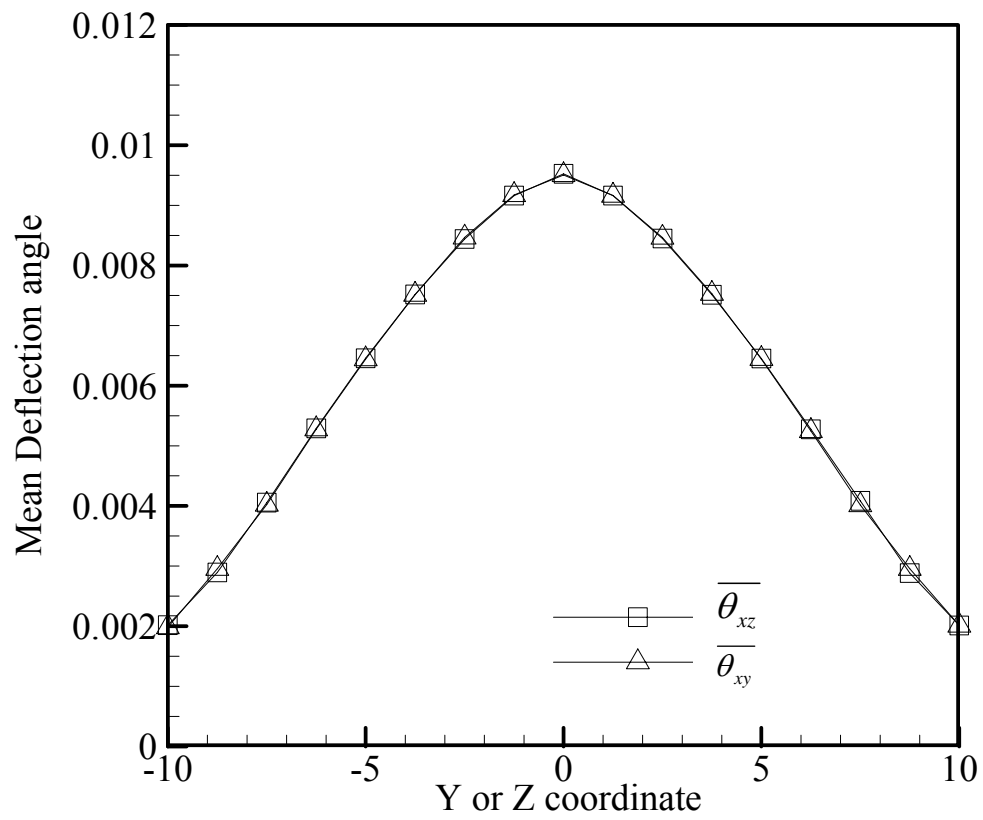


Figure 5.46. Mean deflection angle profiles in y and z directions.

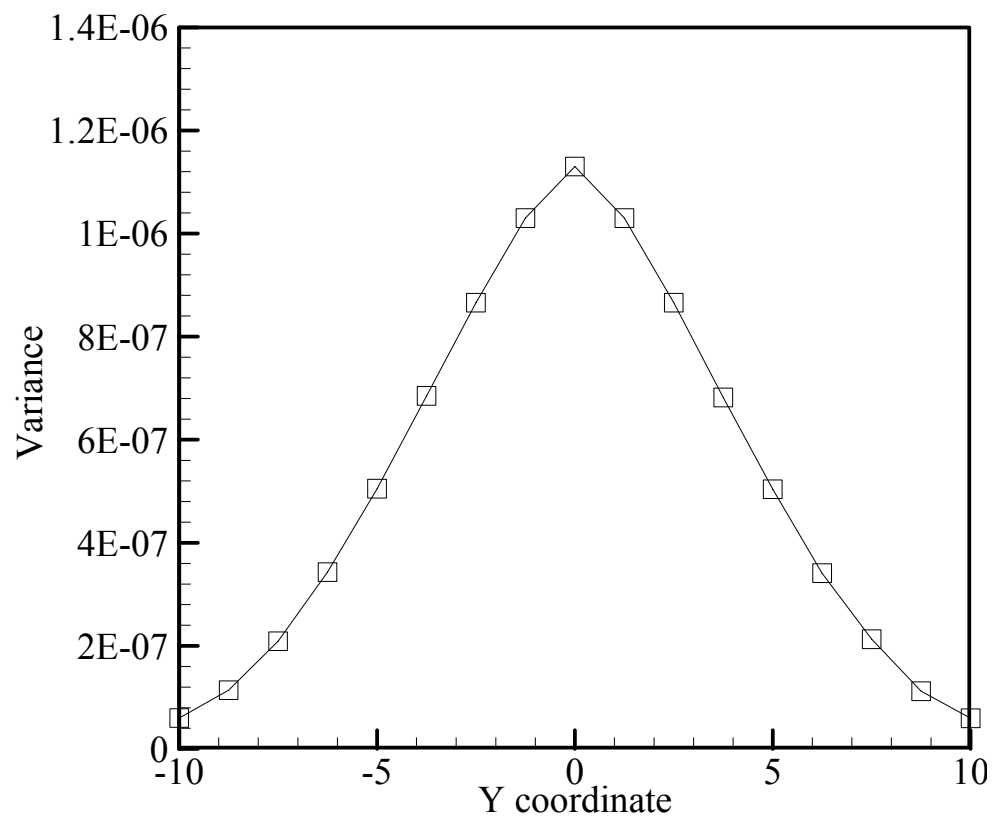


Fig. 5.47. Profile of deflection angle variance along the z direction.

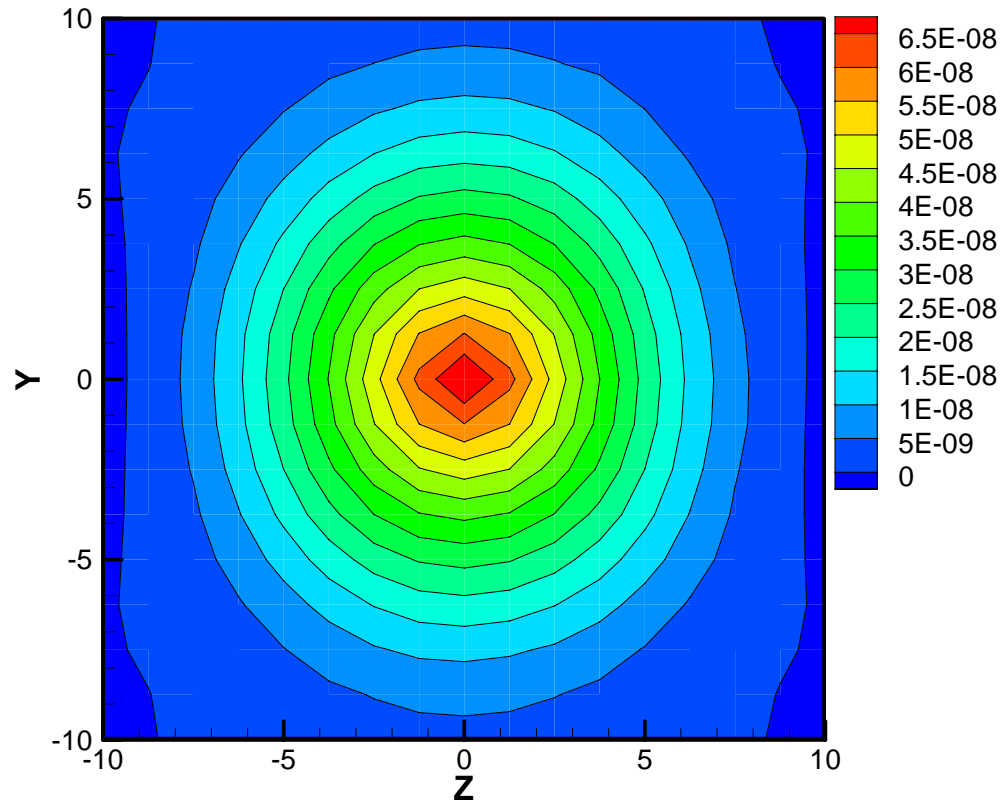


Fig. 5.48. Contour plot of z-direction mixing function (f_z) given in eq. 5.16.

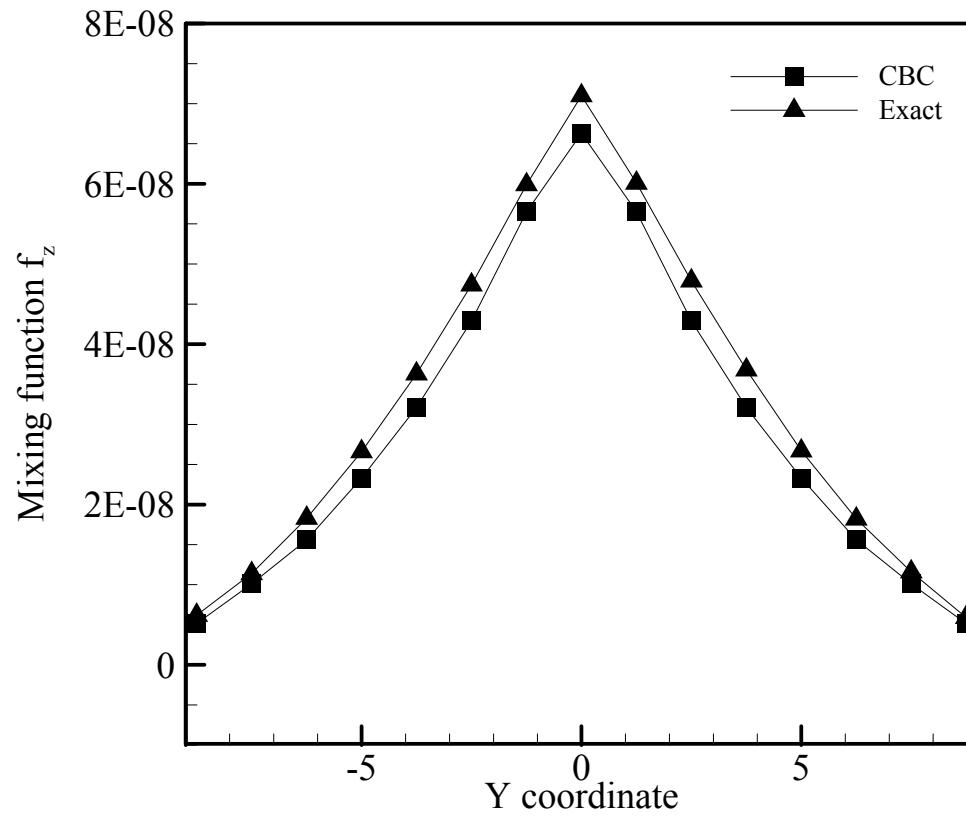


Fig. 5.49. Exact Vs CBC based z-direction mixing function (f_z) profiles.

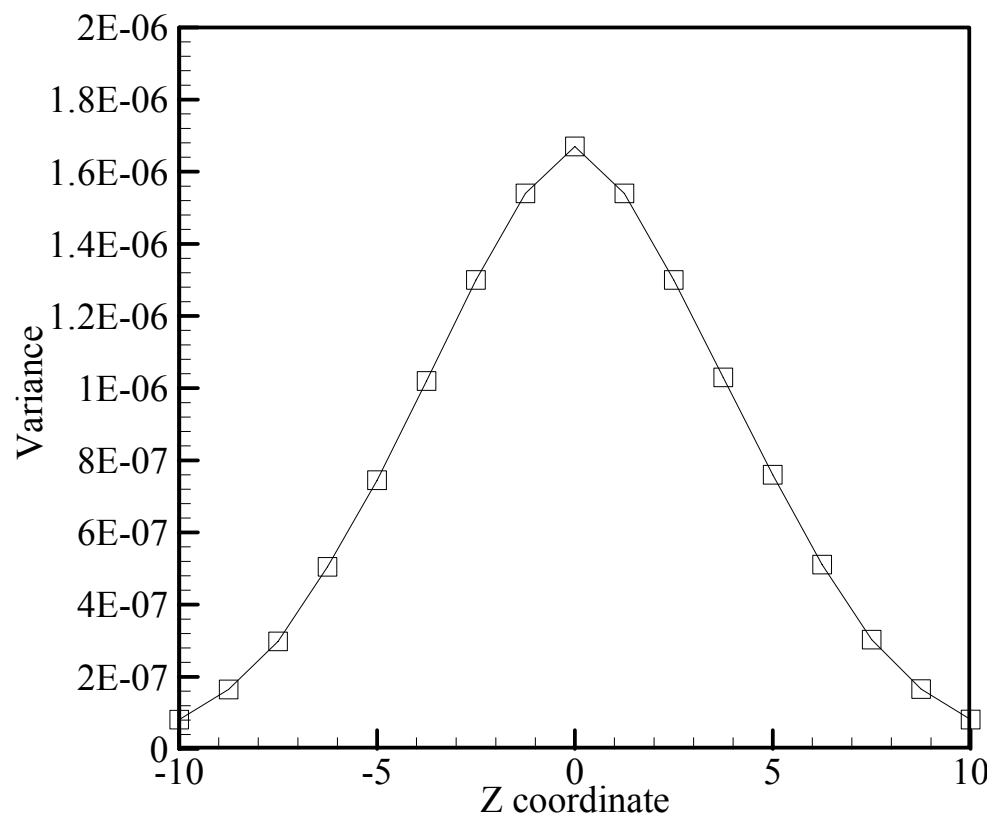


Fig. 5.50. Profile of deflection angle variance along the y direction.

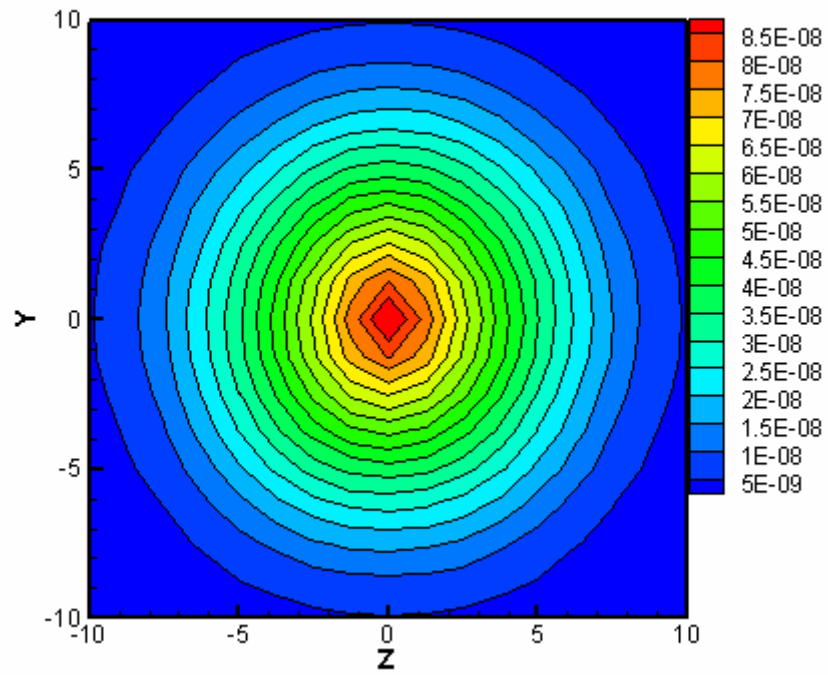


Fig. 5.51. Contour plot of y-direction mixing function (f_y) given in eq. 5.17.

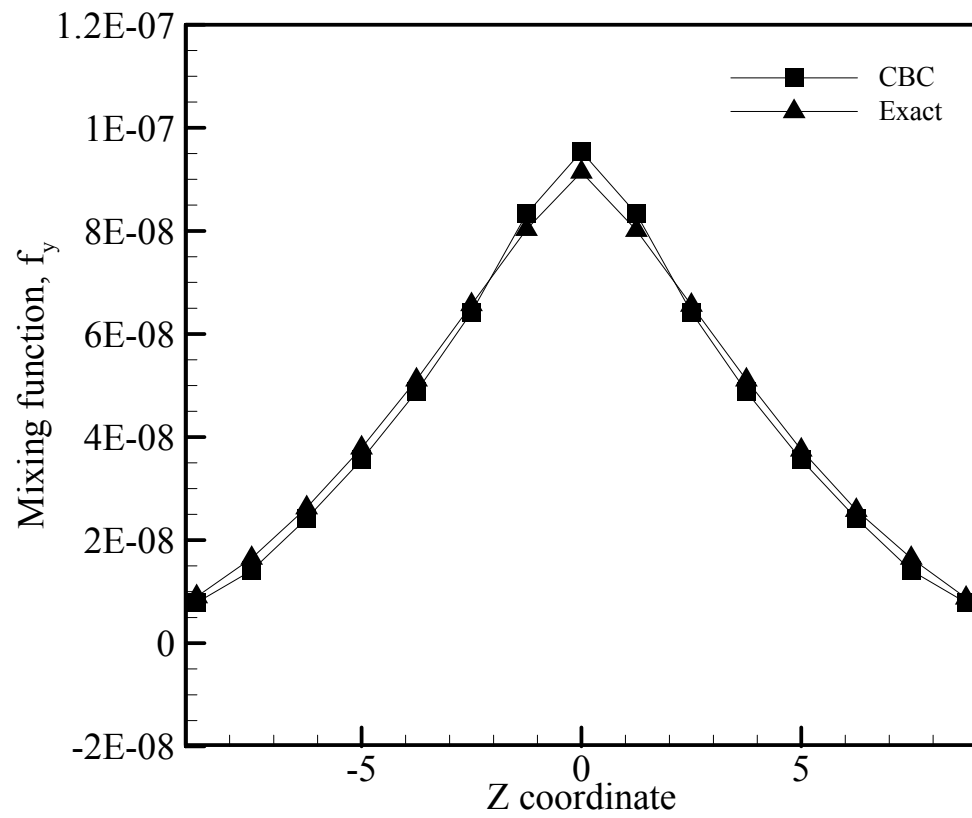


Fig. 5.52. Exact Vs CBC based mixing function (f_y) profiles.

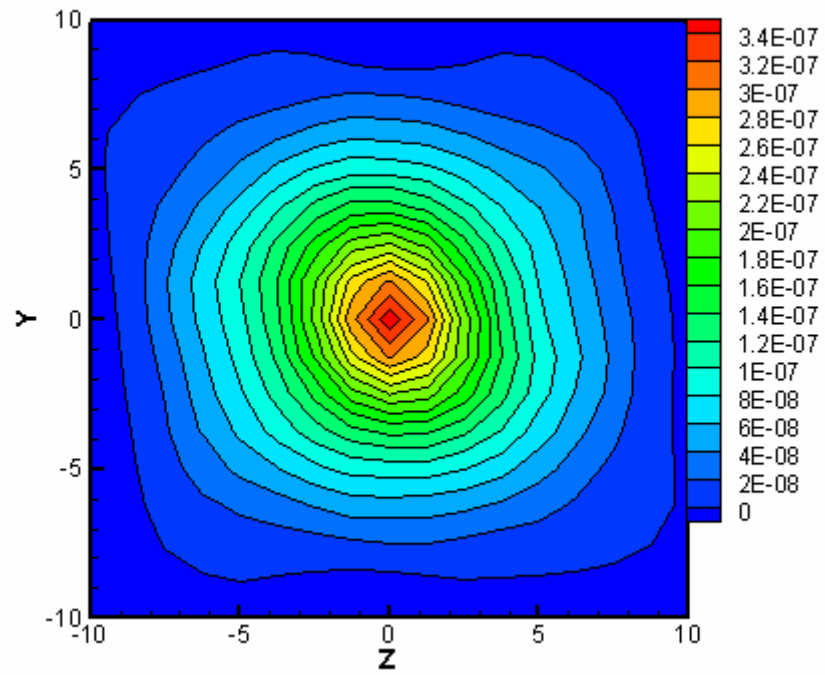


Fig. 5.53. Contour plot of crossed beam covariance of deflection angles.

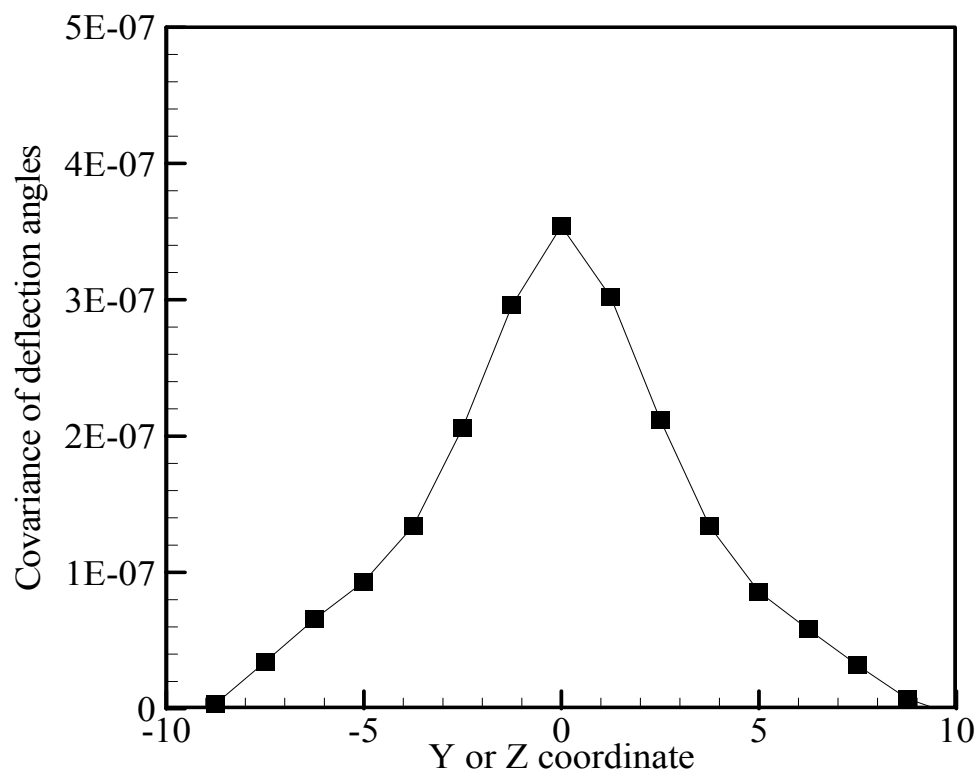


Fig. 5.54. Profile of the crossed beam covariance of deflection angles.

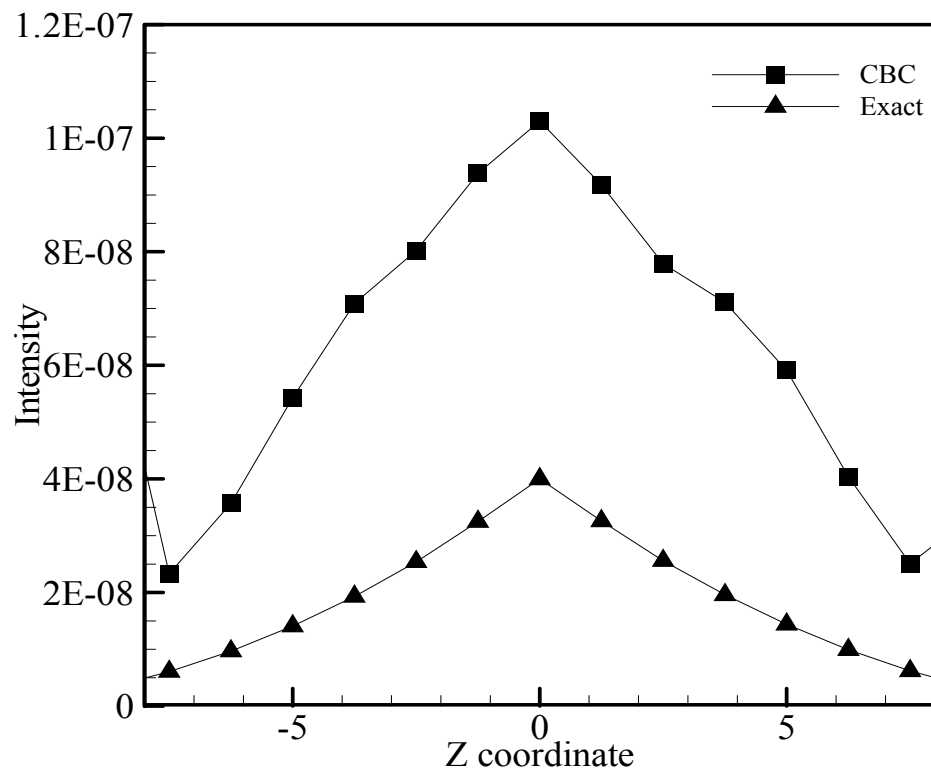


Fig. 5.55. Refractive index gradient intensity calculated using eqs. 5.27 & 5.28.

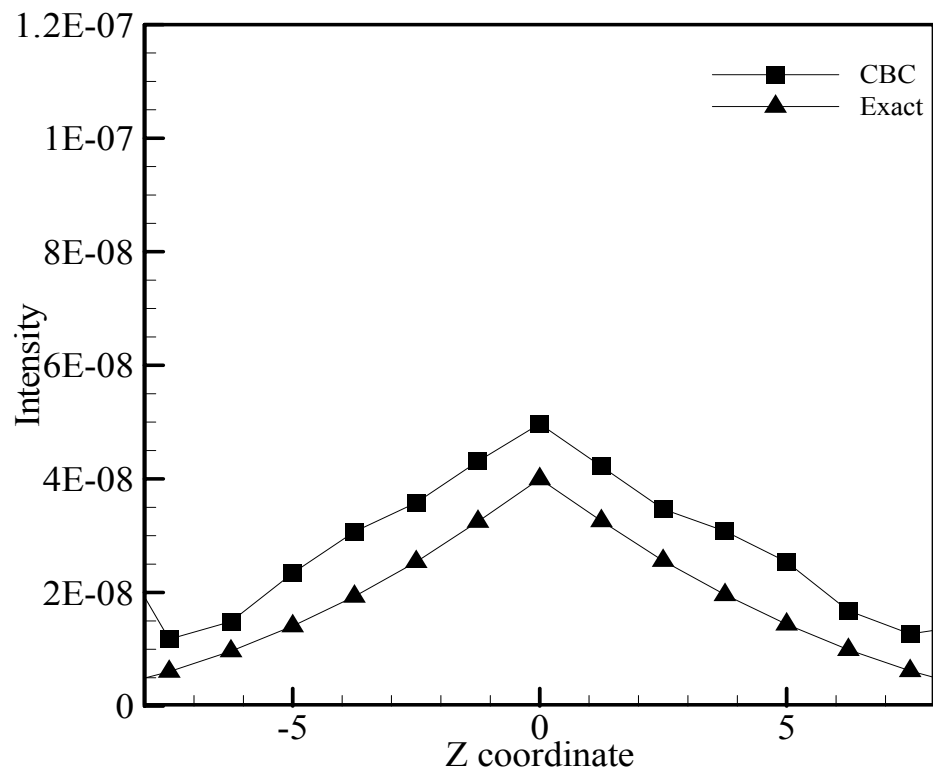


Fig. 5.56. Refractive index gradient intensity calculated using eqs. 5.29 & 5.30.

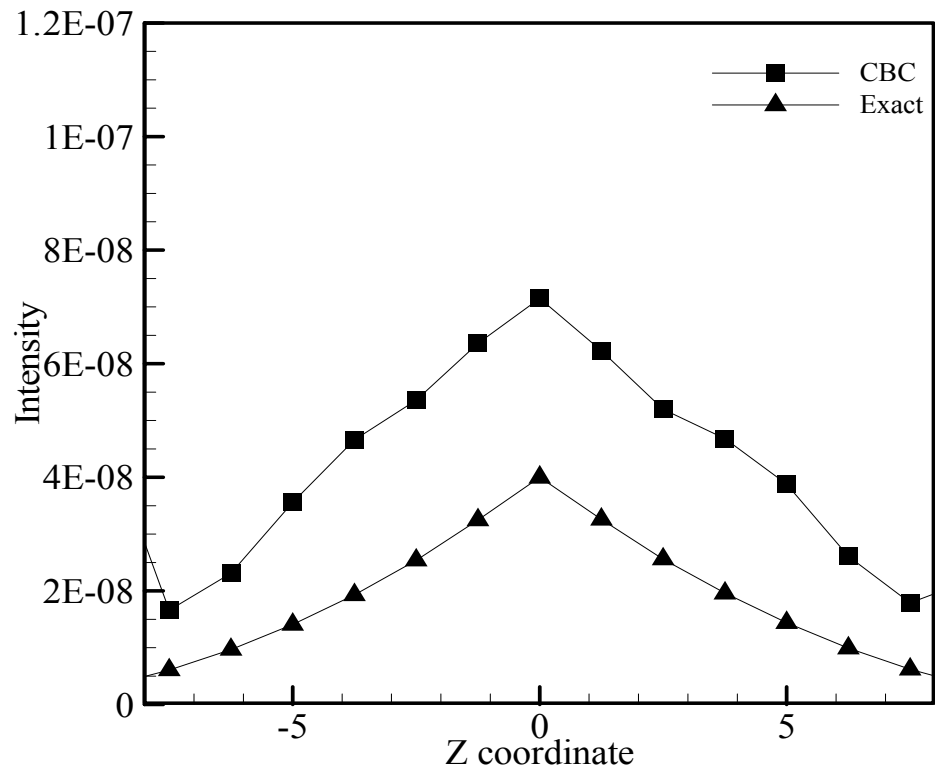


Fig. 5.57. Refractive index gradient intensity calculated using eqs. 5.31, 5.32 & 5.33.

CHAPTER 6. MINIATURE RAINBOW SCHLIEREN DEFLECTOMETRY SYSTEM

6.1 Overview of the Chapter

The study of turbulent jets/flames requires non-intrusive diagnostic systems with high spatial and temporal resolutions for resolving the fine scales of turbulence. In this chapter, literature review emphasizing the need for a miniature rainbow schlieren system to probe micro scale fluid flow phenomena is first presented. In the experimental section, the optical instrumentation, hardware improvements and analysis procedures are explained. The capability of the system is demonstrated by obtaining concentration measurements in a helium micro-jet and temperature and concentration measurements in a hydrogen jet diffusion flame from a micro-injector. Further, the flow field of under-expanded nitrogen jets is visualized to reveal details of the shock structures existing downstream of the jet exit.

6.2 Literature Review

Recent advances in the field of micro fluidics and turbulent transport have created the need for obtaining flow measurements at high spatial and temporal resolutions. For example, in a turbulent flow, the size of the smallest length and thickness of the boundary layer decreases as the Reynolds number is increased. Depending upon the Reynolds number, the smallest length scale can be on the order of few micrometers. Thus, measurements at high spatial and temporal

resolution (micron resolution) are desired to resolve such fine structures in the flow field.

The scientific community has also made remarkable progress in the area of micro-scale devices with applications ranging from bio-chemical analysis to propulsion and power generation. These micro-scale systems offer several advantages over their macro-scale counterparts including compact size, disposability, and improved functionality. In particular, microfluidics has emerged as an important area of research with interdisciplinary applications such as drug delivery, thermal management of Micro-Electro Mechanical Systems (or MEMS), micro propulsion and combustion, ink jet printing, etc.(Gad-el-Hak (1999), Gravesan (1993)). An understanding of the flow and heat transfer processes in these devices requires miniature diagnostics systems capable of measuring various flow properties with micron-scale spatial resolution. The diagnostic tools are needed to investigate the small-scale flow phenomena as well as to develop new theoretical and empirical models for related systems. The present study deals with the development and application of miniature rainbow schlieren apparatus to obtain quantitative scalar measurements in micro-scale flow systems.

The small size of micro-scale flow systems and fine scales of turbulence generally preclude the use of traditional intrusive probes for flow measurements of high spatio-temporal resolution. Hence, non-intrusive optical diagnostic

techniques are sought to resolve the flow characteristics of such flows. In the past few years, the development of micro-Particle Image Velocimetry (micro-PIV) has led to velocity measurements in micron-size channels. Santiago et al. (1998) used micro-PIV to measure the velocity field in the Hele-Shaw flow around a 30 μm elliptical cylinder. Meinhart and Zhang (2000) examined the flow in an inkjet printer cartridge using a micro-PIV system. Synnergren et al. (2002) employed digital speckle photography to measure the velocity field in a micron-size fiber network. In recent years, novel adaptations of the laser Doppler velocimetry technique (Buttner et al. (2005), Onofri (2006)) have also been developed for microfluidic applications

Although several techniques are available to measure the velocity field, the diagnostics of scalar fields (e.g., temperature and species concentration) in micro-scale flows has received little attention. Kihm (2003) reviewed flow visualization techniques for applications in microscale heat and mass transport measurements. Scroggs and Settles (1996) used a conventional knife-edge schlieren system to visualize the scalar flow structure in converging-diverging nozzles of diameter ranging from 600 to 1200 μm . Phalnikar et al. (2001) used a knife-edge schlieren system to visualize the shock cell structure in under-expanded nitrogen jets from tubes of inside diameter varying from 100 to 400 μm . Note that the knife-edge schlieren technique allows only the qualitative flow

visualization. Hence, quantitative details of the scalar flow field were not obtained in the above experiments.

In recent years, the quantitative Rainbow Schlieren Deflectometry (RSD) technique has been developed and applied to obtain temperature and species concentration measurements in several non-reacting and reacting flow configurations (Greenberg et al. 1995, Agrawal and co-workers (1998, 1999, 2003, 2006), Feikama (2006), Xiao et al. (2002), Ibaretta (2003)). In the RSD technique, the knife-edge filter in a schlieren system is replaced by a computer generated color filter to relate the angular ray deflection to color (or hue) in the rainbow schlieren image (Greenberg et al. 1995). The RSD technique has been used in non-reacting flows, for example, to measure species concentration in helium jets and temperature in a heated air jet. The RSD technique has also been used to measure the temperature and/or species concentration in diffusion flames partially premixed flames and premixed flames. The schlieren apparatus employed in these studies was macro-scale in size. For example, Albers and Agrawal (1999) used a lens-based system with 80 mm field-of-view to characterize the temperature field of a flickering gas-jet diffusion flame with spatial resolution of 140 μm and temporal resolution of 60 Hz.

Two obvious questions provided the motivation for the present study: (i) could a miniature RSD apparatus be developed using off-the-shelf optical hardware, and (ii) would the miniature RSD apparatus yield quantitative

measurements in non-reacting and reacting micro-scale flows? The results and discussion presented in this paper provide an affirmative answer to both of these questions. To the best of our knowledge, our lens-based system is the smallest schlieren apparatus reported in the literature. Through a careful selection of optical components and the rainbow filter, we were able to obtain quantitative measurements across the whole-field in non-reacting and reacting micro-scale flows at spatial resolution of 20 μm . Further, the shock flow structure of an under-expanded nitrogen jet was visualized at spatial resolution of 4 μm . The experimental details, results and discussion are provided in the following sections.

6.3 Experimental Details

The experiments to be detailed in this section were conducted at the flow diagnostics laboratory at the University of Alabama, Tuscaloosa. The miniature schlieren apparatus is the first of its kind although the optical configuration of the miniature schlieren apparatus is similar to that of macro-scale systems. However, its development required a careful evaluation of each optical component. In this section, details of the experimental system and associated optical hardware followed by descriptions of the test media and analysis procedures are presented.

6.3.1 Experimental System

Figure 6.1 shows photograph of the experimental system, wherein the major optical components are also identified. Broadband light from a 150 W halogen light source (Fig.6.2) is transmitted by a 600 μm fiber optics cable to a 5

μm wide, 3 mm high source aperture. The source aperture is placed at the focal point of an achromatic lens of 10 mm diameter and 40 mm focal length (f_1). The collimated light rays pass through the test medium and deflected rays are decollimated by a 10 mm diameter lens of 100 mm focal length (f_2). The image of the source aperture displaced by the test medium is formed at the focal point of the decollimating lens, wherein a rainbow filter is placed. The filtered image is acquired by a CCD array together with a camera lens and extension tubes.

6.3.2 Optical Hardware

In the previous section, a brief overview of the experimental setup based on the macro-scale rainbow schlieren systems was presented. However, miniaturization of the optical hardware presented unique challenges, which required special considerations to minimize the measurement errors. In the following section, the key issues associated with each optical component are identified, and then alternatives are recommended to minimize the optical errors in future designs. Figure 6.3 shows an optical layout of the rail-mounted miniature schlieren apparatus.

6.3.2.1 Light Source, Fiber Optics Cable and Source Aperture

The light source and the fiber optics system used in this study are identical to those in the macro-scale schlieren apparatus. The light source consists of a 150-watt halogen lamp with a focusing optics assembly to focus light onto the upstream end of a multimode fiber of 600 μm diameter. Light rays following

different paths inside a multimode fiber result in concentric bands of low and high intensity at the downstream terminal of the fiber. A single mode fiber could provide more uniform light distribution, although the small core diameter of these fibers reduces the light throughput to adversely affect the exposure time (or temporal resolution) of the CCD array. In this study, a 5 μm wide source aperture (the smallest width available commercially) was used. In contrast, the macro-scale systems typically use 50 to 200 μm wide source aperture. In general, a source aperture of smaller width improves the measurement resolution and sensitivity. However, the light throughput also decreases by decreasing the aperture width. Nevertheless, the source aperture used in this study allowed acquisition of schlieren images at exposure time down to 10 μs . The small width of the source aperture compared to the fiber diameter also alleviated the problem of non-uniform light distribution at the fiber terminal. The source aperture was positioned directly in front of the bright region of the optical fiber terminating with an SMA connector. A customized holder was fabricated in-house to ensure precise positioning of the optical fiber with respect to the source aperture. A separation distance of 2 to 3 mm was maintained between the fiber terminal and source aperture.

6.3.2.2 Collimating and Decollimating Lenses

Chromatic aberration is the most serious concern in the lens-based rainbow schlieren apparatus. Thus, achromatic lenses are necessary for

collimation and decollimation to perform quantitative analysis of the rainbow schlieren images. Accurate alignment of lenses is another key requirement. Initially, we used 6 mm diameter lenses with self-adjusting lens holders. However, the vertical and horizontal alignment of lenses with this type of holders proved to be extremely cumbersome. Thus, we switched to the smallest off-the-shelf fixed lens holder of 10 mm diameter. The lens in the fixed lens holder is held by a set of circular rings, which limited the field-of-view to 7 mm.

The focal length of the collimating lens ($f_1 = 40$ mm) was chosen to maximize the collection of the light from the source aperture and also to minimize the total length of the system. The light rays deflected by the test medium are focused at the focal point of the decollimating lens or the filter plane. A key parameter affecting the measurement accuracy is the transverse ray displacement at the filter plane give as:

$$d(y) = f_2 \varepsilon(t) \quad (6.1)$$

where $\varepsilon(t)$ is the angular ray deflection at the projected location 't'. A large value of f_2 increases the transverse ray displacement and hence, improves the measurement accuracy. Initially, we employed a lens combination using off-the-shelf achromatic lenses to obtain f_2 exceeding 300 mm. However, the minor chromatic aberrations were magnified by the lens combination, and hence, the rainbow schlieren images were not amenable to quantitative analysis. Finally, an achromatic lens of the largest available focal length of 100 mm was used for

decollimation. Note that the image of the source aperture at the filter plane is magnified by a factor of 2.5, i.e., the ratio of the focal lengths of the decollimating and collimating lenses (f_2/f_1).

6.3.2.3 Rainbow Filter

The transverse ray displacement at the filter plane depends upon the angular ray deflection (see Eq. 6.1), which is proportional to the density gradient integrated over the path length of the test medium. The smaller path length of the micro-scale test medium decreases the angular ray deflection. The transverse ray displacement is further constrained by the small f_2 of the miniature schlieren apparatus. Accordingly, severe restrictions are placed on the maximum usable width of the rainbow filter. After several trials, a 0.5 mm wide symmetric filter with hue varying from 70-350 degrees was used, compared to the 2-3 mm wide filters used in macro-scale systems. The rainbow filter is a 35 mm slide printed with spatial resolution of 115 pixels per mm (Figure 6.4). Thus, the 0.5 mm wide color band provides nearly 60 distinct colors (or hues) in the filter plane. Figure 6.5 shows the filter calibration curve obtained by traversing the filter without the test media, in steps of 0.01 mm, and recording the corresponding background schlieren image. The average calibration curve in Fig. 6.5 represents the average hue in the background schlieren image, which differs from calibration curves for the individual pixel locations. As discussed in section 6.3, the calibration curves for each pixel location were used in this study to post-process the schlieren

images. For helium jet, owing to the very small angular ray deflections, only one side of the symmetric filter was utilized. However, both sides of the filter were used for hydrogen jet diffusion flame and under-expanded nitrogen jet.

6.3.2.4 Camera System

The filtered image of the test section was acquired by a CCD array with a lens. Achieving high spatial resolution together with good quality schlieren images required a detailed evaluation of the camera system. We used a 50 mm camera lens for helium jet and hydrogen flame and a 100 mm lens for the nitrogen jet experiments. However, the minimum working distance of the lens exceeded the small optical length of the system. Thus, a set of extension tubes was placed in between the CCD array and camera lens to decrease the minimum working distance. The extension tubes magnified the image as illustrated in Fig. 6.6. Thus, the field-of-view and hence, the spatial resolution in the schlieren image were determined by the length of the extension tubes and focal length of the camera lens. The camera shutter was controlled electronically to yield the exposure times down to 10 μ s.

6.3.3 Test Media

The miniature schlieren system was used with the following micro-scale flows: helium jet in air, hydrogen jet diffusion flame, and under-expanded nitrogen jet. Commercially available hypodermic tubes of stainless steel with inside diameter (d) ranging from 100 to 1500 μ m were used. Similar to Phalnikar

et al. (2001), injectors were fabricated by starting out with larger diameter tubing and then concentrically inserting smaller straight sections of hypodermic tubing until the tube diameter of the desired size was obtained. The junctions of different size tubes were made leak proof by a careful process of soldering and then applying high-strength glue. This procedure proved unsuccessful for the 50 μm diameter tube because of the difficulty in cutting and holding the tiny tube without creating dents or bends. Thus, experiments with 50 μm injector were conducted using an O'Keefe micro-orifice. Figure 6.7 shows a photograph of different size injectors used for the experiments together with the lens and fixed lens holder.

Injectors for helium jet and hydrogen flame experiments were mounted vertically upwards through a plenum and hence, the schlieren system sensed density gradients in the transverse direction. The injector for the nitrogen jet experiments was oriented horizontally to visualize the density gradients in the streamwise direction. The gas flow was supplied from compressed gas cylinder fitted with pressure regulator and a control valve to regulate the mass flow rate measured by a mass flow meter.

6.3.4 Analysis Procedure

In a rainbow schlieren image, the color represented by hue according to the HSV (Hue-Saturation-Value) model relates to the transverse (or axial) ray displacement at the filter plane according to the filter calibrating curve. As

discussed previously, the filter calibration curve is obtained by traversing the filter without the test media and then measuring the hue in the background schlieren image taken at each traverse location. However, inaccuracies in printing a small width filter with large hue gradients, minor optical misalignments and chromatic aberrations produce a background schlieren image with non-uniform hue distribution, as depicted by error bars of standard deviation of hue for the average hue curve in Fig. 6.5. To minimize the associated errors, filter calibration curves were obtained for each pixel location in the background schlieren image; two such calibration curves are shown in Fig. 6.5. The analysis begins by converting the hue measured at a pixel location in the schlieren image to transverse ray displacement using the filter calibration curve at that particular pixel location. The remaining analysis is identical to that used in previous studies i.e., the angular ray deflection is found from Eq. 6.1 and then, the refractive index difference field is computed by Abel inversion. Finally, the refractive index difference is related to the species concentration and/or temperature using the ideal gas law and appropriate state relationships.

6.4 Results and Discussion

A series of experiments were conducted with helium jets (non-reacting) and hydrogen jet diffusion flames (reacting) to obtain quantitative data across the whole field. Experiments were also conducted to visualize the scalar flow structure of an under-expanded nitrogen jet.

6.4.1 Helium Jet

Figure 6.8 shows a color schlieren image of the helium jet for $d = 650 \mu\text{m}$ and jet Reynolds number, $Re = 375$. The image depicts the near field laminar region at spatial resolution of $20 \mu\text{m}$. The tube exit and the outer surface are visible as black regions in the image. Figure 6.8 clearly shows color gradations in the shear layer region ($r/d = 0.5$) with large density gradients. In the center region of the jet, the density gradients are small and hence, the color matches that in the background. Interestingly, the schlieren image of the micro-scale helium jet is similar to that of the macro-scale helium jet obtained by Al-Ammar et al. (1998). Figure 6.9 shows hue contours on one side of the jet, wherein the axial and radial coordinates are normalized by the tube inside diameter. The contour plot reveals hue varying from 140 to 180 degrees corresponding to the latter half of the filter calibration curve in Fig. 6.5. The range of hue in Fig 6.9 pertains to the maximum transverse ray displacement of about 0.05 mm in the helium jet.

Figure 6.10 shows the radial profiles of helium mole percentage at three axial locations. Results depict significant mixing of helium with air, which is consistent with measurements in macro-scale flows (Al-Ammar et al. 1998). The profiles clearly show increased diffusion of the jet flow in the downstream direction. Towards the jet center, the density gradients are small and the measurement errors increase exponentially by the Abel inversion process. Hence, the present measurements are considered inaccurate for $r/d < 0.2$. Figure 6.11

shows the contour plot of helium mole percentage across the whole field. The waviness in the contours is reminiscent of the buoyancy-induced flow oscillations observed in macro-scales systems (Pasumarthi and Agrawal 2003). Results show that the miniature schlieren system is capable of providing quantitative measurements at high spatial resolution. Furthermore, the structural features of the flow field are similar in both macro-scale and micro-scale helium jets.

6.4.2 Hydrogen Jet Diffusion Flame

Figure 6.12 shows the rainbow schlieren image of a hydrogen jet diffusion flame at spatial resolution of $20\text{ }\mu\text{m}$ for $d = 50\text{ }\mu\text{m}$, $Re = 410$. The schlieren image depicts an axisymmetric laminar flame in the near field. Figure 6.13 shows the corresponding hue contours with hue varying from 60 to 110 degrees. According to the filter calibration curve, this hue range signifies a maximum transverse ray displacement of about 0.05 mm . Figures 6.14 and 6.15 show, respectively, the radial profiles of temperature and oxygen concentration at three axial locations. In these figures, the radial location with the peak temperature or zero oxygen concentration pertains to the flame boundary, located between $12 < r/d < 18$. The peak temperature of about 2400 K and the trend of the radial profiles matches with similar measurements taken in macro-scale hydrogen jet diffusion flames (Albers and Agrawal 1999, Wong and Agrawal 2006). Figures 6.16 and 6.17 show the contour plots of temperature and oxygen concentration across the whole field. Only one side of the flame is shown and the coordinate

dimensions are normalized by the injector inside diameter. Figure 6.16 depicts an increase in radial gradients towards the flame surface. The curvature of the contours reveals large axial gradients near the injector exit that decrease in the axial direction. Overall, these results are similar to those obtained in macro-scale systems (Albers and Agrawal (1999), Wong and Agrawal (2006)).

6.4.3 Under-Expanded Nitrogen Jet

Figures 6.18-19 show color schlieren images of under-expanded nitrogen jet from injectors with $d = 650 \mu\text{m}$ and $300 \mu\text{m}$ at different supply pressures. The spatial resolution in the image is $4 \mu\text{m}$. The formation of shock diamonds at supply pressure of 60 psi is depicted in Fig. 6.18. The schlieren image shows color gradations caused by density gradients in the shock cells. The shock cell diamonds in the image represent the characteristic features of an under expanded jet. Interestingly, the overall shock flow structure is similar to that observed in macro-scale jets. The supply pressure was varied between 300 psi and 450 psi for both injectors to obtain the near-field flow structure depicted in Fig. 6.19.

Images show expansion and compression fans, free jet boundary, oblique shock waves and mach disks. The shock cell spacing, the formation and length of the mach disk, supersonic core length and angle of the oblique shock waves were affected by the supply pressure. Although the flow characteristics of under-expanded jets have been documented at different scales (Phalnikar et al. 2001), the color schlieren images at such a high spatial resolution have not been

presented before. Together with appropriate state relationships, one could obtain density, temperature, and/or pressure fields from the refractive index difference field determined by the rainbow schlieren technique.

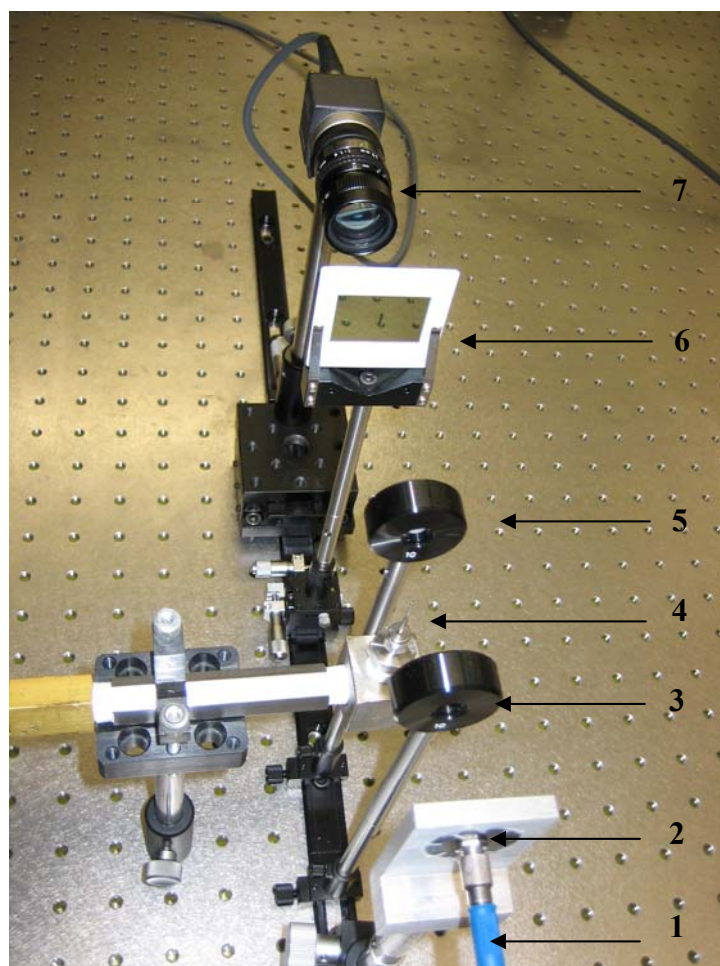
6.4.4 Unsteady flows

The use of the miniature schlieren system to investigate steady jets and flames was demonstrated in the preceding sections. As a next step, time-dependent behavior, in particular the jet/flame instabilities could also be studied using the schlieren system. Figure 6.20 shows representative rainbow schlieren images of an unsteady hydrogen jet diffusion flame from a 50 μm orifice. The images are shown at a spatial resolution of 12 $\mu\text{m}/\text{pixel}$. As the Reynolds number is increased, the breakpoint separating the laminar and turbulent regimes moves closer to the jet exit.

6.5 Conclusions

A miniature rainbow schlieren apparatus has been developed using off-the-shelf optical hardware. The spatial resolution of the system was determined by the focal length of the camera lens and the length of the extension tubes placed between the CCD array and camera lens. Although the miniature schlieren system was built on principles of the macro-scale rainbow schlieren apparatus, a careful evaluation of the optical components was performed. The miniature system was used to measure species concentration and/or temperature across the whole field of non-reacting and reacting micro-scale flows at spatial resolution of

20 μm . Results show that the structural features of macro-scale flows are replicated in micro-scale flows. The miniature schlieren apparatus was also used to visualize the shock flow structures of an under-expanded nitrogen jet at spatial resolution of 4 μm . The schlieren apparatus presented in this study is the smallest system of its kind, and it offers the prospects of developing a readily portable schlieren device for quantitative scalar measurements in non-reacting and reacting micro-scale flows, and eventually in turbulent flows.



- | | |
|----------------------|-----------------------|
| 1. Fiber optic cable | 5. Decollimating lens |
| 2. Slit /Aperture | 6. Rainbow Filter |
| 3. Collimating lens | 7. Camera Unit |
| 4. Test media | |

Figure 6.1. A photograph of the rainbow schlieren apparatus.



Figure 6.2. A photograph of the light source and the camera control unit.

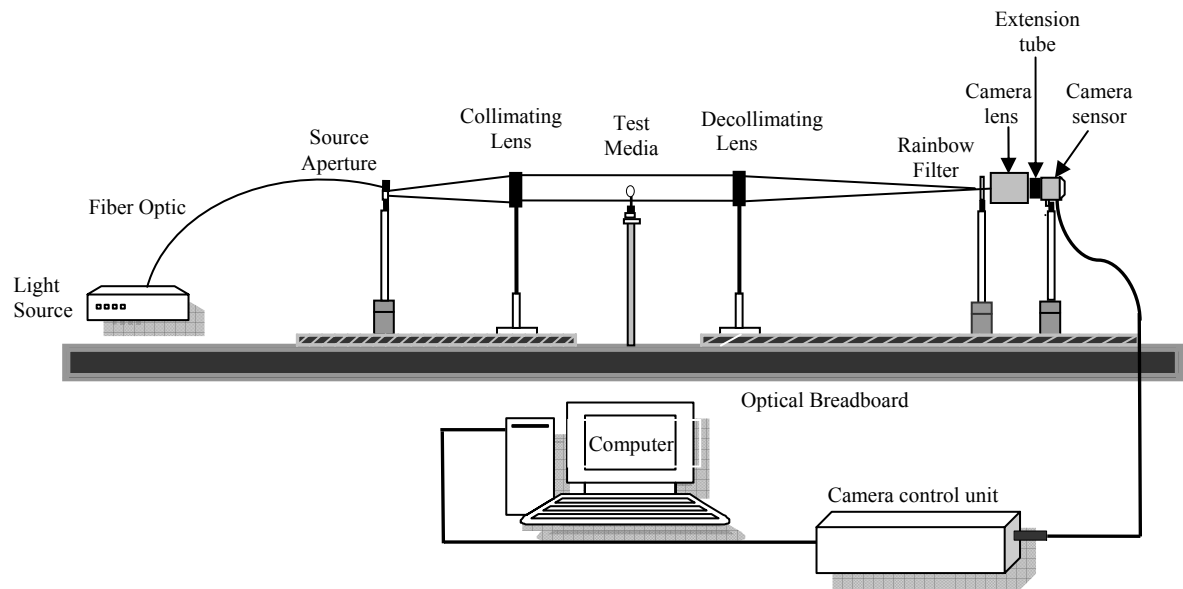


Figure 6.3. Optical layout of the miniature schlieren apparatus.



Figure 6.4. Rainbow filter.

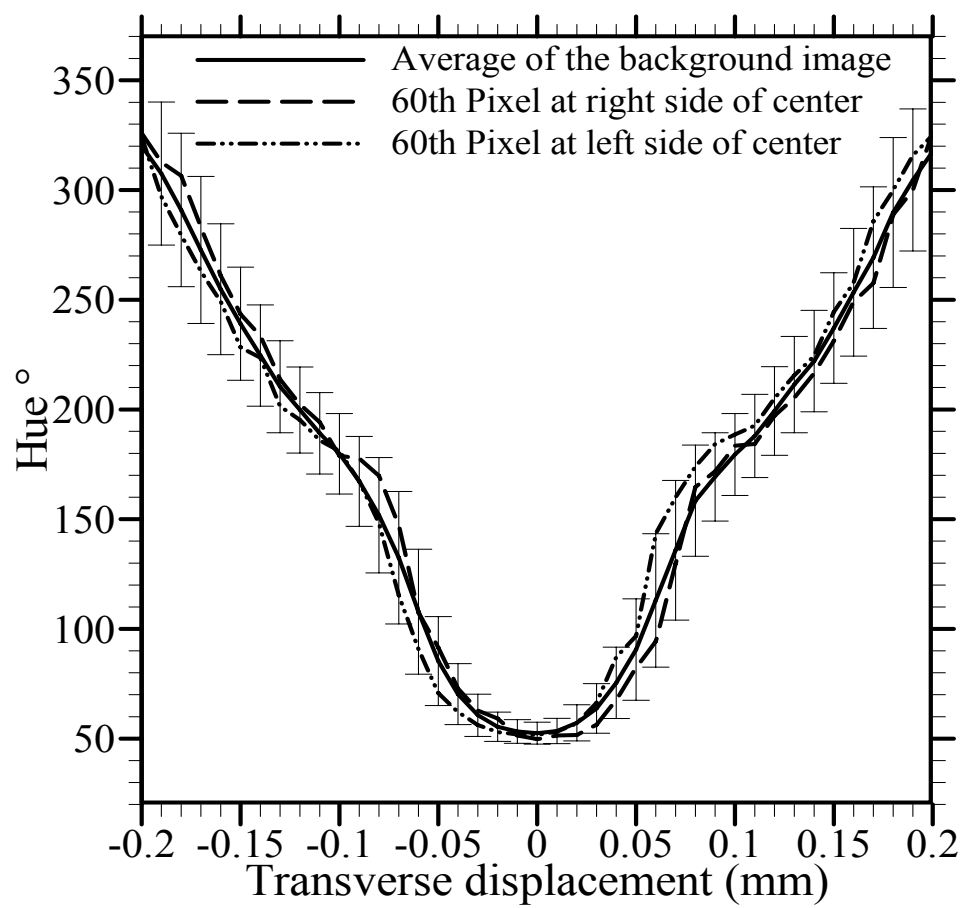


Figure 6.5. Filter calibration curves.

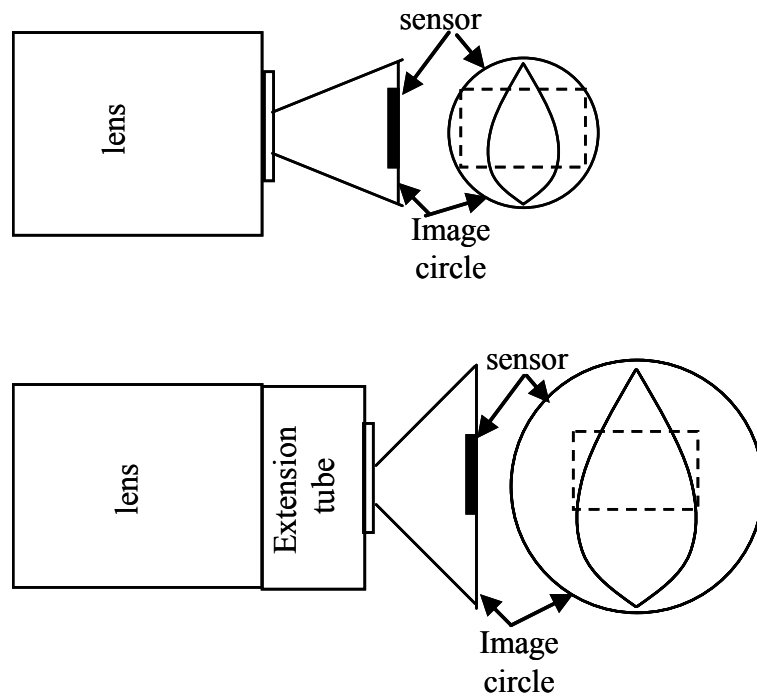


Figure 6.6. Schematic showing the working of the camera unit with (bottom) and without (top) the extension tube.

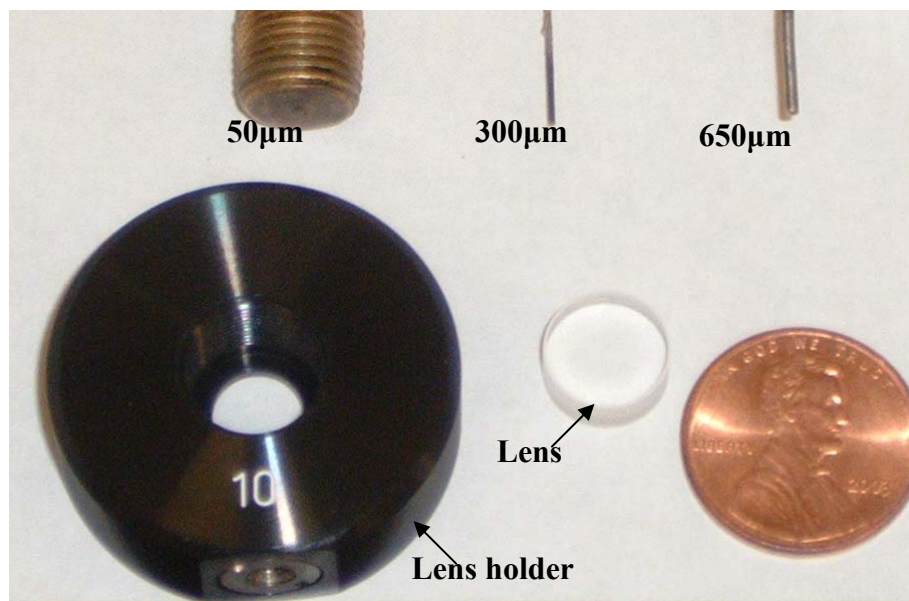


Figure 6.7. Optical components and injectors used for experiments.



Figure 6.8. Rainbow schlieren image for the helium jet, $d = 650 \mu\text{m}$, $\text{Re} = 375$.

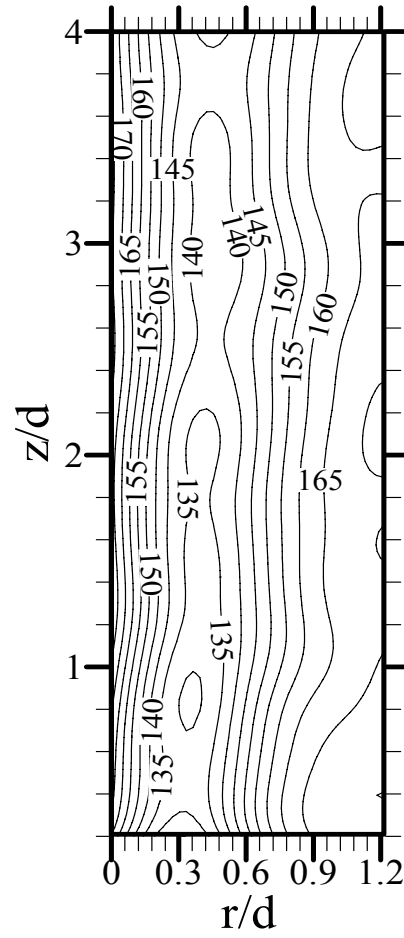


Figure 6.9. Hue contours for the helium jet, $d = 650 \mu\text{m}$, $\text{Re} = 375$.

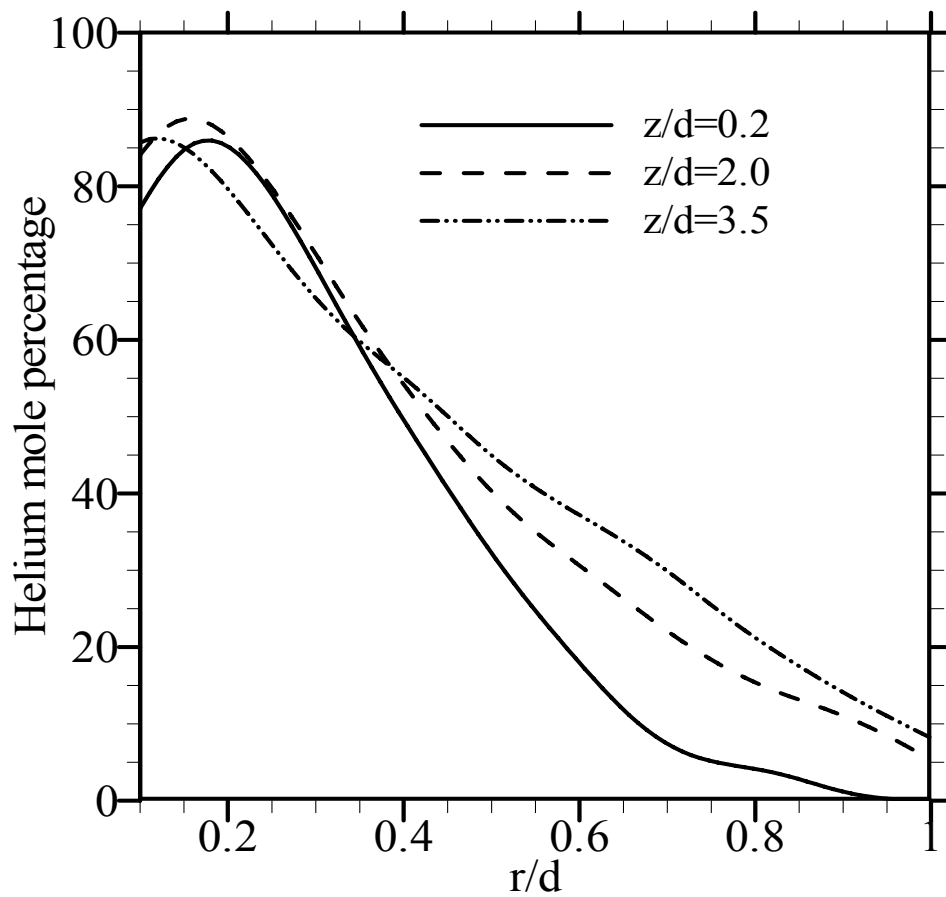


Figure 6.10. Radial profiles of helium mole percentage, $d = 650 \mu\text{m}$, $\text{Re} = 375$.

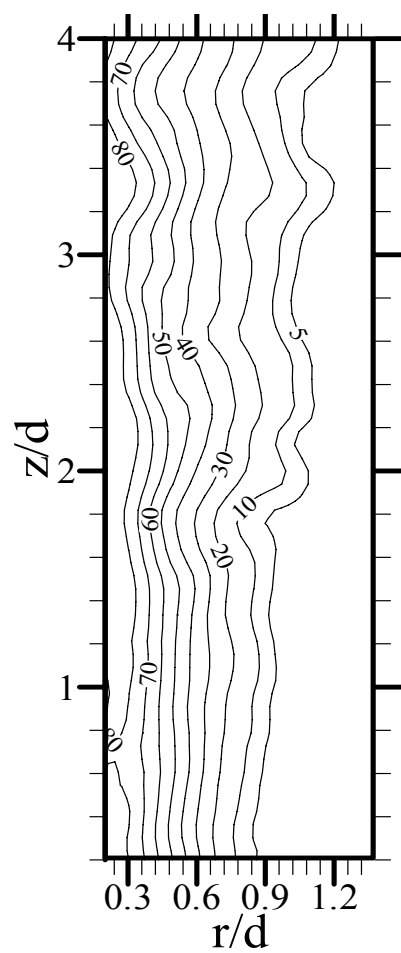


Figure 6.11. Contours of helium mole percentage, $d = 650 \mu\text{m}$, $\text{Re} = 375$.

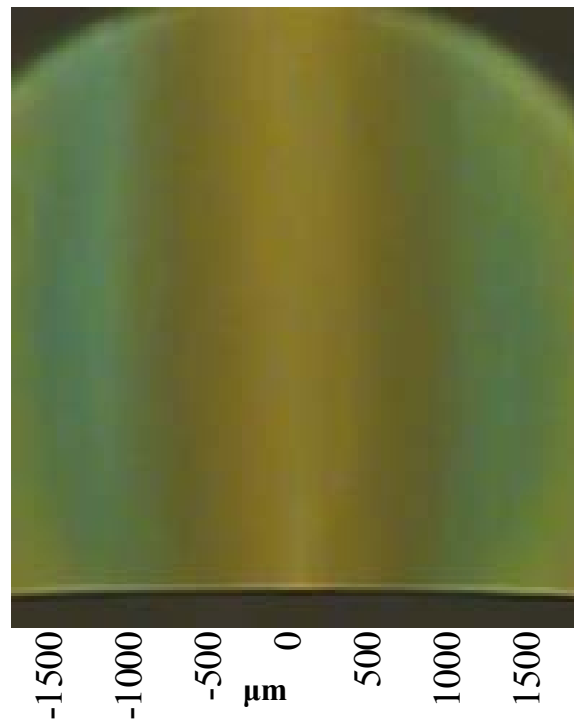


Figure 6.12. Rainbow schlieren image for the hydrogen diffusion flame, $d = 50 \mu\text{m}$, $\text{Re} = 410$.

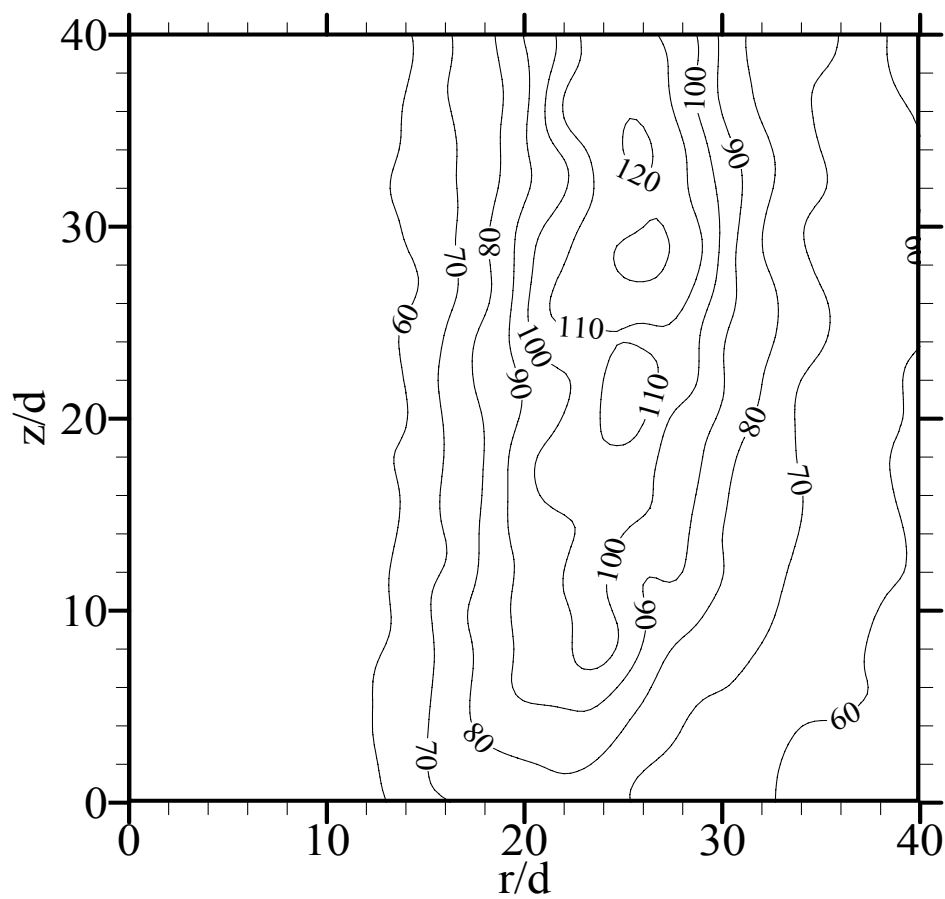


Figure 6.13. Hue contours for the hydrogen diffusion flame, $d = 50 \mu\text{m}$, $\text{Re} = 410$.

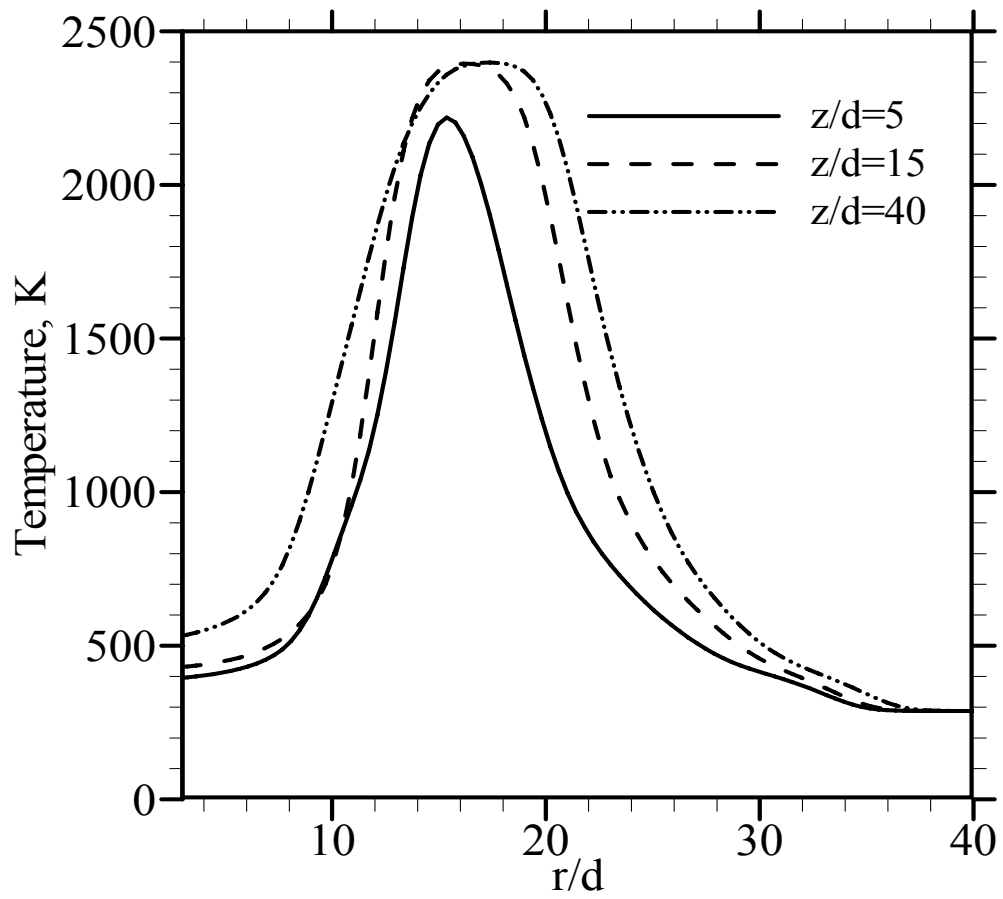


Figure 6.14. Radial profiles of temperature distribution, $d=50\text{ }\mu\text{m}$, $Re=410$.

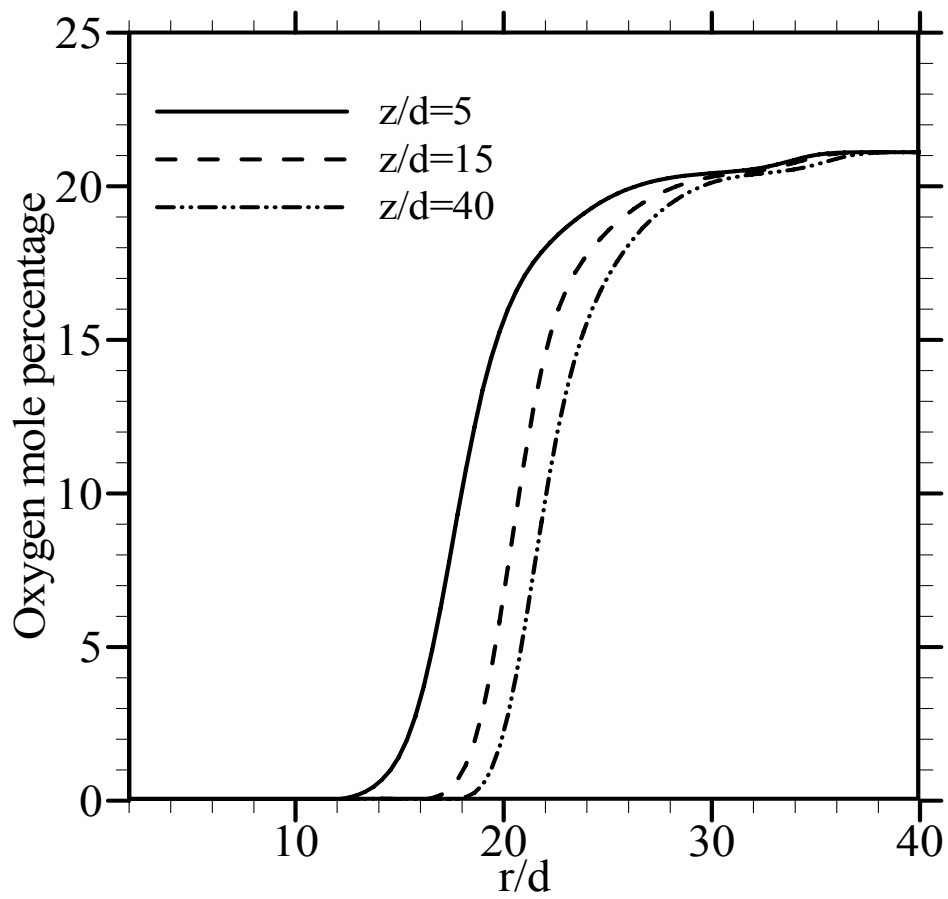


Figure 6.15. Radial profiles of oxygen mole percentage, $d=50\text{ }\mu\text{m}$, $Re=410$.

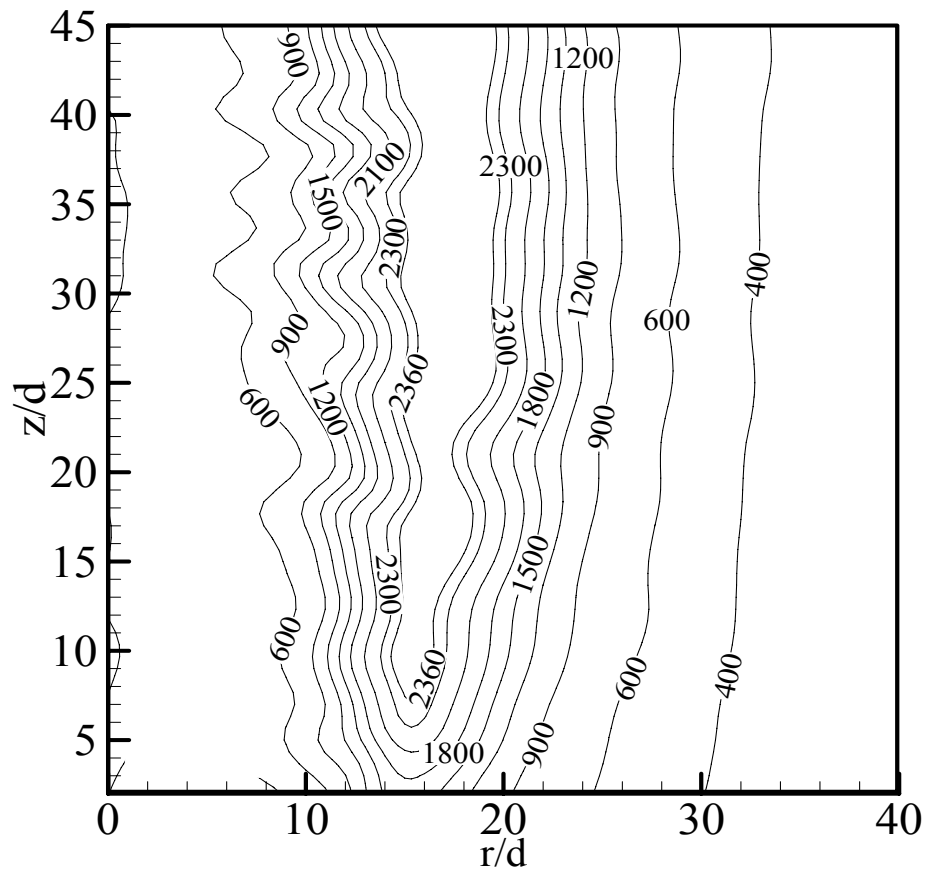


Figure 6.16. Contours of temperature distribution, $d = 50 \mu\text{m}$, $\text{Re} = 410$.

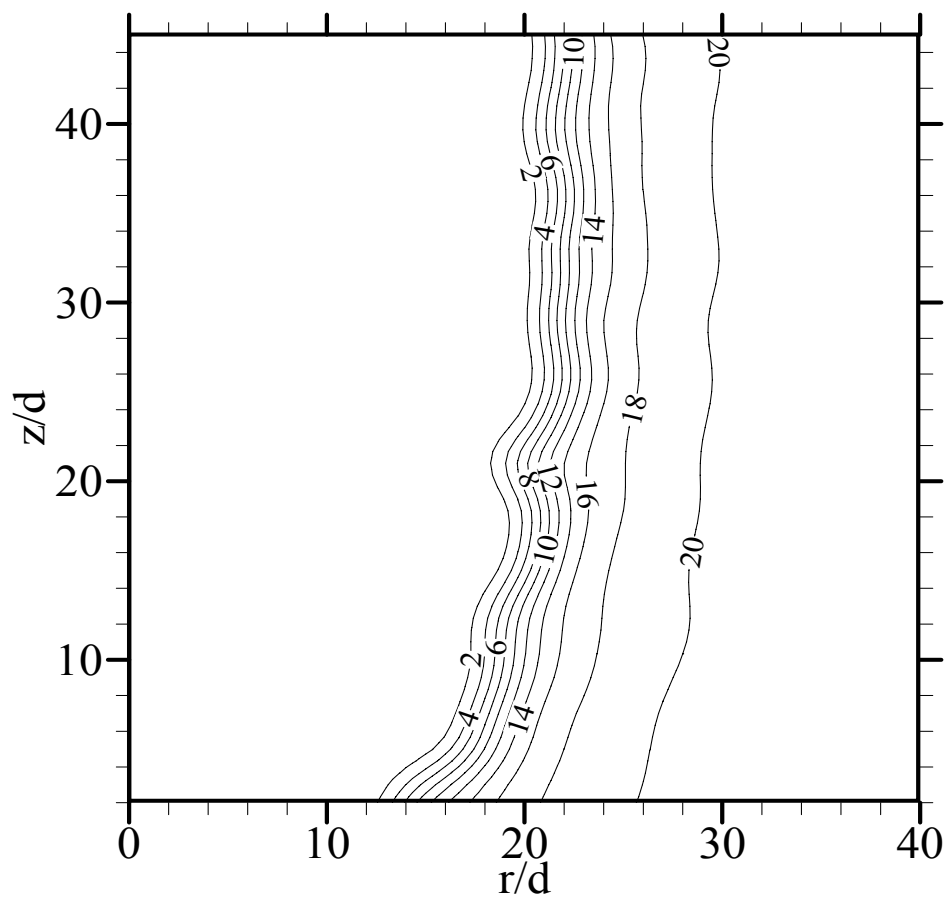


Figure 6.17. Contours of oxygen mole percentage, $d = 50 \mu\text{m}$, $\text{Re} = 410$.

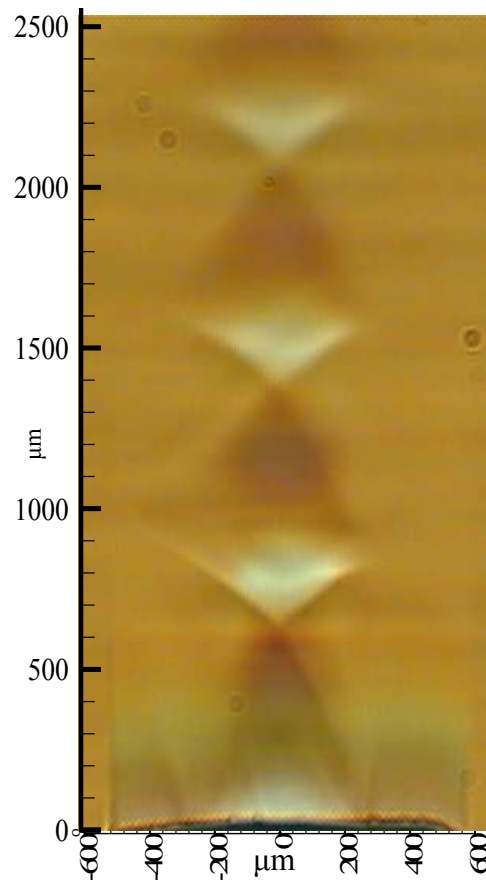


Figure 6.18. Schlieren images showing the formation of shock diamonds, $d = 650 \mu\text{m}$ at 60psi.

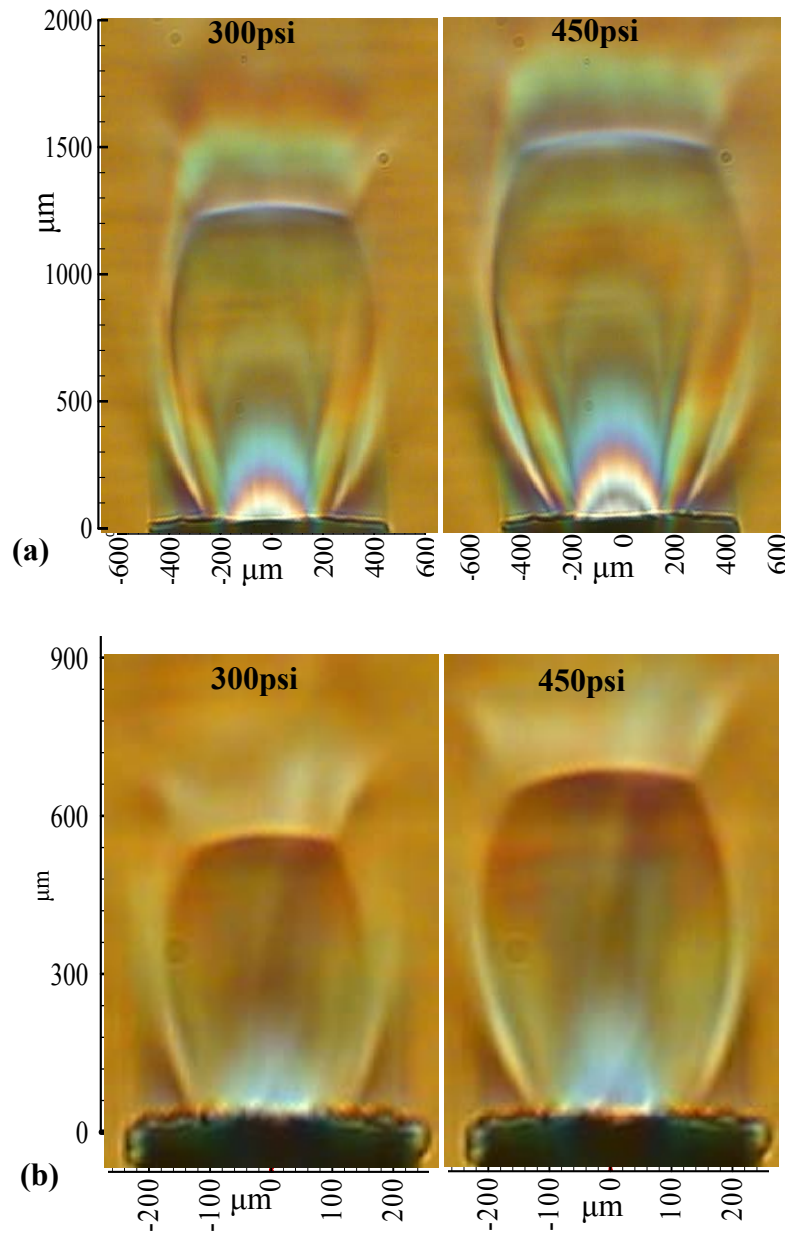


Figure 6.19. Schlieren images showing the effect of supply pressure on shock cell structure, a) $d = 650 \mu\text{m}$, b) $d = 300 \mu\text{m}$.

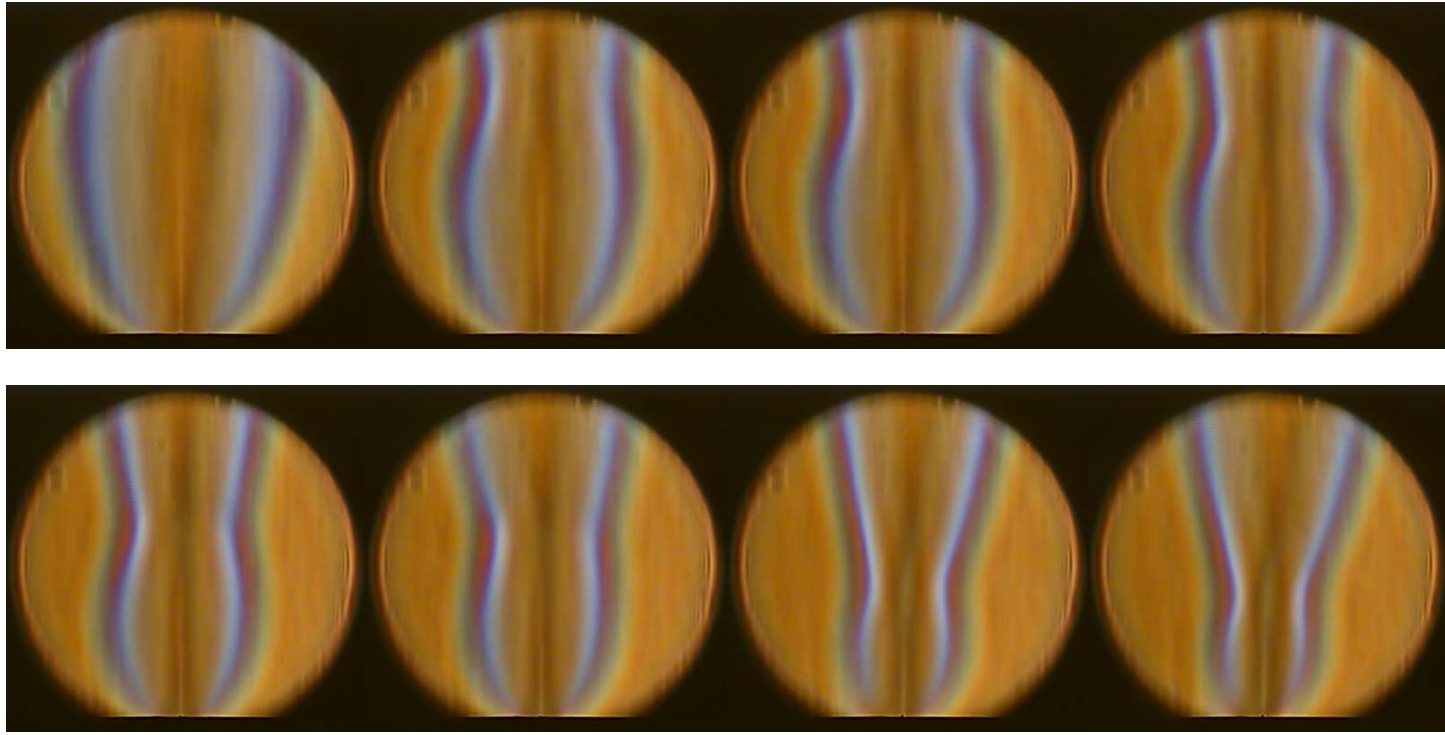


Figure 6.20. Schlieren images of a hydrogen diffusion flame, $d = 50 \mu\text{m}$.

7. CONCLUSIONS

The present research involved a combination of computational, theoretical and experimental studies to gain insight into the flow structure of laminar-turbulent jets/flames. The important conclusions of this study are given as follows:

- A CFD based model was developed to understand the global flow structure of laminar low-density gas jets. The validity of the model was verified by comparing computed results with existing experimental data. The unique flow features of steady and oscillating low-density gas jets were quantified by explaining the interactions among velocity and concentration fields. The mechanism of the laminar instability was also explored by relating to the shape of the concentration (or density) shear layer near the tube exit.
- The computational model was extended to delineate the effects of buoyancy in buoyant and inertial gas jets. It was found that a self-excited buoyant jet in Earth gravity becomes steady in microgravity. In an inertial jet, the flow oscillations occur at the same frequency regardless of the buoyancy, although the oscillation amplitude decreases in microgravity. Overall, the

physical implications of self-excited instability in low-density gas jets were explored.

- A crossbeam rainbow schlieren deflectometry (CRSD) system was developed to measure scalar turbulence quantities in jets and flames. Instantaneous, mean and RMS rainbow schlieren images of helium-air jets and hydrogen jet diffusion flames were presented to demonstrate the capability of the CRSD system. Analysis procedure to compute the scalar turbulence parameters from schlieren images obtained at orthogonal view angles was presented. Validity of the analysis procedures was verified using synthetic laminar/turbulent data.
- A miniature RSD system was developed to measure species concentration and/or temperature across the whole field of non-reacting and reacting micro-scale flows at spatial resolutions down to 20 μm . It was found that the structural features of macro-scale flows were replicated in micro-scale flows. The miniature schlieren apparatus was also used to visualize the shock flow structures of an under-expanded nitrogen jet at spatial resolution of 4 μm .

8. RECOMMENDATIONS

The current research involving numerical and experimental studies of jets/flames provides scope for several future investigations. Some of the recommendations are listed below:

- 1) The CFD model can be extended to study the oscillating flow structure of low-density gas jets by varying the operating conditions like jet-ambient fluid density ratio, exit velocity profiles, co-flow velocity, and tube configurations.
- 2) Based on the CFD analysis of non-reacting jets, numerical models incorporating chemical reactions could be developed to simulate reacting gas jet diffusion flames.
- 3) The laminar CFD model could serve as a valuable tool in eventually developing turbulence based models (DNS/LES) for conducting a complete laminar-turbulent simulation of jets/flames.
- 4) In the present study, the CRSD system was used to provide only schlieren visualizations of turbulent jets/flames. As a next step, the schlieren images must be post-processed using the crossbeam analysis procedures to obtain local turbulence data.
- 5) The local isotropy condition of turbulence is not completely satisfied in the synthetic data in part because of the inherent noise. Turbulent flow generation techniques which can exactly satisfy conditions of

local isotropy and homogeneity should be explored to provide a definite validation of crossbeam correlation technique.

- 6) The miniature RSD system could be extended to study the unsteady flow dynamics of oscillating jets and flickering flames at high spatial resolution.
- 7) The miniature RSD system could be configured in the crossbeam mode and used to resolve the fine scales of turbulence in jets and flames. In fact, one could configure the system in multiple angles to measure non-homogeneous anisotropic turbulence.
- 8) The optical hardware associated with the miniature RSD system could be further miniaturized. The prospects of using fiber optics instead of lenses should be explored.

BIBLIOGRAPHY

- Agrawal A.K., Butuk N., Gollahalli S.R., Griffin D. (1998), "Three-dimensional rainbow schlieren tomography of temperature field in gas flows," *Journal of Applied Optics*, 37, pp. 479-485.
- Al-Ammar K., Agrawal A.K., Gollahalli S.R., Griffin D. (1998), "Application of rainbow schlieren deflectometry for concentration measurements in an axisymmetric helium jet," *Experiments in Fluids*, 25, pp. 89-98.
- Albers B.W. and Agrawal A.K. (1999), "Schlieren analysis of flicker in an oscillating gas-jet diffusion flame," *Combustion and Flame*, 119, pp. 84-94.
- Ball G.A. and Bray K.C. (1990), "Measurement of turbulent density fluctuations by crossed beam correlation," *AIAA Journal*, 28 (6), pp. 1057-1064.
- Bird R.B., Stewart W.E., Lightfoot E.N. (1960). Transport phenomena. 1st edition. Wiley, New York.
- Buttner L., Czarske J., Knuppertz H. (2005), "Laser-doppler velocity profile sensor with submicrometer spatial resolution that employs fiber optics and a diffractive lens," *Journal of Applied Optics*, 44, pp. 2274-2280.
- Cetegen B.M. and Ahmed T.A. (1993), "Experiments on the periodic instability of buoyant plumes and pool fires," *Combustion and Flame*, 93, pp.157-184.
- Cetegen B.M. and Kasper K.D. (1996), "Experiments on the oscillatory behavior of buoyant plumes of helium and helium-air mixtures," *Physics of Fluids*, 8 (11), pp. 2974-2984.
- Cetegen B.M. (1997a), "Behavior of naturally unstable and periodically forced axisymmetric buoyant plumes of helium and helium-air mixtures," *Physics of Fluids*, 9 (12), pp. 3742-3753.
- Cetegen B.M. (1997b), "Measurements of instantaneous velocity field of a non-reacting pulsating buoyant plume by particle image velocimetry," *Combustion Science and Technology*, 123 (1-6), pp. 377-387.

- Corrsin S. (1943), "Investigation of flow in an axially symmetrical heated jet of air," NACA, Wash. Wartime Report, W-94.
- Corrsin S. and Uberoi M.S. (1950), "Further experiments on the flow and heat transfer in a heated turbulent air jet", NACA Rep. TN 1865.
- Corrsin S. (1951), "On the spectrum of isotropic temperature fluctuations in isotropic turbulence," *Journal of Applied Physics*, 22, pp. 469-473.
- Corrsin S. and Uberoi M. S. (1951), "Spectra and diffusion in a round turbulent jet," NACA Rep, 1940.
- Dai Z., Tseng L.K., Faeth G.M. (1994), "Structure of round, fully developed, buoyant turbulent plumes," *Journal of Heat Transfer*, 116 (2), pp.409-417.
- Dasch C.J. (1992), "One-dimensional tomography: a comparison of Abel, onion-peeling, and filtered back projection methods," *Applied Optics*, 31 (8), pp. 1146-1152.
- Davis M.R. (1975), "Intensity, scale and convection of turbulent density fluctuations," *Journal of Fluid Mechanics*, 70, pp. 463-479.
- Davis M.R. and Rerkshanandana P. (1993), "Schlieren measurement of turbulent structure in diffusion flame," *Experimental Thermal and Fluid Science*, 6, pp. 402-416.
- Davis M.R. and Rerkshanandana P. (1994), "Integral scales and mixing lengths in turbulent mixing and combustion," *Experimental Thermal and Fluid Science*, 8, pp. 239-244.
- Davis M.R. and Rerkshanandana P. (1991), "Influence of large eddies on thermal mixing," *International Journal of Heat and Mass Transfer*, 34 (7), pp. 1633-1647.
- Davis M.R. (1989), "Turbulent refractive index fluctuations in a hydrogen diffusion flame", *Combustion Science and Technology*, 64, pp. 51-65.
- Dehmani L., Doan Kim-Son, Gbahoue L. (1996), "Turbulent structure of an axisymmetric plume penetrating strong density stratification," *International Journal of Heat and Fluid Flow*, 17 (5), pp.452-459.

- Dowling D.R. and Dimotakis P.E. (1990), "Similarity of the concentration field of gas phase turbulent jets," *Journal of Fluid Mechanics*, 218, pp.109-141.
- Fay J.A. (1973), "Buoyant plumes and wakes," *Annual Review of Fluid Mechanics*, 5, pp.151-160.
- Feikema D.A. (2006), "Quantitative rainbow schlieren deflectometry as a temperature diagnostic for nonsooting spherical flames," *Journal of Applied Optics*, 45, pp. 4826-4832.
- Fisher M.J. and Krause F.R. (1967), "The crossed-beam correlation technique," *Journal of Fluid Mechanics*, 28 (4), pp. 705-717.
- Fluent 6 User's guide, FLUENT Inc., Lebanon, NH (2005).
- Gad-el-Hak M. (1999), "The fluid mechanics of microdevices – the freeman scholar lecture," *Journal of Fluids Engineering*, 121, pp. 5-33.
- Geankoplis C.J. (1972). *Mass Transport Phenomena*. Holt, Rinehart and Winston, New York.
- Gebhart B. (1973), "Instability, transition, and turbulence in buoyancy-induced flows," *Annual Review of Fluid Mechanics*, 5, pp. 213-246.
- Gravesen P., Branebjerg J., Jensen O.S. (1993), "Microfluidics - a review," *Journal of Micromech Microeng*, 3, pp.168-182.
- Greenberg P.S., Klimek R.B., Buchele D.R. (1995), "Quantitative rainbow schlieren deflectometry," *Journal of Applied Optics*, 34, pp. 3810-3822.
- Hamins A., Yang J.C., Kashiwagi T. (1992), "An experimental investigation of the pulsating frequency of flames," *Proceedings of the Combustion Institute*, 24, pp.1695-1705.
- Hussein H.J., Capp S.P., George W.K. (1994), "Velocity measurements in a high Reynolds number, momentum-conserving axisymmetric turbulent jet," *Journal of Fluid Mechanics*, 258, pp. 31-75.
- Ibarreta A.F. and Sung C.J. (2005), "Flame temperature and location measurements of sooting premixed bunsen flames by rainbow schlieren deflectometry," *Journal of Applied Optics*, 44, pp. 3565-3575.

- Kalghatgi G.T., Cousins J.M., Bray K.N.C. (1981), "Crossed beam correlation measurements and model predictions in a rocket exhaust plume," *Combustion and flame*, 43, pp. 51-67.
- Katta V.R. and Goss L.P. (1994), "Numerical investigations of transitional H₂/N₂ jet diffusion flames," *AIAA Journal*, 32, pp. 84-94.
- Kihm K.D. (2003), "Development and applications of advanced flow visualization techniques for microscale heat and mass transport," Proceedings of PSFVIP-4, Chamonix, France.
- Kraichnan R. (1970), "Diffusion by random velocity field," *Physics of Fluids*, 11, pp.43-52.
- Kyle D.M. (1991), "The instability and breakdown of a round variable-density jet," *Doctoral Dissertation*, Yale University.
- Lai J.C.S. (1984), "Unsteady effects in mechanically excited turbulent plane jets," *International Journal of Heat and Fluid Flow*, 5 (4), pp. 215-221.
- List E.J. (1982), "Turbulent jets and plumes," *Annual Review of Fluid Mechanics*, 14, pp.189-212.
- Meinhart C.D. and Zhang H. (2000), "The flow structure inside a microfabricated inkjet printhead," *J. Micro electromechanical systems*, 9, pp. 67-75
- Mell W.E., McGrattan K.B., Baum H.R. (1996), "Numerical simulation of combustion in fire plumes," *Proceedings of the Combustion Institute*, 26, pp.1523-1530.
- Mollendorf J.C. and Gebhart B. (1973), "An experimental and numerical study of the viscous stability of a round laminar vertical jet with and without thermal buoyancy for symmetric and asymmetric disturbances," *Journal of Fluid Mechanics*, 61, pp. 367-399.
- Monkewitz P.A., Bechert D.W., Bariskov B., Lehmann B. (1990), "Self excited oscillations and mixing in a heated round jet," *Journal of Fluid Mechanics*, 213, pp. 611-639.

- Onofri F. (2006), "Three interfering beams in laser doppler velocimetry for particle position and micro flow velocity profile measurements," *Journal of Applied Optics*, 45, pp. 3317-3324.
- Panchapakesan N.R. and Lumley J.L. (1993), "Turbulence measurements in axisymmetric jets of air and helium. Part 2. Helium jet," *Journal of Fluid Mechanics*, 246, pp. 225-248.
- Papanicolaou P.A. and List E.J. (1988), "Investigations of round vertical turbulent buoyant jets," *Journal of Fluid Mechanics*, 195, pp. 342-391.
- Pasumarthi K.S (2004), "Buoyancy effects on flow structure and instability of low-density gas jets," *Doctoral Dissertation*, University of Oklahoma.
- Pasumarthi K.S. and Agrawal A.K. (2005), "Buoyancy effects on flow transition in low-density inertial gas jets," *Experiments in Fluids*, 38, pp. 541-544.
- Pasumarthi K.S. and Agrawal A.K. (2003), "Schlieren measurements and analysis of concentration field in self-excited helium jets," *Physics of Fluids*, 15 (12), pp. 3683-3692.
- Pera L. and Gebhart B. (1963), "On the stability of laminar plumes: Some numerical solutions and experiments," *International Journal of Heat and Mass Transfer*, 14, pp.597-606.
- Phalnikar K.A., Alvi F.S., Shih C. (2001), "Behavior of free and supersonic impinging microjets," AIAA paper 2001-3047, Anaheim, CA.
- Richards C.D. and Pitts W.M. (1993), "Global density effects on the self-preservation behavior of turbulent free jets," *Journal of Fluid Mechanics*, 254, pp. 417-435.
- Rodi W. (1982), "Turbulent buoyant jets and plumes," *International Journal of Heat and Fluid Flow*, 3 (4), pp.194.
- Santiago J.G., Wereley S.T., Meinhart C.D., Beebe D.J., Adrian R.J. (1998), "A micro particle image velocimetry system," *Experiments in Fluids* 25, pp. 316-319

- Sato H., Kushida G., Amagai K., Arai M. (2002), "Numerical analysis of the gravitational effect on the buoyancy-driven fluctuations in diffusion flames," *Proceedings of the Combustion Institute*, 29, pp. 1671-1678.
- Satti R.P. and Agrawal A.K. (2004), "Numerical analysis of flow evolution in a helium jet injected into ambient air," ASME Heat Transfer/ Fluids Engineering Summer Conference, HT-FED2004-56811.
- Satti R.P. and Agrawal A.K. (2006), "Flow structure in the near-field of buoyant low-density gas jets," *International Journal of Heat and Fluid Flow*, 27(2), pp. 336-347.
- Scroggs S.D. and Settles G.S. (1996), "An experimental study of supersonic microjets," *Experiments in Fluids*, 21, pp. 401-409.
- Shenoy A.K., Agrawal A.K., Gollahalli S.R. (1998), "Quantitative evaluation of flow computations by rainbow schlieren deflectometry," *AIAA Journal*, 36, pp. 1953-1960.
- Soteriou M.C., Dong Y., Cetegen B.M. (2002), "Lagrangian simulation of the unsteady near field dynamics of planar buoyant plumes," *Physics of Fluids*, 14 (9), pp. 3118-3140.
- Smirnov A., Shi S., Celik I. (2001), "Random flow generation technique for large eddy simulations and particle dynamics modeling," *ASME Journal of Fluids Engineering* 123, pp.359-371
- Sreenivasan K.R., Raghu S., Kyle D.M. (1989), "Absolute instability in variable density round jets," *Experiments in Fluids*, 7, pp. 309-317.
- Subbarao E.R. and Cantwell B.J. (1992), "Investigation of a co-flowing buoyant jet: experiments on the effects of reynolds number and richardson number," *Journal of Fluid Mechanics*, 245, pp. 69-90.
- Synnergren P., Larsson L., Lundstrom T.S. (2002), "Digital speckle photography: visualization of mesoflow through clustered fiber networks," *Journal of Applied Optics*, 41, pp. 1368-1373.
- Tenner A.R. and Gebhart B. (1971), "Laminar and axisymmetric vertical jets in a stably stratified environment," *International Journal of Heat and Mass Transfer* 14 (12), pp. 2051-2062.

- Wilson L.N. and Damkevala, R.J. (1970), "Statistical properties of turbulent density fluctuations," *Journal of Fluid Mechanics*, 43, pp. 291-303.
- Winarto H. and Davis M.R. (1984), "Fluctuations of density, pressure and temperature in a turbulent mixing region", *Proceedings of Royal Society London A* 395, pp. 203-228.
- Wong T. and Agrawal A.K. (2006), "Quantitative measurements in an unsteady flame using high-speed rainbow schlieren deflectometry," *Measurement Science and Technology*, 17, pp.1503-1510.
- Wynanski I. and Fiedler H.E. (1969), "Some measurements in the self preserving jet," *Journal of Fluid Mechanics*, 38, pp. 577-612.
- Xiao X., Puri I.K., Agrawal A.K. (2002), "Temperature measurements in steady axisymmetric partially premixed flames using rainbow schlieren deflectometry," *Journal of Applied Optics*, 41, pp.1922-1928.
- Yep T.W., Agrawal A.K., Griffin D.W. (2003), Gravitational effects on near field flow structure of low density gas jets," *AIAA Journal*, 41, pp.1973-1979.
- Yildirim B.S. and Agrawal A.K. (2005), "Full-field measurements of self-excited oscillations in momentum-dominated helium jets," *Experiments in Fluids*, 38, pp. 161-173.

APPENDIX A: NOMENCLATURE

d	tube inside diameter (mm)
D_b	mass diffusion coefficient (m^2/s)
f	frequency (Hz)
g	acceleration due to gravity (m/s^2)
r	radial coordinate
Re	Jet Reynolds number, $Re=U_j d/\nu_j$
Ri	Jet Richardson number, $Ri=gd(\rho_\infty - \rho)/\rho U_j^2$
St	Jet Strouhal number, $St=fd/U_j$
U_j	average jet exit velocity (m/s)
v_r	radial component of velocity (m/s)
v_z	axial component of velocity (m/s)
Y	mole fraction
z	axial coordinate

Greek Symbols

μ	dynamic viscosity of jet fluid (kg-m/sec)
ν_j	kinematic Viscosity of jet fluid (m^2/sec)
ρ_j	density of jet fluid (kg/m^3)
ρ_∞	density of ambient fluid (kg/m^3)

APPENDIX B: DETAILS OF THE CFD MODEL

FLUENT

Version: axi, segregated, spe, lam, unsteady (axi, segregated, species, laminar, unsteady)

Models

<u>Model</u>	<u>Settings</u>
Space	Axisymmetric
Time	Unsteady, 2nd-Order Implicit
Viscous	Laminar
Species Transport	Non-Reacting (2 species)

Zones

<u>name</u>	<u>id</u>	<u>type</u>
fluid	2	fluid
jetinlet	9	velocity-inlet
interior	3	interior
wall	4	wall
pressureinlet	5	pressure-inlet
pressureoutlet1	6	pressure-outlet
pressureoutlet	7	pressure-outlet
symmetry	8	axis
default-interior	11	interior

```
-----
Time Step (s)                0.00167
Max. Iterations Per Time Step 250
```

Relaxation

<u>Variable</u>	<u>Relaxation Factor</u>
Pressure	0.2
Density	0.2
Body Forces	0.2
Momentum	0.2
he	0.2

Discretization Scheme

<u>Variable</u>	<u>Scheme</u>
Pressure	Standard
Momentum	QUICK
he	QUICK

Material Properties

Material: air (fluid)

Property	Units	Method	Value(s)
Density	kg/m ³	constant	1.225
Cp (Specific Heat)	J/kg-K	constant	1006.43
Thermal Conductivity	W/m-K	constant	0.0242
Viscosity	kg/m-s	constant	1.7894e-05
Molecular Weight	kg/kmol	constant	28.966

Material: helium (fluid)

Property	Units	Method	Value(s)
Density	kg/m ³	constant	0.1625
Cp (Specific Heat)	J/kg-K	constant	5193
Thermal Conductivity	W/m-K	constant	0.152
Viscosity	kg/m-s	constant	1.99e-05

Wilke's mixture averaged formula for mixture viscosity:

$$\mu = \frac{\sum_i X_i \mu_i}{\sum_j X_i \phi_{ij}} = \frac{X_1 \mu_1}{X_1 \phi_{11} + X_1 \phi_{12}} + \frac{X_2 \mu_2}{X_2 \phi_{21} + X_2 \phi_{22}} \quad (6)$$

$$\phi_{ij} = \frac{\left[1 + \left(\frac{\mu_i}{\mu_j} \right)^{1/2} \left(\frac{M_{w,j}}{M_{w,i}} \right)^{1/4} \right]^2}{\left[8 \left(1 + \frac{M_{w,i}}{M_{w,j}} \right) \right]^{1/2}}$$

where subscripts 1 and 2 represent helium and air, respectively.

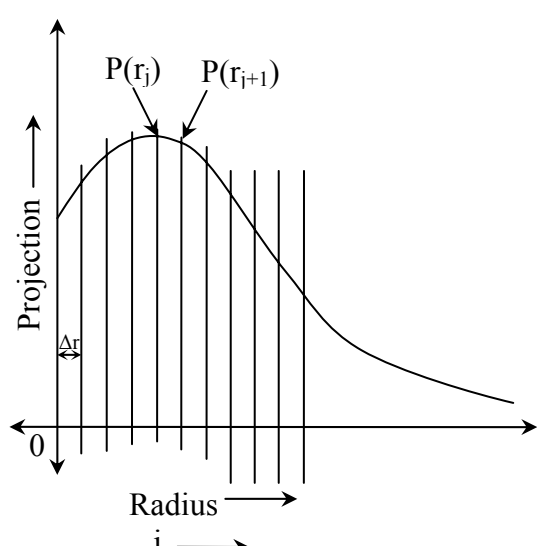
APPENDIX C: ABEL INVERSION

Derivation of Dasch's 2-point formula (1992):

Projection Data: $P(r) = 2 \int_y^\infty r \cdot f(r) \cdot \frac{dr}{\sqrt{(r^2 - y^2)}} \quad (\text{forward integral})$

Inversion: $f(r) = \frac{-1}{\pi} \int_y^\infty P'(r) \cdot \frac{dr}{\sqrt{(r^2 - y^2)}} \quad (\text{Abel's integral transform})$

Above equation is broken into various segments



$$f(r_i) = \frac{-1}{\pi} \sum_{j=i}^{\infty} \left(\int_0^{\Delta r} P'(r_j + \delta) \cdot \frac{d\delta}{\sqrt{((r_j + \delta)^2 - r_i^2)}} \right)$$

Substituting
 $P'(r_j + \delta) = [P(r_{j+1}) - P(r_j)] / \Delta r$
 & $r_j = j \times \Delta r$

$$f(r_i) = \frac{-1}{\pi} \cdot \frac{1}{\Delta r} \cdot \sum_{j=i}^{\infty} \left(\int_0^1 [P(r_{j+1}) - P(r_j)] \cdot \frac{d\delta}{\sqrt{((j + \delta)^2 - i^2)}} \right)$$

$$\Rightarrow f(r_i) = -\frac{1}{\Delta r} \cdot \sum_{j=i}^{\infty} \left[[P(r_{j+1}) - P(r_j)] \cdot \frac{1}{\pi} \cdot \left(\int_0^1 \frac{d\delta}{\sqrt{((j + \delta)^2 - i^2)}} \right) \right]$$

$$\Rightarrow f(r_i) = -\frac{1}{\Delta r} \cdot \sum_{j=i}^{\infty} \left[[P(r_{j+1}) - P(r_j)] \cdot J_{i,j} \right] \quad \& \quad J_{i,j} = \frac{1}{\pi} \cdot \left(\int_0^1 \frac{d\delta}{\sqrt{((j + \delta)^2 - i^2)}} \right)$$

The integral expression J_{ij} can be solved analytically

$$J_{i,j} = \frac{1}{\pi} \cdot \ln \left(\frac{j+1 + \sqrt{(j+1)^2 - i^2}}{j + \sqrt{j^2 - i^2}} \right)$$

Similar expression can be written for $f(r_{i-1}) = -\frac{1}{\Delta r} \cdot \sum_{j=i}^{\infty} \left[\left[P(r_j) - P(r_{j-1}) \right] \cdot J_{i,j-1} \right]$

Collecting the common terms yield

$$f(r_i) = \frac{1}{\Delta r} \cdot \sum_{j=i}^{\infty} (D_{ij} \cdot P(r_j))$$

where $D_{i,j} = 0$ for $j < i$; $D_{i,j} = J_{i,j}$ for $j = i$ & $D_{i,j} = J_{i,j} - J_{i,j-1}$ for $j > i$

$$D_{i,j} = \frac{1}{\pi} \cdot \ln \left(\frac{j+1 + \sqrt{(j+1)^2 - i^2}}{\sqrt{(j-1)^2 - i^2} + j-1} \right)$$

APPENDIX D: TRAPEZOIDAL RULE OF INTEGRATION

The trapezoidal rule of integration is an approximate method for finding an approximate value of a definite integral. Suppose we have the definite integral

$$\int_a^b f(x)dx$$

First, the area under the curve $y=f(x)$ is divided into n strips, each of equal width $h = (b-a)/n$. The area of each strip is then approximated to be that of a trapezium. The sum of these trapezoidal areas gives an approximation for the definite integral $\int_a^b f(x)dx$. The shape of each strip is approximated to be like that

of a trapezium. Hence the area of the first strip is approximately

$$\frac{h}{2}(f(a) + f(a+h))$$

similarly we approximate the area of the i^{th} strip to be

$$\frac{h}{2}(f(a+(i-1)h) + f(a+ih))$$

Adding up these areas gives us an approximate value for the definite integral:

$$\int_a^b f(x)dx \approx \sum_{i=1}^n \frac{h}{2}(f(a+(i-1)h) + f(a+ih))$$

This estimate generally improves as n increases.